2015-07-02

Crystal Chemistry of Zircon and Monazite: Crystal Structure, Major and Trace Elements, and Radiation Damage

Zaman, Md. Mashrur

UNIVERSITY OF CALGARY

Crystal Chemistry of Zircon and Monazite: Crystal Structure, Major and Trace Elements, and Radiation Damage

By

Md. Mashrur Zaman

A THESIS

SUBMITTED TO THE FACULTY OF GRADUATE STUDIES

IN PARTIAL FULFILMENT OF THE REQUIREMENTS FOR THE

DEGREE OF DOCTOR OF PHILOSOPHY

GRADUATE PROGRAM IN GEOLOGY AND GEOPHYSICS

CALGARY, ALBERTA

JUNE, 2015

Abstract

This study investigates the crystal structural variations and their relation to chemical composition and radiation effects of detrital zircon and monazite, and the elevated radionuclide concentrations in zircon and monazite-rich heavy mineral deposits in Cox's Bazar, Bangladesh. Several experimental techniques such as electron-probe micro-analysis (EPMA), single-crystal X-ray diffraction (SCXRD), synchrotron high-resolution powder X-ray diffraction (HRPXRD), gamma-ray spectroscopy with hyper-purity germanium detector (GRS-HPGe), and gravity, magnetic, and electrical mineral separators have been used to carry out this research. In addition, several software programs including SHELX, WinGX, GSAS-EXGUI, Crystal Maker, and Gamma-W have also been applied for data processing and analysis.

The unit-cell parameters for the eight zircon samples vary linearly with increasing unit-cell volume, *V*. The detrital zircon sample 7:PIF (Perry Island Formation) from the Canadian Arctic Islands has the lowest unit-cell parameters and bond distances, ideal stoichiometric composition, and is unaffected by α-radiation damage. Thus, sample 7:PIF is chemically and structurally pure zircon. Sample 8 from Jemaa, Nigeria shows the significant change throughout the synchrotron HRPXRD trace and reveals the largest structural parameters after the Rietveld refinement. Samples 1 to 7 show very good correlations between the *V* and Zr and Si *apfu* contents. They received α-radiation doses which are lower than ~3.5×10^{15} α-decay events/mg. Substitutions of other cations at the Zr and Si sites control the variations of structural parameters for samples 1 to 7. The sample 5 shows relatively long unit-cell parameters and bond distances because the Zr site accommodates other cations that have higher ionic radii. Geological age increases the radiation doses in zircon and it is also related to the *V*.

The *a* and *b* unit-cell parameters for monazite samples 1, 2, 3, and 4 vary systematically with *V*, although each monazite sample contains several cations that occupy the Ce/Sm site in the monazite structure. However, the *c* unit-cell parameter shows limited variation. The increase or

decrease of the average <Ce/Sm-O> distances is dependent on the type of cations occupying the Ce site in the monazite structure but the average <P-O> distances is independent showing a rigid body behavior obtained with SCXRD and EPMA. The HRPXRD data shows pegmatitic Ce-dominated monazite contains multiple phases and Sm-dominated monazite has a single phase. The multiple phases in sample 2a may not be crystallized at the same time because the average <P-O> distances differ. Redistribution of Ce and P site cations with Y in sample 2a is also indicative late recrystallization of phases 2a and 2c. As the pegmatitic monazite sample 2a received a high amount of α-radiation doses, the phase changes occur for the effects of α-radiation.

The activity concentrations for ^{238}U, ^{235}U, ^{232}Th and ^{40}K in bulk beach sand samples are found to be considerably high and positively correlated to the amount of heavy minerals present in the sands. In the separated mineral fractions, the highest activity concentration was found in the zircon followed by garnet, rutile, ilmenite and magnetite fractions. The determination of the radium activity, several radiation hazard indices, and absorbed and effective gamma doses allow to assess the related exposure of the coastal environment and the local population to elevated radioactivity. It becomes evident from the present study that if raw sands or mineral fractions mined in the study area are used for building purposes or industrial use, their activity concentrations have to be considered from a radio-ecological perspective and if mining and processing of the minerals is being considered, U and Th may become strategically significant by-products.

Acknowledgements

I would like to express my deepest gratitude and cordial thanks to my supervisor, Dr. Sytle M. Antao for allowing me this opportunity to study under her supervision. Her continuous encouragement, valuable instructions, criticisms, and appropriate guidance inspired me to accomplish this research. I express my cordial thanks to my Ph. D. supervisory committee members for valuable discussions and precise comments after seeing my thesis.

I am grateful to Dr. Robert Marr for his kind help in collecting electron-probe micro-analysis data and to Dr. Masood Parvez, Department of Chemistry, University of Calgary, for his help in collecting single-crystal X-ray diffraction data.

The HRPXRD data were collected at the X-ray Operations and Research beamline 11-BM, Advanced Photon Source (APS), and Argonne National Laboratory (ANL). Use of the APS was supported by the U.S. Department of Energy, Office of Science, Office of Basic Energy Sciences, under Contract No. DE-AC02-06CH11357. Part of this study was supported with an NSERC Discovery grant.

Gamma-ray spectroscopic analysis was conducted under a Technical Cooperation project (BGD/7/006) of international atomic energy agency (IAEA) at the Department of Analytical Chemistry of the Centre for Environmental Research (UFZ) in Leipzig, Germany. I am thankful to the IAEA for this technical and financial support. I am also grateful to the Department of Analytical Chemistry of UFZ for the help in gamma-ray spectroscopic analysis.

I would like to extend our thanks to the scientific and technical staffs of Beach Sand Minerals Exploitation Centre, Bangladesh Atomic Energy Commission, Bangladesh for their help during sampling and sample preparation.

Dedication

This thesis is dedicated to my mother who always encourages, supports, and inspires me in every aspect of life with her positive, grateful, and respectful attitudes in life.

Table of Contents

List of Tables

List of Figures

List of Symbols, Abbreviations and Nomenclature

Symbol	Definition
a, b & c	Unit-cell axial dimension
V	Unit-cell volume
α, β & γ	Unit-cell angular dimension
U	Atomic displacement parameter
Z	Formula unit per unit-cell
a, **b** & **c**	Crystallographic axes
x, y & z	Atom coordinates
ρ	Density
α	Alpha emission
β	Beta emission
γ	Gamma-ray
REE	Rare earth element
LREE	Light rare earth element
MREE	Middle rare earth element
HREE	Heavy rare earth element
wt. %	Weight percent
Bq/kg	Becquerel per kilogram
g/cm^3	Gram per cubic centimetre
α/mg	Alpha disintegrations per milligram
keV	Kilo electron volt
nm	Nanometer
Å	Angstrom

Chapter 1: Introduction

1.1 Objectives and Organization of this Thesis

In Chapter 1, the zircon and monazite minerals and radioactivity are introduced and the experimental techniques for their examinations are discussed in Chapter 2. The remainder of the thesis contains Chapters 3 to 7, References, and Appendices. Their brief contents are given below.

Crystal chemistry and structural variations in zircon are examined in Chapter 3. Specific objectives are (1) to characterize the crystal structure of detrital zircon grains with single-crystal X-ray diffraction technique concerning the chemistry, received radiation doses, and ages in order to find the structural properties of "pure" crystalline zircon; (2) to examine the crystal structure of fully and partially crystalline zircon with synchrotron high-resolution powder X-ray diffraction (HRPXRD) technique concerning the effects of radiation damage on the unit-cell parameters; and (3) to elucidate the variations of structural properties and their possible reasons.

The findings in Chapter 2 were presented in the 2014 GSA Annual Meeting in Vancouver, British Columbia (19–22 October 2014) as a poster entitled "zircon: crystal chemistry, structural variations, and radiological effects". A manuscript entitled "crystal chemistry and structural variations in zircon" has been submitted to *Contributions to Mineralogy and Petrology* and it is under review.

Crystal structure and chemistry of monazite-Ce and monazite-Sm is investigated in Chapter 4. Specific objectives are (1) to determine the crystal structure of detrital and pegmatitic monazite with SCXRD and to find the variations of the structural properties of monazite, and (2) to elucidate the control of chemical compositions on the structural properties of monazite. A manuscript entitled "crystal structure and chemistry of monazite-Ce and monazite-Sm" is being prepared for publication.

Evidence of radiation-induced phase transition in monazite is examined in Chapter 5. Specific objectives are (1) to determine chemical variability in monazite-Ce and monazite-Sm with EPMA; (2) to examine the multiple phases in monazite with synchrotron HRPXRD; and (3) to find the effects of radiation and evidence of radiation-induced phase transition in monazite. Based on the findings an abstract for poster presentation (crystal structure, chemistry and evidence of radiation-induced phase transition in monazite) is accepted for the 16th annual conference on applications of X-ray analysis, 3–7 August 2015, Westminster, Colorado, U.S.A. and a manuscript will be prepared for publication.

Radioactivity in placer minerals and possible radiological effects is examined in Chapter 6. Specific objectives are (1) to measure the activity concentrations of ^{238}U, ^{235}U, ^{232}Th, and ^{40}K in bulk samples and mineral fractions from Cox's Bazar coast, Bangladesh with GRS-HPGe and (2) to assess the radiological effects on the coastal environmental and on the workers involved in the mineral processing using some widely used radiological hazard indices. A paper has been published based on the findings of Chapter 6: "Zaman, M, Schubert, S., and Antao, S. (2012) Elevated radionuclide concentrations in heavy mineral-rich beach sands in the Cox's Bazar region, Bangladesh and related possible radiological effects. Isotopes in Environmental and Health Studies, 48, 1-14".

At least four publications and two conference presentations are expected from this work. Chapters 3 to 6 are written in publication format.

Chapter 7 summarizes the major findings from Chapter 3 to 6 and also includes some recommendations. Structural factors data obtained with SCXRD for zircon and monazite and gamma-ray spectroscopy data for bulk beach sands and mineral fractions samples are given in the Appendices.

1.2 Crystal Chemistry and Radioactivity: A Brief Review

1.2.1 Zircon

Zircon is an important mineral and is widely distributed as an accessory component in igneous, sedimentary and metamorphic rocks. It commonly occurs as detrital grains in sediments. Because zircon is one of the first minerals to crystallize from a magma, its grains are often encased as inclusions in other minerals such as biotite, feldspar or quartz (Pirkle and Podmeyer 1992). When the rocks containing zircon grains are exposed at the surface of the Earth's crust, they are subjected to weathering and erosional processes by which rocks are broken into smaller fragments. Subsequently, rock fragments are transported with various transporting agents (wind, water, glaciers, etc.). Zircon grains become liberated from their host rock fragments at some stage of weathering, erosional and transportation processes, and eventually, they become concentrated in the sediments forming a deposit that bears a commercial importance.

Zircon is a very tough, durable and resistant mineral and is not affected by low temperature processes, and consequently, the chemical diffusion of elements in it is limited. Because of this characteristic, the formula (e.g., Zr, Si) and non-formula (e.g., Hf, U, Th, and so on) elements remain undisturbed in the zircon crystal (Pirkle and Podmeyer 1992; Selby 2007). U and Th, and their daughters in zircon slowly experience radioactive decay events and produce stable Pb in zircon. The energy release during the radioactive decay events trigger the change of the zircon structure but still zircon can preserve its chemical (e.g., U/Th and Pb content) and structural properties (Vaczi et al. 2009). For this reason, zircon is used as an important mineral for U-Th-Pb geochronological study to unveil the records of the entire history of the Earth. For example, the characterization of the Hadean age zircon was recently carried out with atom-probe tomography (Valley et al. 2014). Zircon structure is also considered as one of the potential nuclear waste forms. Selected physical and optical properties are given (Table 1.1).

Table 1.1 Selected physical and optical properties for zircon

Properties	
Density (g/cm^3)	4.6 - 4.7
MOHS hardness	7.5
Colour	Mostly colourless but other colours such as gray, red, pick, brown, green, and violet are also common
Magnetic property	Non-magnetic
Electrical property	Non-conducting
Radioactivity	low
Refractive Index	$n_\omega = 1.99$ $n_\varepsilon = 1.93$
Birefringence (δ)	0.06
Optic sign	Uniaxial (+)

1.2.2 Chemistry of Zircon

Zircon is chemically made up of Zr, Si, and O atoms. Zircon contains minor amount of Hf^{4+} because the Hf^{4+} can replace Zr^{4+}, as the ionic radius of Hf^{4+} (0.83 Å) is close to the ionic radius of Zr^{4+} (0.84 Å) (Shannon 1976). Usually crystalline zircon does not contain Ca^{2+}, but metamict zircon contains Ca^{2+} in its structure (Horie et al. 2006). The presence of Ca^{2+} is the most common indicator of alterations in zircon (Geisler et al. 2007). The predominant trace elements (TE) incorporated into zircon are the heavy rare earth elements (HREE) from Ho to Lu and Y. As the ionic charge of nearly all the REE is 3+, they, therefore, do not substitute as easily as U^{4+}, Th^{4+}, or Hf^{4+} in the Zr^{4+} site in the structure. The replacement of Zr^{4+} by REE^{3+} requires compensation of the charge difference by P^{5+}, Nb^{5+} or Ta^{5+}. The individual concentration of other trace and rare earth elements is so low as to have a negligible effect on unit-cell parameters of zircon structure. As a result, basically all the variations in unit-cell parameters in different zircon samples is related to α-decay damage resulting from the decay of U and Th (Murakami et al. 1991). The chemical durability of detrital zircon in weathering environments decreases dramatically when the radiation dose exceeds 3.5×10^{15} α-decay/mg (Balan et al. 2001).

1.2.3 Crystal Structure of Zircon

Zircon is an orthosilicate mineral. The crystal structure of zircon was first determined by Vegard (1916), and confirmed by several others (Krstanovic 1958; Hassel 1926; Wyckoff and Hendricks 1928). It has a tetragonal crystal system ($a = b \neq c$ and $\alpha = \beta = \gamma = 90°$). Its structure consists of isolated SiO_4 tetrahedra and ZrO_8 dodecahedra (Fig. 1.1). The SiO_4 and ZrO_8 polyhedra share O-O edges to form a chain parallel to the **c** axis. Its ideal chemical formula is $ZrSiO_4$ (formula unit, $Z = 4$), space and point groups are $I4_1/amd$ and $4/m\ 2/m\ 2/m$, respectively. The SiO_4 tetrahedron is a tetragonal disphenoid (symmetry $2m$) elongated parallel to the [001] direction because of repulsion between the Zr^{4+} - Si^{4+} cations, whose polyhedra share a common edge (Robinson et al. 1971). The Zr atom is coordinated to eight O atoms and forms a dodecahedron with symmetry $2m$. According to Nyman et al. (1984), the ZrO_8 dodecahedron in the zircon structure can be described as two interpenetrating ZrO_4 tetrahedra in which one is elongated along the [001] direction and the other is compressed along the [100] and [010] directions. There are small voids and open channels in between SiO_4 and ZrO_8 polyhedra (Finch and Hanchar 2003). These structural voids and channels are considered as potential interstitial sites for impurity atoms. Such sites can accommodate interstitial atoms without excessive structural strain (Finch and Hanchar 2003). The role of interstitial sites in the zircon structure is not known.

The crystal structure of gem quality and synthetic zircons are well studied under ambient conditions and elevated pressure, temperature conditions (Robinson et al. 1971; Hazen and Finger 1979; Mursic et al. 1992; Kolesov et al. 2001; Finch et al. 2001) (Table 1.2). The refinement statistics and structural parameters (e. g., unit-cell, atom coordinates, anisotropic displacement parameters, bond distance, and angle) for zircon are given in Tables 1.2, 1.3, 1.4, 1.5, and 1.6.

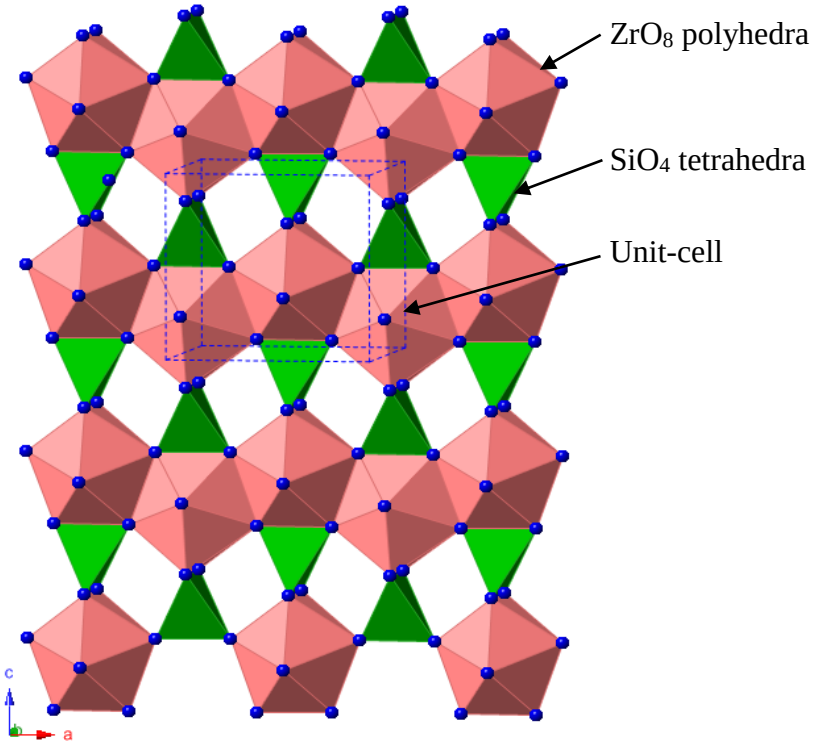

Figure 1.1 Polyhedral representation of the zircon structure projected down the **b** axis.

Robinson et al. (1971) did an anisotropic structure refinement of a non-metamict zircon from a syenite in Kragero, Norway and indicated that Si-Zr repulsion across shared edges probably accounts for the elongation of the SiO_4 tetrahedra along the **c** axis. Hazen and Finger (1979) studied the crystal structure and compressibility of a natural zircon at high pressure and indicated that zircon is one of the most incompressible silicate minerals; both *a* and *c* unit-cell parameters decrease with increasing pressure.

Table 1.2 Zircon structure studies with single-crystal X-ray diffraction available in literature

References	Zircon sample	Host rocks and sample locations	Zircon chemistry	Technique	Reference ID
Robinson et al. (1971)	Non-metamict zircon	Syenite; Kragero, Norway	Impurity – 1 wt. % Hf	Equi-inclination weissenberg single-crystal diffractometer using Nb-filtered Mo radiation and a scintillation counter.	I
Hazen and Finger (1979)	Non-metamict zircon Size: (0.09 × 0.09 × 0.03) mm^3	Kimberlite; zircon was colourless and gem quality; Finsch Pipe near Kimberley, South Africa; age- 94 Ma	Nearly pure; contains 1.2 wt. % HfO_2 and 26 ppm U	Automated 4-circle Picker diffractometer with Nb-filtered Mo$K\alpha$ radiation.	II
Siggel and Jansen (1990)	Zircon			4-circle diffractometer (AED2) (STOE-Siemens) with Mo$K\alpha$ radiation and graphite monochromator.	III
Mursic et al. (1992)	Metamict zircon	Ratnapura, Sri Lanka		D19 4-circle diffractometer at the ILL equipped with a vertically curved 2-dimensional position-sensitive detector.	IV
Rios et al. (2000a)	Partially metamict zircon Size: 0.03 mm^3	Sri Lanka; age- 570 ± 20 Ma	Zr- 49.2(2); Si- 14.54(2); Hf-1.30(3); U- 0.11(1); O- 34.85 wt. %	Philips PW1100 4-circle diffractometer with monochromatic Mo$K\alpha$ radiation.	V
Kolesov et al. (2001)	Synthetic zircon Size: 0.15 × 0.05 × 0.05 mm^3	Optically clear and gem quality	Pure $ZrSiO_4$	Enraf Nonius CAD4, sealed tube Mo$K\alpha$ radiation and graphite monochromator	VI
Finch et al. (2001)	Synthetic zircon		Pure $ZrSiO_4$	Bruker PLATFORM 3-circle goniometer equipped with a 1K SMART charge-coupled device (CCD) detector	VII

Table 1.3 Crystal structure refinement data for zircons available in literatures (Reference ID are given in Table 1.2)

Ref. ID		I	II	III	IV	V	VI	VII
Unit cell parameters	*a*	6.607(1)	6.6042(4)	6.6052(3)	6.610(5)	6.618(3)	6.6039(6)	6.6102(8)
(Å)	*c*	5.982(1)	5.9796(3)	5.9802(4)	6.002(5)	6.019(3)	5.9783(4)	5.986(1)
Volume, V (Å^3)		261.13	260.80	260.9	262.2	263.58	260.72	261.57
c/a		0.9054	0.9154	0.9054	0.9080	0.9095	0.9053	0.9056
Density$_{calc}$ (g/cm^3)		4.714						4.655
Absorption coefficient (mm^{-1})			4.43			4.421		4.382
2θ range for data				88.6° (max.)		4°-100°	112° (max.)	9.18°-56.50°
Index ranges						-14=<h=<14		-8=<h=<7
						-14=<k=<14		-8=<k=<8
						-0=<l=<12		-7=<l=<4
Total reflections		550	505	4298	575	2659	3672	641
Unique reflections				294	61	373	394	96
R_{int}						0.0243	0.022	0.0368
GooF on F^2							1.077	1.257
R_1		0.0190	0.0370			0.0160	0.0154	0.0422
wR_2		0.0220	0.0510	0.0230	0.0140	0.0390	0.0389	0.1065
Extinction coefficient						0.023(3)		2.1(4)
Largest difference peak and hole (e/Å^3)						1.101		1.302
						-1.010		-2.688
Mosaicity (°)							Very low	

Table 1.4 Atom coordinates and anisotropic displacement parameters (Å^2) for zircons available in literature (Reference ID are given in Table 1.2)

Ref. ID	I	II	III	IV	V	VI	VII
Coordinates and U_{ij} for O (x = 0; U_{12} = U_{13} = 0)							
y	0.0661(1)	0.0660(4)	0.0660(1)	0.0646(4)	0.06580(8)	0.06586(7)	0.0657(5)
z	0.1953(1)	0.1951(4)	0.1953(2)	0.1967(3)	0.19545(8)	0.19533(7)	0.1961(7)
U_{11}	0.0082(8)	0.0106(8)	0.0087(3)	0.0336(7)	0.01292(18)	0.0093(1)	0.010(2)
U_{22}	0.0069(7)	0.0049(8)	0.0042(3)	0.0241 (7)	0.00716(15)	0.0045(1)	0.006(2)
U_{33}	0.0052(7)	0.0036(8)	0.0039(3)	0.0250(5)	0.00690(14)	0.0058(1)	0.003(2)
U_{23}	0.0000(8)	-0.0012(8)	-0.0007(2)	-0.0022(5)	-0.00100(12)	-0.0008(1)	0.000(1)
U_{eq}	0.0067(3)	0.0063(3)				0.00656(5)	0.006(1)
U_{ij} for Si (x =0; U_{23} = U_{12} = U_{13} = 0)							
y	¾	3/4	1/4	1/4	3/4	3/4	1/4
z	5/8	5/8	3/8	3/8	5/8	5/8	3/8
U_{11}	0.0031(3)	0.0038(2)	0.0031(2)	0.026(1)	0.00644(10)	0.00402(8)	
U_{22}	0.0031(3)	0.0038(2)	0.0031(2)	0.026(1)	0.00644(10)	0.00402(8)	
U_{33}	0.0049(5)	0.0029(2)	0.0022(5)	0.022(2)	0.00382(14)	0.0041(1)	
U_{eq}	0.0057(3)	0.0039(3)				0.0041(10)	
U_{ij} for Zr (x =0, y = 3/4, z = 1/8; U_{23} = U_{12} = U_{13} = 0)							
U_{11}	0.0021(2)	0.0038(2)	0.0031(1)	0.025(1)	0.00600(6)	0.00364(6)	
U_{22}	0.0021(2)	0.0038(2)	0.0031(1)	0.025(1)	0.00600(6)	0.00364(6)	
U_{33}	0.0022(2)	0.0029(2)	0.0027(2)	0.024(1)	0.00566(7)	0.00427(7)	
U_{eq}	0.0029(1)	0.0035(1)				0.0038(1)	

Mursic et al. (1992) did structure refinements of a metamict zircon from Ratnapura, Sri Lanka at room temperature, 1573, and 1823 K using single-crystal neutron diffraction and found that the unit-cell parameters increase with increasing temperature. Rios et al. (2000a) carried out a structure refinement of a radiation damaged zircon and observed elongation of 0.17 % along the **a** axis and 0.62 % along the **c** axis compared with the undamaged zircon. This increase in *a* and *c* parameters arise from expansion of the ZrO_8 polyhedra. They also observed that the overall shape of the SiO_4 tetrahedra remains essentially undistorted. Kolesov et al. (2001) conducted structure refinement for a synthetic pure zircon and observed that the Zr^{4+} cation is tightly bonded and its vibrational behavior is not strongly anisotropic. Finch et al. (2001) studied

the incorporations of REE and P in the zircon structure and observed that the limits of REE and P incorporations in the Zr and Si sites depend on not only the ionic radii of REE and P but also the structural strain at the Zr and Si sites.

Table 1.5 Bond distances (Å) and angles (°) in the ZrO_8 dodecahedron for zircons from other studies (Reference ID are given in Table 1.2)

Ref. ID		I	II	III	IV	V	VI	VII
Zr-O^{I}	4x	2.131	2.128	2.129	2.124	2.133	2.128	2.130
Zr-O^{II}	4x	2.268	2.267	2.268	2.287	2.282	2.268	2.275
<Zr-O> [8]		2.200	2.198	2.199	2.206	2.208	2.198	2.203
O-O (dodecahedral edges)	8x	2.842	2.840	2.841	2.842	2.849	2.840	2.842
	4x	3.071	3.068	3.069	3.064	3.075	3.067	3.072
	4x	2.495	2.491	2.493	2.511	2.509	2.492	2.503
	2x	2.430	2.430	2.431	2.451	2.439	2.432	2.437
<O-O> [18]		2.770	2.768	2.769	2.774	2.778	2.768	2.773
O-Zr-O (corresponding to the dodecahedral edges)	8x	80.40	80.43	80.40	80.15	80.32	80.40	80.28
	4x	92.23	92.22	92.23	92.35	92.27	92.24	92.29
	4x	69.01	68.95	68.99	69.28	69.18	68.98	69.16
	2x	64.76	64.82	64.79	64.81	64.59	64.83	64.73
<O-Zr-O> [18]		78.76	78.76	78.759	78.74	78.75	78.76	78.75
O-O (distance without dodecahedral edges)	4x	4.200	4.196	4.199	4.232	4.225	4.198	4.213
	4x	4.046	4.043	4.045	4.062	4.060	4.044	4.054
	2x	4.177	4.174	4.175	4.159	4.180	4.172	4.174
<O-O> [10]		4.134	4.130	4.133	4.149	4.150	4.131	4.142
O-Zr-O (without dodecahedral edges)	4x	135.50	135.46	135.48	135.46	135.61	135.45	135.51
	4x	133.77	133.77	133.78	134.10	133.76	133.81	133.89
	2x	157.23	157.29	157.22	156.62	157.06	157.21	156.95
<O-Zr-O> [10]		139.15	139.15	139.15	139.15	139.16	139.15	139.15

Table 1.6 Bond distances (Å) and angles (°) in the SiO_4 tetrahedron and in between ZrO_8 dodecahedron and SiO_4 tetrahedron for zircons available in literature (Reference ID are given in Table 1.2)

Ref. ID		I	II	III	IV	V	VI	VII
Si-O	4x	1.622	1.623	1.622	1.627	1.629	1.623	1.622
O-O (tetrahedral edges)	4x	2.752	2.754	2.752	2.754	2.765	2.752	2.749
	2x	2.430	2.430	2.431	2.451	2.438	2.432	2.437
<O-O> [6]		2.645	2.646	2.645	2.653	2.656	2.645	2.645
O-Si-O	4x	116.04	116.06	116.03	115.63	116.11	115.99	115.84
	2x	97.00	96.97	97.03	97.75	96.88	97.09	97.37
<O-Si-O> [6]		109.69	109.70	109.70	109.67	109.70	109.69	109.68
Zi-Si	2x	2.991	2.990	2.990	3.001	3.010	2.989	2.993
Zr-Zr	2x	3.626	3.625	3.625	3.630	3.635	3.624	3.628
Zr-O-Si	1x	149.89	149.84	149.90	150.57	149.91	149.94	150.21
	1x	99.12	99.11	99.09	98.72	99.26	99.04	98.95
Zr-O-Zr	1x	111.00	111.05	111.01	110.72	110.83	111.02	110.84

1.2.4 Monazite

Monazite is an anhydrous phosphate containing light rare earth elements (LREE). Most monazite is light yellow to golden yellow in colours but other colours such as light brown, red, gray, and light to dark green are also common in monazite. It is transparent to translucent in small grains. Common physical and optical properties of monazite are given (Table 1.7).

Monazite is distributed in a wide range of geological settings as an accessory mineral. It occurs in intermediate to high grade metamorphic rocks. Monazite may also be present in biotite granites, syenitic and granitic pegmatites, quartz veins and carbonatites (Fleischer and Altschuler 1969; Rapp and Watson 1986). Monazite can occur as a detrital mineral in placer deposits, beach and river sands. The occurrence of monazite in sediments and sedimentary rocks is controversial because diagenetic monazite is also reported (Alipour-Asll et al. 2012).

Table 1.7 Selected physical and optical properties of monazite

Properties	
Density (g/cm^3)	4.8-5.5
MOHS hardness	5-5 ½
Relief	High (+)
Refractive index	α = 1.77 – 1.80
	β = 1.78 – 1.80
	γ = 1.83 – 1.85
Optic sign	Biaxial (+)
2V	10 - 20°

1.2.5 Chemistry of Monazite

The chemical composition of monazite is (Ce,La,Nd,Sm,Y,Th)PO_4. Rare earth elements (REE) are a group of 15 chemically similar metallic elements consisting of the lanthanide series (Ln^{3+}) in the Periodic Table. Yttrium (Y^{3+}) and scandium (Sc^{3+}) are sometimes considered REE as they have similar physical and chemical properties. Ln^{3+} are lanthanum (La), cerium (Ce), praseodymium (Pr), neodymium (Nd), samarium (Sm), europium (Eu), gadolinium (Gd), terbium (Tb), dysprosium (Dy), holmium (Ho), erbium (Er), thulium (Tm), ytterbium (Yb), and lutesium (Lu). Ln^{3+} series is subdivided into the light rare earth elements (LREE) – La through to Nd, the middle rare earth elements (MREE) – Sm through to Dy, and the heavy rare earth elements (HREE) – Ho through to Lu. LREE is common in the Earth's crust compared to HREE.

Ln^{3+} series cations exhibit a decreasing ionic radius as the atomic number increases. This change of ionic radii controls the crystal structure of rare earth orthophosphates. Murata et al. (1953) studied the mode of variation of REE in monazite samples from different source rocks (e.g., pegmatites, granites, beach sands, alluvial sands, etc.) and observed that the presence of Σ(La + Nd), Pr, and Σ(Ce + Sm + Gd + Y) are 42 ± 2, 5 ± 1, and 53 ± 3 atomic percent,

respectively. Spear and Pyle (2002) indicated that most metamorphic monazites contain 0.20, 0.43, and 0.17 cations per 4 O atoms for La, Ce, and Nd, respectively. Although almost all monazites contain Ce, this cation is not consistently found as a dominant cation in monazite. Thus, monazite may be termed as monazite-Ce, monazite-Sm, monazite-Nd, and monazite-La, based on the dominancy of Ce, Sm, Nd, and La among REE in monazite.

1.2.6 Crystal Structure of Monazite

Monazite belongs to the monoclinic crystal system and its crystal structure is made up of irregular 9-coordinated Ce, La, Y, and Th atoms linked together by distorted tetrahedral PO_4 groups (Beall et al. 1981; Ni et al. 1995) (Fig. 1.2). This type of structure is generally described as an equatorial pentagon, which is formed by 5 O atoms belonging to monodentate anionic tetrahedrons, interpenetrated by a tetrahedron, which is built by four O atoms belonging to two bidentate tetrahedra (Clavier et al. 2011).

The crystal structure of phosphates of trivalent La^{3+}, Ce^{3+}, Pr^{3+}, and Nd^{3+} were determined by X-ray diffraction techniques in 1944 for the Manhattan Project (Mooney 1948). The crystals were dimorphic (Mooney 1948). One phase was isomorphous with monazite, and monoclinic, and the other was a new phase belonging to the hexagonal crystal system. The crystal structure of natural monazite was first investigated by Ueda (1967) using a monazite sample from Ishikawa-yama, Fukushima Prefecture in Japan. He refined the structure and obtained very high *R* values (16-19 %), and unreliably large P-O distances. Ghouse (1968) studied the structure of natural monazites from Kerala beach sand, and observed a small difference in the structure of the natural monazites after heat treatments up to 1130° C. He also obtained P-O distances as long as 1.69 Å.

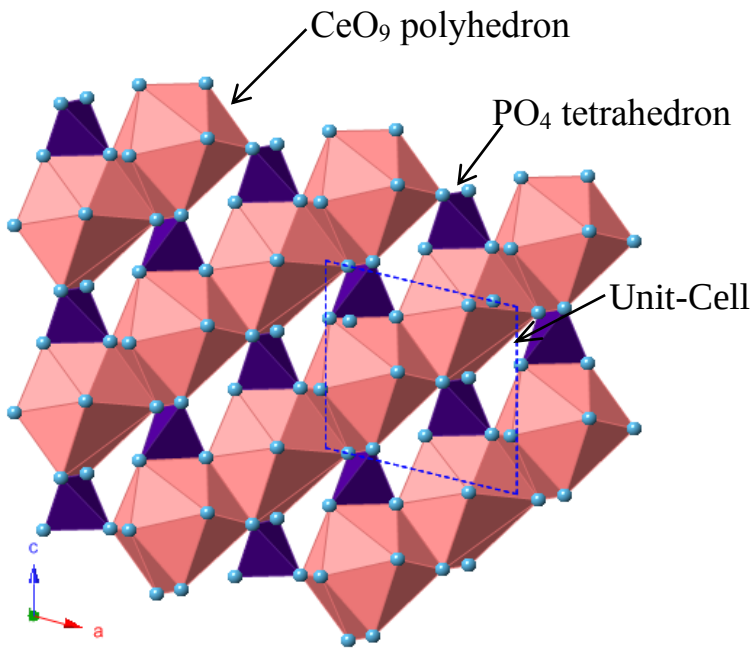

Figure 1.2 Polyhedral representation of the monazite-Ce structure projected down the **b** axis, which consists of edge sharing PO_4 tetrahedra and CeO_9 polyhedra along the **c** axis.

After reviewing the literature related to the structural characterizations of monazite with SCXRD, a summary of sample information, structure refinement statistics, unit-cell parameters, and selected bond distances and angles for monazite-Ce, monazite-Sm, synthetic monazite-Ce, and synthetic monazite-Sm,Tb are given in Tables 1.8, 1.9, and 1.10.

Table 1.8 Monazite sample information for SCXRD studies available in literature

References	Monazite sample	Host rocks and sample locations	Monazite chemistry	Technique	Reference ID
Ni et al. (1995)	Monazite-Ce	Kangankunde carbonatite, Malawi; Crystal was euhedral shape, optical-quality; Size-0.07-0.16 mm	$(Ce_{0.51}La_{0.29}Nd_{0.14}Pr_{0.05}Sm_{0.01})_{\Sigma 1.00}PO_4$	CAD4 automated diffractometer with graphite-monochromated Mo$K\alpha$ radiation	a
Masau et al. (2002)	Monazite-Sm	Annie Claim #3 granitic pegmatite, southeastern Manitoba; Crystal was platy, subhedral and yellow in colour	$(Sm_{0.20}Gd_{0.18}Ce_{0.15}Th_{0.13}Ca_{0.11}Nd_{0.09}La_{0.03}Y_{0.03}Pr_{0.02}Tb_{0.02}Zr_{0.02}Dy_{0.02}Pb_{0.02})_{\Sigma 1.00}(P_{0.96}Si_{0.04})_{\Sigma 1.00}PO_4$	Bruker automated four-circle diffractometer equipped with a CCD detector using Mo$K\alpha$ radiation	b
Ni et al. (1995)	Monazite-Ce	Synthetic	$CePO_4$	CAD4 automated diffractometer with graphite-monochromated Mo$K\alpha$ radiation	c
Mullica et al. (1996)	Monazite-(Sm,Tb)	Synthetic	$(Sm_{0.50}Tb_{0.50})_{\Sigma 1.00}PO_4$	Enraf-Nonius CAD4-F diffractometer (Mo$K\alpha$ radiation)	d

Table 1.9 Crystal structure refinement statistics for monazite available in literature (Reference ID as in Table 1.8)

Ref. ID		a	b	c	d
Unit cell parameters	a (Å)	6.7902(10)	6.725(1)	6.788(1)	6.650(1)
	b (Å)	7.0203(6)	6.936(1)	7.0163(8)	6.8534(9)
	c (Å)	6.4674(7)	6.448(1)	6.4650(7)	6.3412(9)
	β (°)	103.38(1)	104.02(1)	103.43(1)	103.99(1)
Volume, V (Å^3)		299.93(9)	291.8(1)	299.49(6)	280.42(8)
Density$_{calc}$ (g/cm^3)			5.512		5.932
Absorption coefficient (mm^{-1})					23.72
2θ range for data		Up to 60°	Up to 60°		3-70°
Total reflections		3541		1910	
Unique reflections		945		943	1201
R_{int}					0.03
R_1		0.015		0.014	0.057
wR_2		0.023		0.019	0.066
Largest difference peak/ hole (e/Å^3)		0.624/-0.766		0.653/-0.632	

Crystal system = monoclinic; space group = $P2_1/n$; formula unit, Z = 4 based on $CePO_4$

Table 1.10 Bond distances (Å) and angles (°) for monazite available in literature (Reference ID as in Table 1.8)

Ref. ID	a	c	d
Ce-O	2.528(2)	2.535(2)	2.473(3)
	2.461(2)	2.452(3)	2.384(3)
	2.776(3)	2.783(2)	2.770(3)
	2.644(2)	2.646(2)	2.574(3)
	2.573(2)	2.563(2)	2.478(3)
	2.585(3)	2.584(3)	2.493(3)
	2.481(2)	2.468(2)	2.370(3)
	2.526(2)	2.524(2)	2.440(3)
	2.455(2)	2.446(2)	2.384(3)
<Ce-O> [9]	2.559(2)	2.556(2)	2.485(3)
P-O	1.534(3)	1.530(3)	1.532(3)
	1.545(3)	1.546(3)	1.530(3)
	1.534(3)	1.539(2)	1.535(3)
	1.531(3)	1.535(3)	1.532(3)
<P-O> [4]	1.536(3)	1.538(3)	1.532(2)
O-P-O	113.65	112.79	112.4(2)
	103.94	105.66	105.2(2)
	113.74	113.35	114.5(2)
	112.39	112.61	112.7(2)
	105.20	104.13	103.2(1)
	108.07	108.41	108.0(2)
<O-P-O> [6]	109.50	109.49	109.5

1.3 Natural Radioactivity and Radiation

1.3.1 Natural Radioactivity

Radioactivity was first discovered by A. H. Becquerel in 1896. When an unstable atomic nuclei disintegrates spontaneously to generate a new nuclei with a higher stability, the disintegration process is called radioactivity. During this process, energy and particles are released in the form of radiations, and also a new radionuclide (also called recoil atom) is formed. Alpha (α) particle, beta (β) particle, and gamma (γ) rays are the most common states of ionizing radiation (Lilley 2001). The radiation properties are widely applied to numerous areas such as power generation, military, medical science, geological science, biological science, agriculture, and industry.

Radiation is generated from both natural radionuclides as well as human activities. The most common source and exposure of radiations in the environment is natural (NCRP 1975). According to the World Nuclear Association (WNA), the recent data of the sources of radiation is given (Fig. 1.3). There are two main contributors for the naturally occurring radiations exposed to the living organisms including human beings (UNSCEAR 2000). The first sources is atmospheric and it comes from cosmic radiation from the outer space and the second source is terrestrial radioactive materials that are present everywhere in the Earth's crust and in the bodies of living organisms. Terrestrial radiations arise commonly from the primordial radionuclides (^{238}U, ^{235}U, and ^{232}Th) which are distributed in almost all geological materials in the Earth's environment (IAEA 2003). The average background concentrations (ppm) and their corresponding activity (Bq/kg) in different types of rocks, sands, and soils are given in Table 1.11. Significant natural background radiations mainly come from the decay of very long lived primordial radionuclides and their decays products (UNSCEAR 2000). The primordial radionuclides have been on the Earth since its formation and they have very long decay half-lives, which are comparable to the age of the Earth (Lilley 2001). There are three significant

radioactive decay series, namely U, Th, and actinium. The detailed decay schemes of three radioactive series (^{238}U, ^{235}U, and ^{232}Th) are presented in Figure 1.4.

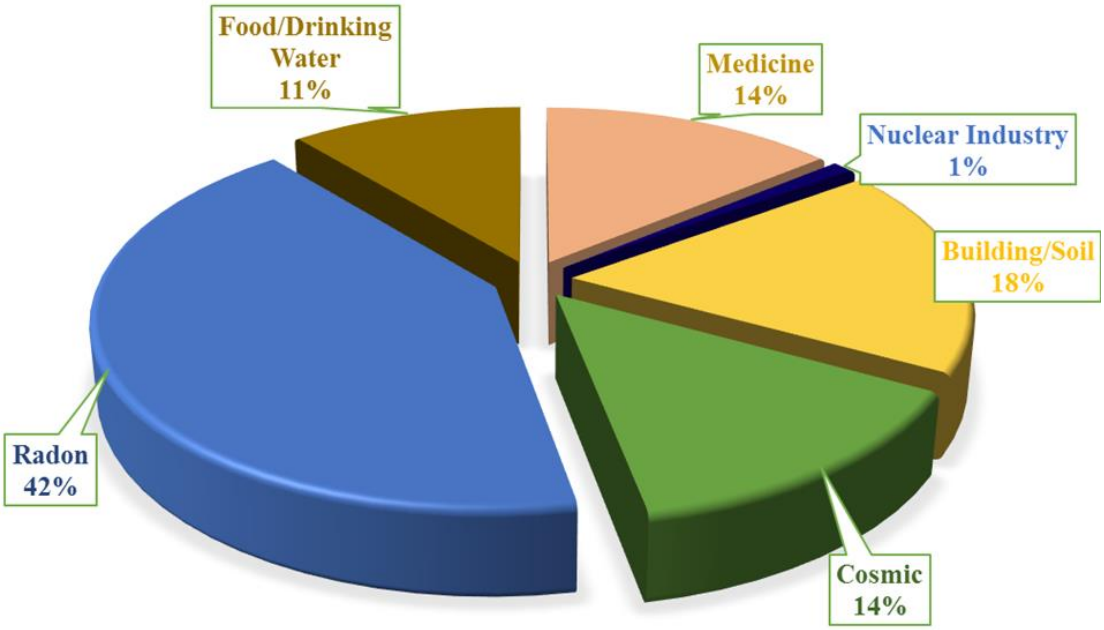

Figure 1.3 Sources and their relative contributions towards radiations in the environment (modified after WNA 2014).

1.3.2 Radioactive Decay and Types of Radiation

Radiation is the energy that is released as particles or rays during radioactive decays. The three main types of radiation emitted by radioactive material are α particle, β particle, and γ-ray. The characteristics of these radiations are given in Table 1.12. α particle can be shielded by a sheet of paper or by human skin; β particles can be stopped by a thin sheet of Cu; and γ-rays can penetrate paper, skin, wood, and other substances and can be stopped by a shield of Pb or a thick concrete wall.

Table 1.11 Average concentrations of ^{238}U, ^{232}Th, and ^{40}K in typical rocks, sands, and soils (Eisenbud and Gesell 1997)

Rock type		^{40}K		^{232}Th		^{238}U	
		wt. %	Bq/kg	ppm	Bq/kg	ppm	Bq/kg
Igneous rocks	Basalt						
	Crustal average	0.8	300	3-4	10-15	0.5-1.0	7-10
	Mafic	0.3-1.1	70-400	1.6, 2.7	7	0.5, 0.9	7
	Salic	4.5	1100-1500	16, 20	60	3.9, 4.7	50
	Granite						
	Crustal average	>4	>1000	17	70	3	40
Sedimentary rocks	Shale, sandstones	2.7	800	12	50	3.7	40
	Clean quartz	<1	<300	<2	<8	<1	<10
	Dirty quartz	2	400	3-6	10-25	2-3	40
	Arkose	2-3	600-900	2	<8	1-2	10-25
	Beach sands (unconsolidated)	<1	<300	6	25	3	40
	Carbonate rocks	0.3	70	2	8	2	25
All rock (range)		0.3-4.5	700-1500	1.6-20	7-80	0.5-4.5	7-60
Continental crust (average)		2.8	850	10.7	44	2.8	36
Soil (average)		1.5	400	9	37	1.8	22

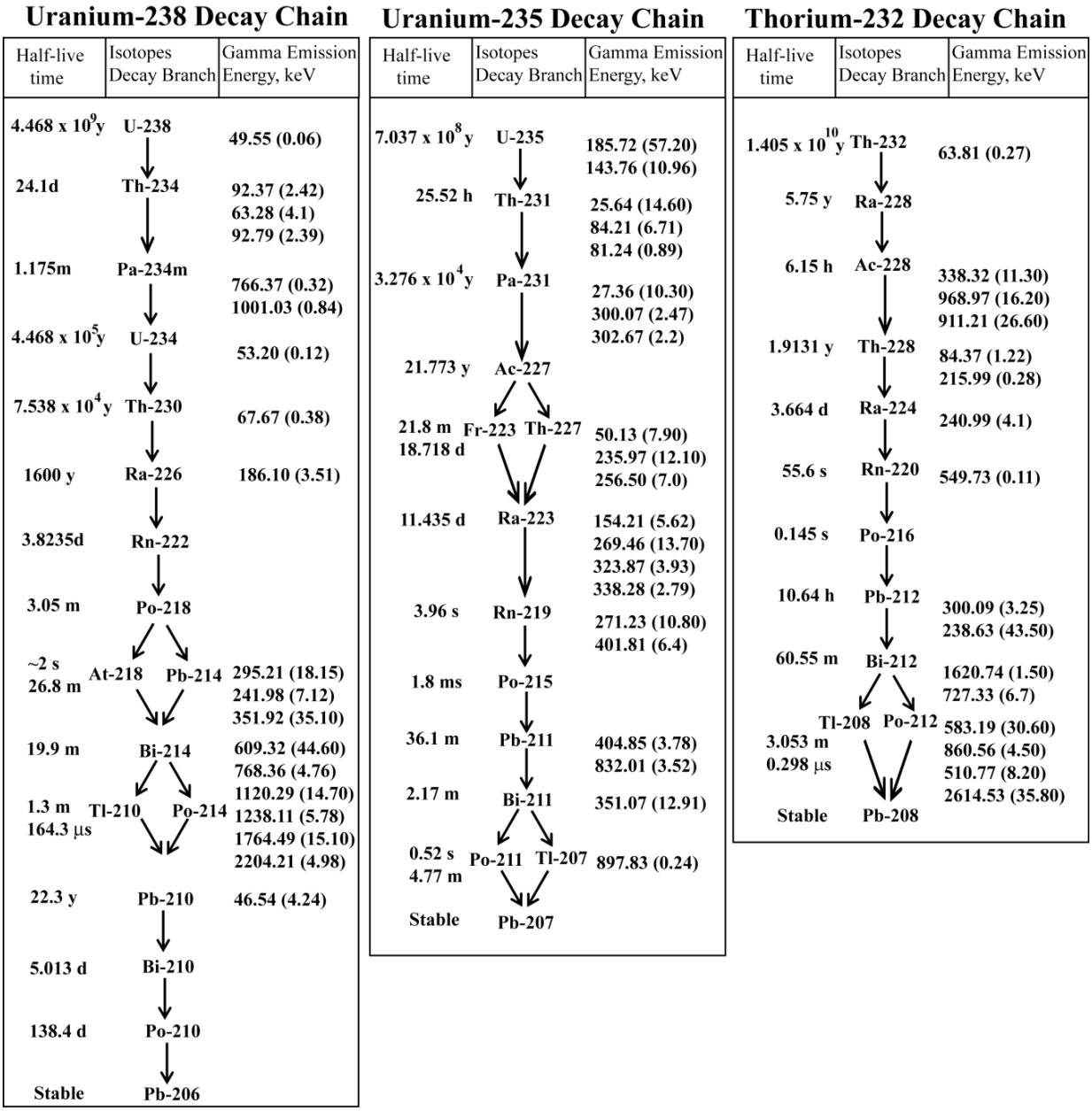

Figure 1.4 Radioactive decay chains for ^{238}U, ^{235}U, and ^{232}Th.

Table 1.12 Main types of radiation and their characteristics (Eisenbud and Gesell 1997)

Radiation type	Description	Electric charge	Example
α particle	Emission of slow He nuclei	2+	α (Ra), 4.9 MeV Range in air: few cm
β particle	Emission of fast electrons or positrons	1- or 1+	β (^{40}K), 1.4 MeV Range in air: few m
γ rays	Emission of high energy (γ quanta) Electromagnetic radiation	0	Wavelength <10 pm Some KeV to MeV per quantum Range in air: few 100 m

The radioactive decay rate is dependent only on the energy state of the radionuclide and is independent of pressure, temperature and chemical composition. The radioactive decay rate can be expressed by the fundamental law of radioactive decay (Burcham 1973):

$$A = -dN/dt = \lambda N ,$$

where, *A* is the activity of an isotopically pure radiation source that is equal to the number, *dN*, of radioactive nuclei decaying in a given time, *dt*, and is proportional to the number, *N*, of radioactive nuclei present at time, *t*, λ is a decay constant, which is the probability per unit of time for the decay of a given nucleus. The negative sign is introduced in the equation because the number of radioactive nuclei decrease with increasing time. The standard unit of radioactivity is becquerel (Bq), is defined as one disintegration per second (Lilley 2001). One Curie (Ci) is equal to 3.7×10^{10} Bq.

After solving the equation an exponential function of radioactivity decay can be written as the following:

$$N_t = N_0 e^{-\lambda t},$$

where, N_0 is the initial number of radioactive atoms present ($t = 0$) and N_t is the number of atoms at time *t*. The rate of radioactive decay can be characterized in terms of half-life, which is the

time required for the disintegration of one-half of the radioactive atoms. Secular equilibrium, which is a steady-state condition, is defined as the half-life of the parent is very much greater than that of the daughter. Usually, after about seven half-lives, the parent and daughter nuclei reach an equilibrium state and the values of parent and daughter activities will be equal (Turner 2007).

1.3.3 Radiation Damage in Minerals

John Jacobs Berzelius, a Swedish physician and mineral chemist, in 1815 first described the unique properties associated with radiation damaged materials (Ewing 1994). In 1893, Broegger first used the term "metamikte" in Danish Encyclopedia (Pabst 1952). Broegger said metamictization in materials results from unspecified outside influences by which materials become less stable. This explanation was rejected by several authors by stating that many materials having complex chemical composition do not show metamictization and some metamict materials have relatively simple chemical composition (Pabst 1952). The first explanation for the reason of metamictization came from Hamberg (1914). He suggested that metamictization in minerals is a periodic to an aperiodic phase transition induced by α-radiation emitted from U and Th decay chains. In 1924, Goldschmidth noticed three conditions, which are required for metamictization in materials (Pabst 1952). Materials have to have (1) ionic bonds and susceptible to hydrolysis to some extent; (2) one or more types of ions that are ready to change its state of ionization; and (3) the influence of strong radioactive decay event either from outside or inside of the materials.

Metamictization is a radiation-induced process by which the crystal structure of a crystalline solid or mineral (periodic) can be partially or completely destroyed leaving the mineral or crystalline solid amorphous (aperiodic) (Ewing et al. 1987; Tole 1985). It is the resultant of two counteractive processes, which are radiation damage accumulation and annealing (Nasdala et al. 2001). Many minerals contain radioactive elements (mainly U and Th).

Because of the spontaneous decay, these radioactive elements (U and Th) emanate α and β particles, and γ-ray causing radiation damage in the crystal structure that cause metamictization in minerals.

The periodic to aperiodic transition in minerals has been investigated mainly at three situations (self-irradiation in minerals, actinide doping, and ion-beam irradiations) for which different units and terminology are used in the calculation of dose. The following discussion focuses mainly on the minerals containing ^{238}U and ^{232}Th in their crystal structure.

There are two possible effects of nuclear radiation available for damaging the crystal structure. These are ionization and atom displacement (Ewing et al. 2003). The ionization is accomplished mainly by α, β and γ radiations and the displacement of atoms mainly by the consequence of recoil nuclei and particles (Holland and Gottfried 1955). The displacement of atoms play the key role to disorder the structure, but in some situations where it is observed that the displacement of atoms can account for only a small fraction of the observed effects, the ionization processes may be responsible for the major portion of the damaged structure. The energy of a U recoil nucleus after α radiation is approximately 74 KeV and this particle may produce several hundred displacements of atoms that roughly count to about 835 in the structure during α emission (Weber 1993). The structure can be completely destroyed after approximately 1.2×10^{16} α disintegrations per mg. There are 1.95×10^{19} atoms per mg of zircon, so that after a dosage of 1.2×10^{16} α/mg approximately 30 % of the atoms in the structure have been displaced owing to collisions with recoil nuclei and α particle. This number of atom displacements would be enough to destroy the structure in a condition that at Earth-surface temperature self-annealing is slow compared to the rate of damage. Therefore, the major part of the damage is caused by direct atom displacements that are predominantly caused by recoil nuclei (Holland and Gottfried 1955).

The self-irradiations are caused by the emission of α, β, and γ decay, as well as from recoil nuclei produced during radioactive decay, and spontaneous fission events. β emission can displace negligible amount of atoms compared to α emission. A single fission event creates

considerable damage but is significantly less probable compared to α decay (decay constants 8.51×10^{-17}/year *vs.* 1.55×10^{-10}/year, respectively, for ^{238}U; this translates to one fission per *ca.* 1.8 million alpha decay chains) (Vaczi 2009). Besides, a single radioactive ion in natural zircon undergoes 6 ^{232}Th, 7 ^{235}U and 8 ^{238}U α disintegrations until stable isotopes ^{206}Pb, ^{207}Pb, and ^{208}Pb are formed. Thus, most of the self-radiation damage in minerals is caused by α-radiation.

The transition from crystallinity to metamictization causes the changes of the physical properties of minerals. Chakoumakos et al. (1987) reviewed the prominent changes in zircon, which are (a) a decrease in density (17%), (b) a decrease in birefringence until the material becomes isotropic, (c) decrease in the elastic modulus (up to 69%), (d) decrease in Poisson's ratio (7%), (e) darkening of color, (f) increasing thermoluminescence, (g) peak broadening, decrease in intensity, and shift in the position of diffraction maxima to lower values of 2θ, which corresponds to an increase in unit-cell volume (5%), (h) decrease in hardness (40%), (i) decrease in thermal conductivity, (j) increase in adsorbed H_2O, (k) increased susceptibility to dissolution, and (l) increased chemical diffusion.

Zircon is sometimes affected by radiation induced swelling. Vaczi (2009) summarized this phenomenon and stated that zircon is most often chemically zoned and when radioactive elements are incorporated into zircon heterogeneously, diverse expansion causes cracking in non-expanded zones. The cracking gives fluids access to move into the internal, damaged zones while increasing the surface area for dissolution. This dissolution might form the pathway to mobilize the major and trace elements and ultimately reduce the radionuclide retention capabilities.

Much less amount of study has been done for the radiation damage in monazite compared to zircon. One of the possible reasons could be the difficulty to find the radiation damage in monazite. Meldrum et al. (1998) studied the α radiation damage in monazite and observed that the monazite received a dose of 1.5 dpa (displacements per atom) is almost completely crystalline; at 5.5 dpa the material has become largely polycrystalline, and the crystallites are randomly oriented; at 8.5 dpa the α-decay dose is large enough that only isolated crystalline

regions remain; and at a dose of 9 dpa the monazite has become completely amorphous. Ewing et al. (2003) reported that despite incorporating high concentrations of Th and U, monazite is almost never found in the metamict state. Seydoux-Guillaume et al. (2002) studied a Brazilian monazite and described it as a mosaic crystal of two separate phases of monazites. They proposed that phase A corresponds to well crystalline monazite where helium atoms were trapped, resulting in increased unit-cell parameters, whereas phase B represents a distorted lattice, which is referred to as old alpha recoil tracks.

Radiation damage in zircon and monazite is not consistent under all conditions. How a crystalline material or mineral becomes metamict depends for the most part on the ratio of damage accumulation and thermal annealing rates specific to the material or mineral itself. Ewing et al. (2000) reviewed the recovery of radiation damage and mentioned that if the recovery processes dominate, the crystallinity is preserved, even at low temperature. For example, monazite remains crystalline in spite of extremely high α radiation doses, whereas zircon is commonly found in a moderately to highly damaged state, indicating that the kinetics of the recovery mechanisms are slower in zircon than in monazite. Meldrum et al. (1998) carried out an ion-beam irradiated experiment with monazite and found that monazite cannot be amorphized by 800 keV Kr^{+} ions at temperatures greater than 175°C and on the other hand, zircon can be amorphized at temperatures up to 740°C. The damage process in radioactive minerals is basically the same as for the ion-beam irradiated samples with the exception of the dose rate which is much lower in the case of natural samples.

There is no common opinion on the recovery mechanisms of partially metamict zircon. Vaczi (2009) summarized this issue and stated that the point defects (also called Frenkel pairs) in the residual crystalline volume are annihilated first, followed by the epitaxial recrystallisation of amorphous domains on existing crystalline zircon. Another opinion says that the recombination of point defects in a crystalline lattice needs more energy than the reorganisation of amorphous domains on crystalline pattern. Heavily metamict zircon separates out its constituent oxides (a mixture of crystalline ZrO_2 and amorphous SiO_2) at high temperatures. During further

annealing, and especially at higher temperatures, the ZrO_2–SiO_2 mixture fuses and forms crystalline $ZrSiO_4$ (Vaczi 2009).

A variety of models have been developed to describe the processes that lead to radiation-induced amorphization of different types of materials. The prominent models are the accumulation of point defects (Gong et al. 1996), interface-controlled amorphization (Motta 1997), multiple cascade overlap (Gibbons 1972) and in-cascade amorphization (Weber 1993). Detail explanation of these models can be obtained in literature (e.g., Weber 2000; Ewing et al. 2000; Ewing et al. 2003).

Chapter 2: Experimental Techniques: A Brief Review

Most of the techniques used in this study are well established and they have been described in many text books (e.g., Reed 1996; Beaman and Isasi 1972; Ingram et al. 1999; Glusker and Trueblood 2010; Cullity (1977); Kasai and Kakudo 2005; Zolotoyabko 2014). Therefore, a brief review is given for the techniques used in the study.

2.1 Electron-Probe Micro-Analysis (EPMA)

Electron-probe micro-analysis (EPMA) is a versatile, non-destructive technique for complete chemical analysis of microscopic volume, surface morphology (shape and roughness), and compositional mapping of solid materials including minerals. An EPMA is essentially a microscope with very high magnification and uses electrons instead of light to examine the sample. The basic principle of EPMA is the same as the scanning electron microscope (SEM) except the added capability of elemental analysis quantitatively.

2.1.1 Operation Principle of EPMA

When the incident electrons bombard the sample, X-rays emitted from a sample are collected with a liquid nitrogen-cooled solid state detector. Based on the energy, these X-rays are analyzed with computer programs and are displayed as an EDS pattern. EDS technique is usually applied to determine the presence of the elements and their relative abundance in the sample, because it is practically a qualitative analysis.

Quantitative analysis can be obtained using a wavelength dispersive spectrometer (WDS). WDS has a high spectral resolution and low detection limits. The WDS analyses the wavelengths of X-rays emitted from the sample using Braggs law: $n\lambda = 2d \sin\theta$.

The X-rays source (measuring spot of sample), the diffracting crystal, and the detector are placed on the circumference of a focusing circle known as the Rowland circle. The diffracting

crystal (a Johansson type) has a radius of curvature of 2R. The schematic geometric configuration is shown (Fig. 2.1). X-rays are dispersed by diffracting crystal with only one wavelength ($n\lambda$) and passed to the detector. The diffracted X-rays are collected into a proportional radiation detector. The detector is a gas-filled sealed tube where gas is ionized by X-rays, yielding a massive multiplication factor. Several types of diffracting crystal are used depending on the coverage of required wavelengths. The most common diffracting crystals are given in Table 2.1.

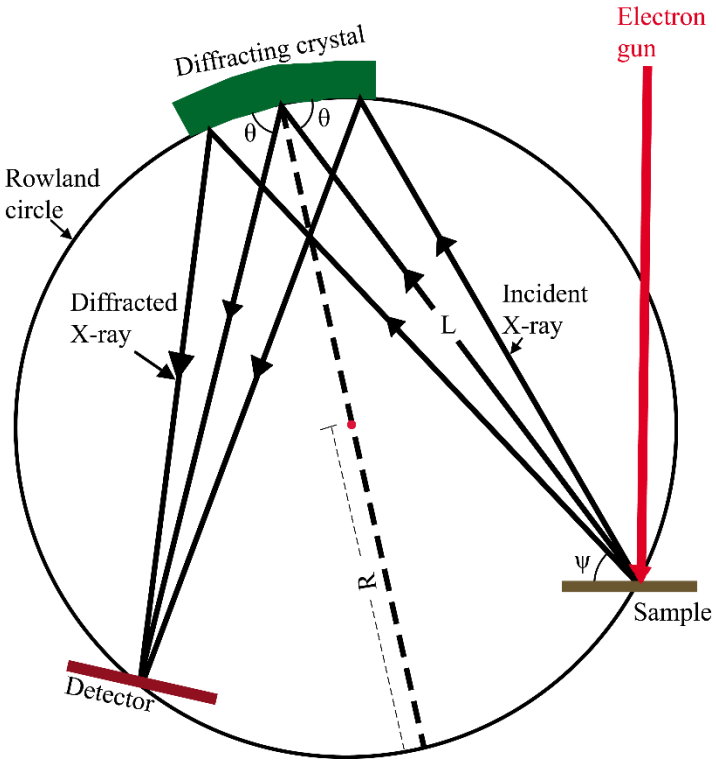

Figure 2.1 Schematic representation of the Rowland circle. The θ and ψ are diffraction and X-ray take-off angle, respectively.

An attempt to quantify the production of X-rays in materials was made in 1951 by Raymond Castaing. According to the approximation of Castaing, the primary generated characteristic X-ray intensities are roughly proportional to the respective mass-fractions of the emitting elements. The relationship between the abundance ratio of the unknown (*u*) and standard (*s*) for element *A* and the ratio of X-ray intensities (*k*-ratio) emitted from the unknown and standard by element *A* is given by:

$$\frac{C_A^u}{C_A^s} \approx \frac{I_A^u}{I_A^s}$$

where, the C_A^u and C_A^s are concentrations and the I_A^u and I_A^s are resulting intensities of element *A* of unknown and standard samples. The matrix effects are taken into consideration and a matrix correction factor (*ZAF* factor), which depends on the composition of sample, are incorporated into the equation as follows.

$$\frac{C_A^u}{C_A^s} \approx \frac{I_A^u}{I_A^s} = k_A \cdot [ZAF]$$

Table 2.1 List of common diffracting crystals and their uses (Beaman and Isasi 1972; Ingram et al. 1999)

Diffracting crystal	Element range		
LDE1	$K\alpha$ lines: N, O, F, and C		
LDE2	$K\alpha$ lines: B, C, N, and O		
TAPJ	$K\alpha$ lines: O-P	$K\beta$ lines: Cr-Nb	$M\alpha$ lines: Pd-Au
TAPH	$K\alpha$ lines: F-Al	$K\beta$ lines: Cr-Br	$M\alpha$ lines: Pd-Au
PETJ	$K\alpha$ lines: Al-Mn	$K\beta$ lines: Kr-Tb	$M\alpha$ lines: Yb-U
PETL	$K\alpha$ lines: Si-Cr	$K\beta$ lines: Kr-Sm	$M\alpha$ lines: Lu-U
PETH	$K\alpha$ lines: Si-Ti	$K\beta$ lines: Rb-Ba	$M\alpha$ lines: Hf-U
LIFH	$K\alpha$ lines: Ca-Br	$K\beta$ lines: Sn-Fr	

2.2 X-ray Diffraction Technique

X-rays were discovered in 1895 by Wilhelm Conrad Röntgen at the University of Würtzburg, Germany. It is an electromagnetic radiation and has the same nature as light but have very short wavelength (0.1 – 10 Å). The unit of measurement of the X-ray wavelength is angstrom (Å), equal to 10^{-8}cm. X-rays are invisible and travel in straight lines. They are much more penetrating than light and can easily pass through the human body, wood, metals, and other objects.

X-ray diffraction is a non-destructive technique widely applied for the determination of crystal structures, the phase identification, the quantitative analysis, the determination of structure imperfections, and the extraction of three-dimensional microstructural properties. Single-crystal and powder X-ray diffraction are two prime techniques.

Single-crystal X-ray diffraction (SCXRD) is commonly used to determine unit-cell parameters, bond distances, angles, ordering of crystallographic site occupancies, and other structural parameters for minerals (Harris et al. 2001). It is a non-destructive technique and does not require any separate standards. The main drawbacks of this technique are the specific required size, high quality sample and the comparatively prolonged time of data collection. The sample for the SCXRD has to be a monocrystalline crystal and be optically clear without any intra-grain boundaries and inclusions. Crystal lattice must be continuous and unbroken in the sample of interest. If we do not have crystals with the appropriate size, quality, and perfect crystallinity, the powder X-ray diffraction (PXRD) can used.

PXRD is a powerful tool to investigate the radiation damaged minerals, although fully damaged minerals are, in general, X-ray amorphous. However, the combined heating, annealing and X-ray diffraction experiments can provide useful structural information about a mineral (e.g. Pabst 1952, Bursill and McLaren 1966; Vance 1975; Weber 1990; Murakami et al. 1991; Colombo et al. 1999). Concerning sample preparation, PXRD is easier and more convenient

than SCXRD technique because it does not require a perfect crystal. The term "powder" does not strictly reflect the usual meaning of the word in common language. The "powder" of a sample for X-ray diffraction study consists of a large number of small, randomly oriented crystallites (typical size: 10 μm or less; Will 2006).

2.2.1 Single-Crystal X-ray Diffraction (SCXRD)

The crystal structural determination involves several steps and each step pose some individual challenges.

- Crystal selecting, handling, and mounting
- Unit-cell determination
- Full data collection
- Data reduction and space group assignment
- Structure refinement
- Structure modelling

The selection of a perfect crystal is usually a time-consuming task. True perfect crystals are uncommon in nature and bear imperfections (e.g., short- or long-range disorder, dislocations, irregular crystal surfaces, twinning, and other defects) to some extent. For this study, a perfect crystal is defined as a mineral or a fragment of a mineral showing well-defined, sharp crystal faces, and optically clear. The crystal must have optimum size (normally less than 100 μm) so that it can be bathed completely in the incident X-ray beam. The crystal should be examined with a polarizing microscope and twinned or zoned crystals are avoided. It is always a good practice to spend some extra time in choosing the right crystal. The next step is to mount the crystal on the tip of a glass fiber (diameter approximately 100 μm) using a glue. The fiber with the crystal is then fixed into a brass pin by a clay material. Thereafter, the brass pin is mounted onto the goniometer head (Fig. 2.2b).

The first task is to determine unit-cell parameters of the crystal under study. Ten images with one degree rotation per frame are collected. The X-ray exposure time per frame is 22 seconds. After getting the expected unit-cell parameters and crystal mosaicity values, a full data set is collected with the increasing number of images and exposure time (42 seconds/frame). The distance between crystal and detector is 35 mm.

After collecting the full data set for a crystal, the intensities are extracted from each frame, data is scaled, the equivalent reflections are merged, and a space group is assigned. Then the raw intensity data are corrected for polarization, Lorentz effects, and absorption. Finally the structure is solved and the instruction (*.ins*) and reflection (*.hkl*) files are created for structure refinement.

2.2.2 SHELX Structure Refinement

The SHELX program is widely used for structure solution and refinement of crystal structure data. It was first written in the late 1960s. SHELX-97 contains several executable programs such as SHELXS, SHELXL, CIFTAB, SHELXA, SHELXPRO, and SHELXWAT. SHELXS is applied for crystal structure solution using mainly the powerful direct method (Sheldrick, 1997). SHELXL is used for the refinement of crystal structure from the single-crystal X-ray diffraction (SCXRD) data primarily. SHELXL needs only two pure ASCII text files (*.hkl* and *.ins*) for the refinement operation. The *.hkl* file is a reflection data file and contains h, k, l, F^2, $\sigma(F^2)$, batch number (BN) in standard SHELX format. Figure 2.3 show the format of an instruction file (*.ins).*

The steps of SHELX refinement are given in Figure 2.4. The *.hkl* file generally has all measured reflections without rejection of systematic absences or merging of equivalent reflections. SHELXL always refines against F^2 (observed reflections from the experiment) in the *.hkl* file. During the initial data processing the SHELXL automatically rejects the systematic reflections based on the space group and merges the equivalent reflections. The reflection indices are converted to standard symmetry equivalents. The systematic absences of certain

reflections indicate the space group, and R_{int} is the indicator of the consistency of reflections. The definitions of R_{int} and R_{sigma} are the following (Sheldrick 1997):

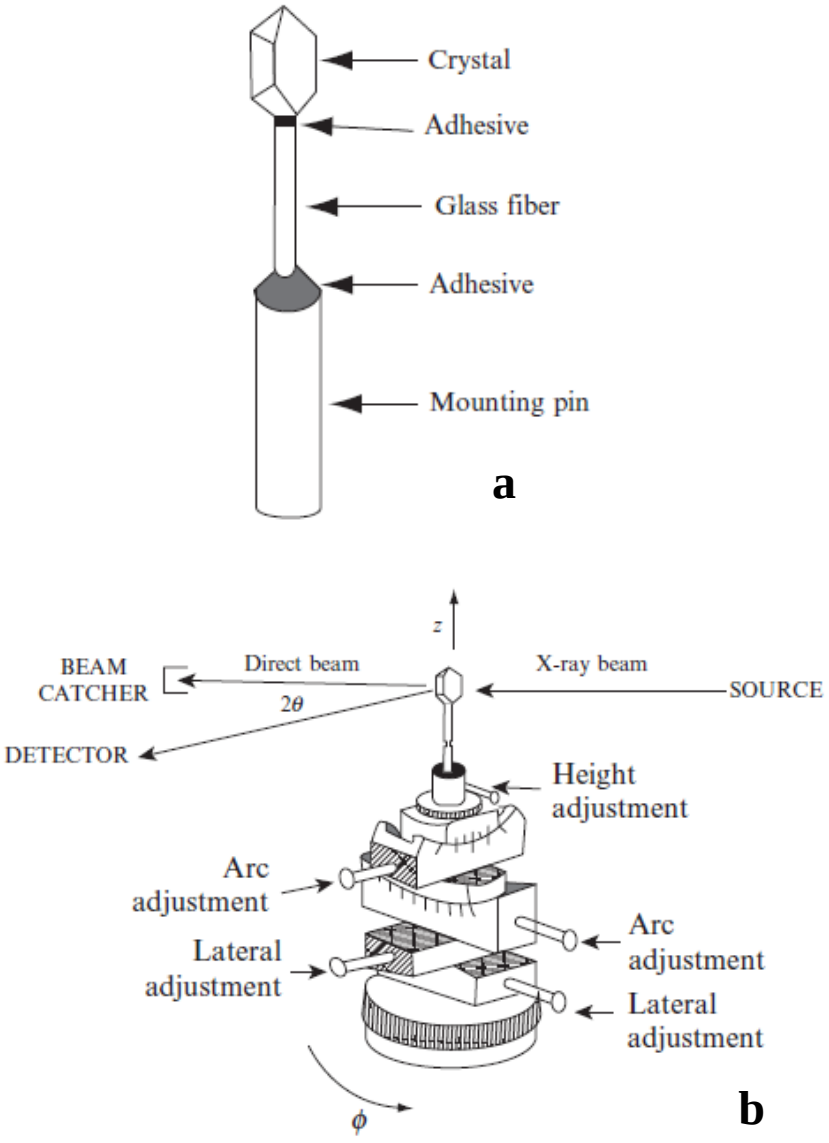

Figure 2.2 Sample mounting for SCXRD experiment, (**a**) crystal mounting and (**b**) goniometer orientations (modified after Glusker and Trueblood 2010).

$$R_{int} = \frac{\sum|F_0^2 - F_0^2(mean)|}{\sum[F_0^2]}$$

and

$$R_{sigma} = \frac{\sum[\sigma(F_0^2)]}{\sum[F_0^2]}$$

where, the F_0^2 is for the experimental observed reflection.

A least-squares (L.S.) full-matrix refinement is normally used because it gives the best convergence per cycle and allows esd's to be estimated. The refinement process can be explained as the minimization of the difference between the observed structural factors, $|(F_0)|$, and the calculated structural factors, $|(F_c)|$. A refinement is generally considered as completed, if convergence is achieved that means all parameter shifts << standard deviation. The refinement completeness is judged by several *R*-indices that are defined as follows:

$$wR_2 = \sqrt{\frac{\sum w\{F_o^2 - F_c^2\}^2}{\sum w(F_o^2)^2}}$$

$$R_1 = \frac{\sum\big||F_o| - |F_c|\big|}{\sum|F_o|}$$

$$GooF = \sqrt{\frac{\{w(F_o^2 - F_c^2)^2\}}{n-p}}$$

where, *GooF* is the goodness of fit, *n* is the number of reflection, and *p* is the number of parameters refined.

```
TITL  Zircon (7:PIF)                                                    -Sample ID
CELL  0.71073   6.5790   6.5790   5.9600   90.000   90.000   90.000     -Wavelength and unit-cell parameters
                                                                         (a, b, c, alpha, beta, and gamma).
ZERR     4.00   0.0006   0.0006   0.0007    0.000    0.000    0.000     -Formula Unit (Z) and errors of
                                                                         respective unit-cell parameters.
LATT   2                                                                 -Lattice type; 2 means lattice is
                                                                         I-centred and centrosymmetric.
SYMM  - X, 1/2 - Y,   Z
SYMM    X, - Y, - Z
SYMM  - X, 1/2 + Y, - Z
SYMM  1/4 - Y, 1/4 - X, 3/4 - Z                                          -Symmetry operators
SYMM  1/4 + Y, 3/4 + X, 1/4 - Z
SYMM  1/4 + Y, 1/4 - X, 3/4 + Z
SYMM  1/4 - Y, 3/4 + X, 1/4 + Z
SFAC  ZR   SI   O                                                        -Structure factors
UNIT  4    4    16                                                       -Number of atoms of each element
                                                                         mentioned in SFAC.
SIZE  0.10 0.10 0.08                                                     -Size of the crystal.
TEMP                                                                     -Crystat temperature during data
                                                                         collection.
TREF                                                                     -Command for the direct method
                                                                         execution.


FVAR    1.0                                                              -overall scale factor, other
                                                                         variables can be added, if needed.
ZR1   1    0.000000    0.750000    0.125000    10.12500    0.00828       -Atom names, type as per SFAC,
SI    2    0.000000    0.750000    0.625000    10.12500    0.00901       fractional coordinates, occupancy,
O     3    0.000000    0.065875    0.194955    10.50000    0.01281       isotropic displacement parameters.
HKLF 4                                                                   -HKLF 4 = h, k, l, F2, σ(F2), BN
END                                                                      -End of file
```

Figure 2.3 An instruction file showing the command lines with the concise explanation.

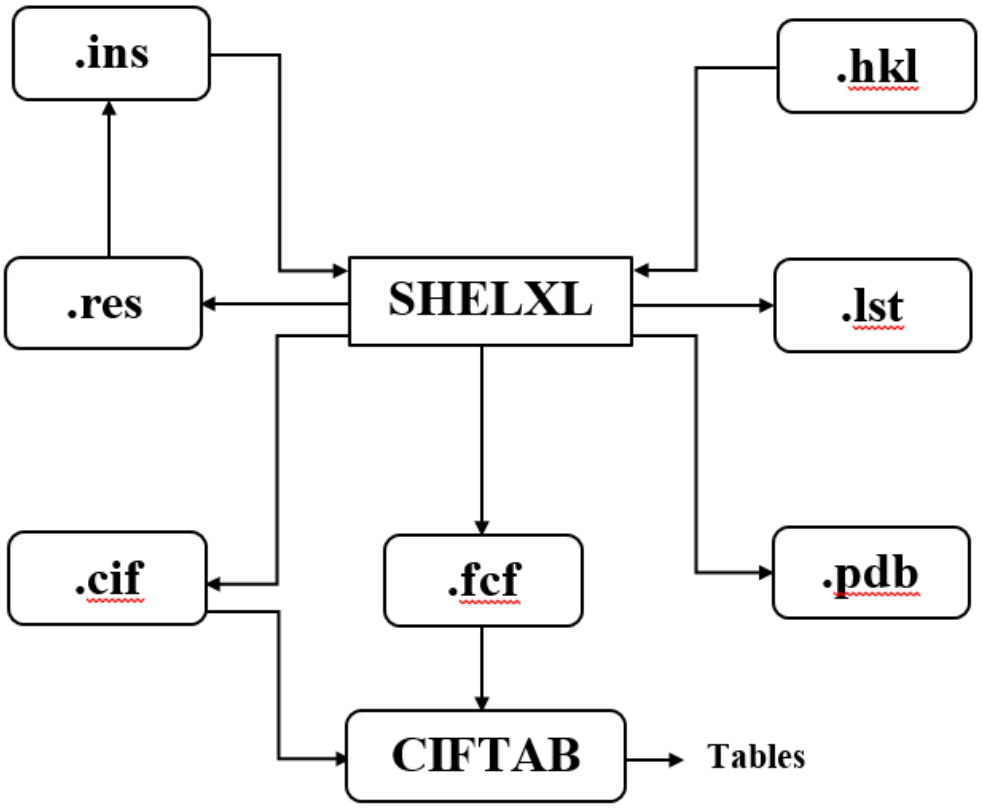

Figure 2.4 Flow chart showing the structure refinement steps on the SHELX program (Sheldrick 1997).

2.2.3 Synchrotron High-Resolution Powder X-ray Diffraction (HRPXRD)

Synchrotron X-rays is used for the powder diffraction data collection in this study. Synchrotron radiations have high brightness and intensity, high collimation, high-level of polarization, and large tunability in wavelength by monochromatization. Using synchrotron high-resolution powder X-ray diffraction (HRPXRD) study, it is possible to obtain the crystal structural information in mineral with an accuracy much higher than the conventional X-ray powder diffraction. It is a powerful tool to investigate the radiation damage in minerals, although fully

metamict minerals are, in general, X-ray amorphous. However, it can provide useful structural information about the partially damaged minerals.

Samples selected using synchrotron HRPXRD study must be of the highest quality ensured by the reflected and stereomicroscopes. Selected crystals are then finely ground in an agate mortar and pestle, loaded into a Kapton capillary, and sealed with glass wool. The HRPXRD data are collected from a synchrotron X-ray diffraction facility at the X-ray Operations and Research beamline 11-BM at the Advanced Photon Source, Argonne National Laboratory.

2.2.4 General Structure Analysis System (GSAS) Refinement

GSAS is a set of programs for the crystal structural analysis of both powder and single-crystal diffraction data obtained with conventional and synchrotron X-rays or neutrons (Von Dreele and Larson 1998). It is one of the best method to handle the diffraction data from a mixture of phases and is capable of extracting the structural parameters for each phase. GSAS has a wide range of constraints and other features useful for complex structural issues and it also includes a number of plotting and utility tools.

EXPGUI is a graphical user interface to GSAS and allow to use the main GSAS capabilities that are needed for Rietveld analysis (Toby 2001; Young 1993). It has some useful tools for viewing fits and refinement results. Least-squares is the main refinement technique used by GSAS and is executed by the program GENLES. For the powder diffraction data, GENLES uses the minimization function defined by the following equation (Rietveld 1969):

$$M_p = \sum w(I_{obs} - I_{calc})^2$$

The goodness of fit, called the reduced χ^2 is defined by the following function (Von Dreele and Larson 1998):

$$\chi^2 = \frac{M_p}{(N_{obs} - N_{vari})}$$

where, the N_{obs} is the total number of observations in the histogram and N_{vari} is the number of variables in the refinement.

The criteria of successful refinement are indicated by the two residual functions for each powder diffraction data (histogram) as follows (Larson and Von Dreele 2004):

$$R_F^2 = \frac{\sum |I_{obs} - I_{calc}|}{\sum I_{obs}}$$

$$R_{wp} = \sqrt{\frac{M_p}{\sum w I_{obs}^2}}$$

In the least-squares refinement the following parameters can be adjusted simultaneously (Will 2006):

- Unit-cell parameters (*a*, *b*, *c*, *α*, *β*, and *γ*)
- 2θ-zero correction
- Overall scale factor
- Atom coordinates (*x*, *y*, *z*)
- Atomic site occupancies
- Atomic displacement parameters, both isotropic and anisotropic
- Profile functions
- Background functions
- Preferred orientation

The information required for the least-squares refinement are:

- Initial values of all the above listed parameters
- 2θ range
- X-ray wavelength

2.3 Gamma-Ray Spectroscopy with HPGe Detector (GRS-HPGe)

A complete gamma-ray spectroscopy system consists of detector (hyper purity germanium (HPGe), silicon lithium, silicon charged particle, scintillation), cooling system, electronics (e.g., preamplifier, analog to digital converter, amplifier, pulse generator, multichannel analyzers, etc.), and analysis software (e.g, Genie 2000, gammaW, etc.). An HPGe detector can cover an extensive range of energies and for a variety of applications. This is the most widely used detector to measure low-level natural radiations. For effective operation, HPGe detectors require cooling to cryogenic temperatures. A liquid cryogen (commonly liquid nitrogen) or an electro-mechanical cooler is commonly used to cool the HPGe detectors. Figure 2.5 shows the main components of gamma-ray spectroscopy with HPGe detector.

Gamma-ray spectrometry with the HPGe has an excellent energy resolution to separate and resolve various close energy gamma-ray peaks in a complex energy spectrum. The full width at half maximum (FWHM) of the full energy peak is usually applied to measure the energy resolution. The units of FWHM is expressed in KeV for HPGe detector and are calibrated using full energy peaks of the standard radioactive sources such as 663 KeV for a ^{137}Cs or 1332 KeV for a ^{60}Co sources. When the incident gamma radiations from the sample interact with a detector a number of electronic charges are generated and are proportional to the amount of gamma-ray energy deposited in the detector. A simplified counting system is illustrated in Figure 2.6. The HPGe detector is enclosed with a 10 cm thick cylindrical lead shield to reduce the background radiation from many natural radiation sources. A thin layer (0.1 cm) of Cu is placed inside of lead shielding to reduce the contribution from Pb X-ray fluorescence.

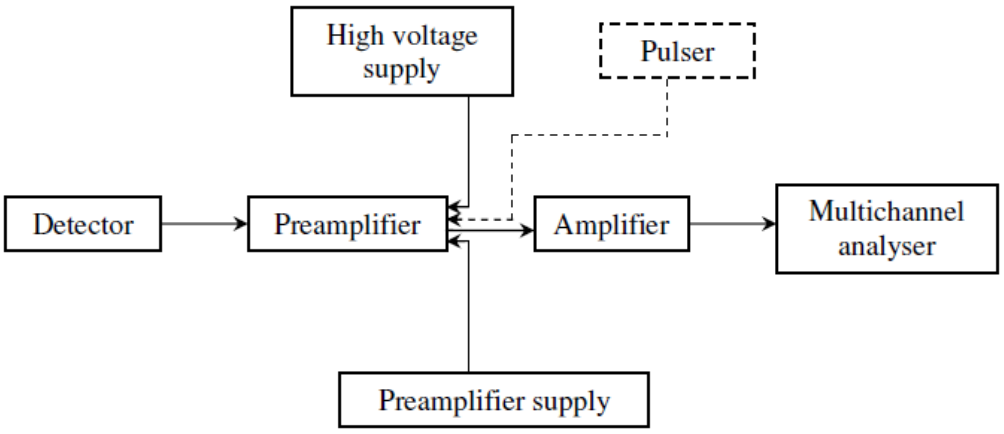

Figure 2.5 Schematic representation of electronic system for gamma-ray spectrometry (Gilmore 2008)

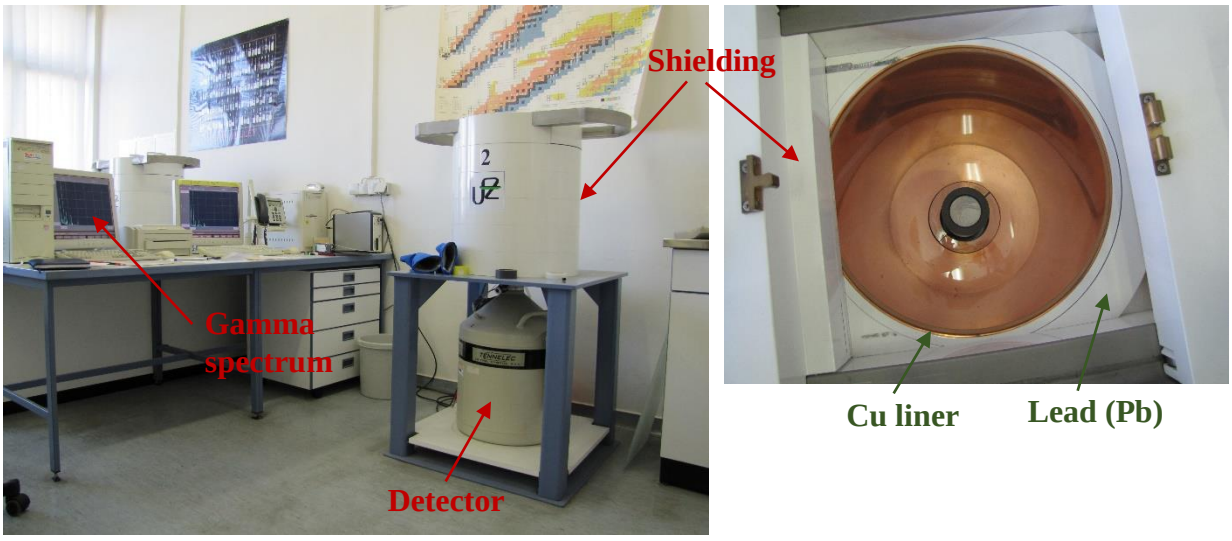

Figure 2.6 Gamma-ray spectroscopy system in the department of analytical chemistry of the Centre for Environmental Research (UFZ) in Leipzig, Germany.

Chapter 3: Crystal Chemistry and Structural Variations in Zircon

3.1 Abstract

This study investigates the variations of structural parameters and chemistry of a partially metamict sample 8 and seven detrital zircons from different localities using single-crystal X-ray diffraction (SCXRD), synchrotron high-resolution powder X-ray diffraction (HRPXRD), and electron-probe micro-analysis (EPMA) techniques. The unit-cell parameters for the eight zircon samples vary linearly with increasing unit-cell volume, *V*. Sample 7 from the Canadian Arctic Islands has the smallest unit-cell parameters, bond distances, ideal stoichiometric composition, unaffected by α-radiation damage, and is chemically pure. Sample 8 from Jemaa, Nigeria has the largest unit-cell parameters because of the effect of α-radiation doses received over a long time (2384 Ma). All the samples show good correlations between the Zr and Si *apfu* (atom per formula unit) versus *V*. The α-radiation doses in the samples are lower than ~3.5×10^{15} α-decay events/mg. Substitutions of other cations at the Zr and Si sites control the variations of the structural parameters for samples 1 to 7, of which sample 5 shows relatively large unit-cell parameters and bond distances because the Zr site accommodates other cations that have larger ionic radii than the Zr atom. Geological age increases the radiation doses in zircon and it is related to the *V*.

3.2 Introduction

The variations of structural parameters in zircon in relation to the contents of Zr, Si, and α-radiation damage are important because they control the stability of zircon. The crystal structure of zircon was first determined by Vegard (1916) and confirmed by others (Krstanovic 1958; Hassel 1926; Wyckoff and Hendricks 1928). The crystal structure of gem quality and synthetic zircons were studied under ambient conditions and elevated pressure, temperature conditions

(Robinson et al. 1971; Hazen and Finger 1979; Mursic et al. 1992; Kolesov et al. 2001; Finch et al. 2001).

The ideal chemical formula for zircon is $ZrSiO_4$ (formula unit, $Z = 4$) and the space group is $I4_1/amd$. Zircon is an orthosilicate and its structure consists of isolated SiO_4 tetrahedra and ZrO_8 dodecahedra (Fig. 3.1). The SiO_4 and ZrO_8 polyhedra share edges to form a chain parallel to **c** axis (Fig. 3.1a). The SiO_4 tetrahedron is a tetragonal disphenoid (symmetry 2*m*) elongated parallel to [001] because of repulsion between the Zr^{4+} - Si^{4+} cations, whose polyhedra share a common edge (Robinson et al. 1971). The Zr atom is coordinated to eight O atoms and forms a dodecahedron with symmetry 2*m*. According to Nyman et al. (1984), the ZrO_8 dodecahedron in zircon can be described as two interpenetrating ZrO_4 tetrahedra in which one is elongated along [001] and the other is compressed along [100] and [010].

Zircon is one of the most incompressible silicate minerals and its unit-cell parameters decrease with increasing pressure (Hazen and Finger 1979). The unit-cell parameters of metamict zircon increase with increasing temperature (Mursic et al. 1992). The increase in *a* and *c* unit-cell parameters arises from expansion of the ZrO_8 polyhedra, but the overall shape of the SiO_4 tetrahedra remains essentially undistorted in partially metamict zircon (Rios et al. 2000a). In synthetic zircon, the Zr^{4+} cation is strongly bonded and its vibrational behavior is not strongly anisotropic (Kolesov et al. 2001). The limits of rare earth elements (REE) and P atom incorporations in the Zr and Si sites in zircon structure depend on not only the ionic radii of REE and P atom, but also the structural strain at the Zr and Si sites (Finch et al. 2001). There are small voids and open channels in between SiO_4 and ZrO_8 polyhedra are considered as potential interstitial sites for impurity atoms (Fig. 3.1). Such sites can accommodate interstitial atoms without excessive structural strain (Finch and Hanchar 2003). The role of these interstitial sites is unknown.

This study examines the structural variations and α-radiation damage in zircon from different localities. Several structural trends are observed and explained on the basis of crystal-chemical principles.

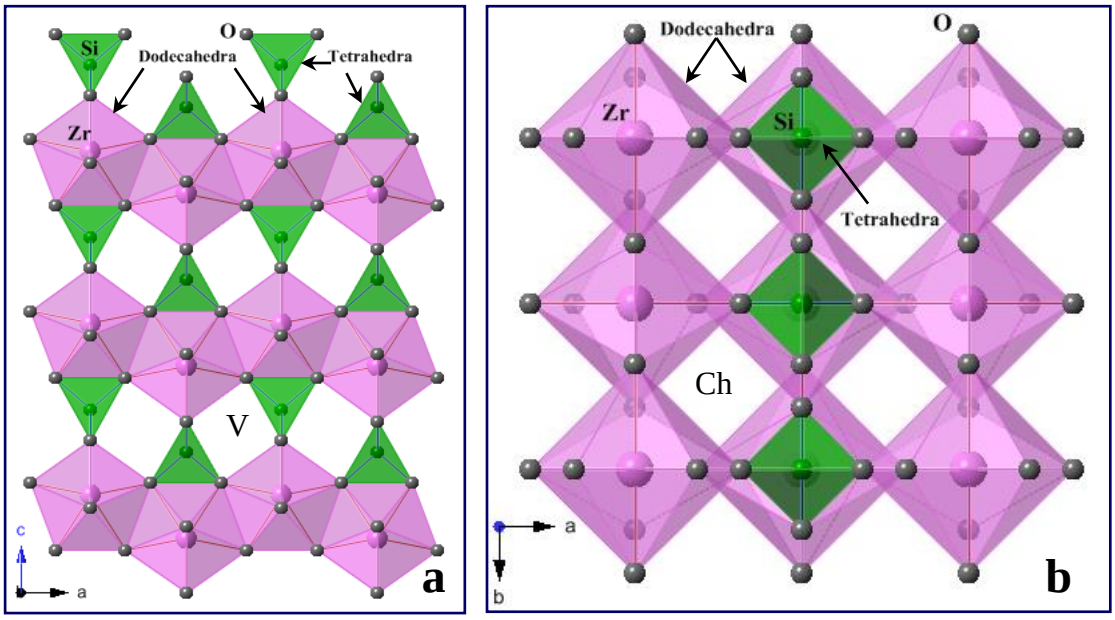

Figure 3.1 Polyhedral representation of the zircon structure, which consists of isolated SiO_4 tetrahedra and ZrO_8 dodecahedra that share their (**a**) edges with each other to form a chain parallel to c axis, and (**b**) corners with other ZrO_8 dodecahedra along the a and b axes. There are small voids (V) and open channels (Ch) in between SiO_4 and ZrO_8 polyhedra.

3.2.1 Sample Description

Seven detrital and one partially radiation damaged zircon samples were used in this study. Samples 1 to 4 are from Cox's Bazar (CB), Bangladesh, samples 5 to 7 are from the Canadian Arctic Island, and sample 8 is from Jemaa, Nigeria (JN). Sample information is given in Table 3.1.

Table 3.1 Zircon sample information

Sample no.	Colour	Sample type	Sample locations
1	Gray	Detrital	Foredune part of recent beach, Cox's Bazar, Bangladesh
2	Colourless		
3	Pink		
4	Red		
5	Gray	Detrital	Beverly Inlet Formation of the Franklinian Basin of the Canadian Arctic Islands, Canada. (GSC Call # C 198959)
6	Gray	Detrital	Hecla Bay Formation of the Franklinian Basin of the Canadian Arctic Islands, Canada. (GSC Call # C 246257)
7	Gray	Detrital	Parry Islands Formation of the Franklinian Basin of the Canadian Arctic Islands, Canada. (GSC Call # C 245984)
8	Dark gray	Massive	Jemaa, Nigeria

Zircon fraction was separated from a raw beach placer sand sample with gravity, conductivity, and magnetic separators at Beach Sand Minerals Exploitation Centre, Bangladesh. Using a stereomicroscope, (1) colourless, (2) pink, (3) gray, and (4) red zircon crystals were selected from the detrital zircon fraction. Three more detrital zircon samples were separated from samples collected from three sedimentary formations: (5) Beverly Inlet Formation (BIF; GSC Call # C 198959), (6) Hecla Bay Formation (HBF; GSC Call # C 246257), and (7) Parry Islands Formation (PIF; GSC Call # C 245984) of the Franklinian Basin, Canadian Arctic Islands, Canada. The separation technique for samples 5 to 7 was given by Anfinson et al. (2012). All zircon samples were examined with a stereomicroscope and a polarized microscope, and high quality, inclusion free, nearly spherical, small, and high purity crystals were selected for examination using single-crystal X-ray diffraction (SCXRD), synchrotron high-resolution powder X-ray diffraction (HRPXRD), and electron-probe micro-analysis (EPMA) techniques.

3.3 Analytical Methods

3.3.1 Electron-Probe Micro-Analyses (EPMA)

All measurements were conducted with a JEOL JXA-8200WD-ED electron-probe micro-analyzer. The JEOL operating program on a Solaris platform was used for ZAF (atomic number, Z; absorption, A; fluorescence, F) correction and data reduction. The wavelength-dispersive (WD) analysis was conducted quantitatively using an accelerated voltage of 15 kV, a beam current of 2.021×10^{-8} A, and a beam diameter of 5 μm. Various minerals and compounds were used as standards [zircon (Zr*L*α and Si*K*α), hornblende (Ca*K*α, Mg*K*α, Fe*K*α, Ti*K*α, and Al*K*α), hafnium (Hf*L*α), YPO_4 (Y*L*α and P*K*α), ThO_2 (Th*M*α), barite (S*K*α), pyromorphite (Pb*M*β), UO_2 (U*M*α), rhodonite (Mn*K*α), NiO (Ni*K*α), strontianite (Sr*L*α), chromite (Cr*K*α), and scapolite (Cl*K*α)] (Table 3.2). A total of 14 spots were analysed for each zircon crystal. The oxide wt. % and the calculated atom per formula unit (*apfu)* for eight samples are given in Table 3.3. The concentrations of U, Th, and ∑(Hf + TE) for 52 zircon crystals are provided in Table 3.4.

Thirty six of the 52 zircon crystals are from Cox's Bazar, Bangladesh, 15 are from Canadian Arctic Islands, and one from Jemaa, Nigeria were analyzed. All 52 crystals were analysed for Hf and trace elements (TE = Ca, U, Th, Pb, Ti, Fe, Sr, Y, Cr, Mg, Mn, Ni, P, S, and Al). The α-radiation doses received by each zircon crystal were calculated for all 52 crystals, but crystals 9 to 52 were not characterized further (Table 3.4).

3.3.2 Calculation of α-Radiation Dose

To calculate α-radiation dose using the equation of Holland and Gottfried (1955), the age of the zircon sample is needed. The ages for samples 5, 6, and 7 were determined by Anfinson et al. (2012). The age of both samples 5 and 6 is 370 Ma, and the age of sample 7 is 365 Ma. The ages of these samples have been used for their radiation dose calculations.

Table 3.2 Setup and measurement condition for EPMA

Element	Standard	X-ray	Crystal	Peak position	Background low (mm)	Background high (mm)	Bias (V)
Ca	Hornblende	*K*α	PETJ	108.284	5.0	5.0	1650
Zr	Zircon	*L*α	PETJ	194.482	5.0	5.0	1676
Hf	Hafnium	*L*α	LIFH	108.484	5.0	5.0	1700
Si	Zircon	*K*α	TAP	77.500	6.0	7.0	1702
Ti	Hornblende	*K*α	PETJ	88.888	5.0	5.0	1650
Th	ThO_2	*M*α	PETJ	132.664	3.0	2.7	1710
Fe	Hornblende	*K*α	LIFH	133.990	5.0	5.0	1700
Y	YPO_4	*L*α	TAP	70.137	1.5	3.0	1702
P	YPO_4	*K*α	PETJ	198.032	4.0	5.5	1650
U	UO_2	*M*α	PETJ	125.385	5.0	5.0	1676
Cr	Chromite	*K*α	LIFH	158.590	5.0	5.0	1700
Sr	Strontianite	*L*α	TAP	74.657	4.5	5.0	1702
S	Barite	*K*α	PETJ	172.915	5.0	5.0	1650
Pb	Pyromorphite	*M*β	PETJ	162.656	2.0	13.4	1730
Mn	Rhodonite	*K*α	LIFH	145.519	5.0	5.0	1700
Mg	Hornblende	*K*α	TAP	107.616	5.5	5.0	1702
Cl	Scapolite	*K*α	PETJ	152.380	5.0	5.0	1650
Ni	NiO	*K*α	LIFH	114.670	3.0	3.0	1700
Al	Hornblende	*K*α	TAP	90.726	6.0	6.5	1702

The ages of zircon samples 1 to 4 and 8 were not previously determined. The concentrations of Pb in these samples are either "zero", or below detection limit (bdl), except sample 3 (Table 3.2). Therefore, the concentrations of U, Th, and Pb from the same batch of samples having the same colour and similar crystal shapes were selected to calculate their chemical ages using "Montel chemical age equation" (Montel at al. 1996). The calculated ages obtained for samples 1 to 4 are: (1) 739, (2) 641, (3) 604, and (4) 948 Ma, and sample 8 is 2384 Ma. The CB beach minerals originated from the nearby exposed Miocene and Pliocene aged Boka Bil and Tipam Formations. The age of zircon grains in the Tipam Formation is between 500-1700 Ma, but few grains have Cenozoic and Cretaceous age (Najman et al. 2012).

Table 3.3 The EMPA data for eight zircon samples[+]

Wt. %	1:CB	2:CB	3:CB	4:CB	5:BIF	6:HBF	7:PIF	8:JN
ZrO_2	65.74	65.19	65.09	65.30	63.47	66.35	65.66	65.01
HfO_2	1.11	1.37	1.59	1.36	1.33	1.11	1.19	1.19
UO_2	0.02	0.06	0.17	0.08	0.12	0.02	0.03	0.02
ThO_2	0.01	0.06	0.01	0.08	0.06	0.02	0.03	0.16
PbO	bdl	bdl	0.02	bdl	0.04	0.01	bdl	0.02
CaO	0.02	0.02	0.01	0.02	0.06	0.01	0.02	0.02
Y_2O_3	0.10	0.04	0.04	0.08	0.28	0.03	0.05	bdl
SrO	bdl	bdl	bdl	bdl	bdl	bdl	bdl	bdl
TiO_2	bdl	bdl	bdl	bdl	bdl	bdl	bdl	bdl
FeO	bdl	0.01	0.01	0.04	0.26	0.01	bdl	0.01
Cr_2O_3	0.01	bdl	bdl	bdl	0.01	bdl	bdl	0.01
MnO	0.01	0.01	0.01	bdl	0.02	0.01	0.01	0.01
MgO	bdl	0.01	0.01	0.01	bdl	0.01	0.01	bdl
NiO	bdl	0.02	0.02	0.02	0.02	bdl	0.01	bdl
SiO_2	32.67	32.11	32.28	32.75	32.16	31.84	31.34	31.28
P_2O_5	bdl	bdl	bdl	bdl	bdl	bdl	bdl	bdl
SO_3	0.03	0.04	0.03	0.03	0.03	0.01	0.02	0.01
Al_2O_3	bdl	bdl	bdl	bdl	0.02	bdl	bdl	bdl
Total	99.71	98.93	99.29	99.78	97.89	99.43	98.38	97.75
Atom per formula unit (apfu) based on 4 O atoms								
Zr	0.984	0.987	0.983	0.978	0.969	1.002	1.004	1.000
Hf	0.010	0.012	0.014	0.012	0.012	0.010	0.011	0.011
U	-	-	0.001	0.001	0.001	-	-	-
Th	-	-	-	0.001	0.000	-	-	0.001
Ca	0.001	0.001	-	0.001	0.002	-	0.001	0.001
Y	0.002	0.001	0.001	0.001	0.005	-	0.001	-
Fe	-	-	-	0.001	0.007	-	-	-
Mn	-	-	-	-	0.001	-	-	-
Mg	-	-	-	-	-	0.001	0.001	-
Ni	-	-	-	0.001	0.001	-	-	-
∑Zr site	0.997	1.003	1.000	0.995	0.998	1.014	1.018	1.014
Si	1.003	0.997	0.999	1.006	1.007	0.986	0.983	0.987
S	0.001	0.001	0.001	0.001	0.001	-	-	-
∑Si site	1.004	0.998	1.000	1.006	1.008	0.986	0.983	0.987
Total*	2.001	2.001	2.001	2.001	2.006	2.001	2.001	2.001

*Total = sum of all cations; bdl = below detection limit; CB = Cox's Bazar, Bangladesh; BIF = Beverly Inlet Formation; HBF = Hecla Bay Formation; PIF = Parry Island Formation: JN = Jemaa, Nigera; [+]The same sample numbers are used in all the Tables.

Table 3.4 Concentrations of U, Th, calculated α-radiation dose (α-decay events/mg), and Hf + TE for 52 zircon crystals*

Sample ID	U (ppm)	Th (ppm)	Radiation dose	Hf + TE (*apfu*)	Sample ID	U (ppm)	Th (ppm)	Radiation dose	Hf + TE (*apfu*)
1:CB	144	103	4.34E+14	0.014	27	707	186	1.67E+15	0.018
2:CB	494	528	1.36E+15	0.017	28	571	381	1.46E+15	0.023
3:CB	1538	98	3.26E+15	0.019	29	903	458	2.10E+15	0.021
4:CB	669	732	2.82E+15	0.018	30	400	432	1.04E+15	0.017
5:BIF	1058	542	1.48E+15	0.029	31	316	350	8.26E+14	0.015
6:HBF	135	149	2.12E+14	0.013	32	236	466	7.13E+14	0.016
7:PIF	300	254	4.42E+14	0.014	33	1214	286	4.34E+15	0.015
8:JN	208	1370	4.80E+15	0.014	34	2900	387	1.02E+16	0.038
9	498	268	1.45E+15	0.013	35	1690	815	6.36E+15	0.033
10	326	19	8.57E+14	0.019	36	809	560	3.17E+15	0.032
11	340	0	8.83E+14	0.017	37	2779	1775	1.08E+16	0.097
12	164	295	5.97E+14	0.011	38	2280	6861	1.29E+16	0.066
13	848	1097	2.84E+15	0.016	39	4549	3334	1.80E+16	0.148
14	702	239	1.96E+15	0.018	40	1672	1008	6.44E+15	0.069
15	2221	631	6.13E+15	0.028	41	624	379	8.89E+14	0.017
16	1209	311	3.32E+15	0.019	42	90	128	1.49E+14	0.024
17	517	170	1.44E+15	0.014	43	275	445	4.72E+14	0.032
18	510	178	1.42E+15	0.015	44	118	130	1.85E+14	0.016
19	1312	334	3.60E+15	0.021	45	117	0	1.46E+14	0.014
20	127	271	4.86E+14	0.016	46	461	176	6.27E+14	0.019
21	3082	1909	9.10E+15	0.084	47	33	139	8.07E+13	0.014
22	3448	475	9.22E+15	0.093	48	566	243	7.67E+14	0.018
23	869	1898	3.35E+15	0.018	49	0	230	6.53E+13	0.019
24	1935	350	4.49E+15	0.024	50	104	278	2.07E+14	0.017
25	1129	582	2.81E+15	0.019	51	175	46	2.28E+14	0.015
26	1070	63	2.42E+15	0.026	52	72	91	1.15E+14	0.012

*Samples 1 to 7 represent the seven zircon used for the SCXRD work and sample 8 was used for the HRPXRD; samples 9 to 23, 24 to 28, 29 to 32, and 33 to 40 are gray, colourless, pink, and red zircon crystals, respectively, collected from Cox's Bazar, Bangladesh; samples 41 to 44, 45 to 46, and 47 to 52 are BIF, HBF, and PIF zircon crystals collected from the Canadian Arctic Islands. The chemical ages for gray, colourless, pink, and red zircons from Cox's Bazar, Bangladesh and for a zircon from Jemaa, Nigeria are 739, 641, 604, 948, and 2384 Ma, respectively. The ages for zircons from the Canadian Arctic Islands are taken from Anfinson et al. (2012).

Our calculated ages for zircons from Cox's Bazar fall in the range determined by Najman et al. (2012). The calculated chemical ages of zircon have been used to calculate α-radiation doses. The α-radiation dose (α-decay events/mg) for each zircon sample is calculated from the average U and Th concentrations using the following equation from Holland and Gottfried (1955):

$$D = 8N_1[exp(\lambda^{238} \cdot T) - 1] + 7N_2[exp(\lambda^{235} \cdot T) - 1] + 6N_3[exp(\lambda^{232} \cdot T) - 1],$$

where D = the dose in α-decay events/mg; N_1, N_2, and N_3 = the present numbers of ^{238}U, ^{235}U, and ^{232}Th in atoms/mg; and λ^{235}, λ^{238}, and λ^{232} = the radioactive decay constants (year^{-1}) of ^{235}U, ^{238}U, and ^{232}Th, respectively. The calculated α-radiation doses for the 52 crystals are given in Table 3.4.

3.3.3 SCXRD Data Collection and Structure Refinement

A zircon crystal was mounted on the tip of a glass fiber (diameter less than 0.1 mm) using an adhesive. The mounted crystal was placed on a goniometer head and the crystal was centered in the X-ray beam for diffraction measurements. SCXRD data were collected at 295 K with a Nonius Kappa CCD on a diffractometer using Bruker Nonius FR591 Rotating Anode with graphite monochromated Mo-Kα radiation (λ = 0.71073 Å). The generator setting was 50 kV and 36 mA, and the cryostat setting for the diffractometer was set to 295 K (room temperature). The detector-crystal distance was fixed at 35 mm. For unit-cell determination, a total of 10 frames were collected and the scan settings were 1° rotation per frame (total rotation = 10°) and 22 seconds X-ray exposure time per frame. After obtaining the satisfactory unit-cell parameters and mosaicity values (less than 1°), complete data sets were collected using a 2° per frame rotation with X-ray exposure of 42-122 seconds per frame.

Table 3.5 Single-crystal structure refinement data for seven zircon samples*

		1:CB	2:CB	3:CB	4:CB	5:BIF	6:HBF	7:PIF
Crystal size (mm)		0.08 × 0.08 × 0.06	0.10 × 0.04 × 0.03	0.08 × 0.08 × 0.08	0.10 × 0.08 × 0.06	0.08 × 0.06 × 0.08	0.10 × 0.08 × 0.06	0.10 × 0.10 × 0.08
Colour		Gray	Colourless	Pink	Red	Gray	Gray	Gray
Crystal shape		Spherical	Prismatic	Prismatic	Spherical	Spherical	Spherical	Spherical
Unit-cell parameters	*a*	6.6040(9)	6.6030(7)	6.6030(5)	6.604(2)	6.6120(7)	6.5840(5)	6.5790(6)
(Å)	*c*	5.9830(6)	5.9800(4)	5.9780(4)	5.985(1)	5.9970(5)	5.9720(5)	5.9600(7)
Volume, V (Å^3)		260.94(6)	260.73(4)	260.64(4)	261.0(1)	262.18(4)	258.88(4)	257.97(4)
Density$_{calc}$ (g/cm^3)		4.666	4.670	4.672	4.665	4.644	4.703	4.720
Absorption coefficient (mm^{-1})		4.461	4.464	4.466	4.459	4.440	4.496	4.512
2θ range		2° – 54.34°	2° – 54.70°	2° – 54.70°	2° – 54.70°	2° – 55.16°	2° – 54.87°	2° – 54.96°
Index ranges		-8=<h=<8	-8=<h=<8	-8=<h=<8	-8=<h=<8	-8=<h=<8	-8=< h=<8	-8=<h=<8
		-8=<k=<8	-8=<k=<8	-8=<k=<8	-8=<k=<8	-8=<k=<8	-8=<k=<8	-5=<k=<6
		-7=<l=<7	-7=<l=<7	-7=<l=<7	-7=<l=<7	-7=<l=<7	-6=< l=<7	-7=< l=<7
Total reflections		442	487	528	487	556	800	255
Unique reflections		88	91	91	91	92	88	85
R_{int}		0.0270	0.0230	0.0224	0.0267	0.0224	0.0252	0.0183
GooF on F^2		0.499	0.569	0.500	0.519	0.567	0.571	0.455
R_1		0.0125	0.0170	0.0110	0.0133	0.0114	0.0114	0.0121
wR_2		0.0494	0.0558	0.0483	0.0516	0.0556	0.0542	0.0436
Extinction coefficient		0.026(4)	0.11(1)	0.076(7)	0.005(2)	0.003(2)	0.019(6)	0.039(8)
Largest difference		0.320	0.825	0.309	0.430	0.250	0.281	0.261
peak/hole (e/Å^3)		-0.330	-2.015	-0.382	-0.295	-0.310	-0.266	-0.268
Mosaicity (°)		0.616(6)	0.540(5)	0.534(4)	0.85(1)	0.733(5)	0.79(1)	0.843(7)

*Space group = $I4_1/amd$; formula unit, Z = 4 based on $ZrSiO_4$; F(000) = 344.

Table 3.6 Atom coordinates and anisotropic displacement parameters (Å^2) obtained with SCXRD for seven zircon samples

	1:CB	2:CB	*2a:CB	3:CB	4:CB	5:BIF	6:HBF	7:PIF
Coordinates and U_{ij} for O (x = 0; U_{12} = U_{13} = 0)								
y	0.0656(2)	0.0657(2)	0.06609(9)	0.0657(2)	0.0659(2)	0.0658(2)	0.0654(2)	0.0659(2)
z	0.1951(3)	0.1953(3)	0.1954(1)	0.1957(2)	0.1948(3)	0.1953(3)	0.1953(3)	0.1950(2)
U_{eq}	0.0094(5)	0.0108(6)	0.0027(2)	0.0097(5)	0.0114(5)	0.0115(5)	0.0124(5)	0.0119(4)
U_{11}	0.0109(9)	0.0131(9)		0.0128(7)	0.0146(10)	0.0130(9)	0.0142(7)	0.0128(6)
U_{22}	0.0092(8)	0.0089(8)		0.0095(6)	0.0079(8)	0.0105(8)	0.0116(6)	0.0123(6)
U_{33}	0.0080(9)	0.0104(10)		0.0067(8)	0.0117(9)	0.0110(9)	0.0116(9)	0.0105(7)
U_{23}	0.0017(5)	-0.0003(6)		0.0005(3)	-0.0005(5)	-0.0006(4)	-0.0002(5)	0.0002(3)
U_{ij} for Si (x =0, y = 3/4, z = 5/8; U_{23} = U_{12} = U_{13} = 0)								
U_{eq}	0.0068(5)	0.0064(7)	0.0014(1)	0.0061(6)	0.0081(6)	0.0086(6)	0.0088(6)	0.0083(5)
U_{11}	0.0070(7)	0.0072(8)		0.0070(7)	0.0083(7)	0.0090(8)	0.0093(8)	0.0090(6)
U_{22}	0.0070(7)	0.0072(8)		0.0070(7)	0.0083(7)	0.0090(8)	0.0093(8)	0.0090(6)
U_{33}	0.0065(12)	0.0046(14)		0.0043(12)	0.0076(12)	0.0077(13)	0.0078(13)	0.0070(11)
U_{ij} for Zr (x =0, y = 3/4, z = 1/8; U_{23} = U_{12} = U_{13} = 0)								
U_{eq}	0.0067(4)	0.0062(5)	0.00023(4)	0.0061(4)	0.0072(4)	0.0081(4)	0.0085(4)	0.0081(4)
U_{11}	0.0068(4)	0.0066(5)		0.0065(4)	0.0072(4)	0.0080(4)	0.0083(5)	0.0083(4)
U_{22}	0.0068(4)	0.0066(5)		0.0065(4)	0.0072(4)	0.0080(4)	0.0083(5)	0.0083(4)
U_{33}	0.0065(6)	0.0056(7)		0.0054(6)	0.0072(5)	0.0083(6)	0.0089(6)	0.0076(5)

*2a:CB is obtained with HRPXRD

Table 3.7 Selected bond distances (Å) and angles (°) obtained with SCXRD for seven zircon samples

		1:CB	2:CB	*2a:CB	3:CB	4:CB	5:BIF	6:HBF	7:PIF
$Zr\text{-}O^{I}$	4x	2.126(2)	2.126(2)	2.1305(6)	2.127(1)	2.128(2)	2.131(2)	2.119(1)	2.120(1)
$Zr\text{-}O^{II}$	4x	2.269(2)	2.270(2)	2.2696(6)	2.271(1)	2.267(2)	2.274(2)	2.263(2)	2.259(1)
<Zr-O> [8]		2.198(2)	2.198(2)	2.2001(6)	2.199(2)	2.198(2)	2.203(2)	2.193(2)	2.190(1)
<O-Zr-O> [18]		78.77(5)	78.76(5)	78.761(1)	78.75(4)	78.77(5)	78.76(5)	78.76(5)	78.77(3)
Si-O	4x	1.625(2)	1.624(2)	1.6220(6)	1.622(1)	1.625(2)	1.626(2)	1.622(2)	1.618(1)
<O-Si-O> [6]		109.69(8)	109.69(9)	106.69(1)	109.69(6)	109.70(8)	109.70(9)	109.69(7)	109.70(6)
Zi-Si	2x	2.9920(3)	2.9900(2)	2.9915(1)	2.9890(2)	2.9930(10)	2.9990(3)	2.9860(3)	2.9800(4)
Zr-Zr	2x	3.6250(4)	3.6242(3)	3.6263(1)	3.6240(3)	3.6250(10)	3.6300(3)	3.6147(2)	3.6112(3)

*2a is obtained with HRPXRD; [ ] = number of bonds and angles; 4x and 2x = number of equal bonds.

The diffraction spots were measured in full, scaled with SCALEPACK, corrected for Lorentz-polarization, and integrated using the Nonius program suite DENZO-SMN (Otwinowski and Minor 1997). The space group $I4_1/amd$ was obtained based on systematic absent of reflections and structure factor statistics. Full-matrix least-squares refinements were carried out with SHELXL-97 using neutral atom scattering factors (Sheldrick 1997). The WinGX program suite was used as the platform for the refinement (Farrugia 1999). The starting structural model was taken from Kolesov et al. (2001). The occupancy factors for Zr, Si, and O sites were assumed to be 1.0. Anisotropic displacement parameters were used for all atoms and the refinement resulted in convergence. Details of the data collection, processing, and refinements are given in Table 3.5. The refined atom coordinates and displacement parameters are given in Table 3.6 and selected bond distances and angles are given in Tables 3.7.

3.3.4 Synchrotron HRPXRD Data Collection

Fragments of zircon sample 8 from Jemaa, Nigeria and detrital grains of a colourless zircon sample 2a (renaming of sample 2 for the purpose of HRPXRD data) from Cox's Bazar were hand-picked under a stereomicroscope, and crushed into fine powder (<10 μm in diameter) using an agate mortar and pestle for the HRPXRD experiment, which was conducted at beamline 11-BM, Advanced Photon Source, Argonne National Laboratory. The typical energy for the beamline 11-BM is 30 keV. The fine powdered samples were loaded into Kapton capillaries (0.8 mm internal diameter), sealed with glass wool, and rotated during the experiment at a rate of 90 rotations per second. Data were collected to a maximum 2θ of about 50° with a step size of 0.001° and a step time of 0.1 s/step. The HRPXRD data were collected using twelve silicon crystal analyzers that allow for high angular resolution and accuracy, high precision, and accurate diffraction peak positions. A silicon (NIST 640c) and alumina (NIST 676a) standard (ratio of ⅓ Si to ⅔ Al_2O_3 by weight) was used to calibrate the instrument and refine the

monochromatic wavelength used in the experiment (Table 3.6). More technical aspects of the experimental set-up are given elsewhere (Antao et al. 2008; Lee et al. 2008; Wang et al. 2008).

3.3.5 Rietveld Structure Refinement

The HRPXRD data for samples 2a and 8 were analyzed with the Rietveld method (Rietveld 1969), as implemented in the GSAS program (Larson and Von Dreele 2000), and using the EXPGUI interface (Toby 2001). The initial unit-cell parameters and atom coordinates for both samples were taken from Robinson et al. (1971). Scattering curves for neutral atoms were used. The background was modeled using a Chebyschev polynomial (24 terms). The peak profiles were fitted with the pseudo-Voigt function (type-3) in the GSAS program (Finger et al., 1994). A full matrix least-squares refinement was carried out by varying the parameters in the following sequence: a scale factor, unit-cell parameters, atom coordinates, and isotropic displacement parameters. The site occupancy factors for Zr and Si were not refined because the chemical analyses showed that these sites were fully occupied (Table 3.3). In the final stage of the refinement, all of the parameters were allowed to vary simultaneously, and the refinement proceeded to convergence. The fitted HRPXRD traces are shown (Fig. 3.2). For sample 8, only the unit-cell parameters are of significance because most of the sample is metamict.

The unit-cell parameters, data collection and refinement statistical indicators for samples 2a and 8 are given in Table 3.8. The atom coordinates and isotropic displacement parameters are given in Table 3.6. The selected bond distances and angles are tabulated in Table 3.7.

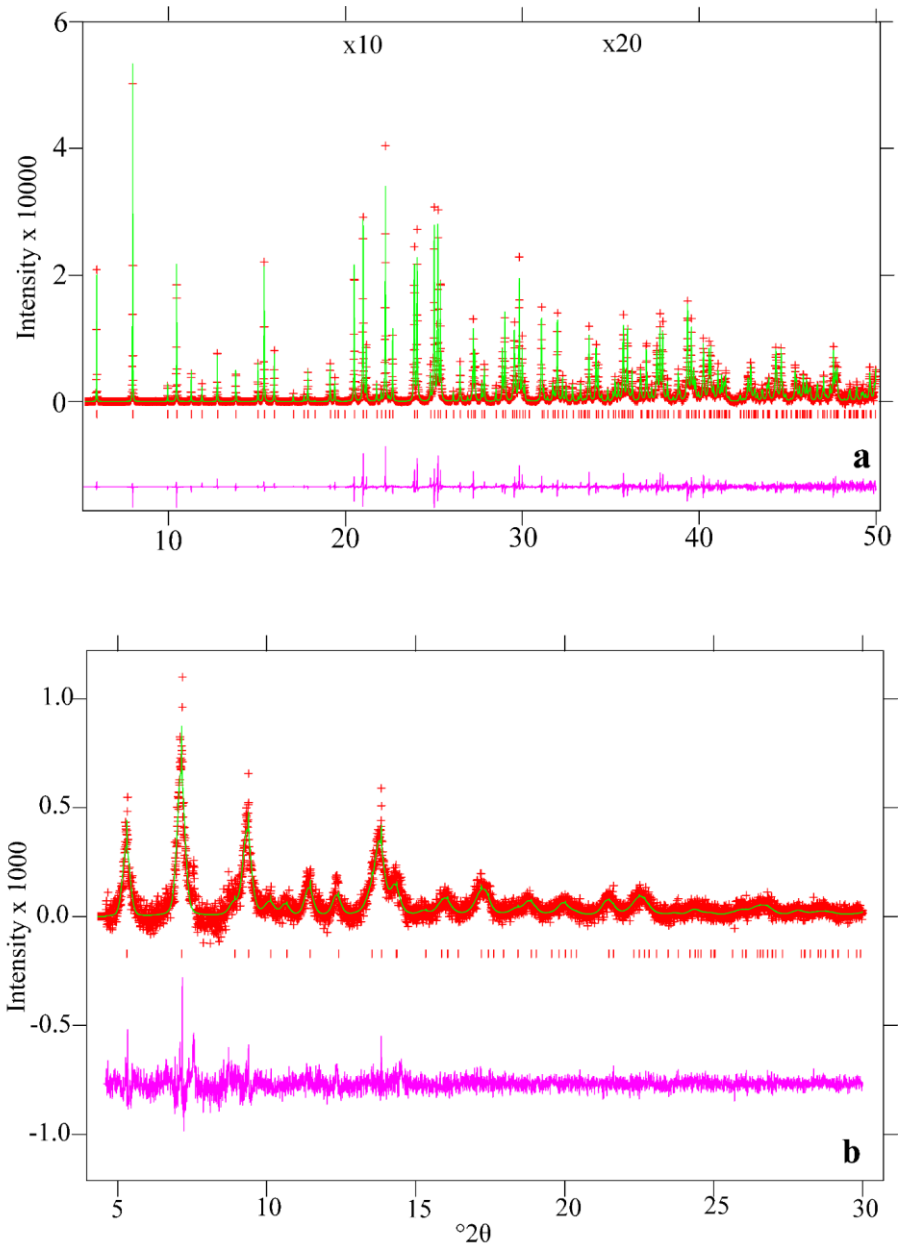

Figure 3.2 The HRPXRD traces for (**a**) sample 2a and (**b**) sample 8 together with the calculated (continuous green line) and observed (red crosses) profiles. The difference curve ($I_{obs} - I_{calc}$) is shown at the bottom (pink) at the same scale as the intensity. The short vertical red lines indicate allowed reflection positions. The intensities for the trace and difference curve for sample 2a that are above 20 and 35° 2θ are multiplied by 10 and 20, respectively. The peaks for sample 2a are very sharp and symmetric, and have very high intensity because of high crystallinity. In contrast, the peaks for sample 8 are broad and asymmetric with lower intensity indicating a large amount of amorphous material resulting from α-radiation doses.

Table 3.8 HRPXRD structure refinement data for samples 2a and 8

	8:JN	2a:CB
a (Å)	6.6541(1)	6.60700(1)
c (Å)	6.03551(6)	5.98303(1)
V (Å^3)	267.237(7)	261.174(1)
$^1N_{data}$	26246	44994
$^2N_{obs}$	159	263
^{3}Overall R_F^2	0.0395	0.0311
Reduced χ^2	0.8608	2.859
λ (Å)	0.41417(2)	0.459001(2)
2θ range	2° - 30°	2° - 50°

$^1N_{data}$ = Number of data points; $^2N_{obs}$ = number of observed reflections; R_F^2 = Overall R-structure factor based on observed (*obs*) and calculated (*calc*) structure amplitudes.

3.4 Results and Discussion

3.4.1 Chemical Composition of Zircon

Zircon has a stoichiometric composition of 67.2 wt % ZrO_2 and 32.8 wt % SiO_2 and may also contain about 20 to 24 trace elements (TE), including Hf and Y as minor elements (Hoskin and Schaltegger 2003). The zircon samples from this study have a composition from 63.47 to 66.66 wt. % ZrO_2 and from 31.28 to 32.75 wt. % SiO_2 (Table 3.3). Zircon may contain Y (0.1 < Y (wt. %) < 1.0), P, and rare earth elements (REE) (Hoskin and Schaltegger 2003). The Y concentration in the samples for this study ranges from bdl (sample 8) to 0.28 wt. % (sample 5). The REE-bearing zircons are commonly enriched with P (Finch and Hanchar 2003). No P was detected in our samples, so it may be assumed that the REE concentrations are very low (Table 3.3). The Hf^{4+} can replace Zr^{4+} cation, as the ionic radius of Hf^{4+} (0.83 Å) is almost the same as that of Zr^{4+} (0.84 Å) for 8-coordination (Shannon 1976). Crystalline zircon may contain a mean value of 1.2 wt. % HfO_2, with a range from 0.75 to 1.64 wt. %, whereas metamict zircon may

incorporate a mean value of 3.0 wt. % HfO_2, with a range from 1.40 to 6.0 wt. % (Zhenmin and Jingming 1986). All our samples contain HfO_2 from 1.11 (sample 1) to 1.59 wt. % (sample 3), which is close to the HfO_2 concentration for crystalline zircon (Table 3.3). Typical concentrations of UO_2 and ThO_2 in crystalline zircon fall between 0.06 and 0.40 wt. %, and in metamict zircon fall between 0.20 and 1.5 wt. %. UO_2 can reach weight percent level but its concentration ranges usually from 0.01 to 0.40 wt. % in crystalline zircon and from 0.20 to 1.50 wt. % in metamict zircon (Zhenmin and Jingming 1986; Murakami et al. 1991; Harley and Kelly 2007). In this study, all samples contain [0.02 (sample 1) to 0.17 wt. % (sample 3)] UO_2 and is within the range for crystalline zircon. The presence of ThO_2 is less than that of UO_2 and is usually range from 0 to 0.20 wt. % in the crystalline zircon and from 0.10 to 1.50 wt. % in the metamict zircon (Zhenmin and Jingming 1986; Murakami et al. 1991; Harley and Kelly 2007). ThO_2 concentrations ranges from 0.01 (sample 1) to 0.16 (sample 8) in samples for this study and fall in the range of crystalline zircon as well. Pb^{2+} is not incorporated in zircon when it crystallizes because it is highly incompatible with both Zr^{4+} and Si^{4+} in terms of its ionic radius (1.29 Å in 8-fold coordination) (Harley and Kelly 2007). However, the radiogenic Pb can develop later due to the decay of ^{238}U, ^{235}U, and ^{232}Th, but its concentration depends on the time and structural state of zircon, which is key to geochronology. The PbO_2 concentrations in the samples from this study are very low and range from "bdl" to 0.04 wt. % (sample 5). Normally crystalline zircon contains trace amounts of Ca^{2+}, but the metamict zircon incorporates Ca^{2+} in its structure. The presence of Ca^{2+} is the most common indicator of alteration in zircon. The highest amount of Ca^{2+} (0.06 wt. %) is observed in sample 5 indicating that zircon may accommodate other cations through the substitution (Table 3.3).

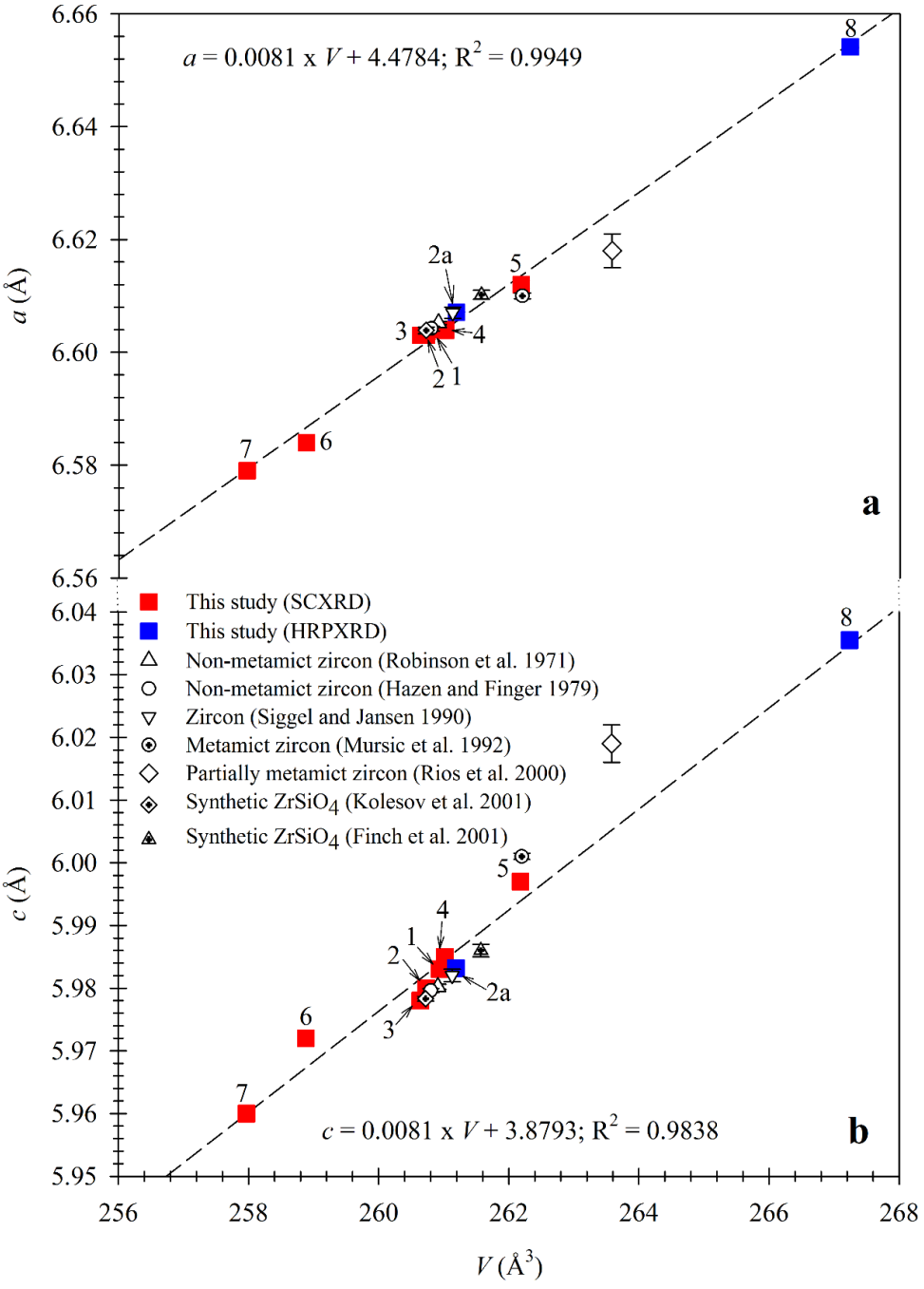

Figure 3.3 Variations of unit-cell parameters for zircons: (**a**) *a* with *V* and (**b**) *c* with *V*. The dashed linear regression lines are based on data from this study and their equations are given as insets. The *a* and *c* parameters vary linearly with *V*. Data from the literature are included for comparison.

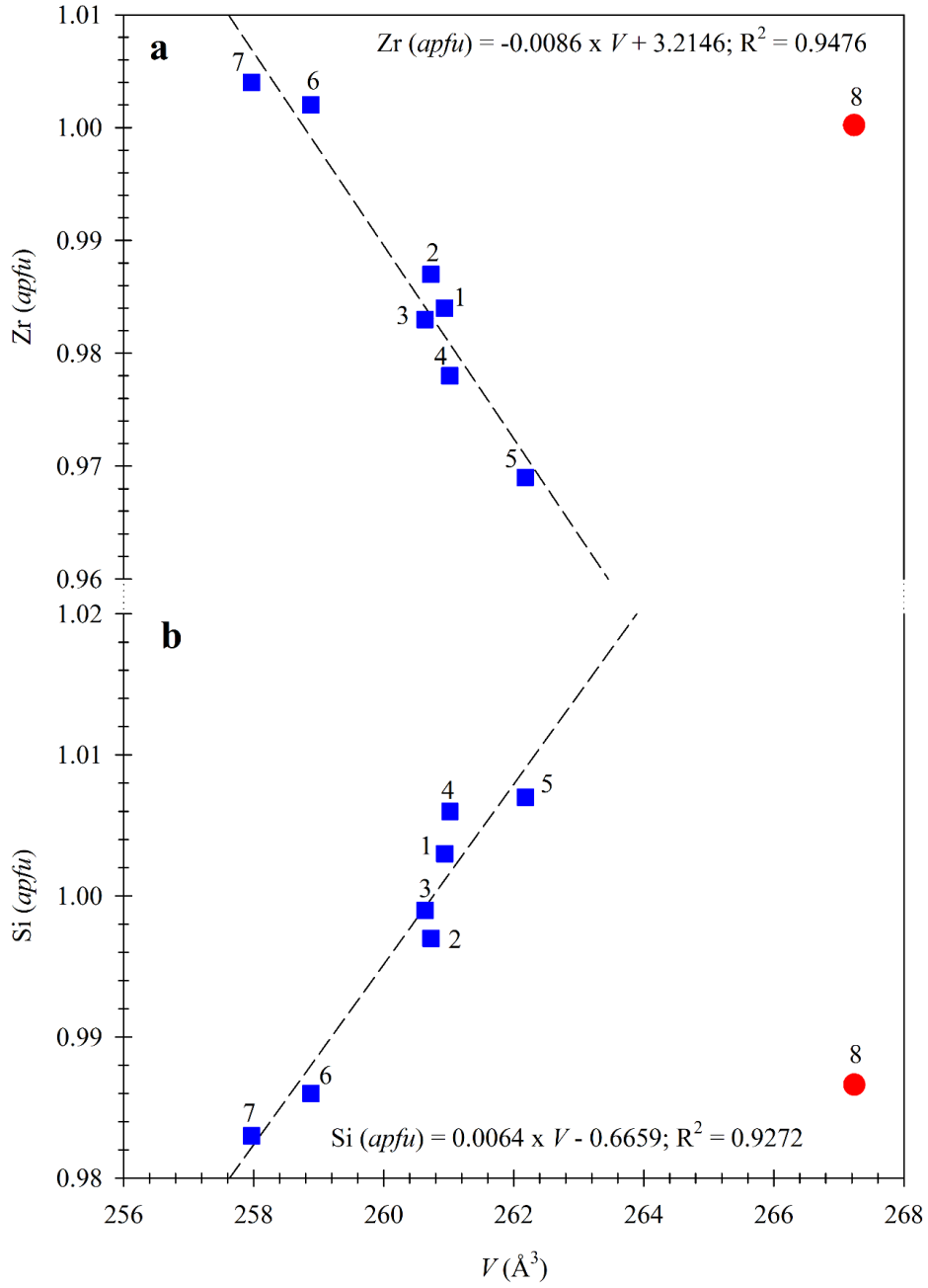

Figure 3.4 The variations of Zr and Si for the eight zircon samples: (**a**) Zr with *V*, and (**b**) Si with *V*. The dash lines represent linear fits for samples 1 to 7 and their equations are given as insets. An inverse linear correlation exists between Zr and *V* in (**a**). A linear correlation exists between Si and *V* in (**b**). The metamict sample 8 is far off the trend lines.

3.4.2 Variations of Unit-Cell Parameters for Zircon

The *a* and *c* unit-cell parameters increase linearly with increasing unit-cell volume, *V* (Tables 3.5 and 3.8; Fig. 3.3). Unit-cell parameters for undamaged, partially and fully damaged, and synthetic zircons from literature are close to the trend line (Fig. 3.3). The unit-cell parameters for samples 1 to 4 from Cox's Bazar are similar to each other and they are similar to the values for undamaged zircon studied by Robinson et al. (1971). The unit-cell parameters for sample 2a is nearly the same as sample 2. Sample 7 has small unit-cell parameters whereas those for sample 8 are the largest because of partial damage by α-radiation (Tables 3.5, 3.8; Fig. 3.3). The unit-cell parameters for zircon generally increase with increasing amount of accumulated α-radiation damage (Holland and Gottfried 1955; Murakami et al. 1991; Rios et al. 2000b). Therefore, the small unit-cell parameters for sample 7 may not be related to α- radiation damage. The unit-cell parameters for sample 5 are close to the metamict zircon studied by Mursic et al. (1992). The slopes of the two linear regression lines for *a* and *c* unit-cell parameters are the same, indicating that the crystal structure change uniformly in the **a** and **c** directions (Fig. 3.3).

3.4.3 Relation Between Unit-Cell Parameters and Chemical Composition

The variations of the unit-cell volume, *V*, with the concentrations of Zr and Si are shown (Fig. 3.4). The *V* increases with decreasing Zr *apfu* and with increasing Si *apfu*. Sample 8 is far away from the two linear regression lines bnecause the *V* is significantly larger than the other samples. The increase of *V* for sample 8 is not related to the concentrations of Zr and Si *apfu* (see Fig. 3.5). The large *V* for sample 8 arises from radiation damage.

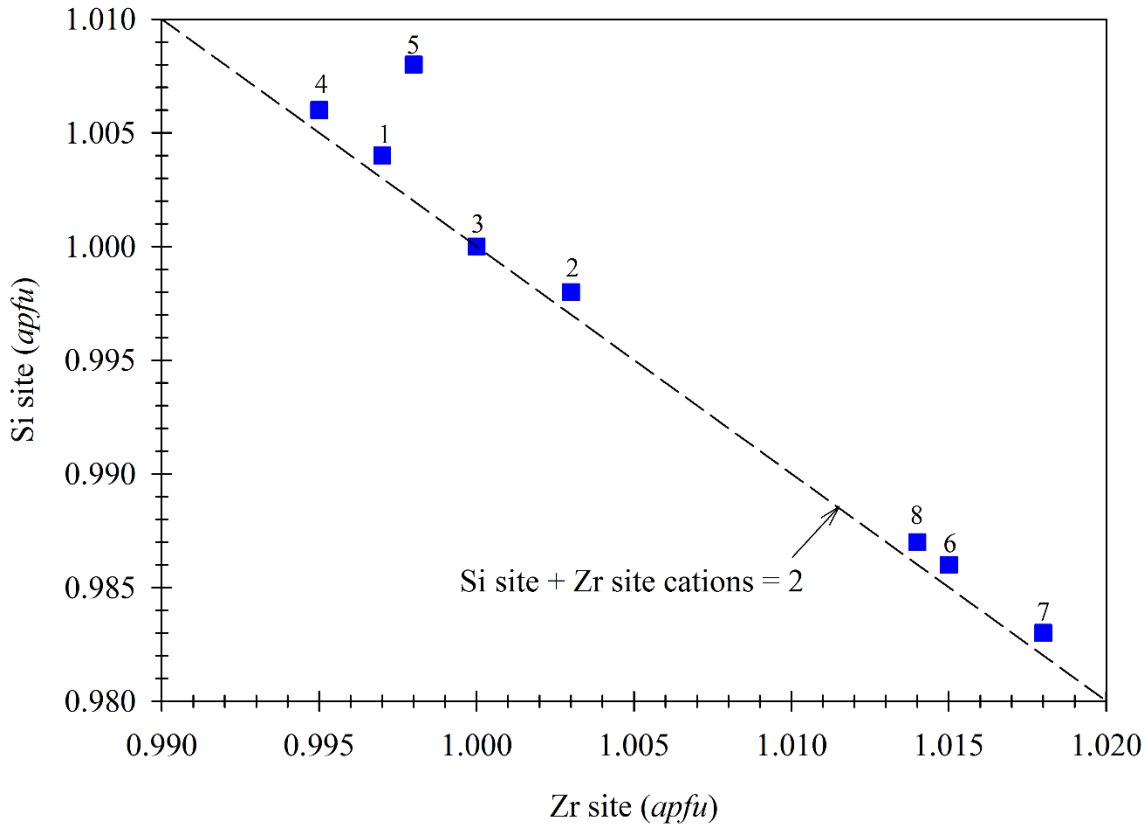

Figure 3.5 Variation in Zr site cations with Si site cations. Sample 3 has at the ideal stoichiometry and the Zr and Si sites are fully occupied. The diagonal dashed line indicates cations sum, Si + Zr = 2, along which all the zircons fall, except sample 5, which does not show ideal stoichiometric composition.

The Hf, U, Th, Ca, Y, Fe, Mn, Ni, and Mg have 8-coordination and close proximity to Zr in terms of their ionic radii, so they substitute for the Zr atom. Only S atom, which has 4-coordination and close in size to Si can substitute for the Si atom. The sum of Zr site cations is plotted against the sum of Si site cations (Table 3.3; Fig. 3.5). Sample 3 has ideal stoichiometry because the concentrations of cations in the Zr and Si sites are 1.0 *apfu* (Table 3.3). All samples, except sample 5, fall close to a dashed diagonal line representing the sum of Zr and Si site

cations = 2 (Fig. 3.5). Samples 6 and 7 show slight non-stoichiometry and display excess cations on the Zr site, which is inversely related to slight deficit in the Si site. Hancher et al. (2001) demonstrated that the excess Zr site cations might occupy Si cation site for REE- and P-doped synthetic zircons. The excess Zr site cations in samples 6 and 7 may occupy the Si site or open spaces in the zircon structure. Sample 5 displays the stoichimetric imbalanced relation between Zr and Si site cations. Substitutions for Zr in sample 5 are higher than that for the other samples. Because most of the cations incorporated in sample 5 have ionic radii larger than that of the Zr atom, the *V* increases (Fig. 3.4).

3.4.4 Relation Between Bond Distances and Chemical Composition

The Zr atom is coordinated to eight O atoms and form ZrO_8 dodecahedra in the zircon structure. Each dodecahedron contains two distinct Zr-O distances (Table 3.7). The $Zr\text{-}O^{II}$ distance is slightly longer than the $Zr\text{-}O^{I}$ distance. The $Zr\text{-}O^{I}$ distance for sample 6 is ~0.57 % smaller and the $Zr\text{-}O^{II}$ distance is ~0.09 % shorter than that in undamaged zircon (Robinson et al. 1971). Usually the long $Zr\text{-}O^{II}$ distance increases along the [001] direction with increasing amount of radiation damage, whereas there is small change in the short $Zr\text{-}O^{I}$ distance (Rios et al. 2000a). Therefore, samples 6 and 7 are not affected by radiation damage.

The average <Zr-O> and Si-O distances vary linearly with *V* (Fig. 3.6). Based on the correlation factor, R^2, the systematic variations of Si-O distances are not as good as the average <Zr-O> distances. The Si-O and average <Zr-O> distances are short in sample 7, which is nearly pure zircon. It contains Zr that is close to 1.0 *apfu* and Si that is close to ~0.98 *apfu* (Table 3.3; Fig. 3.7). There are no other cations in the Si site (e.g., P and S). Thus, the short Si-O distance of 1.618(1) Å for sample 7 is not substitutional, and may represent the pure Si-O distance that is similar to that in quartz where Si-O = 1.608 Å (Antao et al. 2008). Sample 5 shows long Si-O and average <Zr-O> distances (Fig. 3.6). The reason could be subtitutional

because the Zr site is not fully occupied (0.969 *apfu*), but the Si site shows full occupancy (1.007 *apfu*). Some cations (e. g., Fe, Y, Ca, etc.) occupy the Zr site in sample 5 that cause the increase in the average <Zr-O> distance (Fig. 3.7).

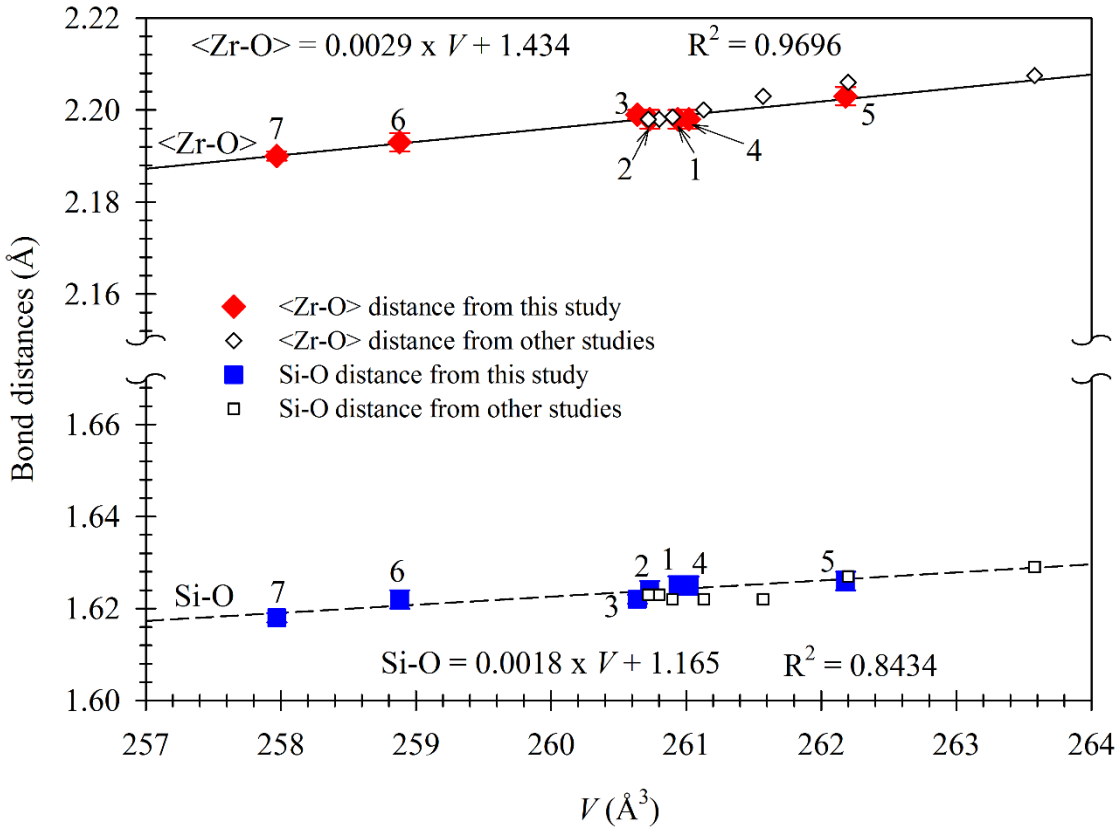

Figure 3.6 The average <Zr-O> and Si-O distances increase linearly with *V* for the 7 zircon samples. The solid and dashed lines denote linear fits with data from this study and their equations are given as inserts.

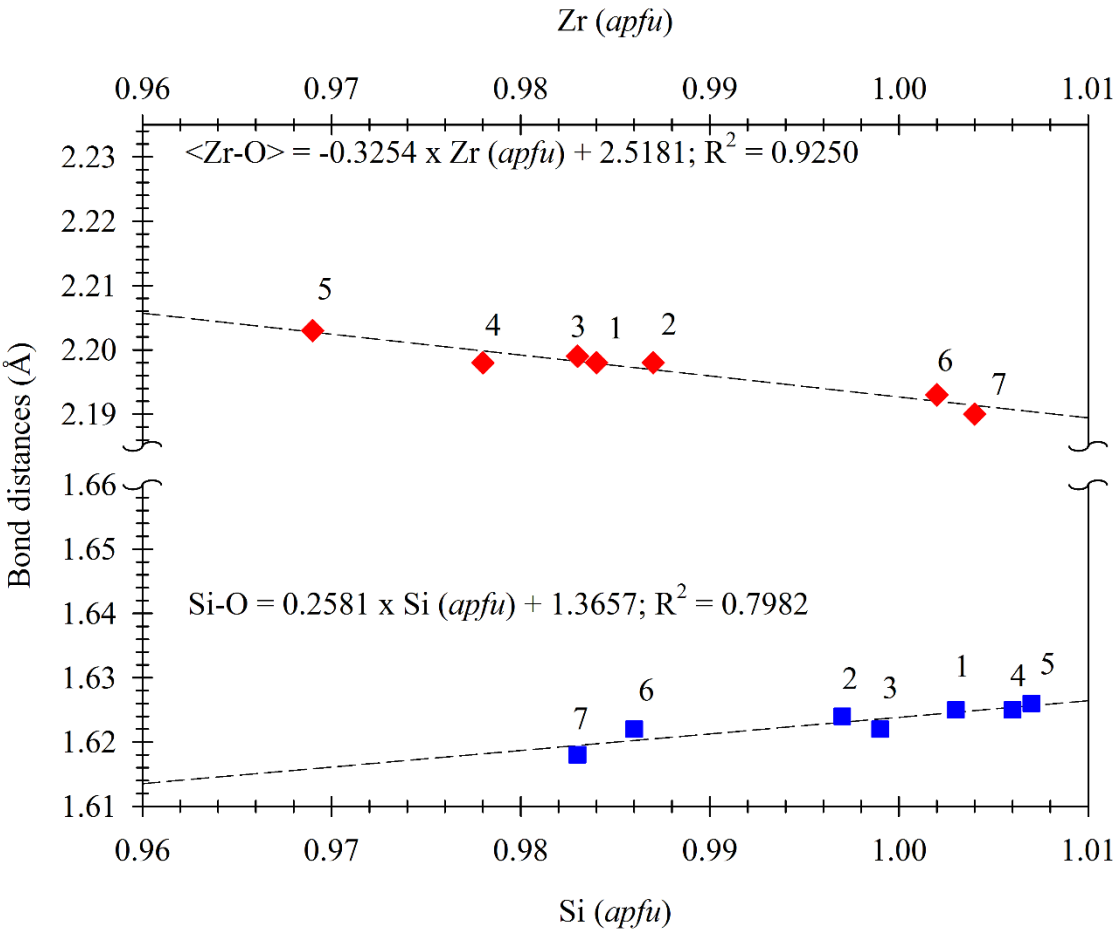

Figure 3.7 Variations of average <Zr-O> distances with Zr and Si-O distances with Si. The dashed lines denote linear fits and their equations are given as inserts. The Si-O distance increases linearly with increasing Si *apfu*, whereas the average <Zr-O> distance decreases linearly with Zr *apfu*.

3.4.5 Effect of α-Radiation Doses in Zircon

The α-radiation doses are plotted against the ∑(Hf + TE) *apfu* for 52 zircon crystals and a good polynomial correlation is obtained (Fig. 3.8). The first percolation threshold of the metamictization process occurs at ~3.5 × 10^{15} α-decay events/mg (Balan et al. 2001). The

isolated amorphous regions resulting from radiation damage are not connected, if zircon receives radiation dose below this threshold value. Samples 1 to 7 are relatively unaffected by radiation damage as they received the α-radiation doses that are lower than the threshold value (Fig. 3.8).

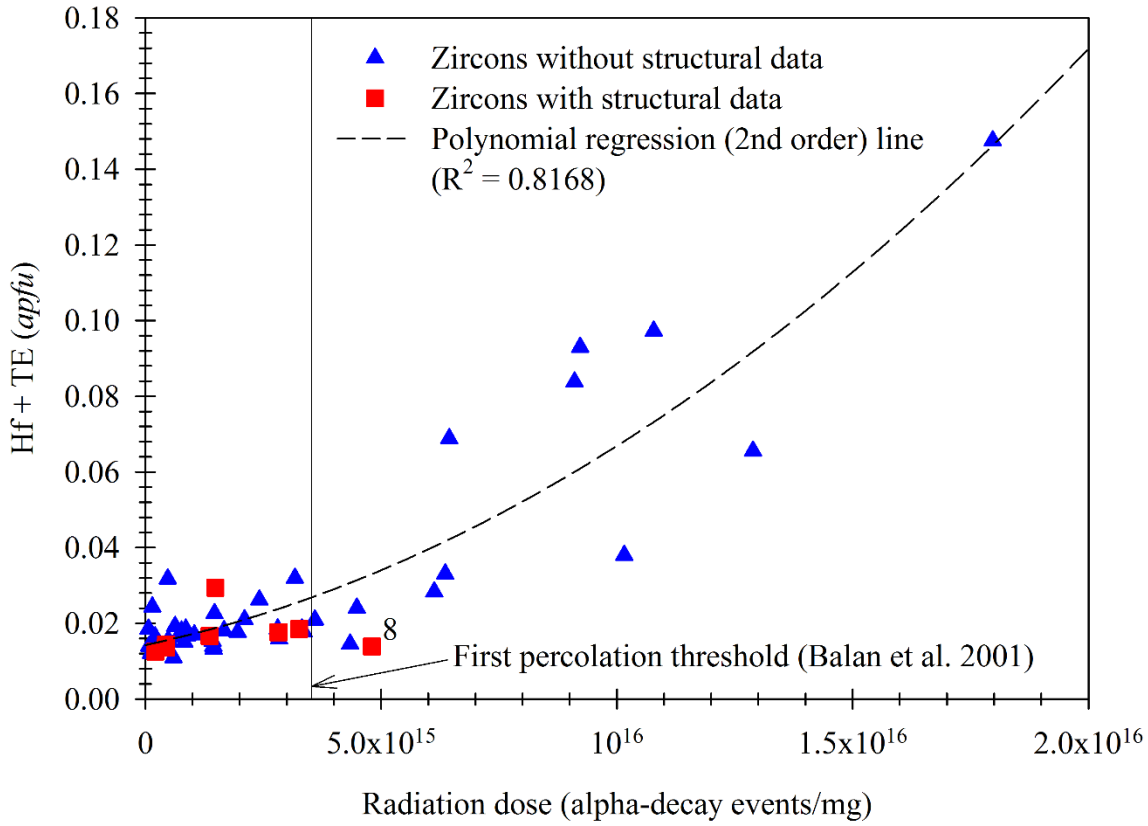

Figure 3.8 Variations of ∑(Hf + TE) with radiation dose in 52 zircon crystals (see Table 3.4). The radiation doses for samples 1 to 7 are below the 1st percolation threshold value (3.5×10^{15} α-decay events/mg). Only the metamict sample 8 received the radiation dose above the 1st percolation threshold value. Crystals 9 to 52 were not characterized structurally.

The maximum amount of radiation dose was received by the metamict sample 8, which is above the threshold value. The α-radiation dose received by sample 8 falls in the range (3.0×10^{15} to 8.0×10^{15} α-decay events/mg), which is 2nd stage amorphization processes, as explained by Murakami et al. (1991). Because of this high amount of radiation dose, the intensity of the synchrotron HRPXRD peaks decreased and the peaks are broadened compared to crystalline zircon (Fig. 3.2). This indicates that the amorphous zones in zircon increases significantly and give rise to large unit-cell parameters for sample 8. Although the crystal structure contains a large amount of amorphous material, it is still chemically similar to crystalline zircon, as indicated by its stoichiometric composition and minor amount of TE content (Fig. 3.8; Table 3.3).

3.4.6 Unit-Cell Volume and Geological Age

The radiation dose for zircon increases with increasing geological age (Lumpkin and Ewing 1988). The control of such age on the unit-cell volume, *V*, is unknown. However, Figure 3.9 shows a relation between age and *V*. Samples 6 and 7 are the youngest zircon and have the smallest *V*. This suggests that they are pure zircon with high crystallinity. Samples 1 to 4 have relatively older ages and have larger *V*. The metamict sample 8 is oldest and has the largest *V*. A positive correlation is obtained where *V* increases with age (Fig. 3.9). Sample 5 is an outlier and has a high *V*, although it is relatively young. Some larger atoms (e. g., Fe, Y, Ca, etc.; Table 3.3) may occupy the Zr site and cause the high *V* for sample 5.

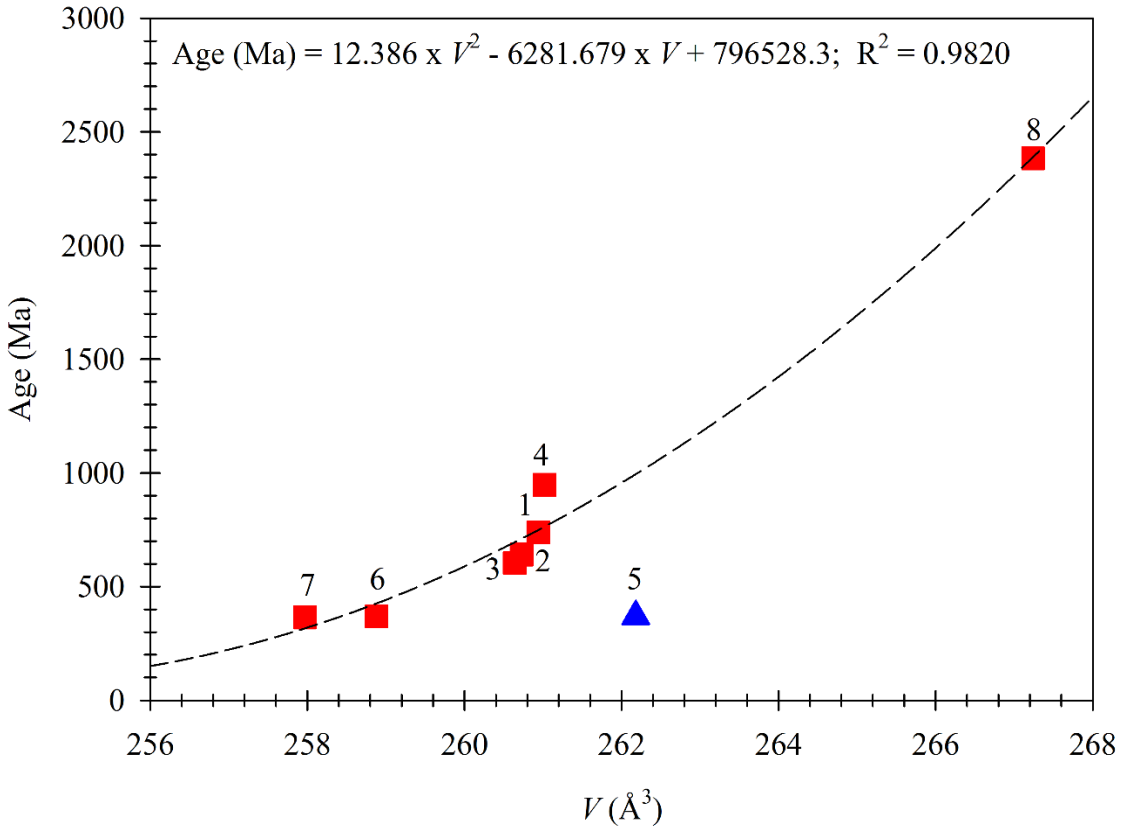

Figure 3.9 The relation between the unit-cell volume, *V* and age for zircons. A good 2nd order polynomial fit (dashed line and equation given as insert) exists between *V* and age for zircon, excluding sample 5 because it has slight non-stoichiometric chemical composition (see Fig. 3.5).

3.5 Conclusions

This study shows some trends among structural (unit-cell parameters and bond distances), chemical composition (Zr, Si, Hf, and TE), and α-radiation doses. If zircon receives low amount of α-radiation doses (< 3.5×10^{15} α-decay events/mg), the concentrations of Zr and Si *apfu* control the variations of unit-cell parameters. The smallest unit-cell parameters and bond distances were obtained for sample 7, which received a minor amount of α-radiation doses (4.42×10^{14} α-decay events/mg) over a short time (365 Ma), so the structure is unaffected. The structural parameters such as unit-cell parameters [a = 6.5790(6), c = 5.9600(7) Å, V = 257.97(4) $Å^3$] and bond distances [<Zr-O> = 2.190(1) Å and Si-O = 1.618(1) Å] may be considered as standard parameters for zircon. Sample 8 received a maximum amount of α-radiation doses (4.80×10^{15} α-decay events/mg) over a long time (2384 Ma) and has the largest unit-cell parameters. Although the V for sample 8 is 3.6 % larger than that for sample 7, the stoichiometric proportions of Zr and Si *apfu* are similar to crystalline zircon. The extreme durability of zircon makes its structure as a prospective host for the disposal of plutonium generated from nuclear power production. A relation exists between age and V for zircon.

Chapter 4: Crystal Structure and Chemistry of Monazite

4.1 Abstract

This study investigates four monazite samples to determine their crystal structure and chemistry using single-crystal X-ray diffraction (SCXRD) and electron-probe micro-analysis (EPMA). After structure refinement with SHELX program, the largest unit-cell parameters [a = 6.7640(5), b = 6.9850(4), c = 6.4500(3) Å, and β = 103.584(2)°] are obtained for sample 1, which is a Th-bearing (0.058 *apfu*) detrital monazite-Ce from Cox's Bazar, Bangladesh. Sample 4, which is a Th-rich (0.169 *apfu*) Monazite-Sm, has the smallest unit-cell parameters [a = 6.7010(4), b = 6.9080(4), c = 6.4300(4) Å, and β = 103.817(3)°]. The a and b unit-cell parameters for samples 1-4 vary linearly with the unit-cell volume, V. The change in a parameter is large (0.2 Å) and is related to the type of cations occupying the Ce/Sm site. The average <Ce/Sm-O> distances vary linearly with V, but the average <P-O> distances are nearly constant, so the PO_4 tetrahedron is rigid. Average distance of four out of nine unique Ce/Sm-O distances are aligned along the [001] direction and they are less affected by the chemical variability of Ce/Sm site cations compared to the average distances of the rest.

4.2 Introduction

Monazite is a rare earth element (REE) phosphate mineral that contain significant variations in REE concentrations (Rapp and Watson 1986). The chemical composition is XPO_4 (X = REE^{3+}, Y^{3+}, Th^{4+}, U^{4+}, Ca^{2+}, and Pb^{2+}). Kersten (1839) first reported the presence of thorium (Th) in monazite, which vary from 0 to 31.5 wt. %. Systematic relations between the unit-cell parameters and Th content in monazite is not established (Murata et al. 1953; Kato 1958). U in monazite is usually less than 0.5 wt. %. Small amounts of Y, Sc, Ca, Mg, Fe, Al, Zr, Mn, Be, Sn, Ti, and Ta occur in monazite. Three major charge-balancing substitution mechanisms occur in monazite (Gramaccioli and Segalstad 1978; Van-Emden 1997; Clavier et al. 2011): (1) (Th,

$U)^{4+} + Ca^{2+} = 2REE^{3+}$, (2) $(Th, U)^{4+} + Si^{4+} = REE^{3+} + P^{5+}$, (3) $4REE^{3+} = 3(Th, U)^{4+}$ + Vacancy. The $LaPO_4$, $CePO_4$, $PrPO_4$, $PdPO_4$, $PmPO_4$, $SmPO_4$, and $EuPO_4$ orthophosphates crystallize in the monoclinic crystal system (space group $P2_1/n$; Z = 4), whereas the $HoPO_4$, $ErPO_4$, $TmPO_4$, $YbPO_4$, and $LuPO_4$ orthophosphates have tetragonal symmetry ($I4_1/amd$; Z = 4) (Boatner 2002). The ionic radii controls the crystal structure of RE orthophosphates. The wide range of chemical variability makes monazite-type minerals useful for containing nuclear waste.

The crystal structures of phosphates with trivalent La^{3+}, Ce^{3+}, Pr^{3+}, and Nd^{3+} cations were determined by X-ray diffraction techniques in 1944 for the Manhattan Project (Mooney 1948). The crystals were dimorphic; one monoclinic phase was isomorphous with monazite and the other was a new hexagonal phase (Mooney 1948). The crystal structure of monazite was first investigated by Ueda (1967) using a sample from Ishikawa-yama, Fukushima Prefecture, Japan. The refined structure gave very high *R* values (16-19 %), and unreliably large P-O distances. Ghouse (1968) studied the structure of monazites from Kerala beach sand, and observed small structural differences after heat treatments up to 1130° C, but the P-O distances were as large as 1.69 Å.

The most complete structural characterizations of natural and synthetic monazites were conducted by Ni et al. (1995). They compared the structural properties of natural and synthetic monazites with those of natural and synthetic xenotimes, and observed that the structural properties of monoclinic monazite and tetragonal xenotime along the [001] chain are similar. The formula for monazite studied by Ni et al. (1995) was $(Ce_{0.51}La_{0.29}Nd_{0.14}Pr_{0.05}Sm_{0.01})_{\Sigma 1.00}(PO_4)$; no U or Th was present. However, the presence of Th in natural monazite is nearly ubiquitous. The crystal-chemical variation in Th-bearing monazite is unknown. Masau et al. (2003) determined only the unit-cell parameters for monazite-Sm from the Annie Claim # 3 granitic pegmatite, southeastern Manitoba, Canada, using both SCXRD and PXRD. The complete crystal structure for monazite-Sm is not determined as yet. Seydoaux-guillaume et al. (2002) determined the unit-cell parameters of two monazites from two different localities using PXRD technique. No complete crystal structure characterization of Th-bearing monazite is

available. Many studies on the crystal structure of synthetic monazites are available in the literature (e.g., Clavier et al. 2011; Dacheux et al. 2013).

Monazite belongs to monoclinic crystal system ($P2_1/n$; Z = 4) and the structure is made up of irregular 9-coordinated Ce/Sm atoms linked together by distorted tetrahedral PO_4 groups (Beall et al. 1981; Ni et al. 1995). The PO_4 tetrahedra are isolated, and are separated by intervening CeO_9 polyhedra (Fig. 4.1). The O atoms coordinate to one P atoms and two Ce. The CeO_9 polyhedra and PO_4 tetrahedra form chains sharing O-O edges along the **c** axis (Clavier et al. 2011).

The aim of this study is to investigate the crystal structure and chemistry of monazite. This study shows variations among unit-cell parameters, bond distances, and chemical compositions of monazite.

4.2.1 Sample Description

Two detrital (1 and 3) and two pegmatitic monazite (2 and 4) samples were used in this study (Table 4.1). The two detrital monazite-rich heavy mineral fractions were separated from two raw beach placer sand samples collected from Cox's Bazar, Bangladesh. All the samples were examined with a stereomicroscope and a polarizing microscope to assess their physical and optical characteristics. High quality, inclusion free, nearly spherical, small, and high purity crystals were selected for single-crystal X-ray diffraction (SCXRD) and electron-probe micro-analysis (EPMA). Fragments of monazite were separated from the two pegmatitic samples with a knife and examined with a stereomicroscope. High purity, optically clear, and inclusion-free fragments were picked for EPMA and SCXRD.

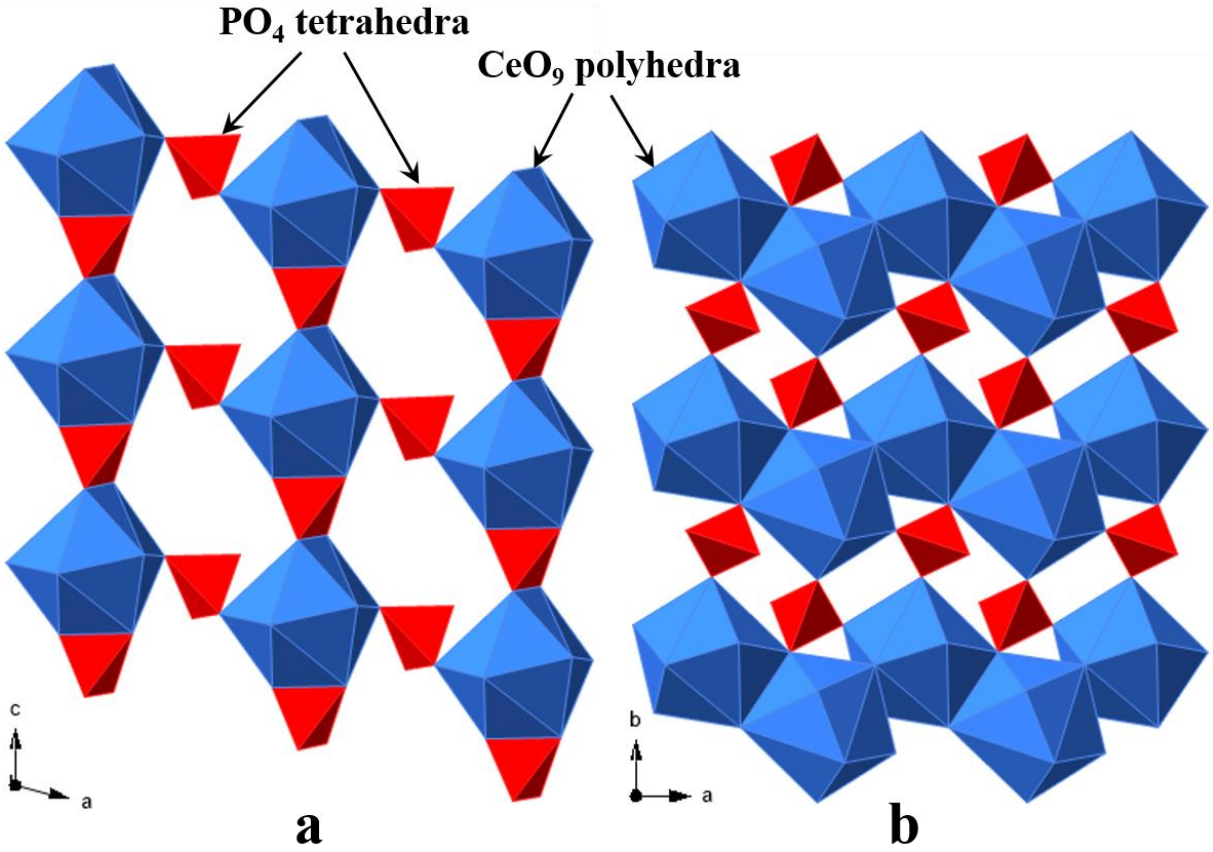

Figure 4.1 Polyhedral representation of the monazite structure: (**a**) isolated PO_4 tetrahedra and CeO_9 polyhedra that share edges to form chains parallel to the **c** axis; and (**b**) CeO_9 polyhedra share common edges along the **a** axis, and PO_4 tetrahedra and CeO_9 polyhedra share corners along the **b** axis.

Table 4.1 Monazite sample information

Sample no.	Locality	Description and occurrence
1	Kolatoli beach, Cox's Bazar, Bangladesh	Detrital monazite grains separated from a bulk beach sand sample. Grains are spherical in shape and greenish yellow.
2	Iveland, Norway	Massive monazite occurs in a quartz pegmatitic rock.
3	Shaplapur paleobeach, Cox's Bazar, Bangladesh	Same as sample 1.
4	Gunnison County, Colorado, USA	Massive dark brown monazite-Sm occurs with cleavelandite feldspar and lepidolite from the brown Derby-1 pegmatite.

4.3 Analytical Methods

4.3.1 Electron-Probe Micro-Analyses (EPMA)

The monazite samples were analyzed using a JEOL JXA-8200WD-ED electron-probe micro-analyzer (EPMA). The JEOL operating program on a Solaris platform was used for ZAF correction and data reduction. The wavelength-dispersive (WD) analysis was conducted quantitatively using an accelerated voltage of 15 kV, a beam current 2.021×10^{-8} A, and a beam diameter of 5 μm. Peak overlapping problems in the elemental analysis of monazite are very common, and were solved following the method described by Pyle et al. (2002). Various minerals and compounds were used as standards ($CePO_4$ for Ce and P; $NdPO_4$ for Nd; YPO_4 for Y; ThO_2 for Th; $LaPO_4$ for La; $SmPO_4$ for Sm; $PrPO_4$ for Pr; $GdPO_4$ for Gd; $DyPO_4$ for Dy; $EuPO_4$ for Eu; $TbPO_4$ for Tb; zircon for Si; Cr-augite for Ca; barite for S; pyromorphite for Pb; UO_2 for U and hornblende for FeO). Fourteen spots were analysed for each sample. The oxide concentrations (wt. %) and the calculated atom per formula unit (*apfu*) based on four oxygen (O) atoms for each sample are given in Table 4.2.

Table 4.2 EPMA data for four monazite samples

	1	2	3	4		1	2	3	4
La_2O_3 (wt. %)	13.98	7.65	11.36	3.80	La (*apfu*)*	0.200	0.113	0.166	0.057
Ce_2O_3	28.42	22.42	25.24	12.42	Ce	0.404	0.330	0.367	0.185
Pr_2O_3	2.80	3.25	2.58	1.92	Pr	0.040	0.048	0.037	0.029
Nd_2O_3	12.05	15.31	11.24	7.12	Nd	0.167	0.220	0.159	0.104
Sm_2O_3	1.81	4.01	1.97	13.73	Sm	0.024	0.056	0.027	0.193
Eu_2O_3	0.11	bdl	bdl	bdl	Eu	0.001	0.000	0.000	0.000
Gd_2O_3	1.23	2.33	1.83	5.77	Gd	0.016	0.031	0.024	0.078
Tb_2O_3	bdl	0.11	bdl	bdl	Tb	0.000	0.001	0.000	0.000
Dy_2O_3	0.25	0.79	0.96	0.27	Dy	0.003	0.010	0.012	0.003
Y_2O_3	0.51	3.92	3.31	0.73	Y	0.011	0.084	0.070	0.016
CaO	1.80	0.27	1.01	2.89	Ca	0.075	0.012	0.043	0.126
FeO	bdl	bdl	bdl	bdl	Fe	0.000	0.000	0.000	0.000
P_2O_5	29.11	27.14	28.18	27.94	P	0.957	0.923	0.946	0.964
SiO_2	0.42	2.06	1.38	1.22	Si	0.016	0.083	0.055	0.050
SO_3	0.94	0.09	bdl	0.09	S	0.027	0.003	0.000	0.003
ThO_2	6.55	8.71	10.10	18.22	Th	0.058	0.080	0.091	0.169
UO_2	0.22	0.36	0.25	0.42	U	0.002	0.003	0.002	0.004
PbO	0.01	0.28	0.13	1.06	Pb	0.000	0.003	0.001	0.012
Total	100.18	98.70	99.56	97.61	Total	2.001	1.998	2.001	1.993
					∑LREE	0.811	0.710	0.729	0.375
					∑MREE	0.045	0.098	0.063	0.274
					∑X site	1.001	0.990	1.000	0.976
					∑P site	1.000	1.009	1.001	1.017

*Atom per formula unit (*apfu*) based on 4 O atoms; bdl = below detection limit; ∑LREE (light rare earth elements) = La + Ce + Pr + Nd; ∑MREE (middle rare earth elements) = Sm + Eu + Gd + Tb + Dy; ∑X site = LREE + MREE + Y + Ca + Fe + U + Th + Pb; ∑P site = P + Si + S

4.3.2 Single-Crystal X-ray Diffraction (SCXRD)

Each monazite crystal was mounted on the tip of a glass fiber (diameter less than 0.1 mm) using an adhesive. The mounted crystal was placed on a goniometer head and centred in the X-ray beam for diffraction. SCXRD data were collected with a Nonius Kappa CCD on a diffractometer using Bruker Nonius FR591 Rotating Anode with graphite monochromated Mo-Kα radiation (λ = 0.71073 Å). The generator setting was 50 kV and 36 mA, and the cryostat setting for the diffractometer was set to 295 K (room temperature). The detector-crystal distance was fixed at 35 mm. For unit-cell determination, a total of 10 frames were collected and the scan settings were 1° rotation per frame (total rotation = 10°) and 22 seconds X-ray exposure time per frame. After obtaining satisfactory unit-cell parameters and mosaicity values, complete data sets were collected using a 2° per frame rotation with X-ray exposure of 42-122 seconds per frame. The diffraction spots were measured in full, scaled with SCALEPACK, corrected for Lorentz-polarization, and integrated using the Nonius program suite DENZO-SMN (Otwinowski and Minor, 1997). The data were corrected for absorption using the analytical absorption correction method. The centrosymmetric space group $P2_1/n$ was obtained based on systematic absence of reflections and structure factor statistics. The crystal structure of monazite was confirmed by direct method followed by Fourier and difference Fourier maps.

4.3.3 Structure Refinements of SCXRD Data

Full-matrix least-squares refinements were carried out with SHELXL-97 with neutral atom scattering factors (Sheldrick 1997). The WinGX program suite was used as the platform for refinement (Farrugia 1999). Atom coordinates for monazite-Ce and $SmPO_4$ from Ni et al. (1995) were used as the starting structure model. Anisotropic displacement parameters of all atoms and refinement of the site occupancies of the Ce and P sites resulted in convergence. Details of the data collection, processing, and refinements are given in Table 4.3. The refined atom

coordinates and displacement parameters are given in Tables 4.4. Selected bond distances and angles are given in Table 4.5.

4.4 Results and Discussion

4.4.1 Chemical Composition of Th-Bearing Monazite-Ce and Monazite-Sm

The EPMA chemical compositions of the four monazite samples are (Table 4.2):

1: $(Ce_{0.40}La_{0.20}Nd_{0.17}Ca_{0.08}Th_{0.06}Pr_{0.04}Sm_{0.02}Gd_{0.01}Y_{0.01})_{\Sigma 0.99}(P_{0.96}S_{0.03}Si_{0.02})_{\Sigma 1.01}O_4$

2: $(Ce_{0.33}Nd_{0.22}La_{0.11}Y_{0.08}Th_{0.08}Sm_{0.06}Pr_{0.05}Gd_{0.03}Dy_{0.01}Ca_{0.01})_{\Sigma 0.98}(P_{0.92}Si_{0.08})_{\Sigma 1.00}O_4$

3: $(Ce_{0.37}La_{0.17}Nd_{0.16}Th_{0.09}Y_{0.07}Pr_{0.04}Ca_{0.04}Sm_{0.03}Gd_{0.02}Dy_{0.01})_{\Sigma 1.00}(P_{0.95}Si_{0.06})_{\Sigma 1.01}O_4$

4: $(Sm_{0.19}Ce_{0.19}Th_{0.17}Ca_{0.13}Nd_{0.10}Gd_{0.08}La_{0.06}Pr_{0.03}Y_{0.02}Pb_{0.01})_{\Sigma 0.98}(P_{0.96}Si_{0.05})_{\Sigma 1.01}O_4$

The Ce atom is dominant in samples 1, 2, and 3 and Sm atom is dominant in sample 4. The Ce/Sm and P sites are fully occupied. The Sm site for sample 4 contains a significant amount Ce atoms (0.19 *apfu*), but is about half that in the other samples. Th is present in all the samples, but sample 4 contains the highest amount (0.17 *apfu*; Table 4.2). The Ce site contains Ln^{3+}, Y^{3+}, Ca^{2+}, Th^{4+}, and U^{4+}. The structure preferentially accommodates La^{3+}, Ce^{3+}, Pr^{3+}, Nd^{3+}, Sm^{3+}, Eu^{3+}, Gd^{3+}, Tb^{3+}, and Dy^{3+}. Ho^{3+}, Er^{3+}, Tm^{3+}, Yb^{3+}, and Lu^{3+} are generally not found in monazite (Boatner 2002), so they are not measured in this study. La^{3+} has the largest ionic radius (1.216 Å) and lowest atomic number (57) and Lu^{3+} has the smallest ionic radius (1.032 Å) and highest atomic number (71) (Shannon 1976). For this study, light REE (LREE) refers to La^{3+}, Ce^{3+}, Pr^{3+}, and Nd^{3+}, and middle REE (MREE) is for Sm^{3+}, Eu^{3+}, Gd^{3+}, Tb^{3+}, and Dy^{3+}. The charge balancing reaction may be written as, $(Ca^{2+} + Th^{4+}) + (Si^{4+} + S^{6+}) = 2P^{5+} + 2(Ln,Y)^{3+}$. The numerous substitutions imply a wide range of flexibility for the monazite structure.

Table 4.3 Single-crystal structure refinement data for four monazite samples

		1	2	3	4
Crystal dimension (mm^3)		0.06 ×0.0 6 × 0.05	0.08 × 0.06 × 0.06	0.10 × 0.10 × 0.08	0.05 × 0.05 × 0.04
Unit cell parameters[+]	*a* (Å)	6.7640(5)	6.7360(8)	6.7590(4)	6.7010(4)
	b (Å)	6.9850(4)	6.9490(7)	6.9770(4)	6.9080(4)
	c (Å)	6.4500(3)	6.4390(8)	6.4480(3)	6.4300(4)
	β (°)	103.584(2)	103.855(6)	103.656(3)	103.817(3)
Volume, *V* ($Å^3$)		296.22(3)	292.63(6)	295.48(3)	289.04(3)
$Density_{calc}$ (g/cm^3)		5.272	5.336	5.285	5.638
Absorption coefficient (mm^{-1})		15.718	15.911	15.758	20.676
2θ range		7.86 – 55.28°	7.86 – 55.22°	7.86-55°	7.92-55°
Index ranges		-8<=h<=8	-8<=h<=8	-8=<h=< 8	-8=<h=<8
		-9<=k<=8	-8<=k<=8	-9=< k=<9	-8=< k=<8
		-8<=l<=8	-8<=l<=8	-8=<l=< 8	-8=<l=<8
Total reflections		2307	2278	2578	2214
Unique reflections		692	676	680	659
Completeness to θ = 27.7 (%)		100	100	100	98.9
R_{int}		0.0282	0.0415	0.0327	0.0506
GooF on F^2		1.206	1.231	1.314	0.789
R_1 [$I > 2\sigma(I)$]		0.0139	0.0237	0.0180	0.0365
wR_2		0.0350	0.0644	0.0471	0.1594
Extinction coefficient		0.0162(8)	0.005(1)	0.013(1)	0.000(3)
Largest difference peak/hole ($e/Å^3$)		0.509 and -0.529	0.750 and -1.213	0.602 and -0.953	2.430 and -1.324
Mosaicity (°)		0.751(3)	0.981(9)	0.803(3)	1.74(3)

[+]Crystal system = monoclinic; space group = $P2_1/n$; formula unit, $Z = 4$ based on $CePO_4$ for samples 1-3 and $SmPO_4$ for sample 4

Table 4.4 Occupancies (*sof*), atom coordinates and anisotropic displacement parameters (Å^2) for four monazite samples

		sof	Atom coordinates			U_{eq}	Anisotropic displacement parameters (*U*ij)					
			x	*y*	*z*		U_{11}	U_{22}	U_{33}	U_{23}	U_{12}	U_{13}
Ce/Sm*	1[+]	0.975(4)	0.28155(3)	0.15901(3)	0.10011(3)	0.0111(1)	0.0115(2)	0.0113(2)	0.0099(1)	0.00123(6)	0.00018(7)	0.00156(8)
	2	0.999(7)	0.28047(5)	0.15821(4)	0.09972(5)	0.0183(2)	0.0193(2)	0.0167(3)	0.0169(2)	0.0020(1)	0.0000(1)	0.0003(1)
	3	0.963(5)	0.28129(3)	0.15862(3)	0.09982(3)	0.0107(1)	0.0103(2)	0.0093(2)	0.0116(2)	0.00156(7)	0.00004(7)	0.0006(1)
	4	0.96(1)	0.28004(8)	0.15793(8)	0.10002(7)	0.0124(5)	0.0119(6)	0.0114(6)	0.0133(6)	0.0027(2)	0.0001(3)	0.0020(3)
P	1		0.3039(1)	0.1629(1)	0.6122(1)	0.0105(3)	0.0108(5)	0.0115(5)	0.0090(4)	0.0002(3)	0.0008(3)	0.0022(3)
	2		0.3028(2)	0.1620(2)	0.6115(2)	0.0178(5)	0.0209(8)	0.0171(9)	0.0141(8)	-0.0002(5)	0.0004(5)	0.0018(5)
	3		0.3036(2)	0.1625(1)	0.6121(2)	0.0107(4)	0.0106(6)	0.0104(6)	0.0106(5)	0.0001(2)	0.0011(3)	0.0017(4)
	4		0.3020(4)	0.1625(3)	0.6122(4)	0.010(1)	0.009(1)	0.013(2)	0.008(2)	0.0007(5)	0.0009(6)	0.000(1)
O1	1		0.2488(4)	0.0064(4)	0.4425(4)	0.0155(6)	0.019(1)	0.016(1)	0.012(1)	-0.0021(9)	-0.000(1)	0.0038(9)
	2		0.2474(6)	0.0070(6)	0.4389(7)	0.022(1)	0.026(2)	0.019(2)	0.021(2)	-0.004(2)	-0.002(2)	0.005(2)
	3		0.2487(5)	0.0059(4)	0.4413(5)	0.0167(7)	0.019(2)	0.016(2)	0.014(1)	-0.002(1)	0.000(1)	0.003(1)
	4		0.249(1)	0.002(1)	0.439(2)	0.017(2)	0.014(3)	0.022(4)	0.013(3)	0.004(3)	0.004(3)	0.000(3)
O2	1		0.3816(4)	0.3318(3)	0.4993(4)	0.0161(6)	0.015(1)	0.015(1)	0.020(1)	0.0030(9)	-0.0016(9)	0.007(1)
	2		0.3817(7)	0.3327(6)	0.4990(7)	0.024(1)	0.025(2)	0.021(2)	0.027(2)	0.004(2)	-0.002(2)	0.007(2)
	3		0.3816(5)	0.3323(4)	0.4997(5)	0.0173(7)	0.015(2)	0.016(2)	0.022(2)	0.004(1)	-0.001(1)	0.005(1)
	4		0.381(1)	0.3317(1)	0.501(1)	0.018(2)	0.020(4)	0.009(4)	0.029(4)	-0.001(2)	-0.008(2)	0.012(4)
O3	1		0.4743(4)	0.1061(4)	0.8044(4)	0.0170(6)	0.015(1)	0.019(1)	0.015(1)	-0.000(1)	0.003(1)	-0.002(1)
	2		0.4744(7)	0.1053(7)	0.8064(7)	0.029(1)	0.028(2)	0.031(2)	0.022(2)	-0.002(2)	0.007(2)	-0.004(2)
	3		0.4739(5)	0.1050(5)	0.8049(5)	0.0185(7)	0.016(2)	0.020(2)	0.017(1)	-0.000(1)	0.005(1)	-0.003(1)
	4		0.475(2)	0.106(1)	0.807(2)	0.019(2)	0.009(3)	0.019(4)	0.023(3)	0.002(3)	0.001(3)	-0.008(3)
O4	1		0.1268(4)	0.2134(4)	0.7104(4)	0.0153(6)	0.015(1)	0.019(1)	0.013(1)	0.001(1)	0.002(1)	0.0049(9)
	2		0.1262(6)	0.2117(7)	0.7100(7)	0.024(1)	0.022(2)	0.032(2)	0.018(2)	0.002(2)	-0.003(2)	0.003(2)
	3		0.1267(4)	0.2133(5)	0.7112(5)	0.0157(7)	0.012(1)	0.020(2)	0.015(1)	0.002(1)	0.001(1)	0.002(1)
	4		0.124(1)	0.217(1)	0.710(1)	0.017(2)	0.028(4)	0.013(4)	0.013(3)	0.002(2)	0.004(3)	0.013(3)

*Atom site; [+]1, 2, 3, and 4 are sample numbers; occupancies for P and O are full (*sof* = 1)

Table 4.5 Bond distances (Å) and angles (°) for four monazite samples

	1		2		3		I		4		
		BV[+]		BV		BV		BV			BV
Ce-O1'	2.445(3)	0.452	2.439(4)	0.459	2.440(3)	0.458	2.528(2)	0.361	Sm-O1'	2.395(8)	0.436
-O1"	2.509(3)	0.380	2.481(4)	0.410	2.503(3)	0.386	2.461(2)	0.433	-O1"	2.484(7)	0.343
-O2'	2.554(2)	0.336	2.526(4)	0.363	2.544(3)	0.346	2.776(3)	0.185	-O2'	2.515(7)	0.315
-O2"	2.630(3)	0.274	2.609(5)	0.290	2.626(3)	0.277	2.644(2)	0.264	-O2"	2.600(8)	0.251
-O2"'	2.779(3)	0.183	2.776(5)	0.185	2.784(3)	0.181	2.573(2)	0.320	-O2"'	2.775(7)	0.156
-O3'	2.461(3)	0.433	2.443(5)	0.454	2.454(3)	0.441	2.585(3)	0.309	-O3'	2.430(7)	0.397
-O3"	2.577(3)	0.316	2.567(5)	0.325	2.573(3)	0.320	2.481(2)	0.410	-O3"	2.565(7)	0.275
-O4'	2.444(3)	0.453	2.440(4)	0.458	2.444(3)	0.453	2.526(2)	0.363	-O4'	2.403(7)	0.427
-O4"	2.514(2)	0.375	2.503(4)	0.386	2.506(3)	0.383	2.455(2)	0.440	-O4"	2.507(6)	0.322
<Ce-O> [9]	2.546(3)	3.202*	2.532(4)	3.330*	2.542(3)	3.244*	2.559(2)	3.084*	<Sm-O> [9]	2.519(7)	2.923*
P-O1	1.530(3)	1.221	1.528(4)	1.228	1.534(3)	1.208	1.534(3)	1.208		1.550(8)	1.157
-O2	1.542(3)	1.182	1.548(4)	1.163	1.545(3)	1.173	1.545(3)	1.173		1.529(7)	1.225
-O3	1.533(3)	1.212	1.540(4)	1.189	1.535(3)	1.205	1.534(3)	1.208		1.539(6)	1.192
-O4	1.522(3)	1.248	1.517(5)	1.265	1.524(3)	1.241	1.531(3)	1.218		1.526(7)	1.235
<P-O> [4]	1.532(3)	4.863[1]	1.533(4)	4.845[1]	1.535(3)	4.828[1]	1.536(3)	4.808[1]		1.536(7)	4.809[1]
O1-P-O2	105.1(2)		104.6(3)		105.1(2)		113.7			104.8(4)	
O1-P-O3	113.8(2)		114.6(3)		113.8(2)		103.9			113.7(7)	
O1-P-O4	112.4(2)		112.7(3)		112.7(2)		113.7			113.8(4)	
O2-P-O3	107.8(2)		107.6(3)		107.9(2)		112.4			107.3(5)	
O2-P-O4	114.1(2)		114.4(3)		114.0(2)		105.2			113.5(4)	
O3-P-O4	103.8(1)		103.2(3)		103.5(2)		108.1			103.9(4)	
<O-P-O> [6]	109.5(2)		109.5(3)		109.5(2)		109.5			109.5(5)	

[+]BV = Bond valence; *Bond-valence sum (BVS) for nine Ce/Sm-O distances; [1]BVS for four P-O distances; I = Literature data for monazite-Ce (Ni et al. 1995)

4.4.2 Variations of Unit-Cell Parameters

The *a*, *b*, *c*, and β unit-cell parameters vary linearly with increasing unit-cell volume, *V*, for $SmPO_4$, $PrPO_4$, $CePO_4$, and $LaPO_4$ (Ni et al. 1995). The *a* and *b* unit-cell parameters for samples 1, 2, 3, and 4 fall close to the linear regression line drawn using the data from Ni et al. (1995; Fig. 4.2a and 4.2b). The *a* and *b* unit-cell parameters vary linearly with *V*, although each sample contains REEs, Y, Ca, U, and Th that occupy the Ce site. The largest *a* and *b* unit-cell parameters obtained for sample 1 of this study differ by about 0.0263 and 0.0353 Å from the Th-free monazite-Ce studied by Ni et al. (1995; Fig. 4.2a and 4.2b). The reason is that weighted average ionic radii for the sample 1 of this study (= 1.182 Å) differ from the Th-free monazite-Ce (= 1.196 Å) studied by Ni et al. (1995). The weighted average radii values were calculated based on the concentration of Ce site cations in each sample and their ionic radii from Shannon (1976).

The *c* unit-cell parameter for samples 1, 2, and 3 are within 0.011 Å and are not significant relative to the variations of the *c* unit-cell parameters for $SmPO_4$, $PrPO_4$, $CePO_4$, and $LaPO_4$ obtained by Ni et al. (1995; Fig. 4.2c). However, *c* unit-cell parameter for sample 4 is less than the others and has large errors. In contrast, two monazite samples studied with the PXRD technique by Seydouax-Guillaume (2002) have the largest *c* values (Fig. 4.2c). The polyhedral arrangement along the [001] in monazite is the O-O edge sharing between CeO_9 polyhedra and PO_4 tetrahedra (Fig. 4.1a), and the PO_4 tetrahedra are stacked along this direction, resulting in limited variation of the *c* parameter. The two O atoms are shared by two adjacent Ce atoms forming a zigzag chain along the [100] direction (Fig. 4.1b). The two O atoms are also partly shared by adjacent P atoms along the [010] direction. The Ce polyhedra along the [100] direction are stacked with each other. Therefore, the increase or decrease of the *a* unit-cell parameter may be dependent on the type of cations occupying the Ce site in the monazite structure. Along the [010] direction, the CeO_9 polyhedra and PO_4 tetrahedra are linked by a corner and have enough space to distort, and result in variations in the [010] direction (Fig. 4.1b).

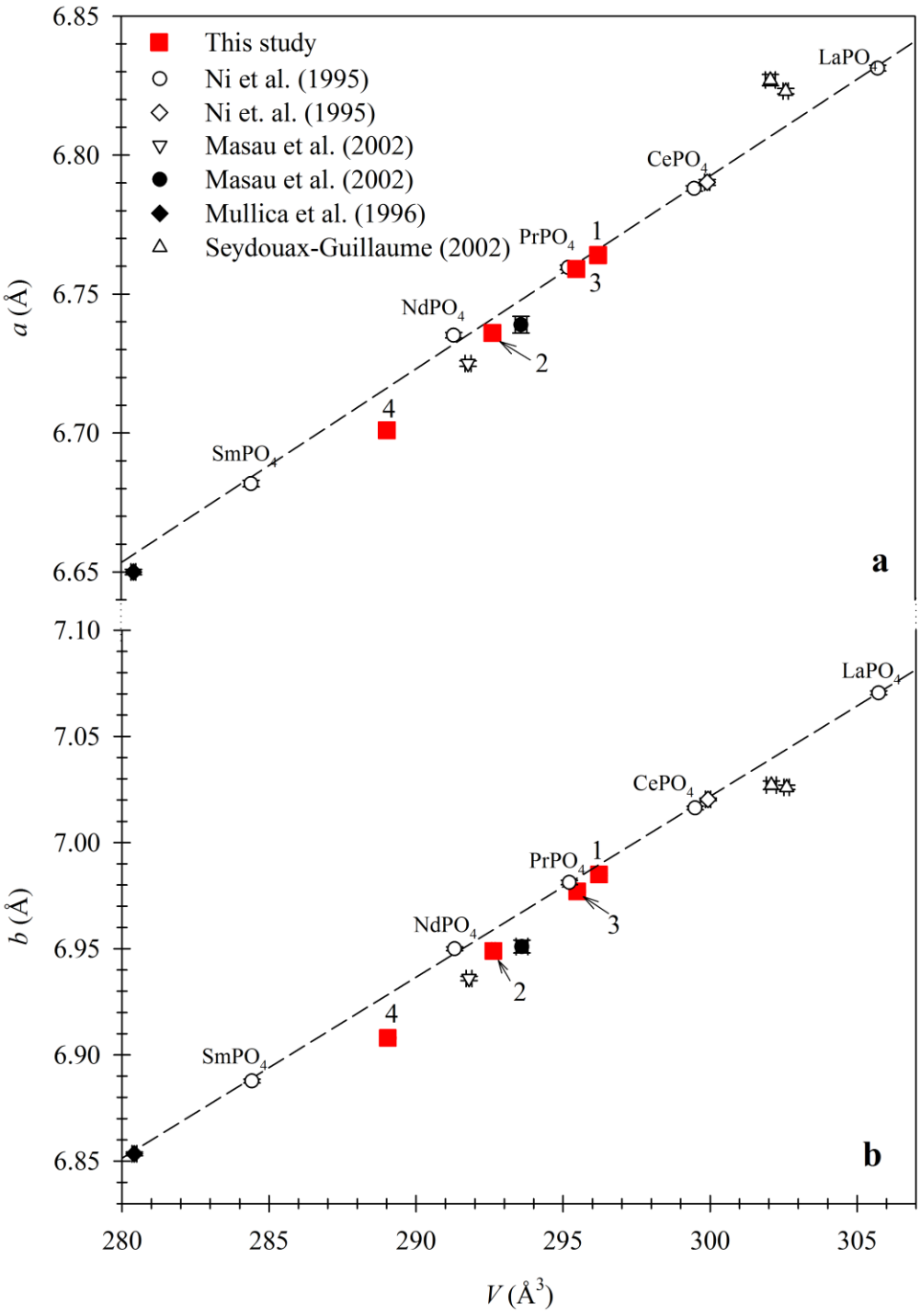
This study
Ni et al. (1995)
Ni et. al. (1995)
Masau et al. (2002)
Masau et al. (2002)
Mullica et al. (1996)
Seydouax-Guillaume (2002)
LaPO4
CePO4
PrPO4
NdPO4
SmPO4
1
2
3
4
a
b
a (Å)
b (Å)
V (Å3)
6.85
6.80
6.75
6.70
6.65
7.10
7.05
7.00
6.95
6.90
6.85
280
285
290
295
300
305

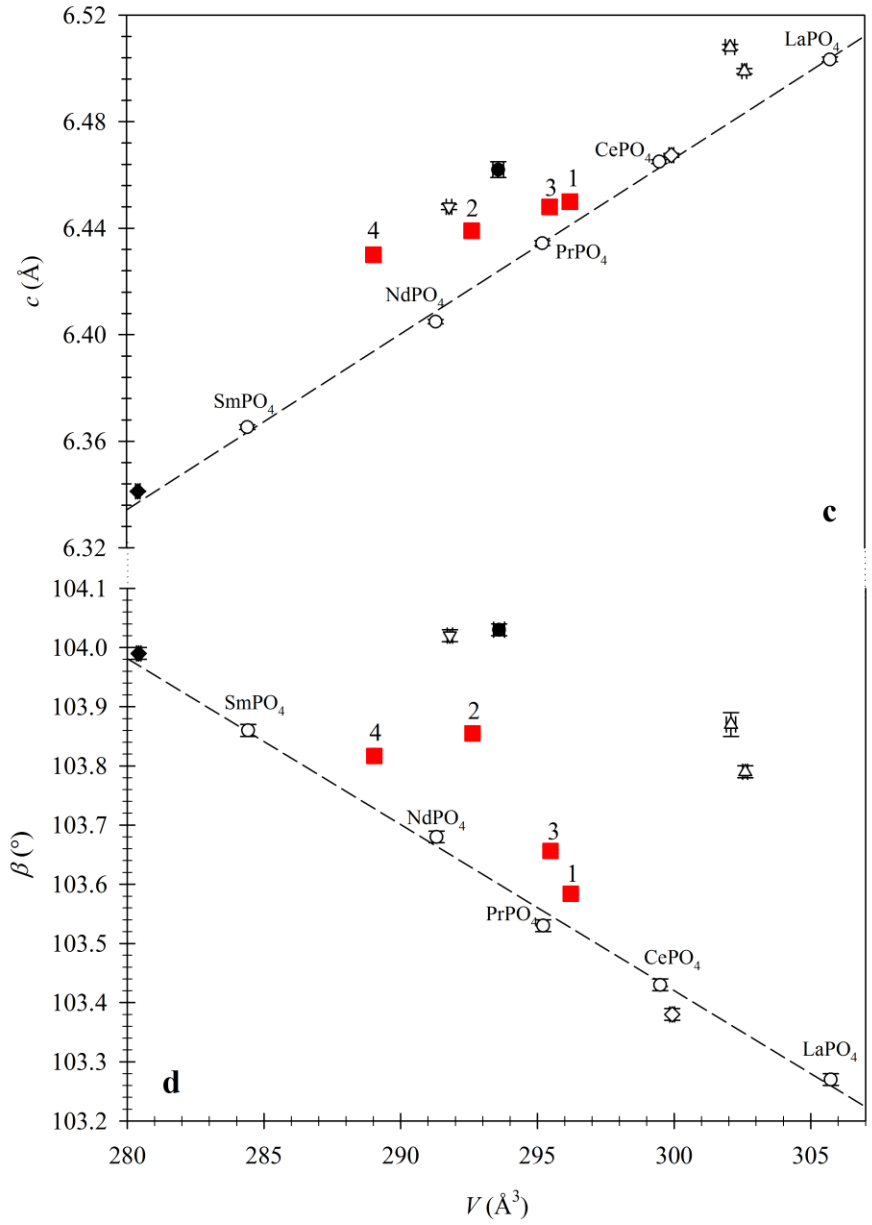

Figure 4.2 Variations of unit-cell parameters in monazite. The dashed line represents the linear regression for unit-cell parameters for $LaPO_4$, $CePO_4$, $NdPO_4$, and $SmPO_4$ (Ni et al. 1995). The *a* and *b* unit-cell parameters in (**a**) and (**b**) from this study vary systematically with *V*, but the *c* and β unit-cell parameters in (**c**) and (**d**) do not vary systematically.

The β unit-cell parameter decreases with increasing V (Fig. 4.2d), as observed for $SmPO_4$, $PrPO_4$, $CePO_4$, and $LaPO_4$ by Ni et al. (1995). The β angle in samples 1, 2, 3, and 4 follow the decreasing trend with increasing V. When the a, b, and c parameters increase, the Ce and P site cations in the unit-cell come close to each other and repulsion occurs, which may be reason for the decrease in the β angle.

4.4.3 Site Occupancy Factors (sof) and Chemical Composition

The *sof* for Ce/Sm for samples 1, 2, 3, and 4 were refined using the dominated Ce/Sm atom and they are 0.975(4), 0.999(7), 0.963(5), and 0.96(1) (see Table 4.4). These *sofs* values indicate that the Ce/Sm site are 96-100 % full by Ce/Sm and may contain a small amount of other cations that are lighter (lower atomic number) than Ce/Sm. In fact, the Ce site for samples 1, 2, and 3 contains 40, 33, and 37 % Ce and the Sm site for sample 4 contains 19 % Sm, as obtained with EPMA data. So, it is difficult to conclude that the Ce/Sm site is only occupied by trivalent Ce or Sm. It is easy to distinguish atoms of different atomic number (or number of electrons). The number of electrons for Ln^{3+} are very close to each other and the *sofs* refinement for Ce/Sm site using only Ce or Sm atom may be biased. For this reason, EPMA chemical data for Ce/Sm site cations are used for the refinement for *sofs* for monazite structure. However, the resulting refinement statistics and structural parameters are the same as the initial refinement.

4.4.4 Bond Distance and Chemical Composition

The difference between the longest and shortest Ce/Sm-O distances for samples 1-3 (monazite-Ce) is the same (0.34 Å) but for sample 4 (monazite-Sm) is slightly large (0.38 Å). The average <Ce/Sm-O> distances vary linearly with V, but average <P-O> distances is nearly constant (Tables 4.5; Fig. 4.3). Data from the literature are close to linear lines (Ni et al. 1995; Mullica et al. 1996).

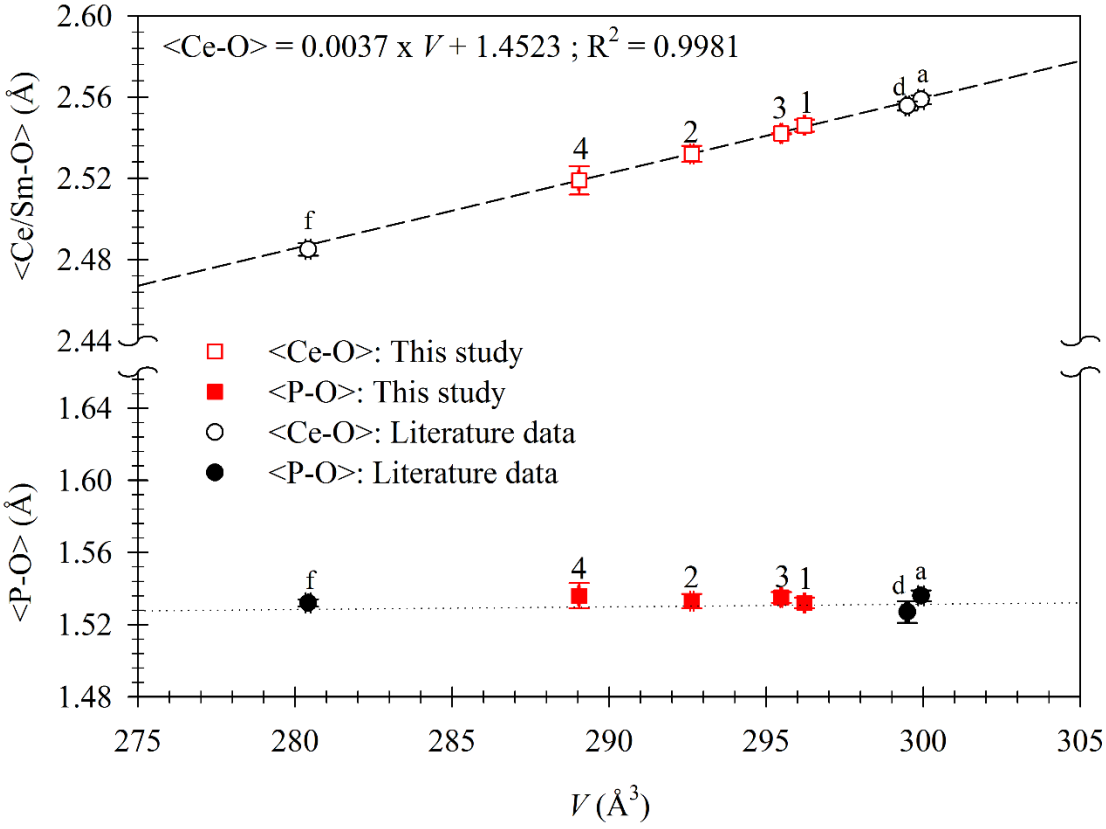

Figure 4.3 The average <Ce-O> and <P-O> distances in monazite. The dashed line is a linear regression line for the average <Ce-O> distances obtained with SCXRD data from this study. The literature data are: a: monazite-Ce and d: $CePO_4$ from Ni et al. (1995), and f: $[Sm_{0.5}Tb_{0.5}]P_{1.0}O_4$ from Mullica et al. (1996). The average <Ce/Sm-O> distances vary systematically with *V*. The literature data also fall close to the linear dashed regression line. PO_4 tetrahedron is rigid and average <P-O> is nearly constant (dotted line).

The P-O distances from the literature are similar to those obtained from this study, PO_4 tetrahedron is rigid with a constant P-O distance. Sample 2 has an anomalously low average <Ce-O> distance [2.532(5) Å] relative to 2.559 Å for the monazite studied by Ni et al. (1995), indicating the presence of cations that have smaller ionic radii. The weighted average ionic radii

for Ln^{3+} in each sample were calculated based on the atomic proportion of Ln^{3+} and its ionic radii (Shannon 1976). When the weighted average of Ln^{3+} increases, the average <Ce/Sm-O> increases (Fig. 4.5). The main substituted cations are Y^{3+}, Ca^{2+}, Th^{4+}, and U^{4+} and they have ionic radii smaller than that for Ln^{3+}. Thus, the main controlling factors for the increase or decrease of average <Ce/Sm-O> distances are the effects of substitutions between Ln^{3+} and the other cations (e.g., Y^{3+}, Ca^{2+}, Th^{4+}, and U^{4+}) in the monazite structure.

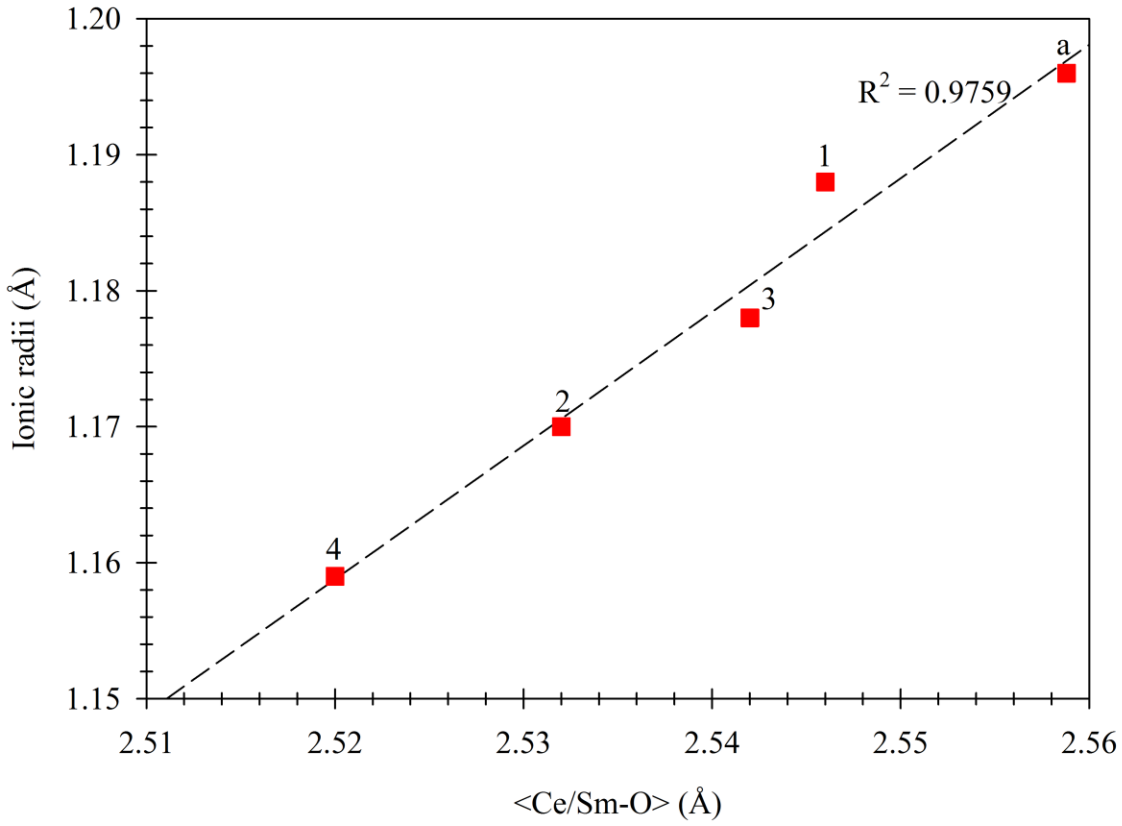

Figure 4.4 The average <Ce/Sm-O> distances vary with the weighted average of ionic radii of Ln^{3+} and Y^{3+}. The dashed line is for samples 1 and 2 from this study and a is from the study of Ni et al. (1995). This indicates that the ionic radii for Ce/Sm site cations control the average <Ce/Sm-O> distances in the monazite structure.

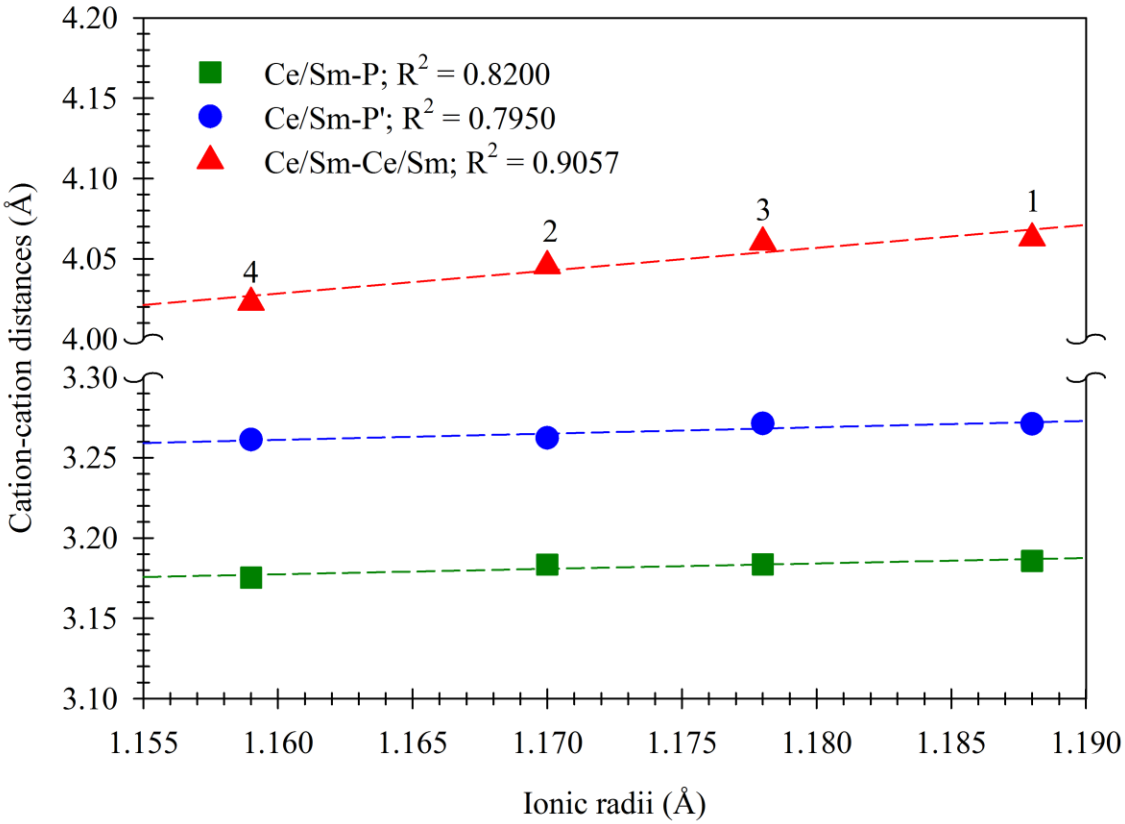

Figure 4.5 Cation-cation distances with the weighted average of ionic radii for Ce/Sm site cations. Radii are from Shannon (1976). The dashed lines are for linear fits.

The Ce/Sm-P distances differ along the [001] direction. Ce/Sm-P distance is shorter than the Ce/Sm-P′ distance. The closest Ce/Sm-Ce/Sm distances vary from 4.0228(9) (sample 4) to 4.0628(3) Å (sample 1). The cation-cation distance vary with linearity with the weighted average of ionic radii of Ce/Sm site cations (Fig. 4.5). The two RE-P distances for synthetic light rare earth phosphates vary linearly with the ionic radii of LREE but the degree of variations differ (Ni et al. 1995). This study shows the degree of variations of two Ce/Sm-P distances are not significant but the Ce/Sm-Ce/Sm distances exhibit significant variation (Fig. 4.5). This

implies the *a* and *b* unit-cell parameters change more compared the c parameter in the monazite structure.

Coordination number for the central Ln^{3+} to the O atoms in the monazite structure is nine (Beall et al. 1981; Ni et al. 1995; Clavier et al. 2011). However, the number can be 8 for an Ln^{3+} polyhedron (Muller and Roy 1975). The Ln^{3+}-O bonds are not directional and they vary from 3 to 12 (Huang 2010). However, the most common coordination number for Ln^{3+} to O is eight or nine (Huang 2010). Ln^{3+} tend to lose three electrons and exhibit a 3+ valence state.

The bond valences (*BV*) for each of the 9 Ln^{3+}-O and 4 P^{5+}-O distances in the monazite structure were calculated based on following equation (Brown 2006):

$$BV = exp\left(\frac{R_0 - R}{B}\right)$$

where *R* is the bond distance, R_0 parameters for Ce, Sm, and P are 2.151, 2.088, and 1.617, respectively, and B parameter is 0.37 (Brese and O'Keeffe 1991; Brown and Altermatt 1985).

The calculated *BV* and bond valance sum (*BVS*) for 9 Ce/Sm-O and 4 P-O distances for samples 1-4 and for monazite-Ce studied by (Ni et al. 1995) are given in Table 4.5. The BVS for 9 Ce/Sm-O distances are 3.202, 3.330, 3.244, and 2.923 for samples 1 to 4, and 3.084 for monazite-Ce (Ni et al. 1995). The ideal *BVS* of 9 Ce/Sm-O distances should be about 3.00 because the Ce/Sm site is occupied by trivalent cations. If Ce is coordinated to eight O atoms, BVS are 3.01, 3.145, and 3.063 for samples 1, 2, and 3, which are Ce-dominated monazite (Table 4.5). So this study indicates that the longest Ce-O‴ distances may be excluded in the Ce polyhedron in Ce-dominated monazite.

4.5 Conclusions

This study characterizes the crystal-chemical properties of three Th-bearing Ce dominated and one Sm dominated monazites. The structural parameters for a detrital Th-bearing monazite-Ce from Cox's Bazar, Bangladesh are: a = 6.7640(5) Å, b = 6.9850(4) Å, c = 6.4500(3) Å, β =

103.584(2)°, V = 296.22(3) Å^3, <Ce-O> = 2.546(3) Å, and <P-O> = 1.532(3) Å. The structural parameters for a pegmatite Th-rich monazite-Sm from Colorado, USA are: a = 6.7010(4) Å, b = 6.9080(4) Å, c = 6.4300(4) Å, β = 103.817(3)°, V = 289.04(3) Å^3, <Sm-O> = 2.519(7) Å, and <P-O> = 1.536(7) Å. Although the a and b unit-cell parameters of monazite vary linearly, the c unit-cell parameter does not vary with the unit-cell volume, V. The change of a unit-cell parameter is very pronounced and is related to the type of cations occupying the Ce/Sm site in monazite structure. The <Ce/Sm-O> distances vary with linearity with V but <P-O> distances do not show any correlation, which explains the rigid body behavior of PO_4 tetrahedron. Bond-valence sum (BVS) of Ce/Sm-O distances indicate that the Ce polyhedron in the monazite-Ce has 8 coordination to O atoms. The EPMA chemical data indicates that the Ce/Sm site can accommodate a wide range of cations that have more or less similar ionic radii. This chemical flexibility in Ce/Sm site in the monazite structure permits the accommodation of Pu. During nuclear power generation, ^{238}U in the fuel system absorbs a neutron, it produces ^{239}Pu. ^{239}Pu has a half-life of 24,100 years. ^{239}Pu decays to ^{235}U and has a half-life of 710,000 years. Therefore, the decay chain of ^{239}Pu emits the hazardous radiations for millions of years. As monazite structure shows a high durability over a long geologic time, it can be a host for the isolation of Pu over million years.

Chapter 5: Evidence of Radiation-Induced Phase Transition in Monazite

5.1 Abstract

This study investigates two pegmatitic monazite samples 2a and 4b to determine crystal chemistry and effects of internal radiation damage in the monazite structure with synchrotron high-resolution powder X-ray diffraction (HRPXRD) and electron-probe micro-analysis (EPMA). EPMA chemical data for samples 2a (monazite-Ce) and 4a (monazite-Sm) reveals huttonite substitution dominates over the cheralite substitution. Structure refinement of HRPXRD data with Rietveld method of sample 2a shows three separate phases (phases 2a: monazite-Ce; 2b: monazite-Ce; and 2c: xenotime-Y) with distinct crystal structural parameters. The change among the unit-cell parameters between two monazite-Ce phases in sample 2a is more pronounce in the *a* parameter followed by the *b* and *c* parameters. Sample 4a contains a single phase (monazite-Sm) although it contains 0.164 *apfu* Th. Phase 2b in sample 2a shows large average <P-O> distances and is related to radiation-induced changes. Phase 2c (xenotime-Y) with the space group $I4_1/amd$ is formed in sample 2a because of the redistribution of La, Ce, Pr, Nd, Sm, Gd, Dy, Si, and Y atoms. The main driving thermal energy for phase changes comes from α-radiation events over a long geological time.

5.2 Introduction

Monazite experiences internal radiation doses because it almost always contains certain amount Th and U but it does not carry any effects of radiation damage (Ewing et al. 2003; Seydoux-Guillaume et al. 2002; Boatner et al. 2002; Nazdala et al. 2006). However, radiation damage in monazite was reported (Karkhanavala and Shankar 1954). Monazite does not carry radiation damage because it has the ability to heal its crystal structure at 373-473 K (Seydoux-Guillaume et al. 2002). Another potential reason could be its structural difference from zircon. Monazite has P-O distances, which are shorter and stronger than the Si-O distances in zircon that may

promote the resistance to radiation damage (Meldrum et al. 1996). Seydoux-Guillaume et al. (2002) found two separate phases in a monazite crystal: phase 1 corresponds to well crystalline monazite where helium atoms were trapped, resulting increased unit-cell parameters, and phase 2 represents a distorted lattice, which is referred to as "old alpha recoil tracks" that is generated by the recoil atoms after a radioactive decay event.

Radiation damage in minerals is not consistent under all conditions. The degree of radiation damage in minerals depends mainly on the ratio of damage accumulation and thermal annealing rates specific. If the recovery processes dominate, the crystallinity is preserved, even at low temperature (Ewing et al. 2000).

The aim of this study is to investigate the crystal-chemical properties and the effects of radiation doses in two pegmatitic monazite samples with synchrotron HRPXRD and EPMA. This study reveals that sample 2a consists of three phases with distinct structural properties but sample 4a is a single phase. The multiple phases in sample 2a indicate an evidence of radiation-induced phase transition in monazite.

5.2.1 Sample Description

Two pegmatitic monazite samples 2a and 4a were used in this study and their description and occurrence are summarized in Table 4.1 (Chapter 4). The reason for selection of the two samples is because both were formed in pegmatitic environment and sample 2a is Ce-dominated and sample 4a is Sm-dominated monazites. Fragments of monazite were separated from the two pegmatitic samples with a knife. The fragments were examined with a stereomicroscope and high purity, optically clear, and inclusion-free fragments were picked for EPMA and synchrotron HRPXRD.

5.3 Analytical Methods

5.3.1 Electron-Probe Micro-Analyses (EPMA)

The monazite samples (2a and 4a) were analyzed using a JEOL JXA-8200WD-ED electron-probe micro-analyzer (EPMA) at the Department of Geoscience, University of Calgary. The JEOL operating program on a Solaris platform was for ZAF correction and data reduction. The wavelength-dispersive (WD) analysis was conducted quantitatively using an accelerated voltage of 15 kV, a beam current 2.021×10^{-8} A, and a beam diameter of 5 μm. Peak overlapping problems in the elemental analysis of monazite are very common, and were solved following the method described by Pyle et al. (2002). Various minerals and compounds were used as standards ($CePO_4$ for Ce and P; $NdPO_4$ for Nd; YPO_4 for Y; ThO_2 for Th; $LaPO_4$ for La; $SmPO_4$ for Sm; $PrPO_4$ for Pr; $GdPO_4$ for Gd; $DyPO_4$ for Dy; $EuPO_4$ for Eu; $TbPO_4$ for Tb; zircon for Si; Cr-augite for Ca; barite for S; pyromorphite for Pb; UO_2 for U and hornblende for FeO). Seventeen spots (S1-S17) were analysed for each monazite sample. The oxide concentrations (wt. %) and the calculated atom per formula unit (*apfu*) based on four oxygen (O) atoms for each monazite sample are given in Tables 5.1 and 5.2. A summary of chemical composition for samples 2a and 4a is also presented (Table 5.3). A backscattered electron (BSE) image of sample 2a and three EDS spectra were also obtained with the EPMA.

Table 5.1 EPMA data for seventeen spots from sample 2a

	S1[+]	S2	S3	S4	S5	S6	S7	S8	S9	S10	S11	S12	S13	S14	S15	S16	S17	Av
La_2O_3	7.75	7.74	7.55	7.74	7.68	7.65	7.91	7.65	7.90	7.63	8.05	9.76	9.95	9.39	8.39	10.20	8.90	8.34
Ce_2O_3	22.80	22.68	21.84	22.61	22.28	22.04	22.62	22.42	22.78	22.33	23.66	28.26	27.95	27.15	24.22	28.40	26.36	24.14
Pr_2O_3	3.16	3.15	3.32	3.10	3.14	3.29	2.97	3.25	3.26	3.35	3.30	3.81	4.06	3.86	3.30	3.68	4.13	3.42
Nd_2O_3	15.03	14.97	15.27	15.07	14.83	15.35	14.92	15.31	15.16	15.20	15.15	17.70	16.99	16.92	15.57	17.35	17.30	15.77
Sm_2O_3	3.96	4.10	4.12	4.24	4.08	4.01	3.88	4.01	3.96	4.10	4.00	4.54	4.47	4.24	4.31	4.42	4.66	4.18
Eu_2O_3	bdl	bdl	bdl	bdl	bdl	bdl	bdl	bdl	bdl	bdl	bdl	bdl	bdl	bdl	bdl	bdl	bdl	
Gd_2O_3	2.44	2.50	2.06	2.25	2.05	2.16	2.20	2.33	2.10	2.30	2.34	1.98	1.91	1.80	1.98	1.96	2.17	2.15
Tb_2O_3	0.05	0.02	0.08	0.03	0.05	0.08	0.14	0.11	0.13	0.06	0.04	bdl	bdl	bdl	0.029	bdl	bdl	0.07
Dy_2O_3	0.74	0.66	0.80	0.61	0.78	0.79	0.74	0.79	0.75	0.85	0.79	0.24	0.25	0.21	0.66	0.16	0.32	0.60
Y_2O_3	3.82	4.16	4.07	3.98	3.78	3.79	3.85	3.92	3.93	4.15	3.90	0.38	0.60	0.70	3.10	0.28	0.92	2.90
CaO	0.29	0.22	0.23	0.26	0.23	0.25	0.23	0.27	0.23	0.25	0.23	0.23	0.33	0.27	0.32	0.22	0.28	0.26
FeO	bdl	bdl	bdl	bdl	bdl	bdl	bdl	bdl	bdl	bdl	0.028	0.00	0.01	0.14	bdl	0.04	0.20	0.07
P_2O_5	26.44	26.89	26.84	26.73	26.01	26.48	26.03	27.14	26.51	26.78	27.31	29.52	28.93	27.56	26.80	29.39	28.52	27.29
SiO_2	2.02	1.94	1.96	2.12	2.05	2.03	2.02	2.06	2.08	1.98	1.74	0.19	0.43	0.47	1.29	0.21	0.74	1.49
SO_3	bdl	0.10	0.03	0.01	bdl	0.02	0.00	0.09	0.07	bdl	bdl	bdl	bdl	0.04	0.03	bdl	0.14	0.05
ThO_2	8.97	8.08	8.80	8.47	8.82	8.65	8.86	8.71	9.02	8.23	7.55	2.12	3.34	4.22	6.64	2.01	3.34	6.81
UO_2	0.27	0.36	0.49	0.31	0.38	0.36	0.35	0.26	0.29	0.40	0.46	0.11	0.28	0.60	0.17	0.12	0.15	0.32
PbO	0.25	0.30	0.30	0.28	0.30	0.29	0.29	0.29	0.30	0.30	0.16	0.02	0.15	0.15	0.16	0.03	0.15	0.22
Total	98.01	97.87	97.76	97.81	96.44	97.25	97.01	98.61	98.43	97.92	98.70	98.87	99.64	97.72	96.97	98.48	98.28	97.99
*apfu**																		
La	0.117	0.116	0.113	0.116	0.118	0.116	0.121	0.113	0.118	0.114	0.119	0.143	0.146	0.143	0.128	0.151	0.132	0.125
Ce	0.341	0.337	0.325	0.336	0.339	0.331	0.343	0.330	0.339	0.332	0.349	0.412	0.409	0.410	0.366	0.416	0.388	0.359
Pr	0.047	0.047	0.049	0.046	0.047	0.049	0.045	0.048	0.048	0.050	0.048	0.055	0.059	0.058	0.050	0.054	0.060	0.051
Nd	0.219	0.217	0.222	0.219	0.220	0.225	0.221	0.220	0.220	0.221	0.218	0.252	0.242	0.249	0.229	0.248	0.248	0.229
Sm	0.056	0.057	0.058	0.059	0.058	0.057	0.055	0.056	0.055	0.057	0.055	0.062	0.062	0.060	0.061	0.061	0.064	0.059
Gd	0.033	0.034	0.028	0.030	0.028	0.029	0.030	0.031	0.028	0.031	0.031	0.026	0.025	0.025	0.027	0.026	0.029	0.029
Tb	0.001	-	0.001	-	0.001	0.001	0.002	0.001	0.002	0.001	-	-	-	-	-	-	-	0.001
Dy	0.010	0.009	0.011	0.008	0.010	0.010	0.010	0.010	0.010	0.011	0.010	0.003	0.003	0.003	0.009	0.002	0.004	0.008
Y	0.083	0.090	0.088	0.086	0.084	0.083	0.085	0.084	0.085	0.090	0.084	0.008	0.013	0.015	0.068	0.006	0.020	0.063
Ca	0.013	0.009	0.010	0.011	0.010	0.011	0.010	0.012	0.010	0.011	0.010	0.010	0.014	0.012	0.014	0.009	0.012	0.011
Fe	-	-	-	-	-	-	-	-	-	-	0.001	-	-	0.005	-	0.001	0.007	0.001
P	0.915	0.923	0.924	0.920	0.914	0.919	0.912	0.923	0.912	0.922	0.931	0.996	0.978	0.962	0.936	0.995	0.970	0.938
Si	0.082	0.079	0.080	0.086	0.085	0.083	0.084	0.083	0.084	0.080	0.070	0.008	0.017	0.020	0.053	0.008	0.030	0.061
S	-	0.003	0.001	-	-	0.001	-	0.003	0.002	-	-	-	-	0.001	0.001	-	0.004	0.001
Th	0.083	0.075	0.081	0.078	0.083	0.081	0.083	0.080	0.083	0.076	0.069	0.019	0.030	0.040	0.062	0.018	0.031	0.063
U	0.002	0.003	0.004	0.003	0.003	0.003	0.003	0.002	0.003	0.004	0.004	0.001	0.002	0.006	0.002	0.001	0.001	0.003
Pb	0.003	0.003	0.003	0.003	0.003	0.003	0.003	0.003	0.003	0.003	0.002	-	0.002	0.002	0.002	-	0.002	0.002
Total	2.006	2.000	1.999	2.002	2.004	2.002	2.006	1.998	2.004	2.004	2.002	1.997	2.003	2.009	2.008	1.997	2.002	2.003

[+]S1-S17 = EPMA spots; **apfu* = atom per formula unit based on 4 O atoms; bdl = below detection limits; Av = Average

Table 5.2 EPMA data for seventeen spots from sample 4a

	S1[+]	S2	S3	S4	S5	S6	S7	S8	S9	S10	S11	S12	S13	S14	S15	S16	S17	Av
La_2O_3	3.91	3.98	4.04	3.76	3.97	4.08	3.83	3.73	3.81	3.81	3.80	3.89	3.88	3.85	3.98	4.23	4.03	3.92
Ce_2O_3	12.12	12.24	12.55	12.03	12.71	12.71	12.24	12.06	12.31	12.43	12.42	12.57	12.69	12.76	12.23	12.84	12.52	12.44
Pr_2O_3	1.63	1.67	1.88	1.72	1.96	1.65	1.82	1.86	1.78	1.74	1.92	1.82	1.87	1.92	1.87	1.89	1.85	1.81
Nd_2O_3	7.11	6.99	7.31	7.32	7.16	7.05	7.36	7.04	7.07	7.05	7.12	7.17	7.16	7.27	7.09	7.20	7.08	7.15
Sm_2O_3	13.81	13.60	13.86	14.16	13.25	13.67	13.75	13.44	13.96	13.53	13.73	13.52	13.47	13.68	13.89	13.34	13.93	13.68
Eu_2O_3	bdl	bdl	bdl	bdl	bdl	bdl	bdl	bdl	bdl	bdl	bdl	bdl	bdl	bdl	bdl	bdl	bdl	0.00
Gd_2O_3	5.73	5.56	5.47	5.74	5.45	5.68	5.76	5.47	5.80	5.40	5.77	5.66	5.05	5.60	5.14	5.28	5.60	5.54
Tb_2O_3	bdl	bdl	bdl	bdl	bdl	bdl	bdl	bdl	bdl	bdl	bdl	0.06	0.07	0.02	0.10	bdl	0.09	0.02
Dy_2O_3	0.34	0.27	0.28	0.29	0.25	0.27	0.27	0.38	0.39	0.34	0.27	0.39	0.37	0.35	0.31	0.20	0.24	0.31
Y_2O_3	0.94	0.78	0.72	0.73	0.40	0.50	0.59	0.39	0.41	0.67	0.73	0.41	0.66	0.78	0.88	0.61	0.70	0.64
CaO	2.92	2.95	2.97	3.02	2.84	2.93	3.03	3.04	2.60	2.97	2.89	3.09	2.96	3.08	3.12	2.91	2.78	2.95
FeO	bdl	bdl	bdl	bdl	bdl	bdl	bdl	0.03	bdl	bdl	bdl	bdl	bdl	bdl	bdl	bdl	0.01	0.00
P_2O_5	28.04	27.85	27.99	28.19	28.28	28.15	27.78	27.08	28.90	27.71	27.94	28.02	27.80	27.92	28.16	27.64	27.87	27.96
SiO_2	1.24	1.26	1.28	1.25	1.15	1.20	1.32	1.19	1.01	1.26	1.22	1.25	1.18	1.21	1.14	1.15	1.24	1.21
SO_3	0.02	bdl	bdl	bdl	bdl	bdl	0.18	bdl	0.03	0.06	0.09	bdl	bdl	0.05	0.11	bdl	0.14	0.04
ThO_2	17.44	17.30	17.67	17.49	17.56	17.78	18.59	16.32	17.82	17.91	18.22	17.80	17.44	17.48	17.28	18.07	17.47	17.63
UO_2	0.41	0.40	0.47	0.47	0.52	0.48	0.49	0.41	0.48	0.44	0.42	0.46	0.47	0.49	0.43	0.53	0.47	0.46
PbO	1.01	1.11	1.02	1.11	1.05	1.19	1.17	1.07	1.01	1.09	1.06	1.25	1.07	0.96	1.06	1.13	1.14	1.09
Total	96.67	95.95	97.49	97.26	96.54	97.34	98.17	93.50	97.37	96.43	97.61	97.36	96.14	97.41	96.77	97.02	97.16	96.83
*apfu**																		
La	0.059	0.060	0.061	0.056	0.060	0.061	0.057	0.058	0.057	0.058	0.057	0.059	0.059	0.058	0.060	0.064	0.061	0.059
Ce	0.182	0.185	0.187	0.179	0.185	0.190	0.182	0.187	0.180	0.187	0.185	0.188	0.192	0.191	0.182	0.194	0.187	0.186
Pr	0.024	0.025	0.028	0.025	0.029	0.025	0.027	0.029	0.026	0.026	0.029	0.027	0.028	0.028	0.028	0.028	0.028	0.027
Nd	0.104	0.103	0.106	0.106	0.105	0.103	0.107	0.106	0.105	0.104	0.104	0.105	0.106	0.106	0.103	0.106	0.103	0.105
Sm	0.195	0.193	0.195	0.199	0.196	0.192	0.193	0.196	0.200	0.192	0.193	0.190	0.191	0.192	0.195	0.189	0.196	0.194
Gd	0.078	0.076	0.074	0.077	0.073	0.077	0.078	0.077	0.077	0.074	0.078	0.077	0.069	0.076	0.069	0.072	0.076	0.075
Tb	-	-	-	-	-	-	-	-	-	-	-	0.001	0.001	-	0.001	-	0.001	0.000
Dy	0.004	0.004	0.004	0.004	0.005	0.004	0.004	0.005	0.004	0.005	0.003	0.005	0.005	0.005	0.004	0.003	0.003	0.004
Y	0.021	0.017	0.016	0.016	0.014	0.011	0.013	0.009	0.009	0.015	0.016	0.009	0.015	0.017	0.019	0.013	0.015	0.014
Ca	0.128	0.130	0.130	0.132	0.124	0.128	0.132	0.138	0.118	0.131	0.126	0.135	0.131	0.134	0.136	0.128	0.122	0.130
Fe	-	-	-	-	-	-	-	0.001	-	-	-	-	-	-	-	-	-	0.000
P	0.971	0.971	0.966	0.971	0.971	0.972	0.956	0.970	0.994	0.966	0.964	0.968	0.971	0.964	0.971	0.964	0.964	0.969
Si	0.051	0.052	0.052	0.051	0.052	0.049	0.054	0.050	0.037	0.052	0.050	0.051	0.049	0.050	0.047	0.047	0.051	0.050
S	0.001	-	-	-	0.001	-	0.005	-	-	0.002	0.003	-	-	0.001	0.003	-	0.004	0.001
Th	0.162	0.162	0.164	0.162	0.161	0.165	0.172	0.157	0.159	0.168	0.169	0.165	0.164	0.162	0.160	0.169	0.163	0.164
U	0.004	0.004	0.004	0.004	0.004	0.004	0.004	0.004	0.004	0.004	0.004	0.004	0.004	0.004	0.004	0.005	0.004	0.004
Pb	0.011	0.012	0.011	0.012	0.013	0.013	0.013	0.012	0.011	0.012	0.012	0.014	0.012	0.010	0.012	0.013	0.013	0.012
Total	1.993	1.994	1.997	1.995	1.992	1.993	1.996	2.000	1.981	1.994	1.993	1.997	1.995	1.999	1.995	1.997	1.992	1.994

[+]S1-S17 = EPMA spots; **apfu* = atom per formula unit based on 4 O atoms; bdl = below detection limits; Av = average

Table 5.3 Summary of chemical composition (*apfu*) for 17 EPMA spots of samples 2a and 4a

	S1	S2	S3	S4	S5	S6	S7	S8	S9	S10	S11	S12	S13	S14	S15	S16	S17
2a																	
ΣCe site	1.008	0.996	0.994	0.996	1.005	0.999	1.011	0.989	1.005	1.001	1.002	0.993	1.008	1.026	1.018	0.994	0.998
ΣP site	0.997	1.005	1.005	1.006	0.999	1.003	0.996	1.009	0.999	1.002	1.001	1.004	0.995	0.983	0.990	1.004	1.004
$\Sigma[(REE^{3+},Y^{3+}) + P^{5+}]$	1.822	1.828	1.819	1.820	1.819	1.820	1.823	1.816	1.818	1.829	1.847	1.959	1.937	1.924	1.874	1.959	1.915
$\Sigma(Th^{4+} + Si^{4+})$	0.166	0.153	0.161	0.165	0.169	0.164	0.167	0.162	0.168	0.157	0.139	0.027	0.048	0.059	0.116	0.027	0.060
$2 \times \Sigma(REE^{3+},Y^{3+})$	1.814	1.810	1.789	1.802	1.809	1.802	1.822	1.785	1.812	1.814	1.831	1.925	1.918	1.925	1.876	1.926	1.891
$\Sigma(Ca^{2+} + Th^{4+})$	0.096	0.084	0.092	0.090	0.094	0.092	0.094	0.091	0.094	0.087	0.079	0.029	0.045	0.052	0.076	0.028	0.043
4a																	
ΣSm site	0.971	0.971	0.979	0.973	0.968	0.972	0.981	0.979	0.950	0.975	0.976	0.978	0.976	0.984	0.974	0.985	0.972
ΣP site	1.022	1.023	1.018	1.022	1.024	1.021	1.015	1.021	1.031	1.019	1.017	1.019	1.019	1.015	1.021	1.012	1.019
$\Sigma[(REE^{3+},Y^{3+}) + P^{5+}]$	1.637	1.634	1.635	1.634	1.636	1.633	1.615	1.637	1.652	1.626	1.629	1.628	1.636	1.636	1.633	1.634	1.635
$\Sigma(Th^{4+} + Si^{4+})$	0.213	0.214	0.216	0.213	0.214	0.214	0.226	0.208	0.195	0.220	0.219	0.216	0.212	0.212	0.207	0.217	0.213
$3 \times Sm^{3+}$	0.584	0.579	0.584	0.596	0.588	0.576	0.578	0.588	0.600	0.576	0.579	0.571	0.574	0.577	0.585	0.568	0.589
$\Sigma(Ce^{3+} + Ca^{2+} + Th^{4+})$	0.472	0.477	0.481	0.473	0.471	0.483	0.486	0.482	0.457	0.486	0.481	0.488	0.486	0.487	0.479	0.491	0.472

5.3.2 Age Determination and Radiation Doses Calculation

The ages of both monazite sample were unknown. Separate data for the concentrations of U, Th, and Pb in nine spots (A1-A9) for sample 2a and 4a were collected retaining the same experimental condition used for full data collection. The chemical age (*T*) was determined using the following relation (Montel et al. (1996):

$$Pb = \frac{Th}{232}[exp(\lambda^{232} \cdot T) - 1] \cdot 208 + \frac{U}{238.04} \cdot 0.9929[exp(\lambda^{238} \cdot T) - 1] \cdot 206$$

$$+ \frac{U}{238.04} \cdot 0.0072[exp(\lambda^{235} \cdot T) - 1] \cdot 207$$

where, Pb, U, and Th = the concentrations in ppm, and λ^{235}, λ^{238}, and λ^{232} = the radioactive decay constants (year^{-1}) of ^{235}U, ^{238}U, and ^{232}Th, respectively.

Assumptions are the initial concentration of Pb must be negligible, meaning that all Pb are radiogenic and the concentrations of U and Th must not be modified by other means except radioactive decay.

The α-radiation doses were calculated using the following relation (Holland and Gottfried 1954):

$$D = 8N_1[exp(\lambda^{238} \cdot T) - 1] + 7N_2[exp(\lambda^{235} \cdot T) - 1] + 6N_3[exp(\lambda^{232} \cdot T) - 1]$$

where, *D* = the dose in α-decay events/mg, and N_1, N_2, and N_3 = the present numbers of ^{238}U, ^{235}U, and ^{232}Th in atoms/mg.

Concentrations of U, Th, and Pb (ppm) in 9 EPMA spots, calculated age and α-radiation doses for samples 2a and 4a are given in Table 5.4.

Table 5.4 Concentrations of U, Th, and Pb, chemical age, and α-radiation doses for samples 2a and 4a

Sample no.	EPMA spots	Th (ppm)	U (ppm)	Pb (ppm)	Age (Ma)	Average age (Ma)	Radiation dose (α-decay events/mg)
2a	S1	79664	2424	2339	604	655 ± 39	4.68E+16
	S2	82696	3693	2757	659		
	S3	82019	3015	2609	643		
	S4	85078	3623	2748	642		
	S5	79005	1745	2664	711		
	S6	74514	4531	2850	724		
	S7	91264	1075	2757	657		
	S8	72168	2459	2126	600		
	S9	63626	2583	2098	659		
4a	S1	150479	3976	9831	1360	1361 ± 90	1.93E+17
	S2	157430	3914	10147	1348		
	S3	160110	3693	9831	1291		
	S4	156419	4020	11605	1548		
	S5	153264	4099	9971	1353		
	S6	153590	4311	8866	1196		
	S7	151832	3746	9822	1353		
	S8	158827	4672	10500	1364		
	S9	153546	4169	10593	1433		

5.3.3 Synchrotron High-Resolution Powder X-Ray Diffraction (HRPXRD)

Fragments of monazite (2a and 4a) were hand-picked under a stereomicroscope, and crushed to a fine powder using an agate mortar and pestle for the HRPXRD experiment that was conducted at beamline 11-BM, Advanced Photon Source, Argonne National Laboratory. The powdered samples were loaded into Kapton capillaries (0.8-mm internal diameter), sealed with glass wool, and rotated during the experiment at a rate of 90 rotations per second. Data were collected to a maximum 2θ of about 50° with a step size of 0.001° and a step time of 0.1 s/step. The HRPXRD data were collected using twelve silicon crystal analyzers that allow for high angular resolution and accuracy, high precision, and accurate diffraction peak positions. A silicon (NIST 640c) and

alumina (NIST 676a) standard (ratio of ⅓ Si to ⅔ Al_2O_3 by weight) was used to calibrate the instrument and refine the monochromatic wavelength used in the experiment. The more technical aspects of the experimental set-up are given elsewhere (Antao et al. 2008; Lee et al. 2008; Wang et al. 2008). The HRPXRD trace for sample 2a shows broad and asymmetrical peaks indicating multiple phases and, therefore, is modeled by three phases. The HRPXRD trace for sample 4a shows relatively narrow and symmetrical peaks and, therefore, is modeled by single phase.

5.3.4 Rietveld Structure Refinement of HRPXRD data

The HRPXRD data for samples 2a and 4a were analyzed with the Rietveld method (Rietveld 1969), as implemented in the GSAS program (Larson and Von Dreele 2000), and using the EXPGUI interface (Toby 2001). The initial unit-cell parameters and atom coordinates for monazite-Ce, monazite-Sm, and xenotime were taken from Ni et al. (1995). Scattering curves for neutral atoms (Ce, Sm, P, O) were used. The background was modeled using a Chebyschev polynomial (24 terms for both samples 2a and 4a). The peak profiles were fitted with the pseudo-Voigt function (profile type-3) in the GSAS program (Finger et al., 1994). A full matrix least-squares refinement was carried out by varying the parameters in the following sequence: a scale factor, unit-cell parameter, atom coordinates, and isotropic displacement parameters. HRPXRD data for sample 2a was refined using three phases: monazite-Ce, monazite-Ce, and xenotime-Y. Site occupancies for Ce for phase 2a and 2b were refined but site occupancies for Y and P for xenotime (phase 3) were fixed to 1. HRPXRD data for sample 4a was refined using a single phase based on the dominant Sm and P atoms. Site occupancies for Sm was refined but for P was fixed to 1. In the final stages of the refinement, all of the parameters were allowed to vary simultaneously, and the refinement converged. The fitted HRPXRD data for samples 2a and 4a are shown in Figure 5.1. The unit-cell parameters and the data collection and refinement statistics are given in Table 5.5. The atom coordinates, isotropic displacement parameters, and

site occupancy factors are given in Table 5.6. Selected bond distances and angles are given in Table 5.7.

5.4 Results and Discussion

5.4.1 Cation Exchange in Th-Bearing Monazite-Ce and Monazite-Sm

Two main substitution mechanisms such as (REE^{3+},Y^{3+}) + P^{5+} = Th^{4+} + Si^{4+} (huttonite) and 2(REE^{3+},Y^{3+}) = (Th, U)$^{4+}$ + Ca^{2+} (cheralite), are commonly observed in the chemical composition of monazites (Van-Emden 1997; Spear and Pyle 2002; Clavier et al. 2011; Hoshino et al. 2012). Cheralite substitution predominates in metamorphic monazite, whereas the huttonite substitution is more common in granitic monazite (Broska et al. 2000; Spear and Pyle 2002). Figures 5.2a and 5.2b show that the huttonite substitution dominates over the cheralite substitution in the chemical composition of sample 2a. The chemical composition of sample 4a exhibits the huttonite substitution (Fig. 5.3a) but no clear cheralite substitution is evident. However, when the (3 × Sm^{3+}) is plotted against the sum of (Th^{4+} + Ca^{2+} + Ce^{3+}), a negative linear relation is obtained (Fig. 5.3b). Therefore, both samples 2a and 4a dominates the huttonite substitution.

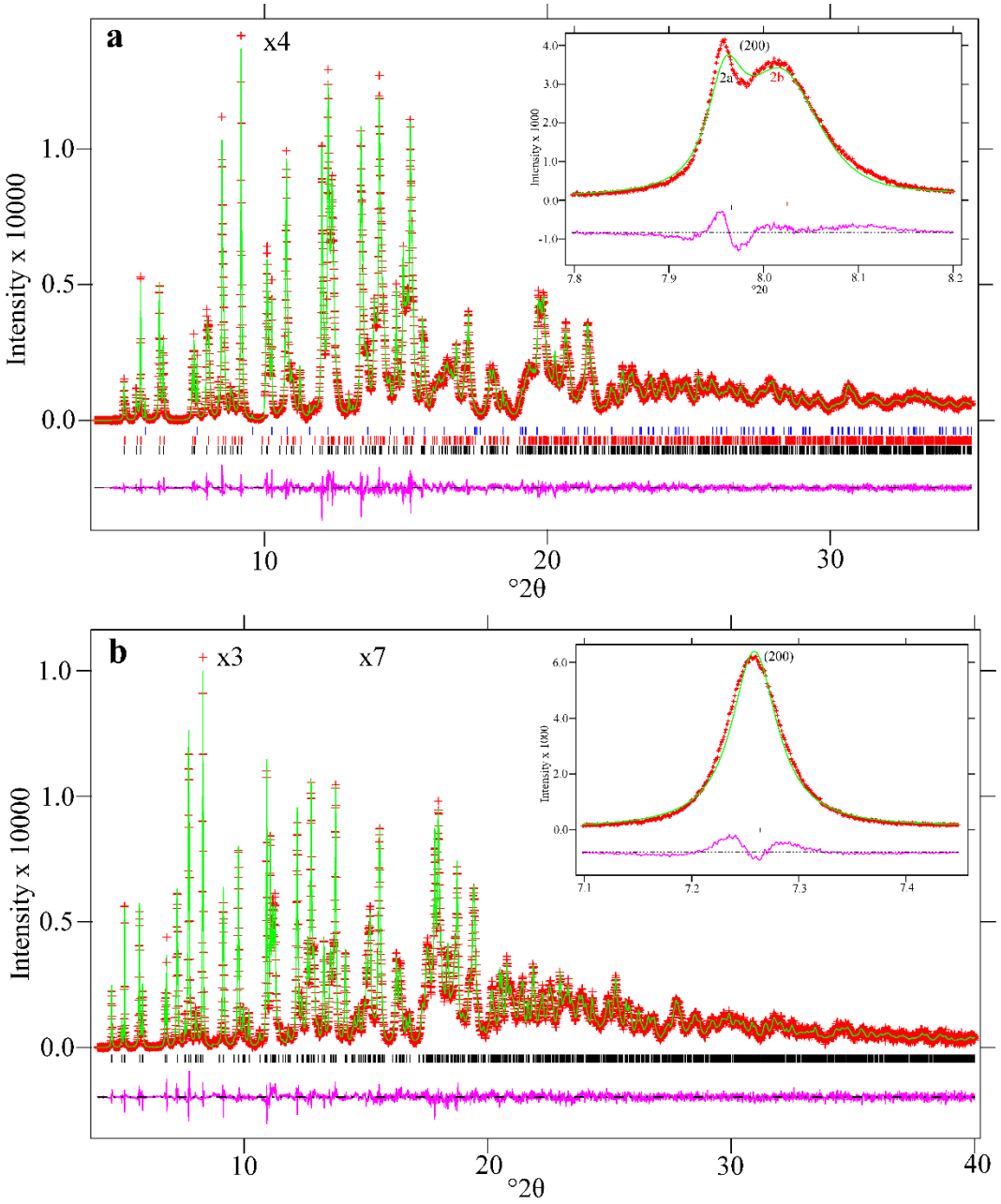

Figure 5.1 HRPXRD traces for samples 2a and 4a showing the calculated (continuous green line) and observed (red crosses) data. The short vertical red lines indicate allowed reflection positions. The intensities for the trace and difference curve for sample 2a (**a**) that are above 10° 2θ are scaled by factors of ×4, respectively. The intensities for the trace and difference curve for sample 4a (**c**) that are above 9 and 15° 2θ are scaled by factors of ×3 and ×7, respectively. Expanded (200) peak for samples 2a and 4a are displayed in the inserts showing the (200) peak splitting for sample 2a because of the presence two monazite phases.

Table 5.5 HRPXRD data and Rietveld refi1111111nement statistics for samples 2a and 4a

	2a			4a
	Phase 2a: Monazite-Ce	Phase 2b: Monazite-Ce	Phase 2c: Xenotime-Y	Monazite-Sm
Space group	*P2₁/n*	*P2₁/n*	*I4₁/amd*	*P2₁/n*
a (Å)	6.8088(1)	6.7565(2)	6.9080(1)	6.73162(6)
b (Å)	7.00799(7)	6.9837(2)		6.9412(1)
c (Å)	6.47541(6)	6.4696(1)	6.0358(1)	6.4467(1)
β (°)	103.7831(9)	103.719(2)		103.8988(6)
V (Å^3)	300.085(6)	296.56(1)	288.030(8)	292.696(4)
wt. %	32.20(3)	62.93(2)	4.87(1)	
[1]N_{data}	30448			38005
[2]N_{obs}	2067			1701
[3]Overall R_F^2	0.0118			0.0167
Reduced χ^2	1.707			1.688
λ (Å)	0.45900(2)			0.41370(2)
2θ range	2 - 35°			2 - 40°

[1]N_{data} is the number of data points; [2]N_{obs} is number of observed reflections; [3]$R_F^2 = \sqrt{\frac{\sum(F_{obs}^2 - F_{calc}^2)}{\sum F_{obs}^2}}$ is defined based on observed (*obs*) and calculated (*calc*) amplitudes

Table 5.6 Atom positions, isotropic displacement parameters, and site occupancy factors (*sofs*) for samples 2a and 4a

Sample no.	Phase	Atom	*sof*	*x*	*y*	*z*	*U*iso
2a	Phase 2a	Ce	1.03(1)	0.2842(2)	0.1574(1)	0.0992(1)	0.0209(3)
		P	1.0	0.3061(7)	0.1651(6)	0.6107(6)	0.022(2)
		O1	1.0	0.234(1)	-0.017(1)	0.432(1)	0.035(2)
		O2	1.0	0.409(1)	0.330(1)	0.523(1)	0.035(2)
		O3	1.0	0.490(1)	0.101(1)	0.827(1)	0.035(2)
		O4	1.0	0.119(1)	0.228(1)	0.697(1)	0.035(2)
	Phase 2b	Ce	0.864(4)	0.2811(1)	0.1605(1)	0.1004(1)	0.0001(2)
		P	1.0	0.2907(5)	0.1543(5)	0.6139(5)	0.0177(9)
		O1	1.0	0.244(1)	0.0246(7)	0.420(1)	0.008(1)
		O2	1.0	0.3778(7)	0.348(1)	0.4834(9)	0.008(1)
		O3	1.0	0.4682(7)	0.1109(8)	0.7936(8)	0.008(1)
		O4	1.0	0.1334(9)	0.2087(8)	0.7192(9)	0.008(1)
	Phase 3c	Y	1.0	0	3/4	1/8	0.012(1)
		P	1.0	0	1/4	3/8	0.017(4)
		O	1.0	0	0.063(1)	0.207(1)	0.027(4)
4a		Sm	0.875(2)	0.28031(5)	0.15785(5)	0.10036(5)	0.0103(1)
		P	1.0	0.2993(2)	0.1635(2)	0.6109(2)	0.0136(4)
		O1	1.0	0.2452(4)	-0.0025(4)	0.4344(5)	0.012(2)
		O2	1.0	0.3873(4)	0.3391(5)	0.5000(5)	0.0140(3)
		O3	1.0	0.4778(5)	0.1032(4)	0.8024(4)	0.030(1)
		O4	1.0	0.1266(5)	0.2101(4)	0.7160(5)	0.021(1)

Table 5.7 Bond distances (Å) and angles (°) for samples 2a and 4a

2a					4a	
	Phase 2a: Monazite-Ce	Phase 2b: Monazite-Ce	Phase 2c: Xenotime-Y		Monazite-Sm	
Ce-O1′	2.568(8)	2.550(5)	Y-O′ ×4	2.218(9)	Sm-O1′	2.486(3)
Ce-O1″	2.295(7)	2.339(6)	Y-O″ ×4	2.383(6)	Sm-O1″	2.372(3)
Ce-O2′	2.935(8)	2.742(5)	<Y-O> [8]	2.301(8)	Sm-O2′	2.803(3)
Ce-O2″	2.667(9)	2.650(4)			Sm-O2″	2.499(3)
Ce-O2‴	2.488(7)	2.434(7)			Sm-O2‴	2.568(3)
Ce-O3′	2.532(8)	2.617(5)			Sm-O3′	2.614(3)
Ce-O3″	2.348(8)	2.526(5)			Sm-O3″	2.417(3)
Ce-O4′	2.628(8)	2.495(6)			Sm-O4′	2.473(3)
Ce-O4″	2.359(9)	2.454(5)			Sm-O4″	2.449(3)
<Ce-O> [9]	2.536(8)	2.534(5)			<Sm-O> [9]	2.520(3)
Ce-P′	3.202(4)	3.164(4)	Y-P	3.0179(1)	Sm-P′	3.190(2)
Ce-P″	3.281(4)	3.308(4)			Sm-P″	3.265(2)
P-O1	1.711(8)	1.521(8)	P-O ×4	1.643(9)	P-O1	1.600(3)
P-O2	1.529(10)	1.769(7)			P-O2	1.598(3)
P-O3	1.701(8)	1.490(5)			P-O3	1.559(3)
P-O4	1.567(10)	1.443(6)			P-O4	1.515(3)
<P-O> [4]	1.627(9)	1.556(7)			<P-O> [4]	1.568(3)
O1-P-O2	113.2(5)	95.08(35)	O-P-O′ x4	112.5(2)	O1-P-O2	106.1(2)
O1-P-O3	113.3(4)	119.6(4)	O-P-O″ x2	103.6(4)	O1-P-O3	111.8(2)
O1-P-O4	108.9(5)	121.1(4)	<O-P-O> [6]	106.6(3)	O1-P-O4	113.9(2)
O2-P-O3	101.1(5)	103.34(30)			O2-P-O3	105.2(2)
O2-P-O4	113.6(6)	112.9(4)			O2-P-O4	116.4(2)
O3-P-O4	106.5(5)	103.4(4)			O3-P-O4	103.4(2)
<O-P-O> [6]	109.4(5)	109.2(4)			<O-P-O> [6]	109.5(2)

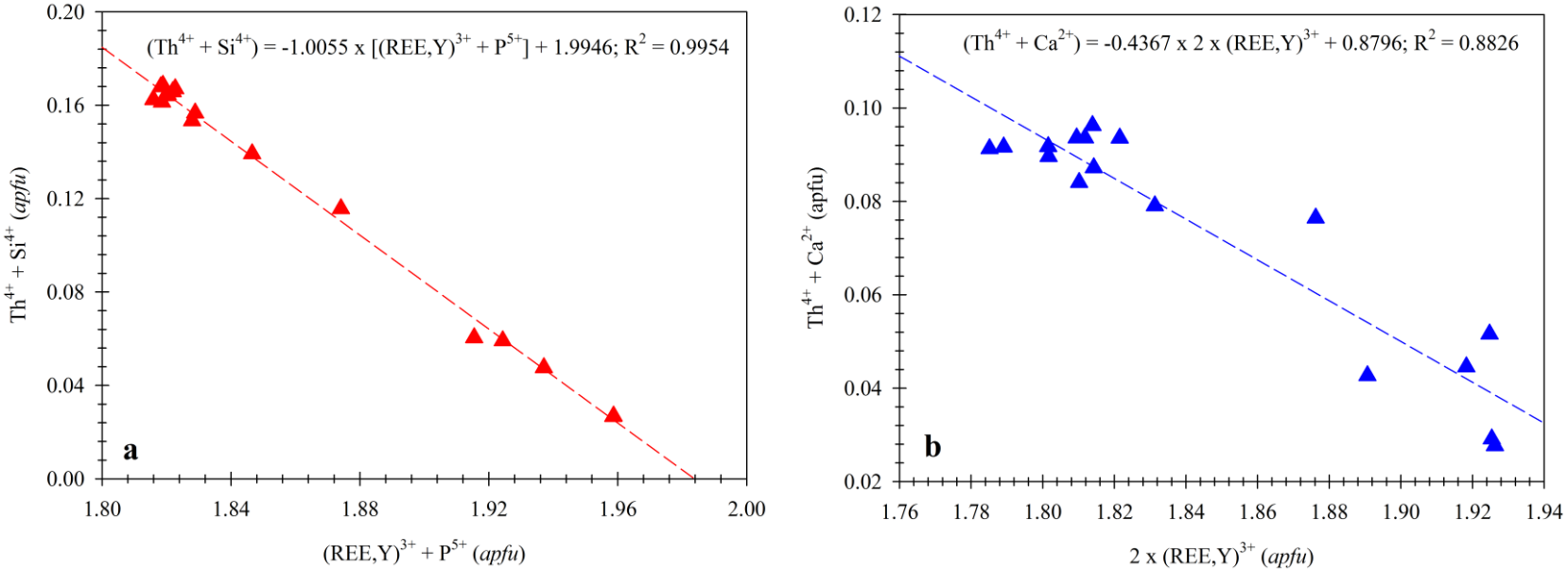

Figure 5.2 Compositional exchanges in sample 2a (monazite-Ce) in terms of the number of atoms per formula unit (*apfu*). Two negative exchanges are obtained: (**a**) between $(REE,Y)^{3+} + P^{5+}$ and $Th^{4+} + Si^{4+}$ (called huttonite substitution) and (**b**) between $(REE,Y)^{3+}$ and $Th^{4+} + Ca^{2+}$ (called cheralite substitution).

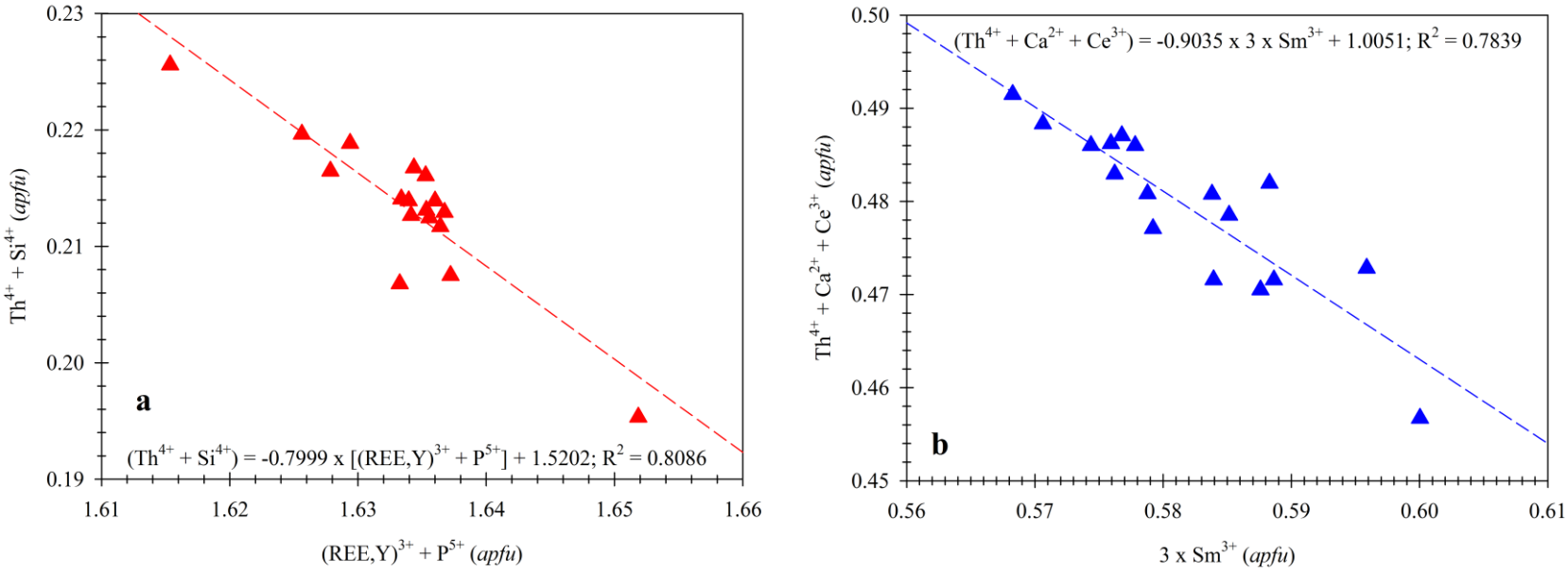

Figure 5.3 Compositional exchanges in sample 4a (monazite-Sm) in terms of the number of atoms per formula unit (*apfu*). Two negative exchanges are obtained: (**a**) between $(REE,Y)^{3+} + P^{5+}$ and $Th^{4+} + Si^{4+}$ (called huttonite substitution) and (**b**) between Sm^{3+} and $Ce^{3+} + Th^{4+} + Ca^{2+}$.

5.4.2 Multiple Phases in Sample 2a: Monazite-Ce

The synchrotron HRPXRD data for sample 2a indicates three different phases, which are monazite-Ce (phase 2a), monazite-Ce (phase 2b), xenotime-Y (phase 2c). The crystal structure of the three different phases was modeled quite well, as indicated by the reduced χ^2 and overall R_F^2 Rietveld refinement indices of 1.707 and 0.0118, respectively (Table 5.5). Splitting of the (200) peaks for phases 2a and 2b in sample 2a is clearly shown in Figure 5.4. A broadening at the peak bases is observed for all peaks due to the presence of two phases 2a and 2b. The broadening is more obvious in the (200) peaks indicating significant structural changes along the **a** direction. Seydoux-Guillaume (2002) reported the existence of phase 2 but it was not fully evaluated structurally. They did not report the phase fractions, bond distances, and angles in their study (Seydoux-Guillaume 2002). Their phase 2 disappeared when the sample was heated to 1000°C. The three distinct peaks are shown in the Figure. 5.4a and they are for (101), (200), and (211) peaks of xenotime-Y, as modeled by the Rietveld method.

The unit-cell volume for phase 2a [V = 300.085(6) Å^3] is 1.19 % larger than that for phase 2b [296.56(1) Å^3] in sample 2a. The phase 2c is xenotime-Y, which was refined with space group $I4_1/amd$ and has a unit-cell volume of 288.030(8) Å^3, which is 0.52% larger than that studied by Ni et al. (1995). The fractions of phase 2a (monazite-Ce), phase 2b (monazite-Ce), and phase 2c (xenotime-Y) are 32.20(3), 62.93(2), and 4.87(1) wt. %, respectively (Table 5.5).

The *a*, *b*, and *c* unit-cell parameters for phase 2a are 0.0523, 0.02429, and 0.00581 Å larger than that for phase 2b in sample 2a. So the difference is more prominent in the *a* parameter followed by the *b* and *c* parameters. However, the unit-cell parameters for phase 2b in sample 2a are more close to the values obtained with SCXRD for the same sample and for samples 1 and 3 (Table 4.3: Chapter 4; Table 5.5).

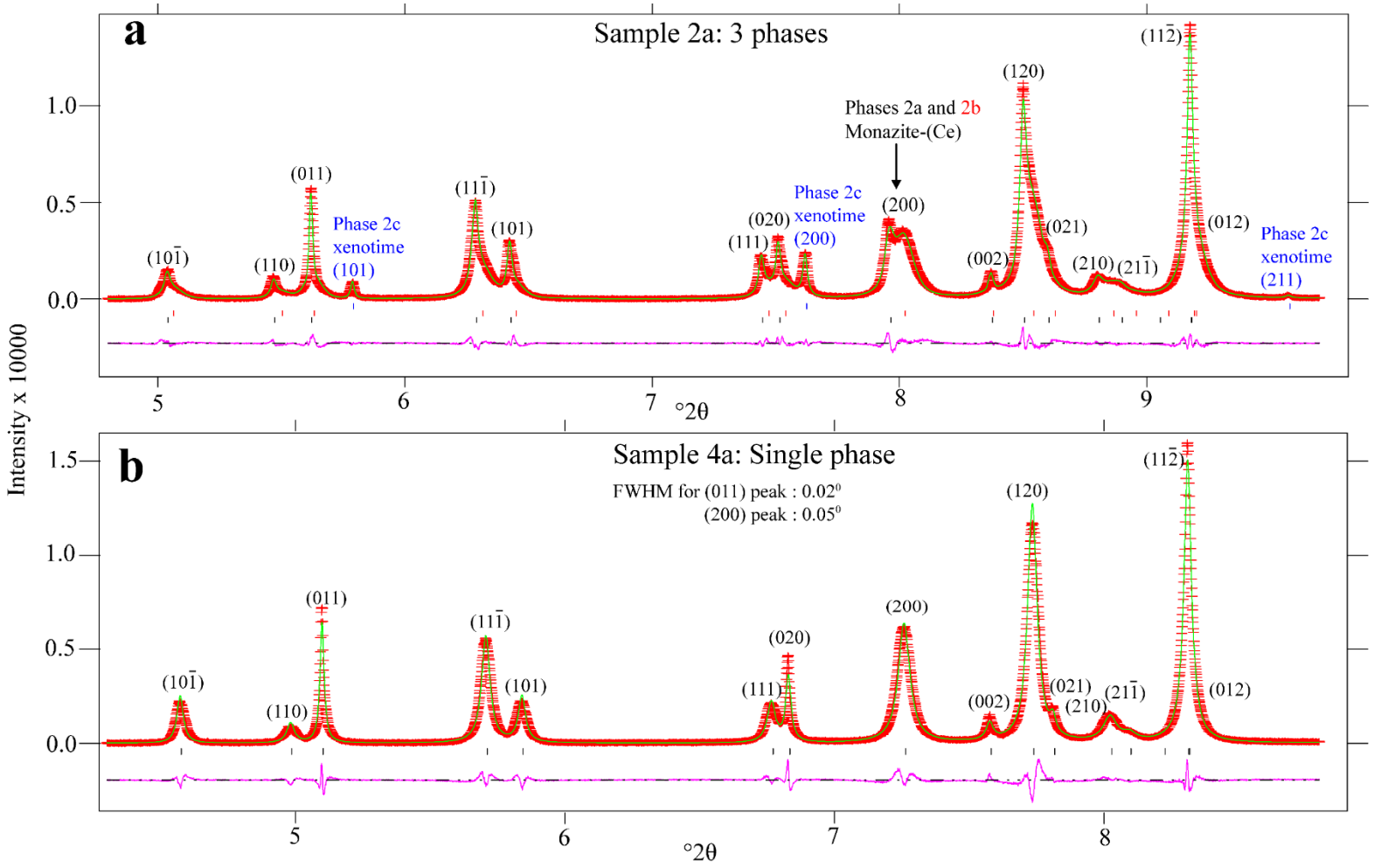

Figure 5.4 Expanded parts of the synchrotron HRPXRD traces: (**a**) multiple phases in sample 2a and (**b**) a single phase in sample 4a.

5.4.3 Single Phase in Sample 4a: Monazite-Sm

Sample 4a contains a single phase of monazite-Sm. Peaks in the HRPXRD trace are symmetric and no peak splitting and abnormal broadenings at the peak bases are observed (Fig. 5.4b). The unit-cell volume for sample 4a [V = 292.696(4) Å^3] is 0.31 % smaller than that for monazite-Sm [V = 293.6(1) Å^3] obtained with PXRD by Masau et al. (2002). The *a*, *b*, and *c* unit-cell parameters of sample 4a are 0.007, 0.010, and 0.015 Å smaller than those of monazite-Sm obtained with PXRD (Masau et al. 2002). The Sm concentrations for sample 4a and for monazite-Sm studied by Masau et al. (2002) are 0.194 and 0.197 *apfu*, respectively. But sample 4a contains significantly less amount of Gd and high quantities of Ce, Th, Ca, Nd, and La *apfu* compared to monazite-Sm studied by Masau et al. (2002) (Fig. 5.5). The difference in chemical compositions between sample 4a and monazite-Sm studied by Masau et al. (2002) may contribute to the small change in the unit-cell parameters.

Although the HRPXRD data for sample 4a is modeled well with the Rietveld method because the reduced χ^2 and overall R_F^2 indices of 1.688 and 0.0167, respectively (Table 5.5), the peaks are not consistent in terms of their FWHM values. For example, (200) peak has higher FWHM than the (020) and (011) peaks (Fig. 5.5). After the refinement of the profile-3 coefficients LX and LY are 0.20(1) and 46.12(0), respectively. The LY value is relatively high. Peak broadening in X-ray diffraction is the result of one or more of the following sources: instrumental, crystallite size, and the presence of micro-strain (Delhez et al. 1993). The instrumental broadening is not expected because this study used high-resolution data. The profile coefficient LX is related to crystallite size and gave very low value for the sample 4a. The LY is related to micro-strain at atomic level. Therefore, the high LY indicates the presence of micro-strain in the 4a sample. Because of this strain, the SCXRD data for the same sample, which has relatively low-resolution, gave very high mosaicity and R_{int}. The source of this strain could be the remnant of radiation damage and accumulation. As sample 4a contains a very high of amount of Th and is relatively older (1361 Ma) in age, it received a large amount of α-

radiation doses (1.93×10^{17} α-decay events/mg) (Table 5.4). The recovery of radiation damage is much faster in monazite relative to zircon. As this monazite-Sm received extremely high α-radiation doses, the damage overcame the recovery. This results the remnant damage in sample 4a.

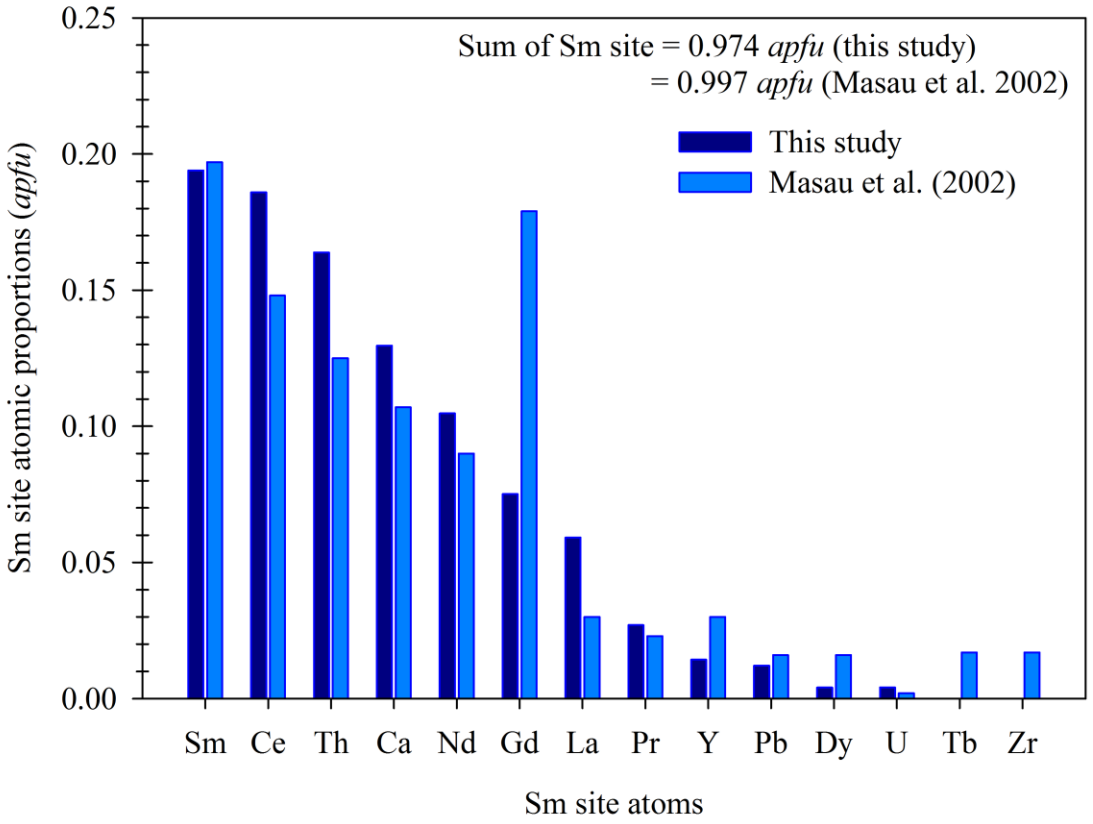

Figure 5.5 Sm site atoms in sample 4a (monazite-Sm) and in monazite-Sm studied by Masau et al. (2002).

5.4.4 Variations of Unit-Cell Parameters

The unit-cell parameters for the three phases of sample 2a and a single phase of sample 4a compare well with the other published structures. The *a*, *b*, and *c* parameters, and β angles for phases 2a, 2b, and 2c in sample 2a, for single phase in sample 4a, and for samples 1 and 3 are plotted with the *V* (Figs. 5.6a, 5.6b, 5.7a, and 5.7b). The unit-cell parameters for samples 1 and 3 are added for comparison. Besides, unit-cell parameters for monazite-Ce and monazite-Sm obtained with SCXRD and PXRD techniques that are available in literature are also incorporated (Ni et al. 1995; Masau et al. 2002; Seydoux-Guillaume et al. 2002). Linear fits are obtained between unit-cell parameters and the *V* for samples 2a (two phases), 4a, 1, and 3. However, the unit-cell parameters for phase 2c (xenotime) in sample 2a are excluded for calculating the linear fits. The slopes of linear equations obtained for the *a*, *b*, and *c* parameters with the *V* indicate that the changes are the highest for the *a* parameter followed by the *b* and *c*. The *a* and *b* parameters from literature fall close to the linear regression lines but the *c* parameters are relatively scattered. This indicates that structural changes along the **a** and **b** directions are consistent and systematic in the monazite structure. The *a*, *b*, and *c* parameters and β angle for the phase 2b in sample 2a fall close to those for samples 1 and 3. The unit-cell parameters for samples 1 and 3 were obtained with SCXRD and both samples are Ce-dominated detrital monazite, which is fully crystalline. However, the *a* and *b* parameters phase 2a in sample 2a are clearly off. This discrepancy may be related to the elapse time for the two monazite formation.

The *a* and *c* parameters for the phase 2c in sample 2a are way off the linear regression lines. This is valid because xenotime belongs to tetragonal crystal system with the space group $I4_1/amd$. However, *b* (= *a*) parameter for xenotime phase 2c falls on the linear regression line (Fig. 5.7a). This indicates that during the monazite-xenotime phase change major resets occurred along the **a** and **c** directions.

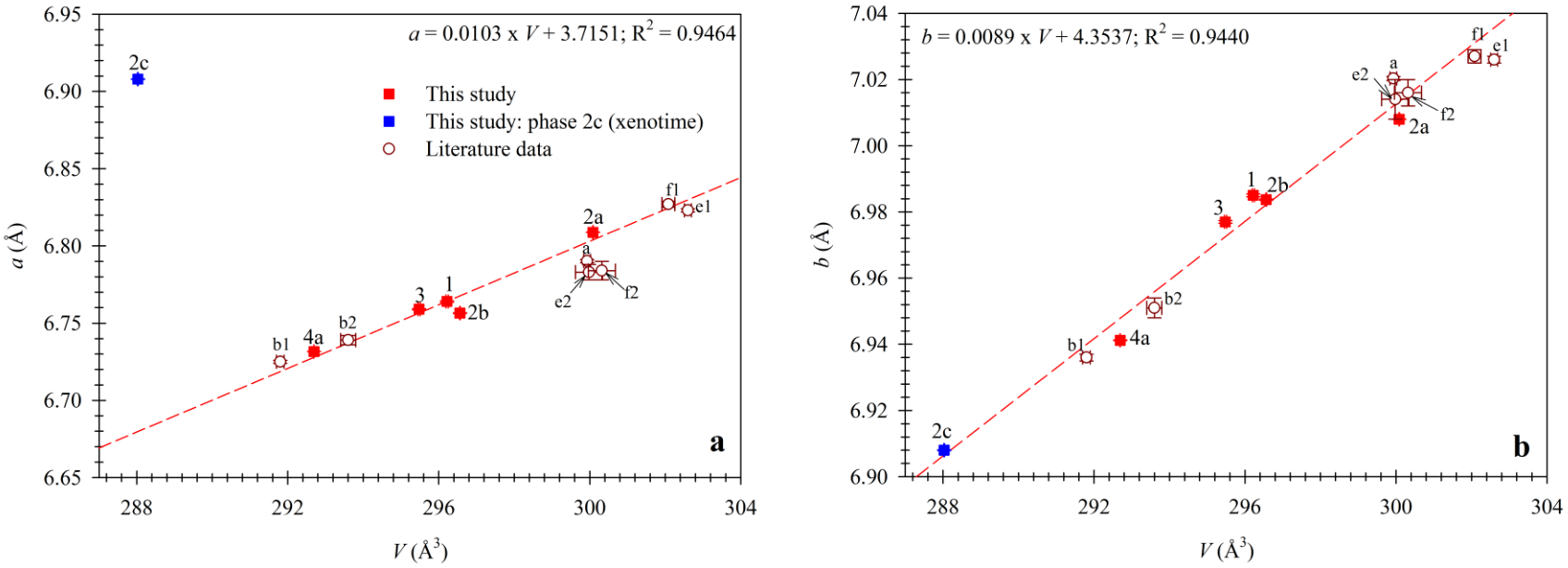

Figure 5.6 Variations of unit-cell parameters in monazite: (**a**) *a* vs *V* and (**b**) *b* vs *V*. The dashed line represents the linear regression for samples 1, 3, phases 2a and 2b in sample 2a, and sample 4a. Phase 2c in sample 2a is excluded from the linear regression. Open symbols are from literature [a: monazite-Ce (Ni et al. 1999); b1 (SCXRD) and b2 (PXRD): monazite-Sm (Masau et al. 2002); e1 (phase 1) and e2 (phase 2): monazite-Ce (Seydoux-Guillaume et al. 2002); f1 (phase 1) and f2 (phase 2): monazite-Ce (Seydoux-Guillaume et al. 2004)]. Some errors are smaller than the symbols. The *a* and *b* unit-cell parameters of this study in (**a**) and (**b**) vary with linearity with the *V*.

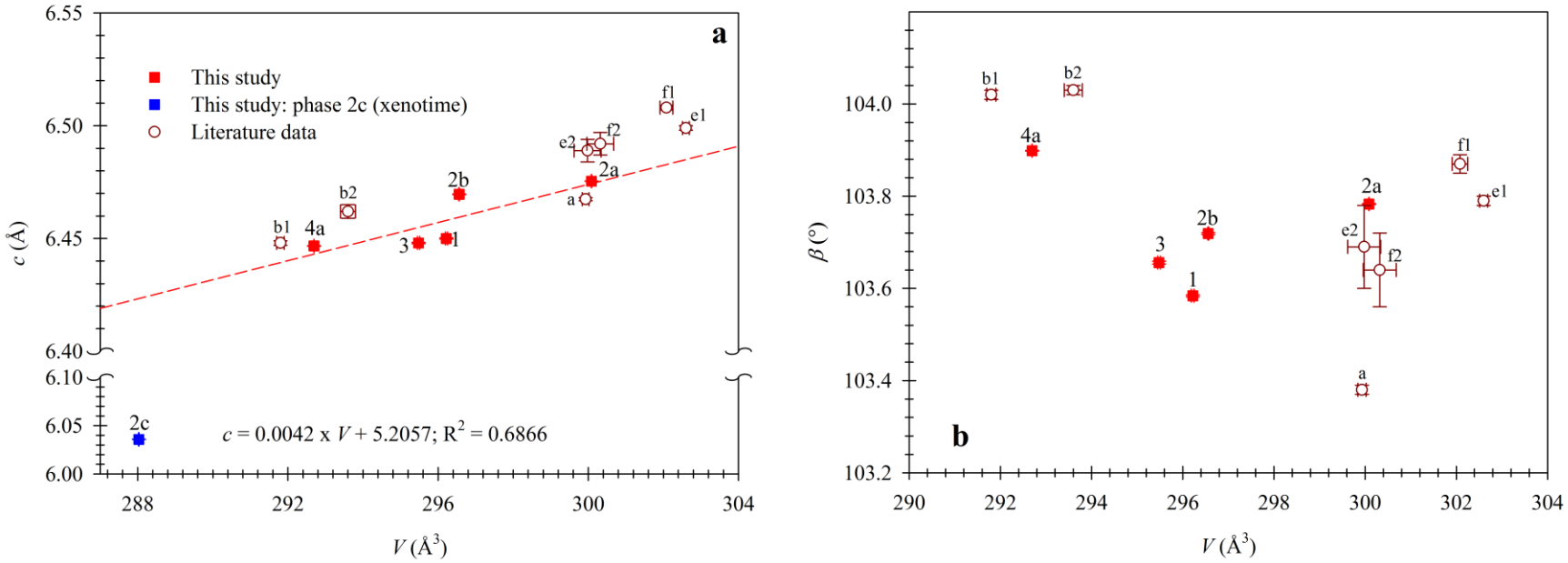

Figure 5.7 Variations of unit-cell parameters in monazite: (**a**) *c* vs *V* and (**b**) *β* vs *V*. The dashed line represents the linear regression for samples 1, 3, phases 2a and 2b in sample 2a, and sample 4a. Phase 2c in sample 2a is excluded from the linear regression. Open symbols are from literature [a: monazite-Ce (Ni et al. 1999); b1 (SCXRD) and b2 (PXRD): monazite-Sm (Masau et al. 2002); e1 (phase 1) and e2 (phase 2): monazite-Ce (Seydoux-Guillaume et al. 2002); f1 (phase 1) and f2 (phase 2): monazite-Ce (Seydoux-Guillaume et al. 2004)]. Some errors are smaller than the symbols. The *c* unit-cell parameter of this study in (**a**) vary with linearity with the *V* but the β in (**b**) shows no correlation.

5.4.5 Bond Distances

The bond distances for Th-free monazite-Ce were determined by Ni et al. (1995) but they were not determined for monazite-Sm. Average <Ce/Sm-O>, <Y-O> and <P-O> are plotted with the *V*. The average <Y-O> and average <P-O> distances for phase 2c (xenotime) are anomalously off from the average <Ce/Sm-O> and average <P-O> distances for monazite. The average <Y-O> for phase 2c (xenotime-Y) in sample 2a is 1.96 % shorter than that for xenotime-Y studied by Ni et al. (1995). There is a positive linear correlation between the average <Ce/Sm-O> distance and the *V* (Fig. 5.8). But the average <Ce-O> distances for phase 2b is slightly and for phase 2a in sample 2a is significantly off the linear regression. The average <P-O> distances for xenotime is 1.540(4) Å (Ni et al. 1995). This P-O distance is almost similar to the average <P-O> distances for monazite-Ce samples 1 and 3 (see Table 4.5: Chapter 4). However, the average <P-O> distances for xenotime-Y phase 2c in sample 2a is 6.69 % longer than the literature value (Ni et al. 1995). The P-O distance in monazite is nearly constant and is about 1.53 Å (see Fig. 5.4: Chapter three). The average <P-O> distances for phase 2a and 2b are 1.04 and 5.65 % longer than the average value (1.53 Å). Figure 5.8 also shows the average <P-O> distances in sample 2a are off from the average line.

The offsets are very prominent in the average <Ce-O> and <P-O> distances for phase 2a and 2c, indicating that these two phases (monazite-Ce and xenotime-Y) are not syngenetic with the phase 2b in sample 2a. The Phase 2b sample 2a was formed during the crystallization of the host rocks. The phase 2a in sample 2a was formed at later stage. The metamorphic processes can trigger the monazite phase transition (Spear and Pyle 2002; Ali 2012). However, the samples 2a is of pegmatitic origin. Therefore, as sample 2a contains significant amount of radioactive substances, radiation-induced phase transition may be involved.

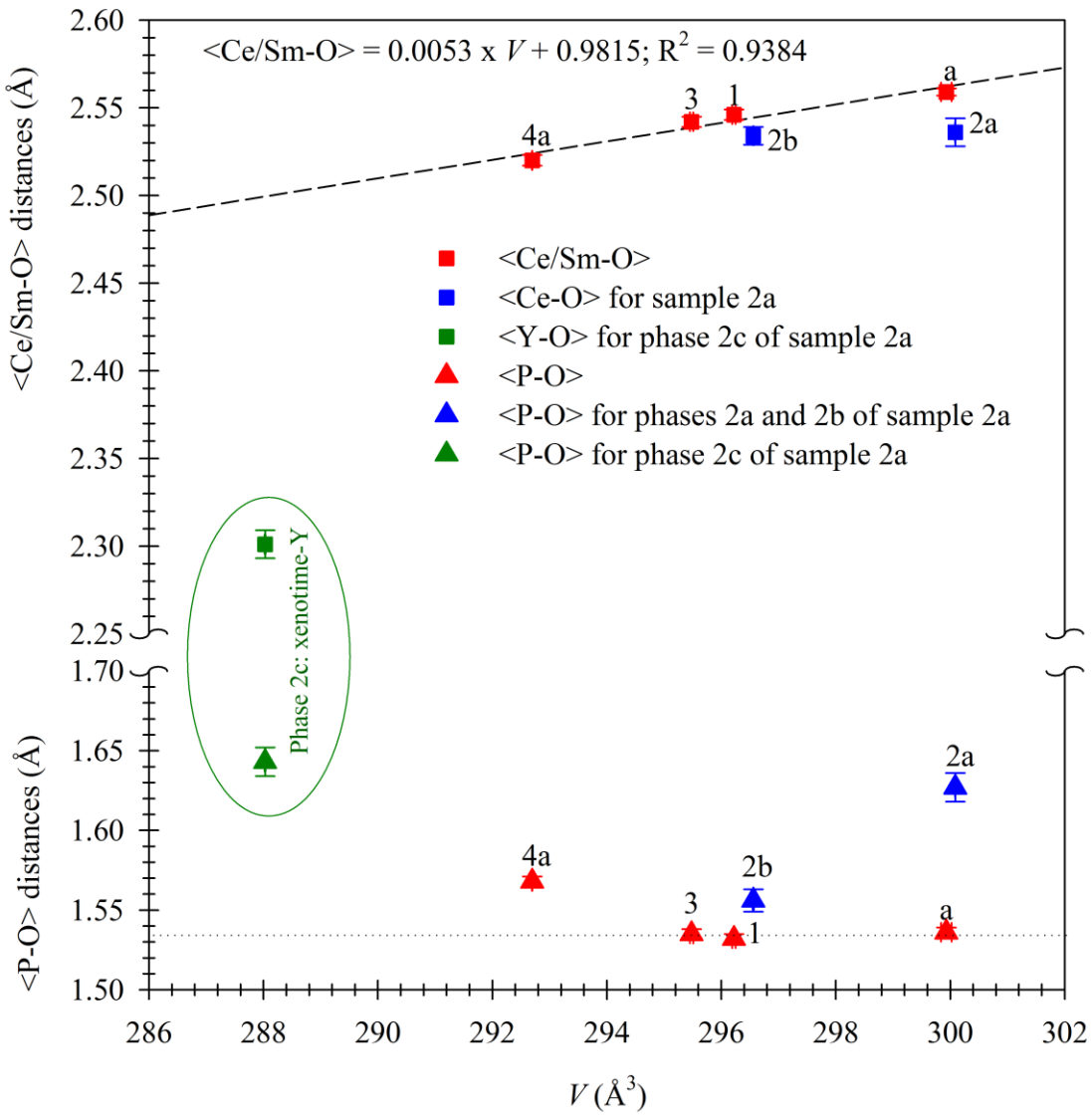

Figure 5.8 The average <Ce/Sm-O>, <Y-O> and <P-O> distances in monazite-Ce, monazite-Sm, and xenotime-Y. The dashed line is a linear fit to the <Ce/Sm> distances for samples 1, 3, 4a, and monazite-Ce studied by Ni et al. (1995) and the equation for this line is given (insert). Bond distances for the 3 phases in sample 2a are excluded from the linear fit. The dotted line is for the average <P-O> distances obtained from Table 4.4 (Chapter 4). The average <Ce-O> and <P-O> distances for phase 2b in sample 2a fall close to the dash and dotted lines but those distances including the average <Y-O> are significantly off the dash and dotted lines. This indicates PO_4 may be distorted by α-radiation effects.

5.4.6 Ce Site Cation Distribution in Sample 2a

The range of variations of oxides in sample 2a is higher than that in sample 4a (Tables 5.1 and 5.2). EPMA chemical data for sample 2a indicates that some cations such as Y^{3+}, Ce^{3+}, La^{3+}, Th^{4+}, and Si^{4+} vary anomalously. Sample 2a contains xenotime-Y as a third phase, so the variations of Ce^{3+}, La^{3+}, Pr^{3+}, Nd^{3+}, Sm^{3+}, Gd^{3+}, Dy^{3+}, Ca^{2+}, and Th^{4+} with Y^{3+} concentration is examined (Fig. 5.9). When the concentration of Y^{3+} decrease, the concentrations of Ce^{3+}, Nd^{3+}, La^{3+}, Pr^{3+}, and Sm^{3+} increase. The changing slopes are Ce^{3+}>Nd^{3+}>La^{3+}>Pr^{3+}>Sm^{3+}. In contrast, the concentrations of Th^{4+}, Dy^{3+}, Gd^{3+}, and Si^{4+} increase with increasing the concentration of Y^{3+}. Thus, the chemical composition also indicates that the formation of phases 2a and 2c may be related to the redistributions of cations in sample 2a. EPMA chemical data for sample 4a do not carry any distinct chemical variability as found in sample 2a.

The back-scattered electron (BSE) image of sample 2a shows the distinct variations of colour and brightness representing the chemical heterogeneity (Fig. 5.10). The dark gray and less bright part (xt) is Y and P rich and Th depleted, whereas light gray and brightest part (tr) is Th and Si rich and Y and REE depleted (Figs. 5.10 and 5.11b,c). The medium dark and brighter part (mz) is REE and P rich domain (Fig. 5.11a). EPMA chemical data spots were selected only in the mz part in sample 2a to measure the chemical composition of monazite quantitatively. Fragments of sample 2a used for synchrotron HRPXRD were examined with polarizing microscope and no twin, cracks, or anomalous birefringence were observed. One of the fragment was also studied with SCXRD and is modeled structurally using single phase with good refinement statistics (Table 4.3: Chapter 4). Therefore, the fragments used for HRPXRD data collected were from the medium dark and brighter part in sample 2a. The multiple phases were found in sample 2a because of the special capability of synchrotron HRPXRD technique.

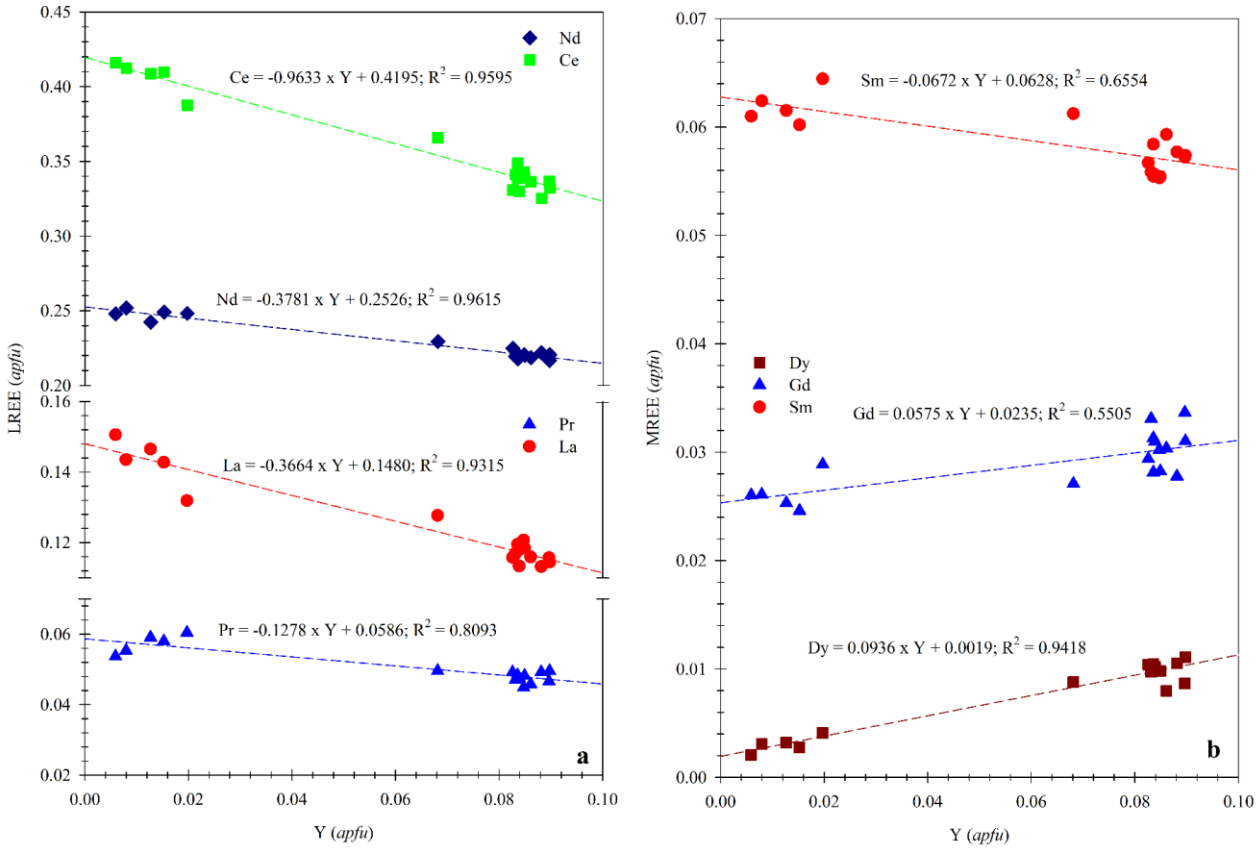

Figure 5.9 Variations of (**a)** LREE and (**b**) MREE with Y in sample 2a. The dashed lines are linear fitted lines and their equations are given (inserts).

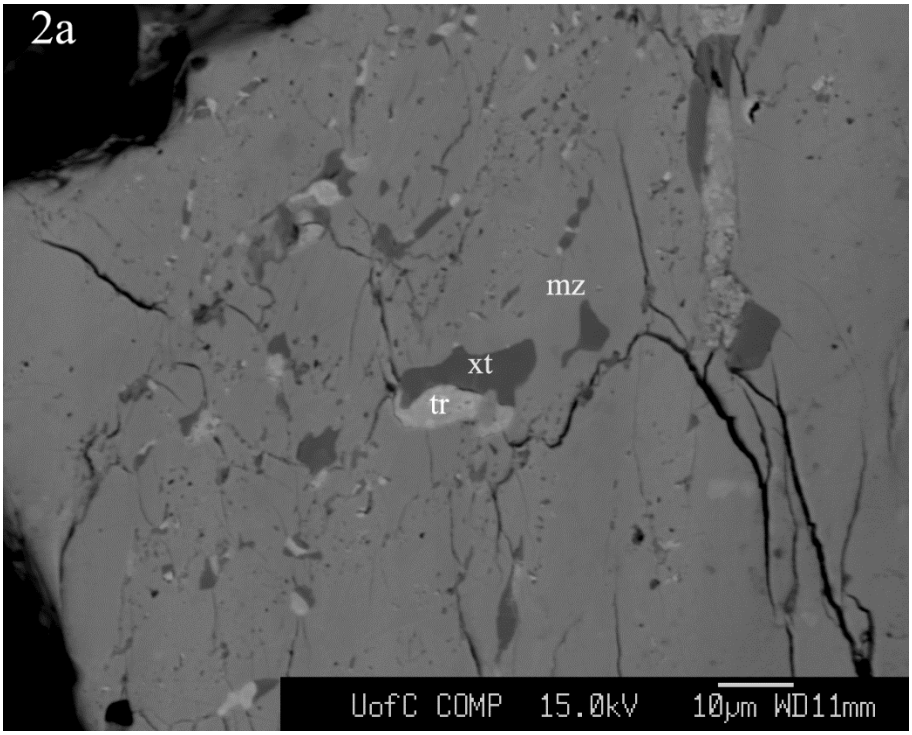

Figure 5.10 Back-scattered electron (BSE) image of sample 2a. Most part of sample shows chemical heterogeneity. The tr, mz, and xt are light gray and the brightest, medium gray and brighter, and dark gray and less bright parts.

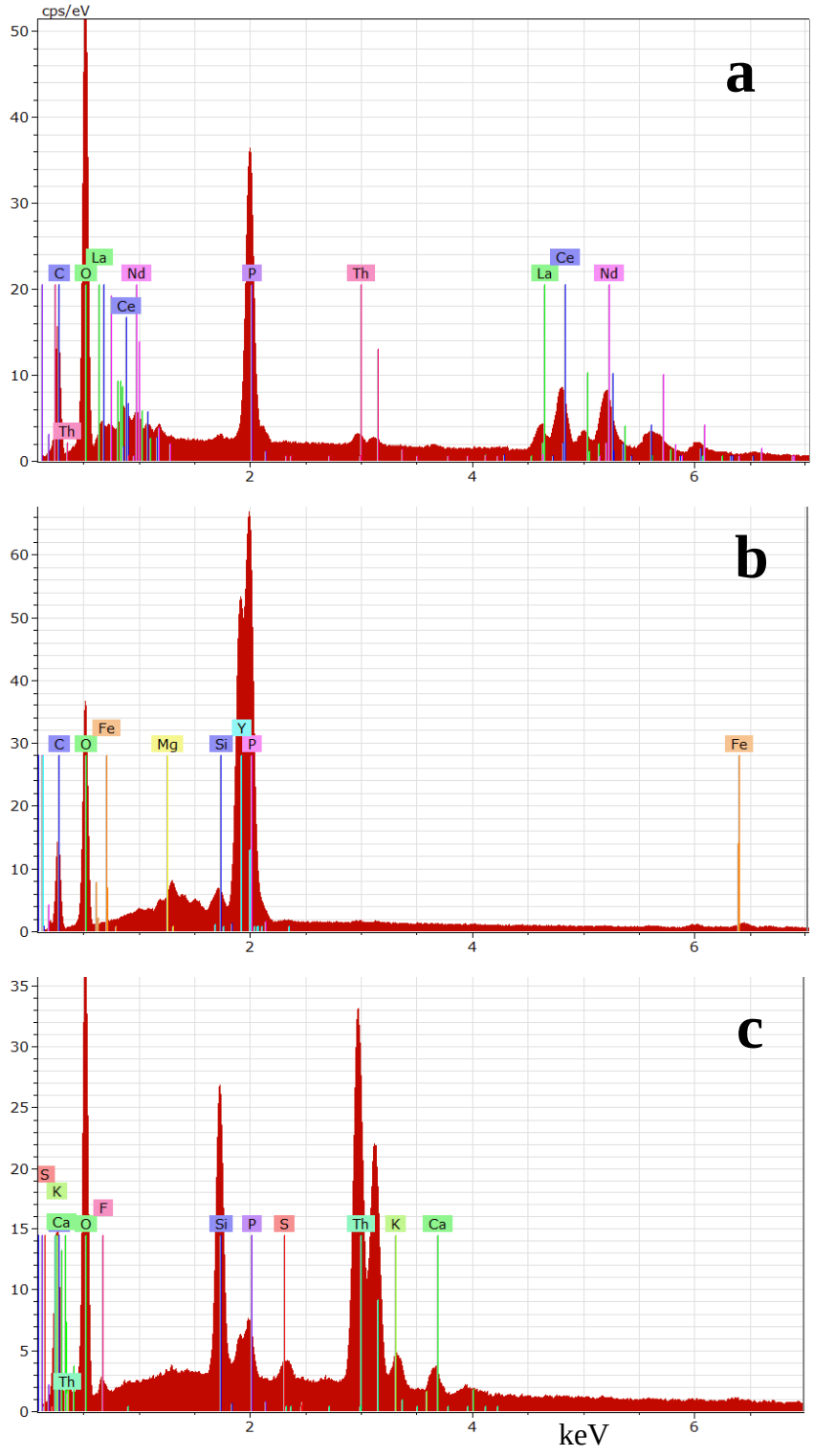

Figure 5.11 EPMA-Energy dispersive spectra (EDS) acquired from the different domains, (**a**) mz, (**b**) xt, and (**c**) tr (Fig. 5.10).

5.4.7 Radiation-Induced Phase Transition in Samples 2a

The chemical ages have been calculated using the concentrations of Th, U, and Pb (ppm) in samples 2a and 4a. The age determination method was explained by Montel et al. (1996). The internal radiation doses received during the ages of samples 2a and 4a have been calculated based on the equation formulated by Holland and Gotfried (1955) (Table 5.4). Both samples 2a and 4a received significant amount of radiation doses of 4.68×10^{16} and 1.93×10^{17} α-decay events/mg, respectively.

Radiation damaged signatures are found in small isolated domains in natural monazite (Black et al. 1984; Meldrum et al. 1998). Seydoux-Guillaume et al. (2002) found two separate phases in a single mosaic crystal and suggested that phase 1 represents well-crystallised areas having relatively high unit-cell parameters resulting from the trapped helium atoms, and phase 2 contains old alpha-recoil tracts and is compressed or expanded resulting the lattice distortions of the adjacent crystalline phase 1. However, our study indicates the redistribution of cations in the monazite. The driving thermal energy for the redistribution of cations comes from the internal radiations of ^{238}U and ^{232}Th. The critical temperatures for the amorphization of monazite and zircon are 430 K and 1100 K, respectively (Meldrum et al. 1996). At very low temperature, natural monazite has the ability to heal fast (Boatner and Sales 1988).

The individual collisions between the internal radiations and crystal structural framework are so complex that it is almost impossible to predict the exact mechanisms in the natural geological settings. However, recent advancement of the analytical techniques and computer simulation facilities helps us to understand the mechanism of radiation-induced changes in a crystal. When a radioactive decay event occurs in a mineral, a significant amount of thermal energy can be produced. Because of this radioactive event the affected volume in the mineral is melted for a fraction of a second and then solidifies. This mechanism is almost analogous to the crystallization of rocks or minerals from a molten magma. Various changes may occur when any mineral experiences internal radiations. The changes are mainly metastable and may depend on

the crystal structural strength of the minerals, the availability of structural voids or spaces for the displaced atoms, intensity of radiation, and the chemical characteristics of minerals (Kinchin and Pease 1955). After recrystallization, physical properties and crystallographic orientation can be reverted to its original state, when healed. Sometimes the affected area may recrystallize in a new phase with distinct crystal structural parameters that are different from the original (Pabst 1952).

Thus, the presence of three phases in sample 2a is the consequence of internal radiation events. As monazite has tremendous ability to recrystalline, no amorphous domains are retained in monazite. Depending on the available cations and amount of internal radiation doses during the recrystallization events, the volume of the affected area can recrystallize as the same phase retains its original space group but has distinct unit-cell parameters, bond distances, and angles, as observed in phase 2a and phase 2b of sample 2a or the separate phase with higher symmetry and different structural parameters, as found in sample 2a as a xenotime-Y.

5.5 Conclusions

The high-resolution powder X-ray diffraction data shows pegmatitic Ce-dominated monazite contains three phases. These phases may not crystallize at the same time because the average <P-O> distances differ. Redistribution of Ce and P site cations with respect to Y in sample 2a is also indicative of late recrystallization. As the pegmatitic monazite received a high amount of α-radiation doses, the phase changes occur from the effects of radiation. Although the monazite-Sm contains a single phase, its structure is affected by micro-strain indicated by the variable FWHM values of HRPXRD peaks. The micro-strain in the monazite-Sm structure is the remnant of radiation damage.

Chapter 6: Radioactivity in Placer Minerals and Possible Radiological Effects

6.1 Abstract

The study focuses on elevated levels of environmental radioactivity present in heavy mineral (HM) deposits located along a 120 km coastal section, south of Cox's Bazar on the eastern panhandle of Bangladesh. There are 18 locations in the coastal area of Bangladesh, where the metallic heavy minerals were deposited as beach placers. The heavy minerals are found to be deposited in the sand dunes, which are distributed in the both recent beach (foredune area) and paleo-beach areas (backdune area). This study investigates radioactivity concentration in bulk beach sands (6 representative samples) and 5 mineral fractions separated from the beach sands in order to assess potential radio-ecological effects and the possible use of the mineral deposits as a source for uranium (U) and thorium (Th). The bulk beach sands and individual mineral fractions were analysed by two gamma-ray spectroscopy systems with high purity germanium (HPGe) detectors. The radioactivity concentrations of ^{238}U, ^{235}U, ^{232}Th and ^{40}K in the bulk beach sand samples appear to be very high and are related to the concentrations of heavy minerals in the bulk beach sand samples. After assessing the Ra_{eq} activity, radiation hazard indices and absorbed and effective gamma doses of each sample, the heavy mineral-rich beach sands (HM >54 wt. %) result the exposure of elevated radioactivity to the coastal environment and the people living in those specific locations. In the mineral fractions, highest activity concentrations were found in the zircon fraction followed by garnet, rutile, ilmenite, and magnetite. From the present data, it becomes evident that (1) if raw sands or mineral fractions mined in the study area are used for building purposes or industrial use their activity concentrations have to be considered from a radio-ecological perspective, and (2) if mining and processing of the minerals is being considered, U and Th may become strategically significant by-products.

6.2 Introduction

Heavy mineral deposits have been discovered at many locations in the coastal area of Bangladesh. These minerals were deposited as beach placer deposits associated with the formation of sand dunes. In 1961, the presence of heavy mineral deposits was first detected at one location of Cox's Bazar district by the Pakistan Geology Survey and reported that the deposits contains radioactive substances (Schmidt and Asad 1963). During the last three decades Bangladesh Atomic Energy Commission (BAEC) operated several large scale exploration activities along the whole coastal area of Bangladesh and confirmed the presence of heavy mineral deposits in many locations along the coast (BSEC 1994). BAEC characterized these deposits in terms of types, mineralogical compositions, grain sizes and reserves (Biswas 1979; 1981; 1982; 1983; Biswas and Kunda 1985; Rahman et al. 1994). BAEC also mapped the deposit areas and classified those deposits based on their physiographic locations into seventeen names (BSEC 1994). Later in 2009, BAEC discovered an eighteenth heavy mineral deposit in the coast (Zaman et al. 2009a). The names of those heavy mineral deposits are Badarmukam, Sabrang, Teknaf, Silkhali, Inani-Monkhali, Cox's Bazar, Foreshore beach of Maheskhali, Kutubjhum, Fakiraghona, Fakirahata, Baraghoriapara, Panirchara, Hoanak, Matarbari Island, Nijhum dwip, Kuakata, Kutubdia Island and Sonapara. Although BAEC reported the presence of several heavy minerals in those placer deposits, such as, ilmenite, garnet, rutile, magnetite, zircon, kyanite, leucoxene, monazite, etc., they were only able to separate out 5 minerals (ilmenite, garnet, rutile, magnetite, and zircon) physically (BSEC 1994).

6.2.1 Background of Radioactivity in Heavy Mineral Deposits, Cox's Bazar

Schmidt and Asad (1963) first pointed out the presence of radioactivity and counted from 0.5 to 1.0 milliroentgen per hour in the magnetite-rich heavy mineral lenses. After 35 year since the radioactivity was detected, Alam et al. (1999b) measured the radioactivity concentrations of ^{238}U, ^{232}Th and ^{40}K in the fractions of zircon, magnetite, ilmenite, rutile and garnet, processed in

a mineral processing pilot plant of BAEC, using a gamma-ray spectrometry with HPGe detector in the laboratory. They found the concentrations of ^{238}U, ^{232}Th and ^{40}K were 6439, 1324 and 472 Bq/kg for zircon; 3951, 7903 and 213 Bq/kg for garnet; 348, 388 and 59.7 Bq/kg for ilmenite; 6643, 11670 and 182 Bq/kg for rutile; and 22.0, 43.1 and 293 Bq/kg for magnetite fractions.

Zaman et al. (2009b) measured the in-situ radioactivity at 178 points in the foredune area (area: 28,000 m^2) from Kalatoli to Sugandha beach of Cox's Bazar at grid pattern (20m × 10m) using a portable Scintrex GRS-500 differential gamma-ray spectrometer and also, measured the heavy mineral concentration using a gravity separator at each point (Fig. 6.1). They observed that the maximum and minimum amount of radioactivity were 6416 (about 55 times higher than that of minimum counts) and 117 cps (counts per second), respectively, and the corresponding heavy mineral concentrations were 72 % and 0.70%, respectively (Fig. 6.2). They also observed very good correlation between the concentration of heavy minerals in bulk beach sand and counts of radioactivity.

Several studies were conducted on the concentration of radioactivity in the beach as well as coastal soils (e.g., Chowdhury et at. 1987; Alam et al. 1997; Alam et al. 1999b). Although elevated concentrations of radioactivity in the bulk beach sand in some studies were observed (Schmidt and Asad 1963; Zaman et al. 2009b), no study was carried out on the concentration of radioactivity in the heavy mineral-rich bulk beach sand deposited in the recent and paleo-beach areas at the coastal area from Cox's Bazar to Bodarmukam.

Figure 6.1 Map showing a part of Cox's Bazar district from Kalatoli to Shugandha beach. The intersections in the grids are the locations where the in-situ radioactivity was measured and samples were collected (Zaman et al. 2009b).

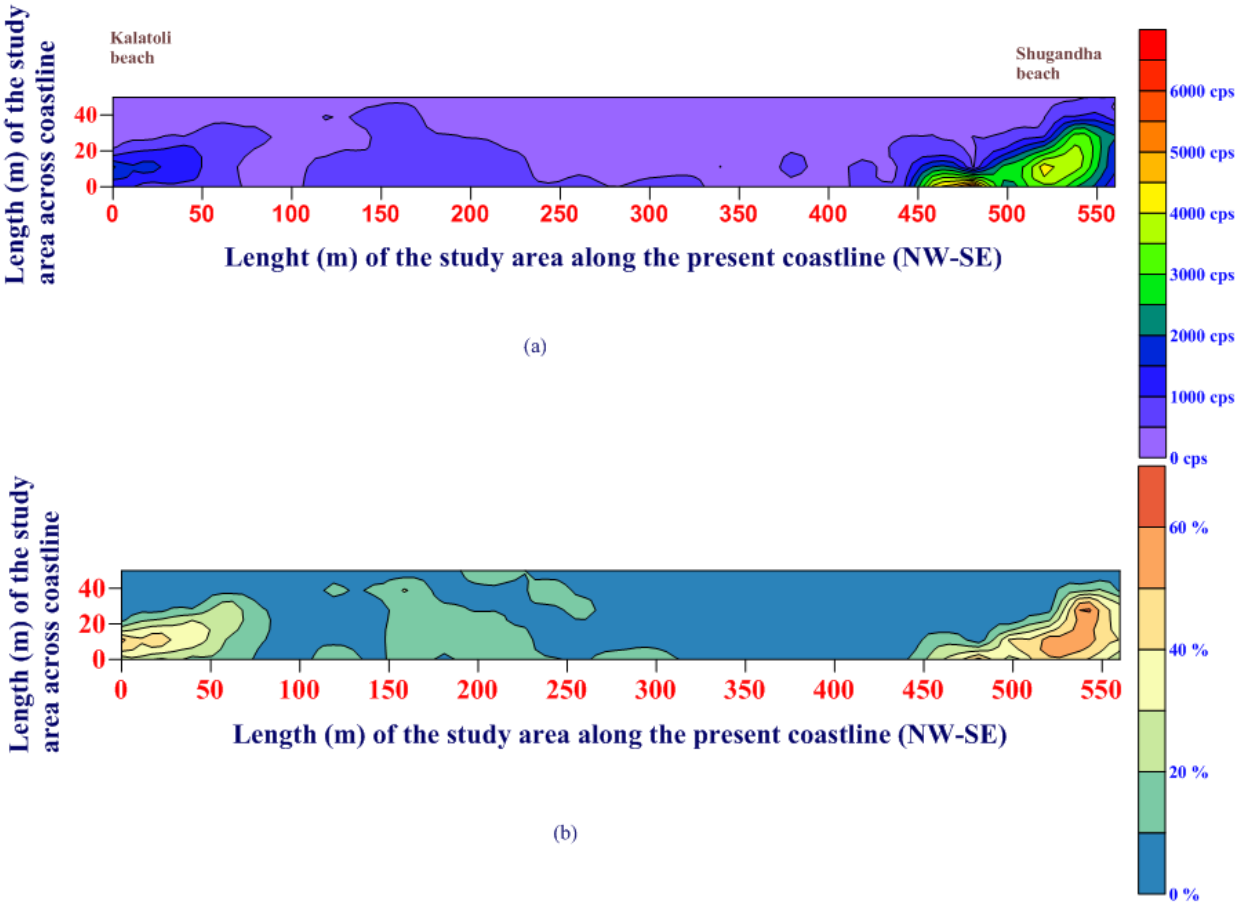

Figure 6.2 (**a**) Natural radioactivity distribution contour map and (**b**) heavy mineral concentration contour map from Kalatoli to Shugandha beach, Cox's Bazar district, Bangladesh (Zaman et al. 2009b).

The aim of this study is to investigate the radioactivity concentration of ^{238}U, ^{235}U, ^{232}Th and ^{40}K in bulk beach sands as well as the 5 mineral fractions separated from bulk beach sands. This study not only assesses the radiological effect on the coastal environment, but also signifies the heavy minerals strategically as the possible source of U and Th.

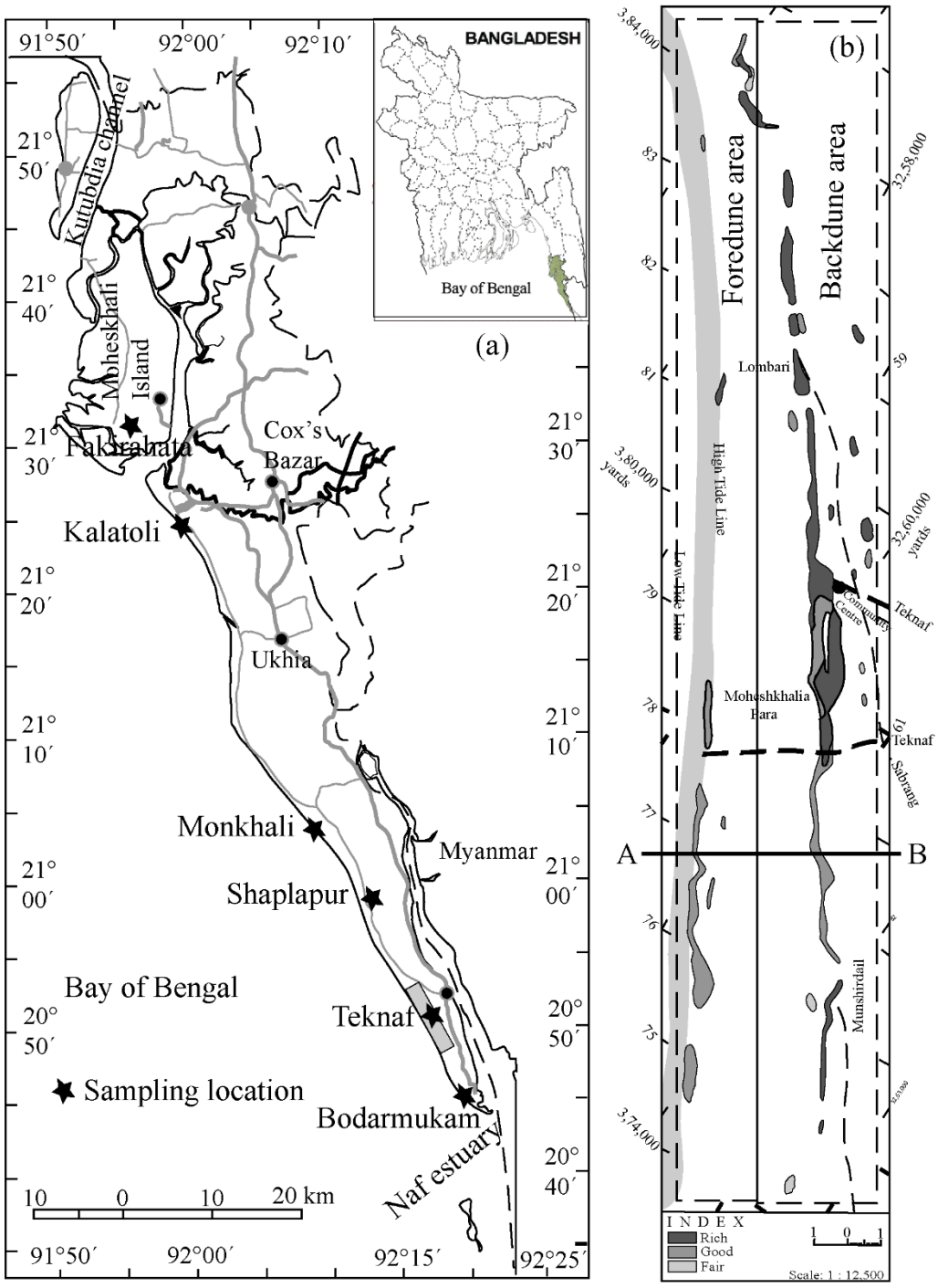

Figure 6.3 Maps: (**a**) sampling locations and (**b**) showing the general distribution of heavy mineral deposits at foredune and backdune areas in Teknaf, Cox's Bazar, Bangladesh (BSEC 1994).

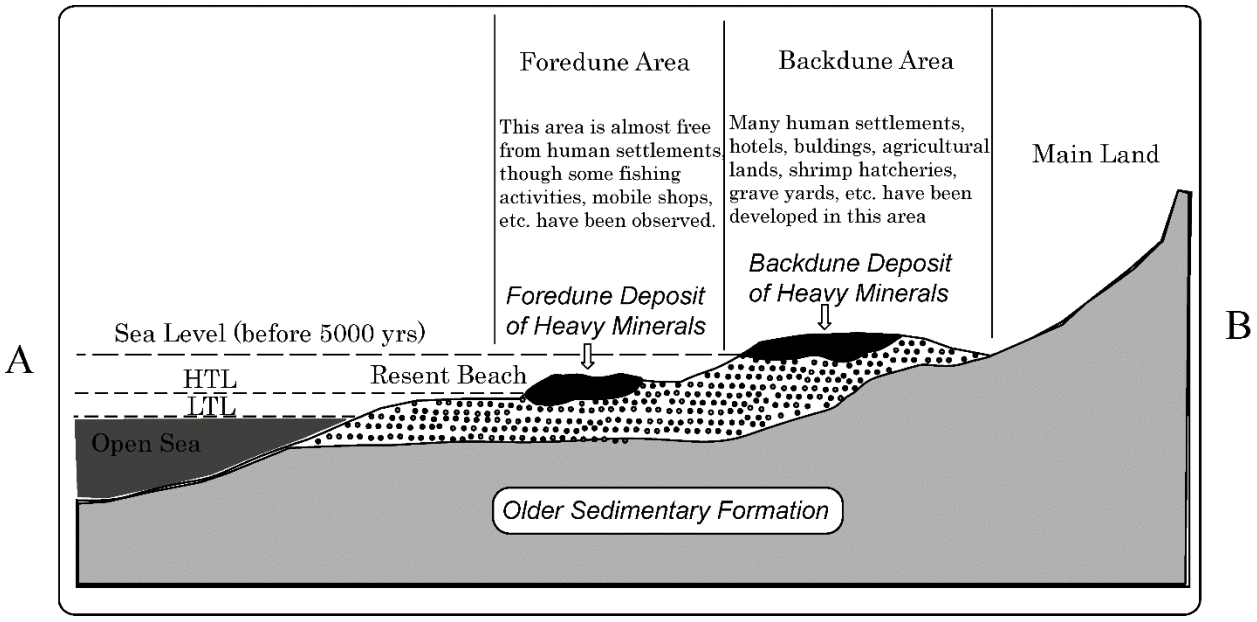

Figure 6.4 A schematic cross section (A-B: Fig. 6.3b) of Teknaf heavy mineral deposit showing the coastal profile (Zaman et al. 2012).

6.2.2 Geological Characteristics of the Study Area

The sample locations are situated along the coastline of the south-eastern panhandle of Bangladesh and bound on the east by small hills (about 100m high relative to mean sea level), hillocks, and high lands, on the west by the Bay of Bengal, on the north Kutuddia channel and on the south by Naf estuary (Fig. 6.3a). The coastal area from Cox's Bazar town to Badarmukam is characterized by a continuous sandy sea beach, which is about 120 km long. The width of the beach varies seasonally from place to place and ranges from 100 to 300 meters with respect to mean sea level. During the rainy season the sea level goes up a little and the width of beach become narrow, and on the other hand the width is wide resulting from the drop of sea level during the winter season. The present beach slopes (from 4 to 6°) gradually towards the sea and the elevation of the foredune part is about 4~5 meters with respect to the mean sea level (Alam et al. 1999a). There are elongated sand dunes formed above the high tide mark which are parallel

to the coastline. These dunes are dynamic which means the positions are being shifted over the years from sea wave and wind actions. The dunes are composed of fine to medium grained sands. The term "foredune area" is used in this study to represent the area of the present beach including the sand dunes (Fig. 6.3b).

The area, which is close to the Tertiary hills and is located in between hills and the present beach area (foredune area), is characterized by the flat lands with sparsely distributed elongated old sand dunes, which are parallel to the present coastline (Fig. 6.3b). The sand dunes are not dynamic because the area is far away from the actions of sea waves and tidal surges. These areas were the sea beach like the present sea beach about 5000 yrs ago (Monsur and Kamal 1994). Because of the drop of sea level, the coastline retreated westward. For this reason, those areas generally do not go under sea water during normal tidal surges. The flat lands in this area are being used as agricultural lands and most of the dune areas are used as human settlements, markets, schools, graveyards, cyclone centers, etc. Lithologically, the dunes are composed of very fine to medium grained sands with some silt and clay. To represent this area the term "backdune area" is used in this study. Figure 6.4 depicts schematically a typical cross-section illustrating the general locations of heavy mineral deposits in the foredune and backdune areas.

The dark brown to black colour sands, which is called "heavy minerals" because the specific gravity is comparatively high ($\rho = 2.85$) (Donoghue and Greenfield 1991), are deposited on the western lap and top of most of the sand dunes located at both foredune and backdune areas. The thickness of the layers of heavy minerals varies from a few centimeters to a few meters. The mineral deposits can be described as lens type features with widths (E-W) from a few meters to over 100 meters and lengths (N-S) from 30 to over 500 meters.

6.3 Material and Analytical Methods

6.3.1 Sample Collection

The sand samples were collected from three foredune and three backdune locations, where a comparatively high concentration of heavy minerals was visual. About 1 kg of sample was collected from each of the 6 locations. About 5 kgs of additional sample was collected from Kalatoli (KTF-3) using the grab sampling method. All samples were dried at 100°C to remove the moisture. Small amount of each of the 6 samples (about 100 gm) was subjected to heavy mineral separation applying gravity separation using a heavy liquid (bromoform, $\rho = 2.89$). The light minerals were mainly quartz. Table 6.1 summaries locations, characteristics and light and heavy mineral contents in each sample.

Table 6.1 Sampling positions and mineral contents in the bulk beach sand sample

Sample no.	Location	Geographical position		Heavy mineral content , wt. %	Light mineral content , wt. %
		Latitude	Longitude		
Foredune area					
BDF-1	Bodarmukam	20°44'43" N	92°20'17" E	97	3
MKF-2	Monkhali	21°06'57" N	92°06'14" E	88	12
KTF-3	Kalatoli	21°24'58" N	91°58'57" E	91	9
Backdune area					
LBB-4	Lomburi	20°52'20" N	92°15'59" E	60	40
SPB-5	Shaplapur	21°05'04" N	92°08'02" E	70	30
FHB-6	Fakirahata	21°32'29" N	91°56'14" E	54	46

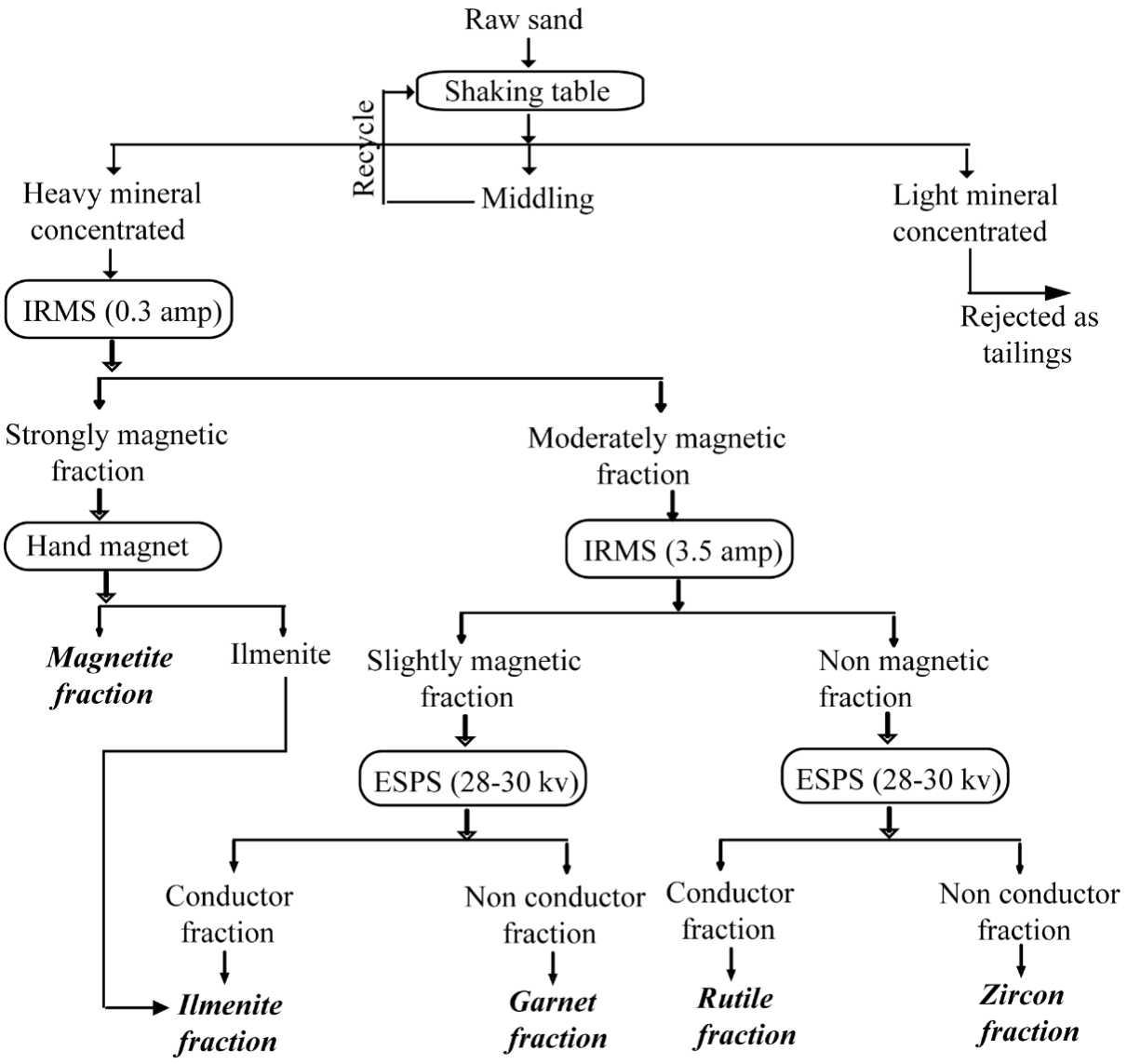

Figure 6.5 Flow chart showing the procedure of separation of 5 mineral fractions from a bulk beach sand sample (IRMS = Induced roll magnetic separator; ESPS = Electro-static plate separator).

6.3.2 Physical Separation of Heavy Mineral Fractions

The beach sand sample collected from the foredune area at Kalatoli, Cox's Bazar, Bangladesh was separated for the concentrations of zircon, garnet, ilmenite, rutile and magnetite fractions. The sample was air-dried and analyzed using a physical separation technique based on the specific gravity, magnetic, and electric properties of minerals. A generalized flow chart was followed to separate out 5 major heavy mineral fractions from the sample KTF-3 (Fig. 6.5).

Using a wet gravity separator (Welfey shaking table) the sample was fractionated into light and heavy fractions. The light fraction was predominantly quartz and was discarded. The heavy fraction was passed into an induced roll magnetic separator (IRMS) at 0.3 ampere condition to get strongly magnetic and moderately magnetic fractions. The strongly magnetic fraction was predominantly magnetite with some ilmenite. The magnetite was purified with a hand magnet. The moderately magnetic fraction was processed using IRMS at the increased magnetic field (3.5 ampere condition) to divide into slightly magnetic and non-magnetic fractions. Thereafter, both fractions were heated at about 200°C for the electric separation. The slightly magnetic fraction was mainly composed of ilmenite and garnet, and non-magnetic fraction, which was mainly composed of rutile and zircon, were processed using an electro-static plate separator (ESPS) at 28-30 KV to separate out the ilmenite fraction as a conductor mineral and the garnet fraction as a non-conductor mineral from slightly magnetic fraction, and the rutile fraction as conductor minerals and the zircon fraction as non-conductor minerals from the non-magnetic fraction.

6.3.3 Light Microscope Analysis

From each of the 5 fractions of minerals, about 300 grains were mounted on glass slides using Canada balsam. Grains on the slides were examined with a reflecting light microscopic for the identifications and quantifications of the dominant mineral as well as other minerals as impurities. The Individual mineral composition (%) in a particular fraction was determined

following the procedure of Macdonald (1972). The mineral composition of each fraction is presented in the Table 6.2.

Table 6.2 Mineral compositions of the mineral fractions acquired from the bulk beach sand sample collected at Kalatoli (KTF-3)

Mineral fraction	Mineral composition
Zircon (ZN-1)	Zircon-99 %, others- 1%.
Garnet (GN-2)	Garnet- 75 %, ilmenite- 20 %, monazite-4 %, others- 1 %.
Ilmenite (IN-3)	Ilmenite- 95 %, leucoxene- 4 %, others- 1 %.
Rutile (RT-4)	Rutile- 60 %, ilmenite- 30 %, garnet- 5 %, monazite- 2 %, others- 5%.
Magnetite (MT-5)	Magnetite- 99 %, others- 1%.

6.3.4 Gamma-Ray Spectroscopy Data Collection

Each dried sample was sealed firmly in a 108 cm^3 cylindrical capsule. The joint of the capsule was wrapped with thick tape to prevent the escape of gaseous ^{222}Rn, ^{219}Rn and ^{220}Rn progenies. Since the half-lives of ^{222}Rn, ^{219}Rn and ^{220}Rn are 3.82 days, 3.96 seconds, and 55.6 seconds, respectively, each sample was stored for at least 3.5 weeks to achieve the secular equilibrium between ^{238}U, ^{235}U, ^{232}Th and their progenies (Evans 1969). The weights of the bulk beach sand and heavy mineral samples ranged from 205.2 to 288.7 gm and from 257.6 to 326.0 gm, respectively. All samples were measured for about 24 h using two low-level gamma-ray spectroscopy systems based on the distinct gamma emission energies of the radionuclides of interest or/and the energies their short lived progeny at the Centre for Environmental Research (UFZ) in Leipzig, Germany. Table 6.3 summarizes the gamma lines used for activity measurements of the respective radionuclides. All measurements were carried out using two coaxial low-energy HPGe detectors, n-type (ORTEC) with an active volume of 39 cm^3 and a 0.5 mm Be window. The gamma-ray spectroscopy-1 (GRS-1) had 24.7 % relative efficiency and

a resolution of 1.89 (keV) at 1.33 (MeV) (^{60}Co). The gamma-ray spectroscopy-2 (GRS-2) had 26.5% relative efficiency and resolution of 1.83 (keV) at 1.33 (MeV) (^{60}Co). Detectors and measuring geometry were calibrated using the certified reference materials RGU, RGTh, and RGK provided by the IAEA.

Activity concentrations of ^{238}U, ^{235}U and ^{232}Th were detected based on the emission lines of their respective short lived progeny. For ^{238}U the gamma lines of ^{234}Th, ^{234m}Pa, ^{214}Pb, and ^{214}Bi were used, for ^{235}U the lines of ^{235}U, ^{227}Th, ^{223}Ra and ^{219}Rn, and for ^{232}Th the lines of ^{228}Ac, ^{212}Pb, ^{212}Bi and ^{208}Tl. Due to the lack of strong and distinct gamma emission lines of the actual radionuclides ^{238}U, ^{235}U and ^{232}Th the daughter radionuclides listed above are generally used to derive the respective activity concentrations, assuming secular equilibrium throughout the decay series (Malanca et al. 1998; Meijer et al. 2001; Alencar and Freitas 2005; El-Kameesy et al. 2008). For data evaluation it was kept in mind that the assumption of decay equilibrium throughout the decay series may not be justified, since geochemical processes with different mobilization effects on the individual radionuclides may have occurred in former geological times. As mentioned above, the gamma line of ^{234m}Pa (at 1001.3 keV) was used for ^{238}U determination in addition to the conventionally used gamma lines of ^{234}Th, ^{214}Pb and ^{214}Bi. That was done in order to minimize statistical uncertainties. Although the 1001.3 keV emission probability is low (0.84 %), it is suitable since it does not interfere with any other peaks, e.g. in the presence of high amount of Th (Yucel et al. 1998; Yucel et al. 2003). For the same reason, the two weak ^{235}U gamma lines at 163.4 and 205.5 keV were used in spite of their low emission probability of 0.22% additionally to the ones of the short-lived progeny. ^{40}K was detected from its distinct gamma line at 1461 keV.

Table 6.3 Gamma energies used for the activity measurements of the respective radionuclides

Parent isotope	Radionuclide	Gamma energy (keV)	Emission probability (%)
^{238}U	^{234Th}	63.3	4.1
	^{234m}Pa	1001.3	0.84
	^{214}Pb	295.2	18.15
		351.9	35.10
	^{214}Bi	609.3	44.6
		1120.3	14.7
		1238.1	5.78
		1764.5	15.1
		2204.1	4.98
^{235}U	^{235}U	163.4	5.08
		205.3	5.01
	^{227}Th	236.0	12.1
		256.3	7.0
	^{223}Ra	323.9	3.93
	^{219}Rn	401.8	6.4
^{232}Th	^{228}Ac	911.1	26.6
		968.9	16.2
	^{212}Pb	238.6	43.5
	^{212}Bi	727.2	6.7
	^{208}Tl	510.8	8.2
		583.1	30.6
		860.1	4.5
		2614.7	35.8
^{40}K	^{40}K	1460.8	

6.3.5 Gamma Spectral Data Processing and Analysis

To determine the radioactivity concentrations in samples two different analytical approaches were applied and compared; a manual approach applying the rule of proportion and an automated approach applying the efficiency calibration of the detector.

The manual approach, which applied the rule of proportion, is explained in the following relationships (Eq. 6.1 and 6.2):

$$ACS = \frac{\left[\left(\frac{PAS}{CTS}\right) - BGD\right] \times FC}{WS} \quad [6.1]$$

$$FC = \frac{1}{PAC / CTC / ACC} \quad [6.2]$$

where,

ACS = Activity concentration of samples (Bq/kg)

WS = sample weight (gm),

CTS = counting time of sample (s),

PAS = peak area of sample (counts),

FC = calibration factor (Bq/cps),

BGD = detector background (cps),

PAC = peak area of calibration standard (counts),

CTC = counting time calibration standard (s), and

ACC = activity concentration of calibration standard (Bq).

Automatic approach for spectra analysis was performed with the software GAMMA-W®. GAMMA-W is a fully automatic or manual controlled high precision gamma-ray spectrum analysis package for the quantitative evaluation of high resolution spectra taken with HPGe detectors. Gamma-W has proven vast applications involving gamma-ray spectrum analysis in neutron activation analysis, radioactive waste quantification and management, low-level environmental radioactivity measurements, etc.

6.3.6 Estimation of Radiation Hazard Indices

Radium equivalent activity (Ra_{eq}): Ra_{eq}, which was defined by Beretka and Mathew (1985), is a representation of the specific radioactivity of ^{226}Ra, ^{232}Th and ^{40}K by a single index. Ra_{eq} (Bq/kg) can be calculated by following equation:

$$Ra_{eq} = A^{226}Ra + 1.43\ A^{232}Th + 0.077\ A^{40}K, \quad [6.3]$$

where, $A^{226}Ra$, $A^{232}Th$, and $A^{40}K$ are the radioactivity concentrations of ^{226}Ra, ^{232}Th, and ^{40}K (Bq/kg), respectively.

Gamma dose rate (D): The gamma dose rates (nGy/h) in air at 1m above the ground surface, where the ^{226}Ra, ^{232}Th and ^{40}K are uniformly distributed, can be estimated by the following relationship (UNSCEAR 1988; 1993):

$$D = 0.462\ A^{226}Ra + 0.621\ A^{232}Th + 0.0417\ A^{40}K, \quad [6.4]$$

Annual effective dose (D_E): D_E (mSv/yr) can be estimated taking the indoor or outdoor occupancy factor of 0.8 or 0.2 and conversion factor 0.7 (Sv/Gy) (UNSCEAR 1988) using the following relationship (El Afifi et al. 2006):

$$D_E\ (mSv/yr) = D\ (nGy/h) \times 8760\ h/yr \times 0.7\ (Sv/Gy) \times Occupancy\ factor \quad [6.5]$$

Gamma hazard index (I_{yr}): I_{yr}, which is formulated by NEA-OECD (1979), is an estimation of the level of gamma radiation hazard associated with ^{226}Ra, ^{232}Th and ^{40}K in specific materials. The I_{yr} (Bq/kg) is given below:

$$I_{yr} = 0.0067\ A^{226}Ra + 0.01\ A^{232}Th + 0.00067\ A^{40}K, \quad [6.6]$$

External (H_{ex}) and internal (H_{in}) hazard indices: The external and internal hazard indices are defined by Beretka and Mathew (1985). The recommended value of both H_{ex} and H_{in} should be equal to or less than one. The equations to estimate H_{ex} and H_{in} are given below:

$$H_{ex} = 0.0027\ A^{226}Ra + 0.00386\ A^{232}Th + 0.00021\ A^{40}K, \quad [6.7]$$

$$H_{in} = 0.0054\ A^{226}Ra + 0.00386\ A^{232}Th + 0.00021\ A^{40}K, \quad [6.8]$$

6.4 Results and Discussion

6.4.1 Mineralogical Composition

The highest (97 wt. %) and the lowest (54 wt. %) concentrations of heavy minerals are obtained in BDF-1 and FHB-6 samples after heavy liquid separation (Table 6.1). The light mineral fractions of 6 samples were discarded because the light fraction contains pure quartz and does

not have any contribution towards radioactivity. Although the concentration of major heavy minerals (e. g., magnetite, ilmenite, garnet, rutile, zircon, monazite, and kyanite) vary, the types of mineral are similar in the 18 heavy mineral deposits along the Bangladesh coast (BAEC 1994). After separating 5 major mineral fractions from the sample KTF-3, each fraction was studied with a microscope. Both zircon and magnetite fractions are the purest and contain 99 % zircon and magnetite grains, respectively. Both garnet and rutile fractions contain small amount of monazite grains (4 and 2 %, respectively) with other minerals (Table 6.2). The microscopic images of 5 mineral fractions are given (Fig. 6.6) and indicates that each fraction contains some other minerals together with the dominant fraction.

6.4.2 Activity Concentrations

The activity concentrations of ^{238}U, ^{235}U, ^{232}Th and ^{40}K in all 5 bulk beach sand samples from the foredune and backdune areas and in the 5 separated mineral fractions from foredune sampling point KTF-3 are summarized (Table 6.4). The listed results represent the mean values of the manual and the automated approaches for gamma spectrometry data assessment, as described above. The radioactivity concentrations of ^{238}U, ^{235}U, ^{232}Th and ^{40}K in the heavy mineral-rich bulk beach sand samples from 6 locations (BDF-1, MKF-2, KTF-3, SPB-4, LBB-5, and FHB-6) Cox's Bazar coast are given (Fig. 6.7). In the foredune area the highest radioactivity concentrations of ^{238}U, ^{235}U, ^{232}Th and ^{40}K are obtained in the sample BDF-1, where the heavy mineral concentration is also very high (97%), followed by MKF-2 (HM = 88 %) and KTF-3 (HM = 91 %). Although the heavy mineral concentration in the bulk sands of Monkhali (MKF-2) is less than that of Kalatoli (KTF-3), the radioactivity concentrations of all radionuclides in sample MKF-2 are relatively high.

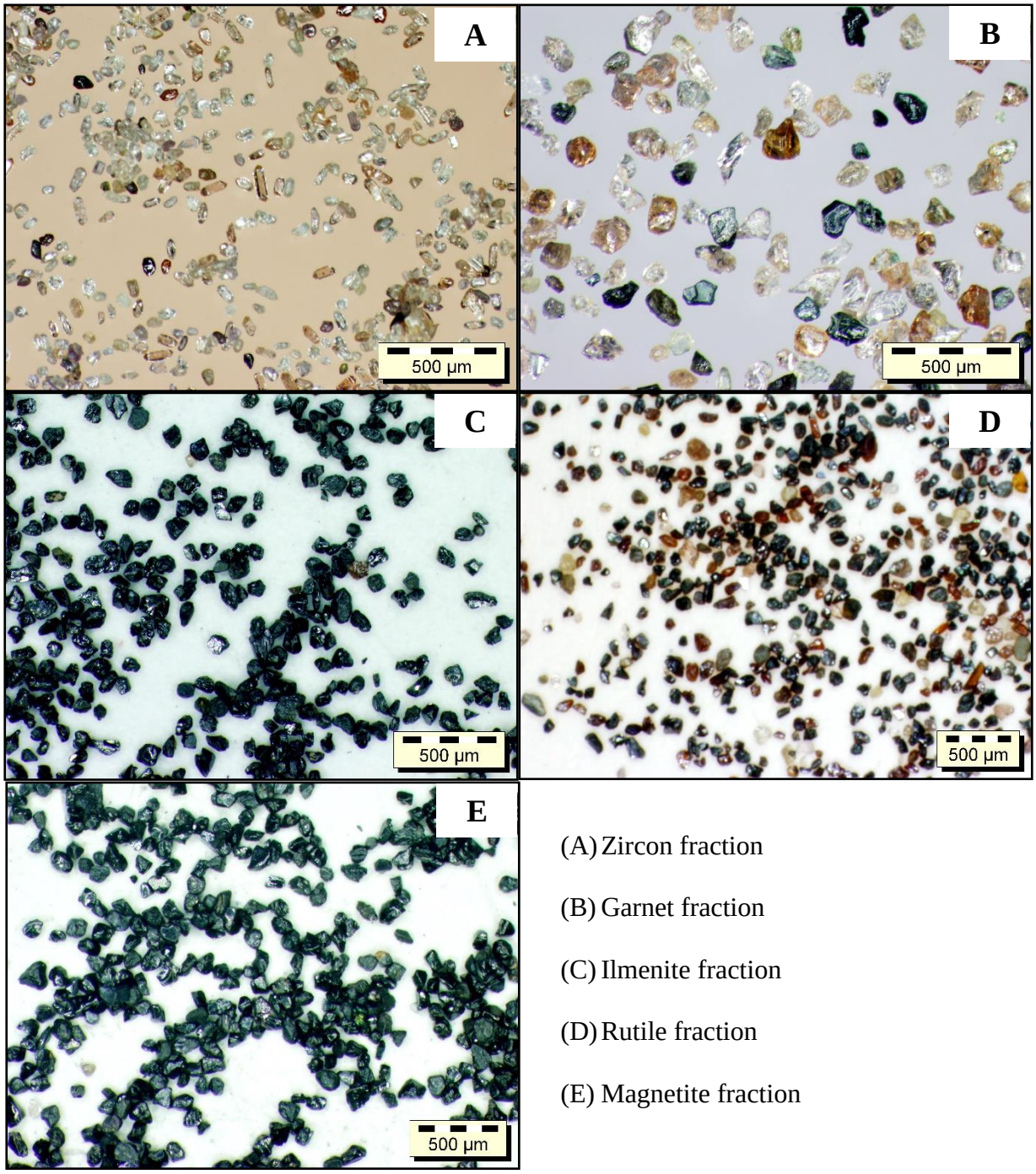

(A) Zircon fraction

(B) Garnet fraction

(C) Ilmenite fraction

(D) Rutile fraction

(E) Magnetite fraction

Figure 6.6 Microscopic images showing the dominant mineral and other minerals in each of the 5 mineral fractions separated from sample KTF-3.

In the backdune area the highest radioactivity concentrations of ^{238}U, ^{235}U, ^{232}Th and ^{40}K are obtained in sample taken at Lomburi (HM = 60 %) followed by samples taken at Shaplapur (HM = 70 %) and Fakirahata (HM = 54 %). Compared to the foredune samples, the radioactivity concentrations of all radionuclides are relatively low. The Fakirahata sample, which shows the lowest heavy mineral content of the three, reveals the lowest radioactivity concentration. Although a general positive correlation between bulk heavy mineral content and bulk radioactivity becomes obvious, the correlation cannot be quantified reasonably. The observed discrepancies are probably due to the varying concentrations of the respective mineral fractions that contain elevated radionuclide concentrations in the bulk sands. However, a very good correlation (R^2 = 0.99) is found between ^{238}U and ^{232}Th concentrations in the 6 bulk sand samples (Fig. 6.8). This correlation indicates that there is a consistency in the presence of the habitually U and Th bearing minerals zircon ($ZrSiO_4$) and minor amount of monazite [$(Ce,La,Nd,Th)PO_4$] in the beach sands, as reported in other studies (Mohanty et al. 2003; Mohanty et al. 2004a; Ramasamy et al. 2004).

The highest radioactivity concentrations in the 5 examined mineral fractions are found in zircon fraction (Fig. 6.9a). Garnet and rutile show significantly less activity, with garnet showing a considerably higher activity than rutile. The radioactivity concentrations in ilmenite and magnetite are insignificant.

The zircon fraction analysed in this study is composed of 99% zircon crystals as confirmed by a binocular microscopic observation (*cf.* Table 6.2). The radioactivity concentrations of ^{238}U and ^{232}Th in the zircon fraction found in this study are higher than the concentrations found in the study conducted by Alam et al. (1999b), who analysed zircons from comparable materials. The radioactivity values are also higher than concentrations reported in other studies on zircon sands collected worldwide (Mohanty et al. 2003; Mohanty et al. 2004b; Righi et al. 2005) (Table 6.5).

Table 6.4 Radioactivity concentrations of ^{238}U, ^{235}U, ^{232}Th and ^{40}K in bulk beach sand samples from the foredune and backdune areas and in separated mineral fractions

Sample ID	^{238}U	^{235}U	^{232}Th	^{40}K
Foredune area				
BDF-1	4245 ± 238	145 ± 18	5537 ± 202	372 ± 10
MKF-2	2217 ± 186	87 ± 14	3217 ± 117	242 ± 10
KTF-3	1651 ± 133	65 ± 13	2625 ± 96	162 ± 8
Backdune area				
LBB-4	1082 ± 105	43 ± 12	1822 ± 67	126 ± 6
SPB-5	1025 ± 88	39 ± 10	1440 ± 58	89 ± 6
FHB-6	754 ± 85	30 ± 8	996 ± 42	110 ± 34
Mineral fractions				
ZC-1	14849 ± 751	124 ± 16	10405 ± 364	806 ± 35
GN-2	3236 ± 233	12 ± 3	7258 ± 261	479 ± 7
IN-4	419 ± 55	63 ± 11	529 ± 24	12 ± 2
RT-3	1676 ± 146	3 ± 1	2011 ± 125	126 ± 10
MT-5	61 ± 13	-	85 ± 5	10 ± 2

Figure 6.9 illustrates the element concentrations of U and Th in the 5 mineral fractions applying the conversion factors 1 mg/kg U = 12.25 Bq/kg ^{238}U and 1 mg/kg Th = 4.07 Bq/kg ^{232}Th (Hendriks et al. 2001). U and Th concentrations in the zircon fraction are of 1212 mg/kg and 2557 mg/kg, respectively (Fig. 6.9b). Commercially zircon is not mined solely for U and Th content. But if the concentrations of U and Th in zircon are above 250 - 350 mg/kg and 100 - 200 mg/kg, respectively, they could be significant by-product in the course of manufacturing zirconia from zircon (Selby 2007). The presence of U and Th in the analysed garnet and rutile fractions may be associated with the minor amount of monazite in the separated fractions (see Table 6.2).

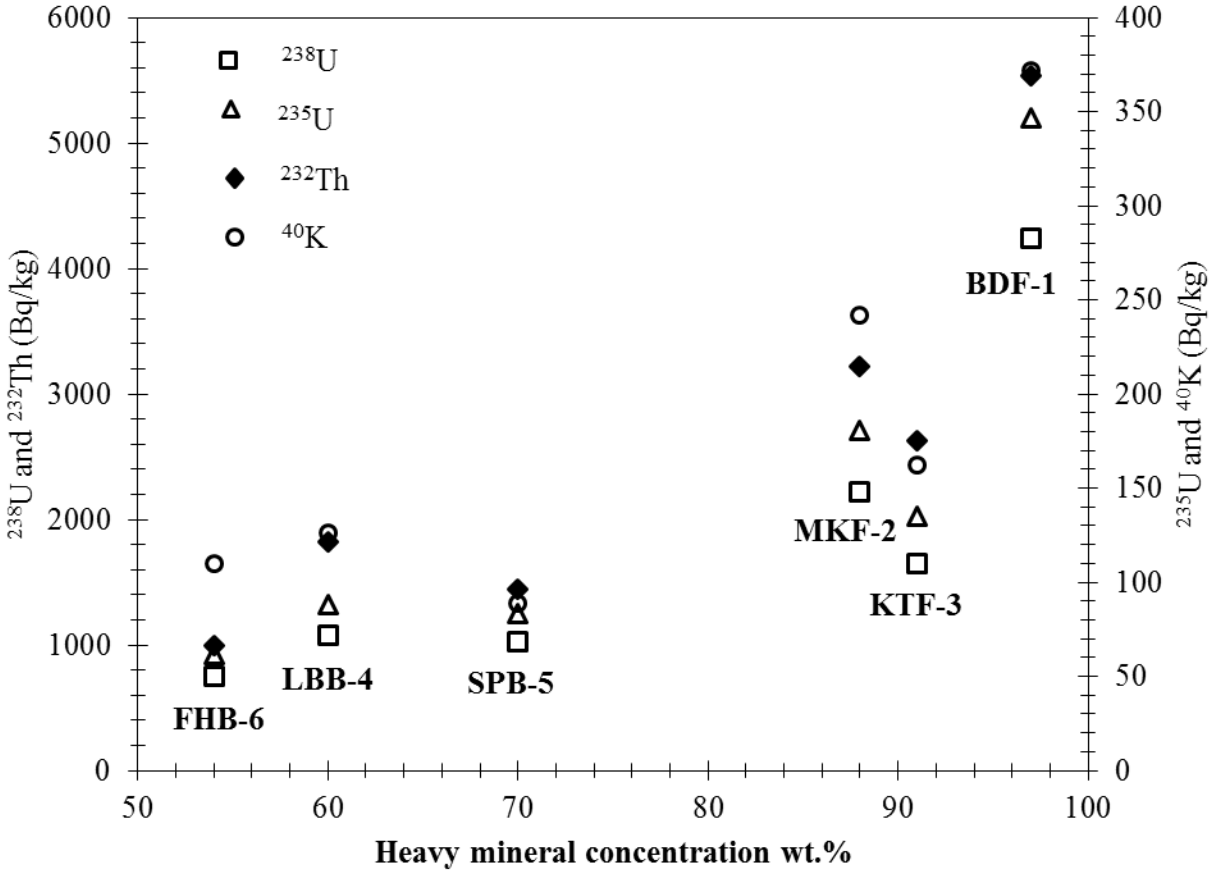

Figure 6.7 Activity concentrations of ^{238}U, ^{235}U, ^{232}Th and ^{40}K with respect to the heavy mineral concentration in the bulk sands collected in the foredune (BDF-1, MKF-2 and KTF-3) and backdune (LBB-4, SPB-5 and FHB-6) areas of Cox's Bazar district, Bangladesh.

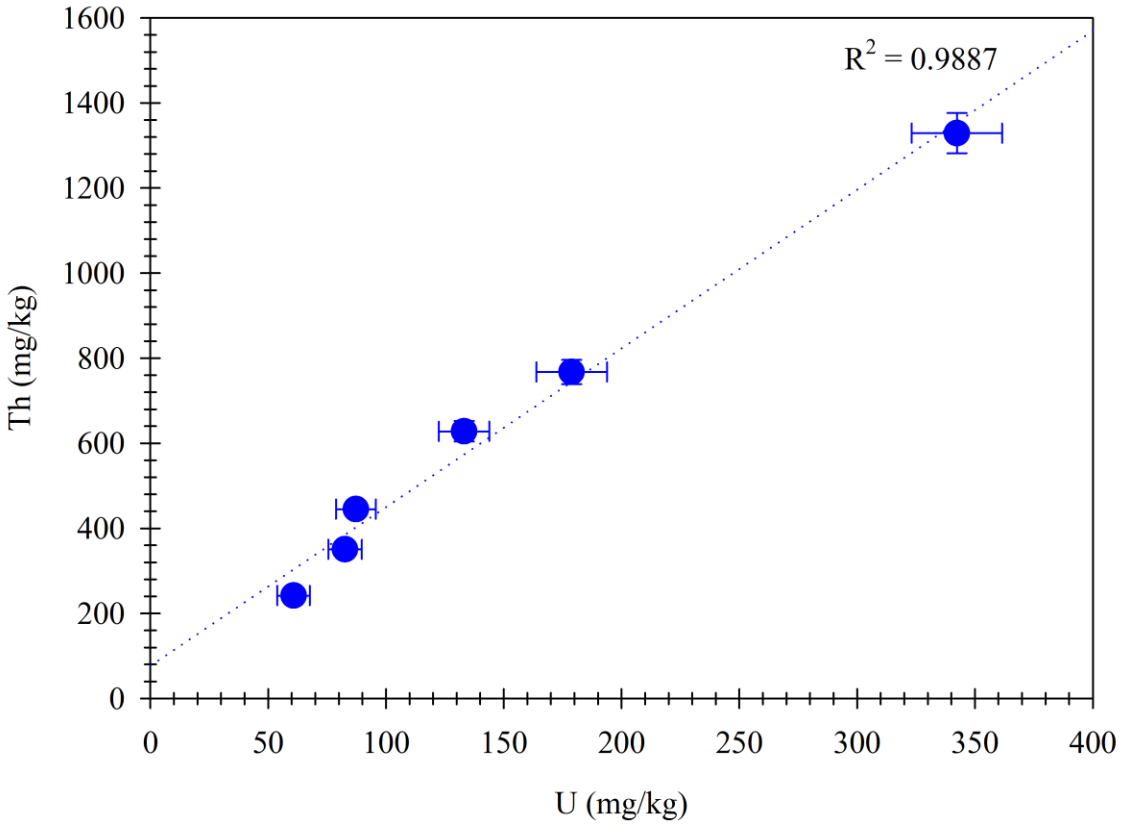

Figure 6.8 Correlation between U and Th concentrations in beach bulk sand samples collected from both foredune and backdune areas.

6.4.3 Potential Radiation Hazard Related to the Bulk Beach Sands

The potential radiation hazard as revealed by the bulk sand materials and separated mineral fractions was estimated and quantified by applying the parameters R_{eq} (Bq/kg), D (nGy/h), I_{yr} (Bq/kg), H_{ex} (Bq/kg) and H_{in} (Bq/kg) as defined by Equations 6.3, 6.6, 6.7 and 6.8. The results are summarized in Table 6.6.

The Ra_{eq} radioactivity in the bulk beach sands of the sampled foredune and backdune locations were found to be 33, 18 and 15 times, and 10, 8 and 6 times, respectively, higher than the related world standard value, which amounts to 370 Bq/kg (IAEA 1996). The gamma hazard

index, I_{yr}, which should be less than or equal to 1 Bq/kg (Alam et al. 1999b) also shows considerably higher values in both, fordune and backdune areas. The external and internal hazard indices (H_{ex} and H_{in}) in the foredune and backdune beach sands should be less than one (Orgun et al. 2007; Murugesan et al. 2011). By evaluating the values found for Ra_{eq}, I_{yr}, H_{ex} and H_{in} it becomes obvious that the bulk beach sands from both foredune and backdune areas should not be used for any kind of construction purposes without previous assessment and, if necessary, processing. The elevated radioactivity levels correlate with high amounts of heavy minerals present in the sand.

Table 6.5 Radioactivity concentrations of ^{238}U and ^{232}Th in zircon sand obtained in this study and some selective locations in the world

Description/Locations	^{238}U (Bq/kg)	^{232}Th (Bq/kg)	Sources
Processed zircon, Kalatoli, Cox' Bazar, Bangladesh	14849 ± 751	10405 ± 364	This study
Processed zircon sand, Cox's Bazar, Bangladesh	6438 ± 326	1324 ± 96	Alam et al. (1999b)
Zircon sand, Chhatrapur, Orissa, India	3450 ± 150	1850 ± 180	Mohanty et al. (2004)
Zircon sand, Erasama, Orissa, India	3500 ± 100	1750 ± 100	Mohanty et al. (2003)
Australian zircon sand	2400 ± 200	520 ± 40	Righi et al. (2005)
Australian zircon sand	2200 ± 200	480 ± 40	Righi et al. (2005)
South African zircon sand	3200 ± 300	520 ± 40	Righi et al. (2005)
South African zircon sand	2900 ± 200	450 ± 40	Righi et al. (2005)
Ukrainian zircon sand	1830 ± 150	370 ± 30	Righi et al. (2005)
Ukrainian zircon sand	1860 ± 160	380 ± 30	Righi et al. (2005)

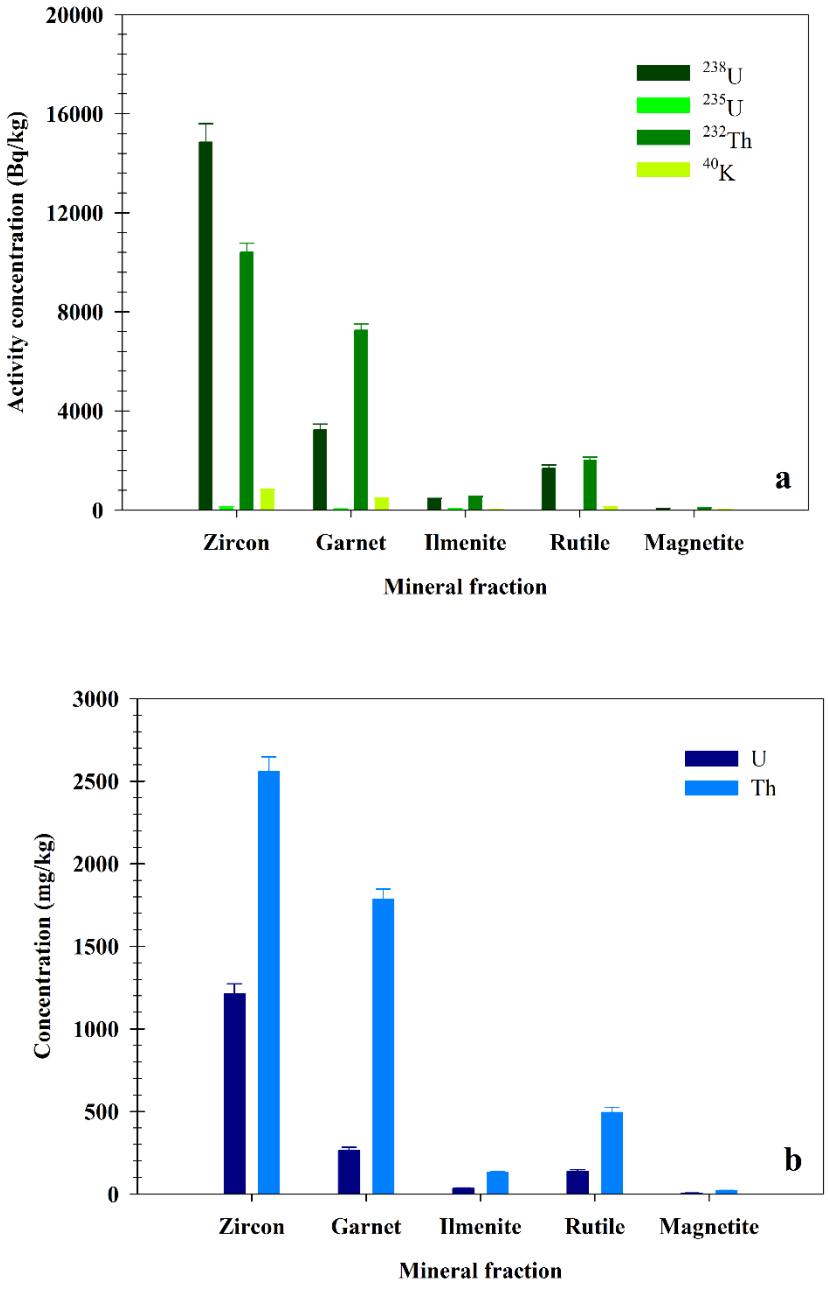

Figure 6.9 (**a**) activity concentrations and (**b**) U and Th concentrations in the 5 mineral fractions separated from the bulk beach sand collected at Kalatoli (KTF-3).

Table 6.6 Equivalent radium concentration (R_{eq}), gamma radiation dose (D), and radiation hazard indices I_{yr}, H_{ex} and H_{in} in bulk beach sands of both foredune and backdune areas and in separated heavy mineral fractions

Sample no.	R_{eq} (Bq/kg)	D (nGy/h)	I_{yr} (Bq/kg)	H_{ex} (Bq/kg)	H_{in} (Bq/kg)
Foredune area					
BDF-1	12192 ± 528	5415 ± 236	84 ± 4	32.91 ± 1.42	44.37 ± 2.07
MKF-2	6836 ± 354	3032 ± 159	47 ± 2	18.45 ± 0.96	24.44 ± 1.46
KTF-3	5417 ± 271	2400 ± 121	37 ± 2	14.62 ± 0.73	19.08 ± 1.09
Backdune area					
LBB-4	3697 ± 201	1637 ± 90	26 ± 1	9.98 ± 0.54	12.90 ± 0.83
SPB-5	3091 ± 171	1372 ± 77	21 ± 1	8.34 ± 0.46	11.11 ± 0.70
FHB-6	2187 ± 148	971 ± 67	15 ± 1	5.90 ± 0.40	7.94 ± 0.63
Heavy mineral fractions					
Zircon	29790 ± 959	13355 ± 574	204 ± 9	80.42 ± 3.44	120.52 ± 5.47
Garnet	13652 ± 475	6022 ± 270	95 ± 4	36.85 ± 1.64	45.59 ± 2.27
Ilmenite	1176 ± 56	523 ± 40	8 ± 1	3.18 ± 0.24	4.31 ± 0.39
Rutile	4561 ± 216	2028 ± 145	31 ± 2	12.31 ± 0.88	16.84 ± 1.27
Magnetite	183 ± 13	81 ± 9	1 ± 0	0.49 ± 0.05	0.66 ± 0.09

The gamma doses (D) related to the bulk beach sands (using Equation 6.4) are also given in Table 6.6. The world average level of D is 55 nGy/h (El Afifi et al. 2006). In the sampled foredune and backdune locations D was found to be 98, 55 and 44 times and 30, 25 and 18 times as high, respectively. Assuming an outdoor occupancy factor of 0.2, the outdoor annual effective doses (D_E) at the foredune and backdune areas can be estimated using Equation 6.5. According to IAEA (1996), the outdoor annual effective dose for public should be below 1 mSv/a above background. In the sampled foredune and backdune areas, however, the outdoor annual effective doses were found to be significantly higher (Fig. 6.10).

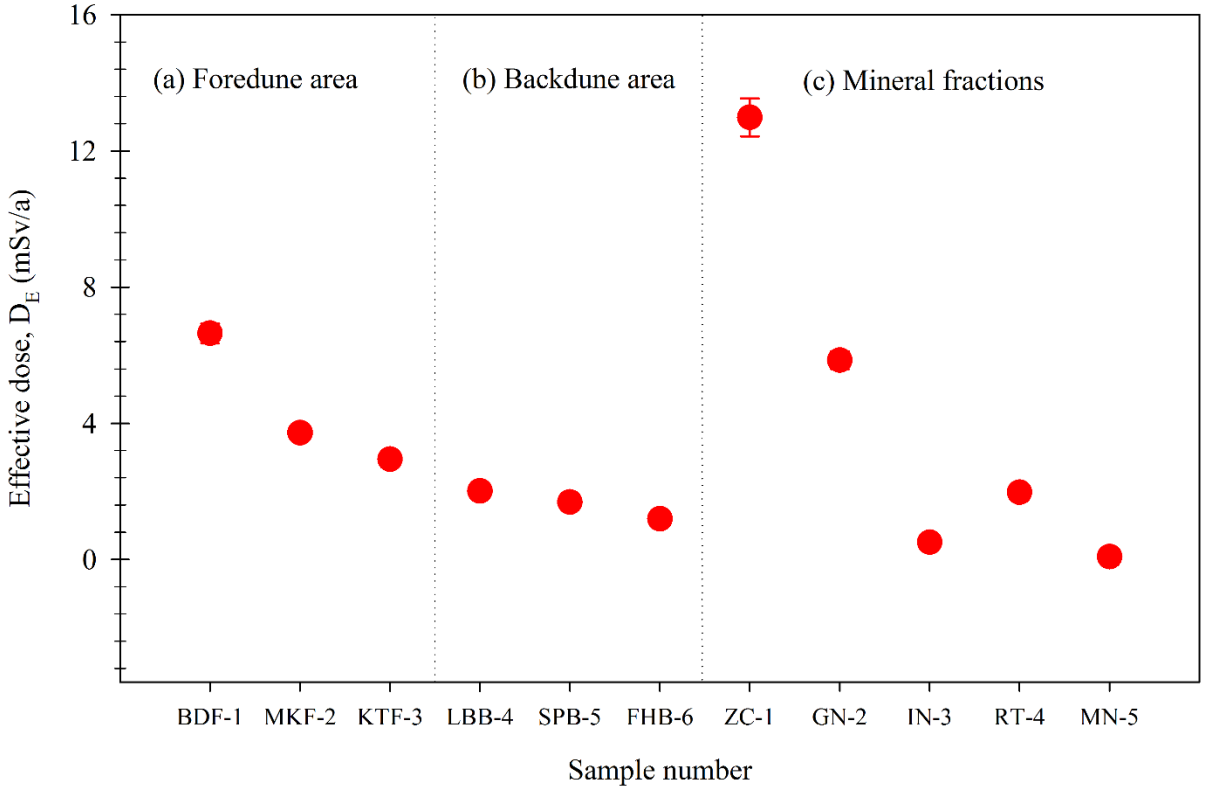

Figure 6.10 Annual effective doses in the heavy mineral-rich (HM >54 wt. %) bulk beach sands collected at 6 different locations of the (**a**) foredune and (**b**) backdune areas and in separated (**c**) mineral fractions.

Comparison of the doses detected in the foredune and backdune areas reveals that the heavy mineral-rich foredune locations are more hazardous for general public use than the backdune area. The foredune area is free of human settlements and mainly used by fishermen. However, the backdune area where dwellings are present (in some places, on top of the heavy minerals deposits) has to be considered generally unsuitable for human settlement from the radio-ecological point of view. The outdoor occupancy factor for estimating D_E in the backdune area was assumed to be 0.2. However, since people are actually living in some of the places

where the heavy mineral concentration is comparatively high and spend more than 20 % of their time there, these estimates are rather underestimating the actual human exposure.

6.4.4 Potential Radiation Hazard Related to the Separated Mineral Fractions

The Ra_{eq}, I_{yr}, H_{ex}, and H_{in} values for the zircon, garnet, ilmenite, rutile and magnetite fractions are summarized in Table 6.6. The Ra_{eq} values for zircon, garnet, ilmenite and rutile fractions are 81, 37, 3 and 12 times higher than the world standard value (370 Bq/kg), respectively but the Ra_{eq} value found for magnetite is below world standard value. The I_{yr} values for zircon, garnet, ilmenite and rutile fractions are found to be significantly higher than 1 Bq/kg, the value for magnetite equals 1. Similarly the H_{ex} and H_{in} values for zircon, garnet, ilmenite and rutile fractions are higher than one and again magnetite is an exception. From these results it becomes evident that the zircon, garnet, ilmenite and rutile fractions have to be considered radio-ecologically hazardous and unsafe for any kind of industrial use. In this regard it has to be kept in mind that the technical staffs that is involved in the mineral processing in the BSMEC pilot plant is exposed to the radiation being emitted from bulk sand and separated mineral fractions. The absorbed gamma doses 1 m above the processed zircon, garnet, ilmenite, rutile and magnetite fractions that are stored in open drums in the mineral processing pilot plant are 243, 109, 10, 37 and 1 times higher than the recommended value, respectively. Considering an indoor occupancy factor at the processing pilot plant of 0.8 and the reported yearly working hours (1736 hours), the D_E related to the stored zircon, garnet, ilmenite, rutile and magnetite fractions are 12.98 ± 0.56, 5.85 ± 0.26, 0.51 ± 0.04, 1.97 ± 0.14 and 0.08 ± 0.01 mSv/a, respectively (Fig. 6.10). The average annual effective dose per year for workers over 5 consecutive years is recommended to be less than 20 mSv/a (IAEA 1996). Therefore, the workers and technical staff at the processing pilot plant are nearly receiving the maximum annual effective dose from the mineral fractions during their work in the mineral processing pilot plant.

6.5 Conclusions

This study indicates that several locations of the recent and paleo-beach areas of Cox's Bazar coast, where the bulk beach sands contain high concentrations of heavy minerals (>54 wt. %), have high concentration of U, Th and K, resulting in the exposure of elevated radioactivity to the coastal environment and the people living in those specific locations. The zircon fraction contains 1212 mg/kg U and 2557 mg/kg Th. Since the garnet and rutile fractions contain monazite, they result 264 and 137 mg/kg U, and 1783 and 494 mg/kg Th, respectively. Considering the economic importance of these metallic minerals if any attempt is taken to mine and process those minerals, U and Th may become significant and strategic by-products.

Chapter 7: Summary of Major Findings and Recommendations

7.1 Summary

The objectives of this thesis are to investigate the crystal-chemical properties and internal radiation damaged effects in the zircon and monazite structures, and to determine the radionuclide concentrations in zircon and monazite-rich heavy minerals and their radiological consequence in the coastal ecosystem at Cox's Bazar, Bangladesh. Several experimental techniques such as electron-probe micro-analysis (EPMA) - WDS, EDS, and BSE, single-crystal X-ray diffraction (SXRD), synchrotron high-resolution powder X-ray diffraction (HRPXRD), gamma-ray spectrometry with hyper purity germanium detector (GRS-HPGe), and several mineral separators (e.g., welfey shaking table, induced roll magnetic separator, electro-static plate separator, and Frantz isodynamic magnetic separator) were used for this study. The key motives of selecting zircon and monazite for this study are: (1) both minerals contain actinides but structurally amorphous monazite due to internal radiation damage is not found; (2) they have a wide range of applications in geochronology; (3) zircon and monazite structures could be suitable for radioactive waste forms; (4) they have major industrial uses because zircon is a source of zirconium metal, and monazite is a source of rare earth elements, phosphorous, and thorium (a future green energy source); and (5) natural occurrence of zircon and monazite may release radionuclides in the geo-environment.

The crystal structure of gem quality "pure" zircon was first refined by Robinson et al. (1971). Their refined structural parameters have been widely referred in the literature and books as a "non-metamict" zircon. However, this study finds that the structural properties for zircon can be small. A detrital zircon crystal from the Perry Island Formation (sample 7:PIF) in the Canadian Arctic Islands has the smallest unit-cell parameters [a = 6.5790(6) and c = 5.9600(7) Å] and bond distances [<Zr-O> = 2.190(1) and Si-O = 1.618(1) Å]. This zircon (sample 7:PIF) received a minor amount of α-radiation doses (4.42×10^{14} α-decay events/mg) over a relatively

short age (365 Ma) and has an ideal stoichiometric composition (Zr = 1.0 and Si = 0.99 *apfu*). Therefore, sample 7:PIF is a structurally pure zircon.

The *a* and *c* parameters increase with increasing α-radiation doses in zircon (Murakami et al. 1992; Holland and Gottfried 1955). In this study smilar effects are observed but if zircon receives significantly low amount of α-radiation doses (<3.5 × 10^{15} α-decay events/mg), the concentrations of Zr and Si control the variations of unit-cell parameters. A detrital zircon (sample 5:BIF) from Beverly Inlet Formation in the Canadian Arctic Islands has relatively large unit-cell parameters [*a* = 6.6120(7) and *c* = 5.9970(5) Å] and bond distances [<Zr-O> = 2.203(2) and Si-O> 1.626(2) Å]. This zircon (sample 5:BIF) also receives a minor amount of α-radiation doses (1.48 × 10^{15} α-decay events/mg) and shows a stoichimetric imbalanced between Zr and Si sites cations. Therefore, substitutions play the key role for the increase of structural parameters in sample 5.

Synchrotron HRXRD study of zircon samples 2a and 8 exhibit the degree of their crystallinity. Sample 2a is a fully crystalline zircon showing narrow, sharp, and high intensity peaks in the diffraction pattern but sample 8 is a partially crystalline zircon and gives broad and low intensity peaks and very high background counts. EPMA chemical data for sample 8 indicates that the Zr and Si atoms are stoichiometrically balanced indicating its chemical stability is preserved, although HRPXRD data detected a significant amount of amorphous domain. This result signifies the zircon structure as a nuclear waste form.

The accumulation of internal α-radiation doses increases with increasing age of zircon. A positive correlation exists between the age and *V* for zircon. However, further study is needed to elucidate a clear relation.

Crystal structure of a gem quality Th-free monazite [$(Ce_{0.51}La_{0.29}Nd_{0.14}Pr_{0.05}Sm_{0.01})_{\Sigma 1.00}(PO_4)$] was characterized by Ni et al. (1995). However, Th-free monazite is rare in nature. Several studies determined only the unit-cell parameters for Th-bearing monazite-Ce and monazite-Sm (Masau et al. 2002; Seydoaux-guillaume et al. 2002; Seydoaux-guillaume et al. 2004). This study investigates the crystal structure and chemistry of two detrital and two

pegmatitic monazite samples with EPMA and SCXRD. Two pegmatitic monazites are further investigated to elucidate effects of α-radiations with synchrotron HRPXRD.

The unit-cell parameters for a detrital monazite ($Ce_{0.40}La_{0.20}Nd_{0.17}Ca_{0.08}Th_{0.06}Pr_{0.04}Sm_{0.02}Gd_{0.01}Y_{0.01})_{\Sigma 0.99}(P_{0.96}S_{0.03}Si_{0.02})_{\Sigma 1.01}O_4$ from Cox's Bazar, Bangladesh are a = 6.7640(5), b = 6.9850(4), c = 6.4500(3) Å, β = 103.584(2)°, and V = 296.22(3) Å^3. The a and b unit-cell parameters of monazite vary linearly with V, but the c unit-cell parameter does not vary with the V. The polyhedral arrangement along the [001] direction in monazite is the O-O edge sharing between Ce polyhedra and P tetrahedra, and the P tetrahedra are stacked along this direction, resulting in limited variation of the c parameter. The change of the a parameter is very pronounced and it is related to the type of cations occupying the Ce/Sm site in the monazite structure. The average <Ce-O> distances for monazites obtained with SCXRD vary with good linearity with V but average <P-O> distances do not show any correlation, which explains the rigid body behavior of the PO_4 tetrahedron. The increase or decrease of average <Ce/Sm-O> distances are controlled by the substitutions between Ln^{3+} and other cations (e.g., Y^{3+}, Ca^{2+}, Th^{4+}, and U^{4+}) in the monazite structure.

Synchrotron HRPXRD data shows three different phases in a pegmatitic monazite sample 2a: monazite-Ce (phase 2a), monazite-Ce (phase 2b), xenotime-Y (phase 2c). The fractions of phase 2a, 2b, and 2c are 32.20(3), 62.93(2), and 4.87(1) wt. %, respectively. Seydoux-Guillaume (2002) reported the existence of two phases in monazite but they were not fully evaluated structurally. Phase 2a in sample 2a shows large average <P-O> distances and is related to the effect of radiation-induced changes. The P-O distance for phase 2c (xenotime) is also anomalously large. The redistribution of La, Ce, Pr, Nd, Sm, Gd, Dy, Si, and Y atoms in sample 2a indicates late recrystallization. The main driving thermal energy for the phase changes came from the α-radiation events during the long geological time.

Sample 4a contains a single phase of monazite-Sm. The V is 0.31 % smaller than that for monazite-Sm obtained with PXRD by Masau et al. (2002). The a, b, c, and β parameters for sample 4a are 6.73162(6), 6.9412(1), 6.4467(1) Å, and 103.8988(6)°, respectively. Some

HRPXRD peaks are not consistent in terms of their FWHM values. This occurred because of the presence of micro-strain in sample 4a. Because of this strain, SCXRD data shows relatively low-resolution and gives very high mosaicity and R_{int}. The source of micro-strain could be the remnant of radiation damage and accumulation. As this monazite-Sm received extremely high α-radiation doses, the damage overcame the recovery. This results in remnant radiation damage in sample 4a.

The study area for the assessment of the radiological effect on the coastal environment for the presence of U and Th in zircon and monazite-rich heavy minerals in bulk placer sands is in Cox's Bazar, Bangladesh. There are at least 18 locations along the coastal belt of Bangladesh in which heavy minerals are very high in concentrations (>20 %). Samples from 6 locations show elevated activity concentrations of ^{238}U, ^{235}U, ^{232}Th, and ^{40}K. The highest activity concentrations were obtained in the fordune area and are $^{238}U = 4245 \pm 238$, $^{235}U = 145 \pm 18$, $^{232}Th = 5537 \pm 202$, and $^{40}K = 372 \pm 10$ Bq/kg. Of the separated 5 mineral fractions, zircon contains the highest activity concentrations of ^{238}U, ^{235}U, ^{232}Th, and ^{40}K and are 14849 ± 751, 124 ± 16, 10405 ± 364, and 806 ± 35 Bq/kg, respectively.

The absorbed gamma dose rate (D) for the 6 samples are 98, 55 and 44 times and 30, 25 and 18 times higher than the world average level (55 nGy/h) (El Afifi et al. 2006). The outdoor annual effective doses (D_E) are found to be 6.64 ± 0.29, 3.72 ± 0.20 and 2.94 ± 0.15 mSv/yr in the foredune area and 2.01 ± 0.11, 1.68 ± 0.09, and 1.19 ± 0.08 mSv/yr in the backdune area. The D_E for the public should be below 1 mSv/yr (IAEA 1996). So the foredune area is riskier than the backdune area for the general public. The foredune area is free from human settlements. People hardly move around the heavy mineral deposit areas. This area is mainly used by the fishermen temporarily. However, backdune area is most vulnerable to radiological exposure where the people built their houses.

The D for 5 mineral fractions are 243, 109, 10, 37, and 1 times higher than the recommended value, and the D_E are 12.98 ± 0.56, 5.85 ± 0.26, 0.51 ± 0.04, 1.97 ± 0.14, and 0.08 ± 0.01 mSv/yr, respectively. The D_E per year for workers over 5 consecutive years is

recommended to be 20 mSv/yr (IAEA 1996). Therefore, the workers and technical staffs are not receiving the anomalous D_E from the mineral fractions during the mineral processing activities in the pilot plant.

If the beach placer sands are mined for construction purposes or industrial use, their activity concentrations have to be considered from a radio-ecological point of view. If mining and processing of the placer minerals are being considered, U and Th may become strategically significant by-products.

7.2 Recommendations

- Crystal-chemical properties of detrital zircon from the Perry Island Formation, Canadian Arctic Islands can be the best choice for citing the crystal structure of "pure" zircon.
- The P-O distance is very strongly covalent bond but this study shows the P-O distance in monazite structure can be significantly increased by the effects of internal α-radiation. Therefore, the average <P-O> distance can be an indicator for the degree of radiation effects in the monazite structure.
- Monazite shows a wide range of chemical variability and a phase transition because of the internal α-radiation effects but shows crystallinity. These characteristics warrant their potential use as a nuclear waste form for high-level radioactive waste management.
- Zircon and monazite are usually very stable against the active natural processes. The internal radiation doses for U and Th can damage the crystal structure and reduce the stability of mineral structure. Eventually, radionuclides can be exposed to the terrestrial environment. Thus, radiation damaged zircon and monazite could be a potential source for radioactivity release in the environment. Radionuclides can be mobilized by erosion processes, re-suspension, groundwater discharge, etc. The concentrations of ^{210}Po and ^{210}Pb in the marine environment are well-reported in literature but their potential routes are not clearly understood. The fate and mobility of ^{210}Po and ^{210}Pb are very crucial

because they can be uptake by marine organisms. The ratio of ^{210}Po and ^{210}Pb in marine organisms vary significantly from 10 to 1000 but the reason of this extreme variation remains unclear.

References

Alam, M.S., Huq, N.E. and Rashidm, M.S. (1999a) Morphology and sediments of the Cox's Bazar coastal plain, south-east Bangladesh. Journal of coastal Research, 15, 902-908.

Alam, M.N., Chowdhury, M.I., Kamal, M., Ghose, S., Islam, M.N., Mustafa, M.N., Miah, M.M.H. and Ansary, M.M. (1999b) The ^{226}Ra, ^{232}Th and ^{40}K activities in beach sand minerals and beach soils of Cox's Bazar, Bangladesh. Journal of Environmental Radioactivity, 46, 243-250.

Alam, M.N., Chowdhury, M.I., Kamal, M., Ghose, S., Mahmood, N., Matin, A.K.M.A., and Saikat, S.Q. (1997) Radioactivity in sediment of the Karnaphuli estuary and the Bay of Bengal. Health Physics, 73(2), 285-387.

Alencar, A.S. and Freitas, A.C. (2005) Reference levels of natural radioactivity for the beach sands in a Brazilian southeastern coastal region. Radiation Measurements, 40, 76-83.

Ali, M.A. (2012) Mineral chemistry of monazite-Nd, xenotime-Y, apatite, fluorite and zircon hosting in lamprophyre dyke in Abu Rusheid area, South Eastern Desert, Egypt. Geologija, 55, 93-106.

Alipour-Asll, M., Mirnejad, H., and Milodowski, A.E. (2012) Occurrence and paragenesis of diagenetic monazite in the upper Triassic black shales of the Marvast region, South Yazd, Iran. Mineralogy and Petrology, 104, 197-210.

Anfinson, O.A., Leier, A.L., Embry, A.F., and Dewing, K. (2012) Detrital zircon geochronology and provenance of the Neoproterozoic to Late Devonian Franklinian Basin, Canadian Arctic Islands. Geological Society of America Bulletin, 124, 415-430.

Antao, S.M., Hassan, I., Wang, J., Lee, P.L., and Toby, B.H. (2008) State-of-the-art high-resolution powder X-ray diffraction (HRPXRD) illustrated with Rietveld structure refinement of quartz, sodalite, tremolite, and meionite. The Canadian Mineralogist, 46, 1501-1509.

Balan, E., Neuville, D.R., Trocellier, P., Fritsch, E., Muller, J.P., and Calas, G. (2001) Metamictization and chemical durability of detrital zircon. American Mineralogist, 86, 1025-1033.

Baretka, J. and Mathew, P.Y. (1985) Natural radioactivity of Australian building materials, industrial wastes and by-products. Health Physics, 48(1), 87-95.

Beall, G.W., Boatner, L.A., Mullica, D.F., and Milligan, W.O. (1981) The structure of cerium ortho-phosphate, a synthetic analog of monazite. Journal of Inorganic and Nuclear Chemistry, 43, 101-105.

Beaman, D.R. and Isasi, J.A. (1972) Electron beam microanalysis. American Society for testing and Materials, Philadelphia.

Biswas, M.A.B. and Kunda, S.K. (1985) Mode of occurrence and origin of heavy mineral deposits of Nijhum Dwip, Hatia. Nuclear Science and Applications, B16,17, 69-75.

Biswas, M.A.B. (1983) Heavy mineral variability in foreshore sediments of Teknaf-Inani beach of Chittagong. Nuclear Science and Applications, B14,15, 88-95.

Biswas, M.A.B. (1982) Size characteristics of Bengal Beach and dune sands from southeastern Bangladesh. Bangladesh Journal of Geology, 1, 9-21.

Biswas, M.A.B. (1981) Mechanism of heavy mineral concentration in the beach sands of Cox's Bazar. Nuclear Science and Applications, B12,13, 74-83.

Biswas, M.A.B. (1979) Lithological criteria of localization of titano-zirconium placers in the inshore sediments of Teknaf coast. Bangladesh Journal of Science Research, B2, 41-51.

Black, L.P., Fitzgerald, J.D., and Harley, S.L. (1984) Pb isotopic composition, colour, and microstructure of monazites from a polymetamorphic rock in Antarctica. Contributions to Mineralogy and Petrology, 85, 141–148.

Boatner, L.A. and Sales, B.C. (1988) Monazite. In W. Lutze and R.C. Ewing, Eds., Radioactive Waste Forms for the Future, p. 495-564. Elsevier, Amsterdam.

Boatner, L.A. (2002) Synthesis, structure and properties of monazite, pretulite and xenotime. In M.L. Kohn, J. Rakovan, and J.M. Hughes, Eds., Phosphates, 48, p. 87-120. Reviews in Mineralogy and Geochemistry, Mineralogical Society of America, Chantilly, Virginia.

Brese, N.E. and O'Keeffe, M. (1991) Bond-valence parameters for solids. Acta Crystallographica, B47, 192-197.

Broska, I., Petrík, I., and Williams, C.T. (2000) Coexisting monazite and allanite in peraluminous granitoids of the Tribeč Mountains, western Carpathians. American Mineralogist 85, 22-32.

Brown, I.D. and Altermatt, D. (1985) Bond-valence parameters obtained from a systematic analysis of the inorganic crystal structure database. Acta Crystallographica, B41, 244-247.

Brown, I.D. (2006) Accumulated table of bond valence parameters. http://www.ccp14.ac.uk/ccp/web-mirrors/i_d_brown.

BSEC (1994) Brochure: Beach sand exploitation centre, Cox's Bazar. Scientific Information Division, Bangladesh Atomic Energy Commission, 1-21.

Burcham, W.E. (1973) Nuclear physics: An introduction (2nd edition), Harlow, Longman.

Bursill, L.A. and McLaren, A.C. (1966) Transmission electron microscope study of natural radiation damage in zircon ($ZrSiO_4$). Physica Status Solidi, 15, 331-343.

Chakoumakos, B.C., Murakami, T., Lumpkin, G.R., and Ewing, R.C. (1987) Alpha-decay induced fracturing in zircon: The transition from the crystalline to the metamict state. Science, 236, 1556-1559.

Chowdhury, M.I., Molla, M.A.R., Mannan, M.A., and Hossain, A. (1987) Detailed survey of radiation levels in monazite bearing area of Cox's Bazar beach and surrounding areas. Nuclear Safety and Radiation Protection Division, BAEC, Dhaka, Bangladesh.

Clavier, N., Podor, R., and Dacheux, N. (2011) Crystal chemistry of the monazite structure, Review. Journal of the European Ceramic Society, 31, 941–976.

Colombo, M., Chrosch, J., and Salje, K.H. (1999) Annealing metamict zircons: a powder diffraction study of a highly defective phase. Journal of the American Ceramic Society, 82, 2711-2716.

Cullity, R.D. (1977) Elements of X-ray diffraction. Addison-Wesley Publishing Company Inc, Reading, Massachusetts, USA and London, England.

Dacheux, N., Clavier, N., and Podor, R. (2013) Monazite as a promising long-term radioactive waste matrix: Benefits of high-structural flexibility and chemical durability. American Mineralogist, 98, 833–847.

Delhez, R., de Keijser, T.H., Langford, J.I., Louer, D., Mittemeijer E.J., and Sonneveld, E.J. (1993) Crystal imperfection broadening and peak shape in the Rietveld method. In R.A. Young, ed., The Rietveld Method, p. 132-166. Oxford University Press.

Donoghue, J.F. and Greenfield, M.B. (1989) Radioactivity of heavy mineral sands as an indicator of coastal sand transport processes. Journal of Coastal Research, 7(1), 189-201.

Eisenbud, M. and Gesell, T. (1997) Environmental radioactivity from natural, industrial, and military sources (4th edition), London: Academic Press.

El Afifi, E.M., Hilal, M.A., Khalifa, S.M. and Aly H.F. (2006) Evaluation of U, Th, K and emanated radon in some NORM and TENORM samples. Radiation Measurements, 41, 627- 633.

El-Kameesy, S.U., El-Ghany, S.A.B.D., El-Minyawi, S.M., Miligy, Z. and El-Mabrouk, E.M. (2008) Natural radioactivity of beach sand samples in the Tripoli region, northwest Libya. Turkish Journal of Engineering and Environmental Sciences, 32, 245-251.

Evans, R.D. (1969) The atomic nucleus. McGraw-Hill, New York.

Ewing, R.C., Chakoumakos, B.C., Lumpkin, G.R., and Murakami, T. (1987) The metamict state. Materials Research Society Bulletin, 12, 58-66.

Ewing, R.C. (1994) The metamict state: 1993 - the centennial. Nuclear Instruments and Methods in Physics Research, B91, 22-29.

Ewing, R.C., Meldrum, A., Wang, L., and Wang, S. (2000) Radiation-induced amorphization. In S.A.T. Redfern and M.A. Carpenter, eds., Transformation processes in minerals, 39, p. 319-361, Reviews in Mineralogy and Geochemistry, Mineralogical Society of America, Chantilly, Virginia.

Ewing, R.C., Meldrum, A., Wang, L., Weber, W.J., and Corrales, L.R. (2003) Radiation effects in zircon. In J.M. Hanchar and P.W.O. Hoskin, eds., Zircon, 53, p. 387-425, Reviews in Mineralogy and Geochemistry, Mineralogical Society of America, Chantilly, Virginia.

Farrugia, L.J. (1999) WinGX suite for small-molecule single-crystal crystallography. Journal of Applied Crystallography, 32, 837-838.

Finch, R.J., and Hanchar, J.M. (2003) Structure and chemistry of zircon and zircon-group minerals. In J.M. Hanchar and P.W.O. Hoskin, eds., Zircon, 53, p. 1-25. Reviews in Mineralogy and Geochemistry, Mineralogical Society of America, Chantilly, Virginia.

Finch, R.J., Hanchar, J.M., Hoskin, P.W.O., and Burns, P.C. (2001) Rare-earth elements in synthetic zircon: Part 2. A single-crystal X-ray study of xenotime substitution. American Mineralogist, 86, 681-689.

Finger, L.W., Cox, D.E., and Jephcoat, A.P. (1994) A correction for powder diffraction peak asymmetry due to axial divergence. Journal of Applied Crystallography, 27, 892-900.

Fleischer, M. and Altschuler, Z.S. (1969) The relationship of the rare-earth composition of minerals to geological environment. Geochimica et Cosmochimica Acta, 33, 725-732.

Geisler, T., Schaltegger, U., and Tomaschek, F. (2007) Re-equilibration of zircon in aqueous fluids and melts. Elements, 3, 43-50.

Glusker, J.P. and Trueblood, K.N. (2010) Crystal structure analysis: A primer (3rd edition). Oxford University Press Inc., New York.

Ghouse, K.M. (1968) Refinement of the crystal structure of heat-treated monazite crystal. Indian Journal of Pure and Applied physics, 6, 265-268.

Gibbons, J.F. (1972) Ion implantation in semiconductors - Part II: Damage production and annealing. Proceedings of Institute of Electrical and Electronics Engineers, 60, 1062-1096.

Gilmore, G.R. (2008) Practical gamma-ray spectrometry (2nd edition), Chichester: John Wiley and Sons Ltd.

Gong, W.L., Wang, L.M., Ewing, R.C., and Zhang, J. (1996) Electron-irradiation- and ion-beam-induced amorphization of coesite. Physical Review, B54, 3800-3808.

Gramaccioli, C.M. and Segalstad, T.V. (1978) A uranium- and thorium-rich monazite from a south-alpine pegmatite at Piona, Italy. American Mineralogist, 63, 757-761.

Hamberg, A. (1914) Die radioaktiven Substanzen und die geologische Forschung. Geologiska Foreningens Stockholm Furhandlingar, 36, 3l-96.

Hanchar, J.M., Finch, R.J., Hoskin, P.W.O., Watson, E.B., Cherniak, D.J., and Mariano, A.N. (2001) Rare earth elements in synthetic zircon: Part 1. Synthesis, and rare earth element and phosphorus doping. American Mineralogist, 86, 667-680.

Harley, S.L. and Kelly, N.M. (2003) Zircon: Tiny but timely. Elements, 3, 13-18.

Hassel, O. (1926) Die Kristallstruktur einiger Verbindungen von der Zusammensetzung MRO_4-I. Zirkon $ZrSiO_4$. Zeitschrift für Kristallographie, 63, 247-254.

Hazen, R.M., and Finger, L.W. (1979) Crystal structure and compressibility of zircon at high pressure. American Mineralogist, 64, 196-201.

Hendriks, P.H.G.M., Limburg, J. and Meijer, R.J. D. (2001) Full-spectrum analysis of natural γ-ray spectra. Journal of Environmental Radioactivity, 53, 365-380.

Holland, H.D. and Gottfried, D. (1955) The effect of nuclear radiation on the structure of zircon. Acta Crystallographica, 8, 291-300.

Horie, K., Hidaka, H., and Gauthier-Lafaye, F. (2006) Elemental distribution in zircon: Alteration and radiation-damage effects. Physics and Chemistry of the Earth, 31, 587-592.

Hoshino, M., Watanebe, Y., and Ishihara, S. (2012) Crystal chemistry of monazite from the granitic rocks of Japan: Petrographic implications. The Canadian Mineralogist, 50, 1331-1346.

Hoskin, P.W.O. and Schaltegger U. (2003) The composition of zircon and igneous and metamorphic petrogenesis. In J.M. Hanchar and P.W.O. Hoskin, eds., Zircon, 53, p. 27-

62. Reviews in Mineralogy and Geochemistry, Mineralogical Society of America, Chantilly, Virginia.

Huang, C. (2010) Rare earth coordination chemistry – fundamentals and applications. John Wiley & Sons (Asia) Pte Ltd, 2 Clementi Loop, 02-01, Singapore 129809.

IAEA (1996) International basic safety standards for protection against ionizing radiation and for the safety of radiation sources. Safety series no. 115, Schedule II, 91-180.

IAEA (2003) Extent of environmental contamination by naturally occurring radioactive material (NORM) and technological options for mitigation. Technical reports series no. 419, IAEA, Vienna.

Ingram, P., Shelburne, J.D., Roggli, V.L., and LeFurgey, A. (1999) Biomedical applications of microprobe analysis. Academic Press.

Kato, T. (1958) A study on monazite from the Ebisu mine, Gifu prefecture. Mineralogical Journal, 4, 224-235.

Kersten, C. (1839) Analyse de la monazite, mineral qui renferme de la thorine et de l'oxide de lantana. Bibliotheque universelle Geneve, new series, 24, 185-192.

Kinchin, G.H. and Pease, R.S. (1955) The displacement atoms in solids by radiation. Reports on Progress in Physics, 18, 1-51.

Kolesov, B.A., Geiger, C.A., and Armbruster, T. (2001) The dynamic properties of zircon studied by single-crystal X-ray diffraction and Raman spectroscopy. European Journal of Mineralogy, 13, 939-948.

Krstanovic, L.R. (1958) Redetermination of the oxygen parameters in zircon ($ZrSiO_4$). Acta Crystallographica, 11, 896.

Larson, A.C., and Von Dreele, R.B. (2000) General structure analysis system (GSAS). Los Alamos National Laboratory Report, LAUR, 86-748.

Lee, P.L., Shu, D., Ramanathan, M., Preissner, C., Wang, J., Beno, M.A., Von Dreele, R.B., Ribaud, L., Kurtz, C., Antao, S.M., Jiao, X., and Toby, B.H. (2008) A twelve-analyzer

detector system for high-resolution powder diffraction. Journal of Synchrotron Radiation 15, 427-432.

Lilley, J. (2001) Nuclear physics: principles and applications. Chichester, John Wiley & Sons, Ltd.

Lumpkin, G.R., and Ewing, R.C. (1988) Alpha-decay damage in minerals of the pyrochlore group. Physics and Chemistry of Minerals, 16, 2-20.

Macdonald, E.H. (1972) Manual of beach mining practice- exploration and evaluation, Department of Foreign Affairs, Canberra, Australia.

Malanca, A., de Pieri, R., and Gazzola, A. (1998) Radiogenic heavy minerals in Brazilian beach sand. Journal of Radioanalytical and Nuclear Chemistry, 230, 557-560.

Masau, M., Cerny, P., Cooper, M.A., Chapman, R., and Grice, J.D. (2002) Monazite-Sm, a new member of the monazite group from the Annie claim #3 granite pegmatite, southeastern Manitoba. The Canadian Mineralogist, 40, 649-1655.

Meijer, R.J.D., James, I.R., Jennings, P.J., and Koeyers, J.E. (2001) Cluster analysis of radionuclide concentrations in beach sand. Applied Radiation and Isotopes, 54, 535-542.

Meldrum, A., Wang, L.M., and Ewing R.C. (1996) Ion-beam-induced amorphization of monazite. Nuclear Instruments and Methods in Physics Research, B116, 220-224.

Meldrum, A., Boatner, L.A., Weber, W.J., and Ewing, R.C. (1998) Radiation damage in zircon and monazite. Geochimica et Cosmochimica Acta, 62, 2509-2520.

Mohanty, A. K., Das, S. K., Van, K. V., Sengupta, D., and Saha, S. K. (2003) Radiogenic heavy minerals in Chhatrapur beach placer deposit of Orissa, southeastern coast of India. Journal of Radioanalytical and Nuclear Chemistry, 258(2), 383-389.

Mohanty, A.K., Sengupta, D., Das, S.K., Vijayan, V., and Sahab, S.K. (2004a) Natural radioactivity in the newly discovered high background radiation area on the eastern coast of Orissa, India. Radiation Measurements, 38, 153-165.

Mohanty, A.K., Sengupta, D., Das, S.K., Saha, S.K., and Van, K.V. (2004b) Natural radioactivity and radiation exposure in the high background area at Chhatrapur beachplacer deposit of Orissa, India. Journal of Environmental Radioactivity, 75, 15-33.

Monsur, M.H. and Kamal, A.S.M.M. (1994) Holocene sea-level changes along the Maiskhali and Cox's Bazar-Teknaf Coast of the Bay of Bengal. Journal of NOAMI, 1(1), 15-21.

Montel, J.M., Foret, S., Veschambre, M., Nicollet, N., and Provost, A. (1996) Electron microprobe dating of monazite. Chemical Geology, 131, 37-53.

Mooney, R.C.L. (1948) Crystal structures of a series of rare earth phosphates. The Journal of Chemical Physics, 16, 1003.

Muller, O. and Roy, R. (1975) Crystal chemistry of non-metallic materials: volume 4. Springer-Verlag, New York, N.Y.

Mullica, D.F., Sappenfield, E.L., and Boatner, L.A. (1996) Monazite- and zircon-type structures of seven mixed (Ln/Ln) PO_4 compounds. Inorganica Chimica Acta, 244, 247-252.

Motta, A.T. (1997) Amorphization of intermetallic compounds under irradiation - a review. Journal of Nuclear Materials, 244, 227-250.

Murakami, T., Chakoumakos, B.C., Ewing, R.C., Lumpkin, G.R., and Weber, W.J. (1991) Alpha-decay event damage in zircon. American Mineralogist, 76, 1510-1532.

Murata, K.J., Rose Jr., H.J., and Carron, M.K. (1953) Systematic variation of rare earths in monazite. Geochimica et cosmochimica Acta, 4, 292-300.

Mursic, Z., Vogt, T., Boysen, H., and Frey, F. (1992) Single-crystal neutron diffraction study of metamict zircon up to 2000 K. Journal of Applied Crystallography, 25, 519-523.

Murugesan, S., Mullainathan, S., Ramasamy, V. and Meenakshisundaram, V. (2011) Radioactivity and radiation hazard assessment of Cauvery River, Tamilnadu, India. Iranian Journal of Radiation Research, 8(4), 211-222.

Najman, Y., Allen, R., Willett, E.A.F., Carter, A., Barfod, D., Garzanti, E., Wijbrans, J., Bickle, M.J., Vezzoli, G., Ando, S., Oliver, G., and Uddin, M.J. (2012) The record of Himalayan

erosion preserved in the sedimentary rocks of the Hatia Trough of the Bengal Basin and the Chittagong Hill Tracts, Bangladesh. Basin Research, 24, 1-21.

Nasdala, L., Wenzel, M., Vavra, G., Irmer, G., Wenzel, T., and Kober, B. (2001) Metamictization of natural zircon: accumulation versus thermal annealing of radioactivity-induced damage. Contributions to Mineralogy and Petrology, 141, 125-144.

Nasdala L., Kronz A., Hanchar J. M., Tichomirowa M., Davis D.D., and Hofmeister W. (2006) Effects of natural radiation damage on back-scattered electron images of single-crystals of minerals. American Mineralogist, 91, 1738–1746.

NCRP (1975) Natural background radiation in the United States, Report no. 45. National Council on Radiation Protection and Measurements, Washington, D.C.

NEA-OECD (1979) Nuclear energy agency, exposure to radiation from natural radioactivity in building materials. Reported by NEA group of experts, OECD, Paris.

Nesse, W.D. (2000) Introduction to mineralogy. Oxford University Press, Inc., New York.

Ni, Y., Hughes, J.M., and Mariano, A.N. (1995) Crystal chemistry of the monazite and xenotime structures. American Mineralogist, 80, 21-26.

Nyman, H., Hyde, B.G., and Andersson, S. (1984) Zircon, anhydrite, scheelite and some related structures containing bisdisphenoids. Acta Crystallographica, B40, 441-447.

Orgun, Y., Altinsoy, N., Sahin, S.Y., Gungor, Y., Gultekin., A.H., Karahan, G. and Karacik, Z. (2007) Natural and anthropogenic radionuclides in rocks and beach sands from Ezine region (Canakkale), Western Anatolia, Turkey. Applied Radiation and Isotopes, 65, 739-747.

Otwinowski, Z., and Minor, W. (1997) Processing of X-ray diffraction data collected in oscillation mode. In C.W. Carter, Jr. and R.M. Sweet, Eds., Methods in Enzymology: Macromolecular Crystallography, A276, p. 307-326, Academic Press, New York.

Overstreet WC (1967) The geologic occurrence of monazite. U.S. Geological Survey Professional Paper 530, Washington, D. C.

Pabst, A. (1952) The metamict state. American Mineralogist, 37, 137-157.

Pirkle, F.L. and Podmeyer, D.A. (1992) Zircon: origin and uses. Transactions, 292, 1880-1972.

Pyle, J.M., Spear, F.S., and Wark, D.A. (2002) Electron microprobe analysis of REE in apatite, monazite, and xenotime: protocols and pitfalls. In M.J. Kohn, J. Rakovan, and J.M. Hughes, Eds., Phosphates, 48, p. 337-362, Reviews in Mineralogy and Geochemistry, Mineralogical Society of America, Washington, D.C.

Radominski, M.F. (1875) Reproduction artificielle de Ia monazite et de la xenotime. Compte Rendu, 80, 304-307.

Rahman, M.H., Islam, M.A., Shine, F.M.M. and Ahmed, F. (1994) Heavy-mineral studies of the Silkhali-Teknaf beach, dune and cliff sands, Cox's Bazar, Bangladesh. Indian Minerals, 48(3), 167-174.

Ramasamy, V., Dheenathayalu, M., Ravisankar, R., Ponnusamy, V., Victor Rajamanickkam, G., Sahayam, D.K., Meenakshisundram, V., and Gajendran, V. (2004) Natural radioactivity measurements in beach-rock samples of south-east coast of Tamil Nadu, India. Radiation Protection Dosimetry, 111(2) 229-235.

Rapp, R.P. and Watson, E.B. (1986) Monazite solubility and dissolution kinetics—implications for the thorium and light rare-earth chemistry of felsic magmas. Contributions to Mineralogy and Petrology, 94, 304–316.

Rietveld, H.M. (1969) A profile refinement method for nuclear and magnetic structures. Journal of Applied Crystallography, 2, 65-71.

Righi, S., Andretta, M., and Bruzzi, L. (2005) Assessment of the radiological impacts of a zircon sand processing plant. Journal of Environmental Radioactivity, 82, 237-250.

Ríos, S., Salje, E.K.H., Zhang, M., and Ewing, R.C. (2000a) Amorphization in zircon: evidence for direct impact damage. Journal of Physics: Condensed Matter, 12, 2401-2412.

Rios, S., Malcherek, T., Salje, E.K.H., and Domeneghetti, C. (2000b) Localized defects in radiation-damaged zircon. Acta Crystallographica, B56, 947-952.

Robinson, K., Gibbs, G.V., and Ribbe, P.H. (1971) The structure of zircon: a comparison with garnet. American Mineralogist, 56, 782-790.

Schmidt, R.G. and Asad, S.A. (1963) A reconnaissance survey of radioactive beach sand at Cox's Bazar, East Pakistan. Interim geological report, The Geological Survey of Pakistan, 3, 1-15.

Selby, J.H. (2007) The industrial uses of zircon and zirconia and the radiological consequences of these uses. Proceedings Series, fifth international symposium on naturally occurring radioactive material, IAEA, 95-116.

Seydoux-Guillaume, A.M., Wirth, R., Nasdala, L., Gottschalk, M., Montel, J.M., and Heinrich, W. (2002) An XRD, TEM and Raman study of experimentally annealed natural monazite. Physics and Chemistry of Minerals, 29, 240-253.

Seydoux-Guillaume A.M., Wirth, R., Deutsch, A., and Scharer, U. (2004) Microstructure of 24-1928 Ma concordant monazites; implications for geochronology and nuclear waste deposits. Geochimica et Cosmochimica Acta, 68, 2517–2527.

Shannon, R.D. (1976) Revised effective ionic radii and systematic studies of interatomic distances in halides and chalcogenides. Acta Crystallographica, A32, 75l-767.

Sheldrick, G.M. (1997) A short history of SHELX. Acta Crystallographica, A64, 112-122.

Siggel, A. and Jansen, M. (1990) Röntgenographische untersuchungen zur bestimmung der einbauposition von seltenen erden (Pr, Tb) und vanadium in zirkonpigmenten. Zeitschrift für anorganische und allgemeine Chemie, 583, 67-77.

Spear, F.S., and Pyle, J.M. (2002) Apatite, monazite, and xenotime in metamorphic rocks. In M.J. Kohn, J. Rakovan, and J.M. Hughes, Eds. Phosphates: Geochemical, Geobiological, and Materials Importance, 48, p. 293-335. Reviews in Mineralogy and Geochemistry, Mineralogical Society of America, Washington, D. C.

Toby, B.H. (2001) Expgui, a graphical user interface for GSAS. Journal of Applied Crystallography, 34, 210-213.

Tole, M.P. (1985) The kinetics of dissolution of zircon ($ZrSiO_4$). Geochimica et Cosmochimica Acta, 49, 453-458.

Turner, J.E. (2007) Atoms, radiation, and radiation protection (3rd edition), Weinheim: Wiley-VCH.

Ueda, T. (1967) Re-examination of the crystal structure of monazite. Journal of the Japanese Association of Mineralogists, petrologists, and Economic Geologists, 58, 170-179.

UNSCEAR (1988) Exposures from natural sources of radiation. Sources, effects and risks of ionizing radiation. Report to the General Assembly. U.N., New York, USA.

UNSCEAR (1993) Sources and effects of ionizing radiations. Report to the General Assembly. U.N., New York, USA.

UNSCEAR (2000) Sources and effects of ionizing radiation, volume 1. Report to the General Assembly, with scientific annexes, United Nations Sales Publication, United Nations, New York.

Váczi, T., Nasdala, L., Wirth, R., Mehofer, M., Libowitzky, E., and Häger, T. (2009) On the breakdown of zircon upon "dry" thermal annealing. Mineralogy and Petrology, 97, 129-138.

Vaczi, M.T. (2009) Mineralogical studies on zircon. Unpublished PhD Dissertation, Institut fur Mineralogie und Kristallographie, Universitat Wien, Austria, 1-22.

Valley, J.W., Cavosie, A.J., Ushikubo, T., Reinhard, D.A., Lawrence, D.F., Larson, D.J., Clifton, P.H., Kelly, T.F., Wilde, S.A., Moser, D.E., and Spicuzza1, M.J. (2014) Hadean age for a post-magma-ocean zircon confirmed by atom-probe tomography. Nature Geoscience, 7, 219-223.

Vance, E.R. (1975) α-recoil damage in zircon. Radiation Effects, 24, 1-6.

Van-Emden, B., Graham, J., and Lincoln, F.J. (1997) The incorporation of actinides in monazite and xenotime from placer deposits in Western Australia. The Canadian Mineralogist, 35, 95-104.

Vegard, L. (1916) VI. Results of crystal analysis. Philosophical Magazine Series, 6, 32, 65-96.

Wang, J., Toby, B.H, Lee, P.L., Ribaud, L., Antao, S.M., Kurtz, C., Ramanathan, M., Von Dreele, R.B., and Beno, M.A. (2008) A dedicated powder diffraction beamline at the

advanced photon source: Commissioning and early operational results. Review of Scientific Instruments, 79, 085105.

Weber, W.J. (1990) Radiation-induced defects and amorphization in zircon. Journal of Material Research, 5, 2687-2697.

Weber, W.J. (1993) Alpha-decay-induced amorphization in complex silicate structures. Journal of the American Ceramic Society, 76, 1729-1738.

Weber, W.J. (2000) Models and mechanisms of irradiation-induced amorphization in ceramics. Nuclear Instruments and Methods in Physics Research B, 166 and 167, 98-106.

Will, G. (2006) Powder diffraction: The Rietveld method and the two stage method to determine and refine crystal structures from powder diffraction data. Springer-Verlag Berlin Heidelberg, Germany.

World Nuclear Association (2014) Nuclear radiation and health effects. http://www.world-nuclear.org/info, Updated December 16, 2014.

Wyckoff, R.W.G. and Hendricks, S.B. (1928) Die kristallstruktur von zirkon und die kriterien fur spezielle lagen in tetragonalen raurngruppen. Zeitschrift für Kristallographie, 66, 73-102.

Young, R.A. (1993) The Rietveld method. Oxford University Press, Oxford.

Yucel, H., Cetiner, M.A., and Demirel, H. (1998) Use of the 1001 keV peak of ^{234m}Pa daughter of ^{238}U in measurement of uranium concentration by HPGe gamma-ray spectrometry. Nuclear Instruments and Methods in Physics Research, A413, 74-82.

Yucel, H., Karadeniz, H., Cetiner, M.A., Demirel, H., and Turhan, S. (2003) Measurement of absolute intensity of 1001 keV gamma-ray of ^{234m}Pa. Journal of Radioanalytical and Nuclear Chemistry, 258(2), 445-447.

Zaman, M, Schubert, S., and Antao, S. (2012) Elevated radionuclide concentrations in heavy mineral-rich beach sands in the Cox's Bazar region, Bangladesh and related possible radiological effects. Isotopes in Environmental and Health Studies, 48, 1-14.

Zaman, M. M., Deeba, F., Kabir, M. Z., Rajib, M., and Rana, S.M. (2009a) Finding a new heavy mineral deposit and its mineralogical composition at Sonarpara, Cox's Bazar. The Journal of National Oceanographic and Maritime Institute, 26, 17-30.

Zaman, M.M, Kabir, M.Z., Deeba, F., Rajib, M., and Rana, S.M. (2009b) Anomalous radioactivity due to the presence of heavy minerals in beach sands of Cox's Bazar. International Conference on Geoscience for Global Development (GeoDev) held at Dhaka, Bangladesh, Abstract Volume, 52.

Zhenmin, G. and Jingming, P. (1986) Factor affecting metamictization in granites. Geochemistry, 5, 181-188.

APPENDIX

A: Structure Factor Tables for Zircon

Table A1 Observed and calculated structure factors for sample 1

h	k	l	10Fo	10Fc	10s	h	k	l	10Fo	10Fc	10s	h	k	l	10Fo	10Fc	10s
0	2	0	1802	1802	19	0	6	2	30	22	7	2	3	5	409	417	2
2	2	0	859	889	5	2	6	2	169	172	1	1	4	5	283	282	4
0	4	0	1478	1507	15	4	6	2	90	87	2	3	4	5	289	288	2
2	4	0	941	950	3	1	7	2	742	745	3	0	5	5	110	108	3
4	4	0	943	941	13	3	7	2	790	788	6	2	5	5	322	314	4
0	6	0	1244	1241	24	0	8	2	185	169	15	1	6	5	132	137	4
2	6	0	916	903	11	0	1	3	856	841	3	1	1	6	939	943	6
4	6	0	877	872	6	1	2	3	304	310	1	0	2	6	120	122	6
6	6	0	810	806	18	0	3	3	484	493	3	1	3	6	701	700	9
0	8	0	677	684	15	2	3	3	118	113	1	3	3	6	494	501	5
2	8	0	470	477	5	1	4	3	373	379	2	0	4	6	62	61	2
0	1	1	562	564	2	3	4	3	213	216	1	2	4	6	49	41	5
1	2	1	235	249	1	0	5	3	544	545	3	1	5	6	793	783	8
0	3	1	961	944	4	2	5	3	279	276	2	0	1	7	193	201	7
2	3	1	652	653	1	4	5	3	322	319	2	1	2	7	330	329	4
1	4	1	288	296	1	1	6	3	407	404	3	0	3	7	72	74	6
3	4	1	545	548	2	3	6	3	285	282	2						
0	5	1	247	245	2	5	6	3	337	344	5						
2	5	1	128	122	1	0	7	3	318	340	6						
4	5	1	162	158	2	2	7	3	154	161	2						
1	6	1	292	286	1	0	0	4	1058	1059	12						
3	6	1	449	449	3	0	2	4	1088	1076	11						
5	6	1	175	177	2	2	2	4	1100	1085	9						
0	7	1	352	349	4	1	3	4	263	275	2						
2	7	1	267	262	1	0	4	4	909	906	5						
4	7	1	252	260	5	2	4	4	914	917	3						
1	8	1	156	155	3	4	4	4	778	794	6						
1	1	2	1274	1276	7	1	5	4	77	74	2						
0	2	2	551	519	2	3	5	4	238	242	1						
1	3	2	1371	1367	8	0	6	4	700	703	10						
3	3	2	1401	1393	7	2	6	4	735	714	6						
0	4	2	216	217	2	4	6	4	629	629	6						
2	4	2	102	104	1	1	7	4	75	72	6						
1	5	2	825	822	4	0	1	5	128	123	3						
3	5	2	902	899	4	1	2	5	430	429	5						
5	5	2	618	605	6	0	3	5	161	157	10						

Table A2 Observed and calculated structure factors for sample 2

h	k	l	10Fo	10Fc	10s	h	k	l	10Fo	10Fc	10s	h	k	l	10Fo	10Fc	10s
0	2	0	1700	1800	8	0	6	2	23	19	3	0	3	5	165	166	2
2	2	0	837	892	3	2	6	2	163	168	1	2	3	5	422	415	3
0	4	0	1496	1502	16	4	6	2	80	84	3	1	4	5	280	283	1
2	4	0	942	954	4	1	7	2	754	747	3	3	4	5	291	289	3
4	4	0	916	942	6	3	7	2	784	785	5	0	5	5	123	122	3
0	6	0	1267	1236	11	0	8	2	166	164	10	2	5	5	318	316	2
2	6	0	912	908	11	2	8	2	36	32	3	4	5	5	221	224	2
4	6	0	860	873	4	0	1	3	857	835	3	1	6	5	140	143	3
6	6	0	823	802	12	1	2	3	310	313	1	1	1	6	977	956	5
0	8	0	694	678	8	0	3	3	492	491	3	0	2	6	111	112	1
2	8	0	475	483	5	2	3	3	119	121	1	1	3	6	710	720	3
0	1	1	579	563	2	1	4	3	379	377	3	3	3	6	512	529	4
1	2	1	237	253	1	3	4	3	215	218	1	0	4	6	64	61	6
0	3	1	952	943	3	0	5	3	541	543	4	2	4	6	32	31	6
2	3	1	650	655	2	2	5	3	285	284	3	1	5	6	806	793	6
1	4	1	291	297	1	4	5	3	313	320	2	0	1	7	195	206	7
3	4	1	544	545	2	1	6	3	412	405	3	1	2	7	338	328	3
0	5	1	257	243	2	3	6	3	292	287	3	0	3	7	89	86	3
2	5	1	138	126	1	5	6	3	347	346	2	2	3	7	196	202	2
4	5	1	161	161	1	0	7	3	332	332	5						
1	6	1	292	292	2	2	7	3	157	165	3						
3	6	1	447	448	3	0	0	4	1079	1070	7						
5	6	1	179	183	3	0	2	4	1105	1090	8						
0	7	1	350	350	3	2	2	4	1120	1101	6						
2	7	1	270	267	2	1	3	4	260	269	1						
4	7	1	264	263	4	0	4	4	929	911	5						
1	8	1	159	161	1	2	4	4	935	923	4						
1	1	2	1293	1279	6	4	4	4	798	794	5						
0	2	2	542	518	2	1	5	4	80	73	2						
1	3	2	1375	1371	3	3	5	4	233	233	4						
3	3	2	1397	1394	10	0	6	4	723	716	5						
0	4	2	215	210	2	2	6	4	732	727	4						
2	4	2	98	104	1	4	6	4	625	637	6						
1	5	2	832	829	4	1	7	4	67	67	4						
3	5	2	911	902	3	0	1	5	135	130	2						
5	5	2	619	615	4	1	2	5	428	426	2						

Table A3 Observed and calculated structure factors for sample 3

h	k	l	10Fo	10Fc	10s	h	k	l	10Fo	10Fc	10s	h	k	l	10Fo	10Fc	10s
0	2	0	1767	1801	26	5	5	2	623	618	7	0	1	5	134	121	1
2	2	0	860	893	4	0	6	2	22	20	2	1	2	5	433	434	2
0	4	0	1500	1504	6	2	6	2	168	170	1	0	3	5	163	156	1
2	4	0	944	955	4	4	6	2	87	85	2	2	3	5	424	419	1
4	4	0	941	943	16	1	7	2	750	750	3	1	4	5	282	285	1
0	6	0	1255	1238	9	3	7	2	793	788	6	3	4	5	289	289	2
2	6	0	908	909	4	0	8	2	166	165	2	0	5	5	119	116	2
4	6	0	884	874	12	2	8	2	35	31	3	2	5	5	319	321	2
6	6	0	806	804	27	0	1	3	839	843	4	4	5	5	220	226	1
0	8	0	692	684	15	1	2	3	306	313	1	1	6	5	140	140	1
2	8	0	476	487	4	0	3	3	487	491	3	1	1	6	971	969	4
0	1	1	573	562	1	2	3	3	119	116	1	0	2	6	117	118	1
1	2	1	235	252	1	1	4	3	380	379	1	1	3	6	712	719	3
0	3	1	961	943	6	3	4	3	214	216	1	3	3	6	513	517	8
2	3	1	654	656	2	0	5	3	539	547	2	0	4	6	62	62	3
1	4	1	289	298	1	2	5	3	283	284	1	2	4	6	35	35	2
3	4	1	542	547	2	4	5	3	324	322	1	1	5	6	807	806	5
0	5	1	250	245	1	1	6	3	409	407	2	0	1	7	206	200	1
2	5	1	135	127	1	3	6	3	288	286	1	1	2	7	335	338	2
4	5	1	163	162	1	5	6	3	339	347	3	0	3	7	67	72	1
1	6	1	291	291	2	0	7	3	330	336	3	2	3	7	204	202	2
3	6	1	447	448	2	2	7	3	163	165	2						
5	6	1	181	183	3	0	0	4	1069	1064	9						
0	7	1	353	350	3	0	2	4	1103	1090	5						
2	7	1	266	266	2	2	2	4	1120	1106	6						
4	7	1	256	263	3	1	3	4	258	277	1						
1	8	1	161	162	2	0	4	4	923	913	4						
1	1	2	1282	1281	5	2	4	4	936	929	3						
0	2	2	540	523	2	4	4	4	792	800	5						
1	3	2	1379	1372	3	1	5	4	78	75	1						
3	3	2	1399	1395	12	3	5	4	235	239	2						
0	4	2	215	214	2	0	6	4	725	714	6						
2	4	2	101	104	1	2	6	4	734	728	5						
1	5	2	832	831	2	4	6	4	641	639	4						
3	5	2	904	904	3	1	7	4	71	69	2						

Table A4 Observed and calculated structure factors for sample 4

h	k	l	10Fo	10Fc	10s	h	k	l	10Fo	10Fc	10s	h	k	l	10Fo	10Fc	10s
0	2	0	1810	1797	10	5	5	2	606	601	8	0	1	5	134	129	3
2	2	0	855	891	4	0	6	2	15	14	15	1	2	5	421	418	2
0	4	0	1504	1491	18	2	6	2	166	167	3	0	3	5	166	168	3
2	4	0	936	946	4	4	6	2	90	84	3	2	3	5	403	410	3
4	4	0	942	929	7	1	7	2	732	731	4	1	4	5	272	279	2
0	6	0	1265	1225	10	3	7	2	768	767	5	3	4	5	275	287	3
2	6	0	909	902	6	0	8	2	156	162	5	0	5	5	128	121	3
4	6	0	868	860	7	2	8	2	34	36	12	2	5	5	311	308	3
6	6	0	771	788	14	0	1	3	838	832	4	4	5	5	217	219	4
0	8	0	657	656	8	1	2	3	309	310	1	1	6	5	139	138	4
2	8	0	463	469	6	0	3	3	483	490	4	1	1	6	943	920	9
0	1	1	560	564	2	2	3	3	122	123	1	0	2	6	113	113	3
1	2	1	237	252	1	1	4	3	375	371	3	1	3	6	686	690	3
0	3	1	947	944	4	3	4	3	214	217	2	3	3	6	501	505	5
2	3	1	647	655	1	0	5	3	522	537	3	0	4	6	69	62	3
1	4	1	285	296	2	2	5	3	276	282	1	2	4	6	33	30	5
3	4	1	540	542	2	4	5	3	315	315	2	1	5	6	755	758	5
0	5	1	244	240	3	1	6	3	402	404	2	0	1	7	198	205	6
2	5	1	136	124	1	3	6	3	286	289	2	1	2	7	322	319	5
4	5	1	160	159	2	5	6	3	340	341	6	0	3	7	90	86	6
1	6	1	288	293	2	0	7	3	320	326	11	2	3	7	185	194	4
3	6	1	450	445	3	2	7	3	163	164	2						
5	6	1	179	183	2	0	0	4	1035	1059	9						
0	7	1	352	346	6	0	2	4	1070	1072	6						
2	7	1	265	265	4	2	2	4	1096	1076	8						
4	7	1	259	259	4	1	3	4	259	268	2						
1	8	1	154	158	5	0	4	4	888	893	6						
1	1	2	1257	1270	5	2	4	4	911	900	4						
0	2	2	538	512	2	4	4	4	771	772	10						
1	3	2	1357	1363	4	1	5	4	81	74	1						
3	3	2	1368	1384	10	3	5	4	229	230	5						
0	4	2	216	208	2	0	6	4	702	698	6						
2	4	2	102	101	1	2	6	4	705	705	7						
1	5	2	823	815	5	4	6	4	614	616	5						
3	5	2	896	887	5	1	7	4	68	65	5						

Table A5 Observed and calculated structure factors for sample 5

h	k	l	10Fo	10Fc	10s	h	k	l	10Fo	10Fc	10s	h	k	l	10Fo	10Fc	10s
0	2	0	1800	1798	9	1	5	2	811	808	4	2	6	4	697	692	3
2	2	0	854	887	5	3	5	2	881	878	3	4	6	4	585	599	3
0	4	0	1501	1489	22	5	5	2	591	589	4	1	7	4	67	65	4
2	4	0	928	938	4	0	6	2	35	21	4	0	1	5	126	120	1
4	4	0	932	920	7	2	6	2	161	166	2	1	2	5	415	414	1
0	6	0	1218	1212	8	4	6	2	87	82	4	0	3	5	155	155	1
2	6	0	897	883	4	1	7	2	722	715	2	2	3	5	400	402	1
4	6	0	855	843	5	3	7	2	755	752	5	1	4	5	266	271	2
6	6	0	774	769	16	0	8	2	161	161	3	3	4	5	275	277	2
0	8	0	660	654	12	2	8	2	44	28	8	0	5	5	111	112	2
2	8	0	450	458	4	0	1	3	839	830	3	2	5	5	301	304	3
0	1	1	561	562	1	1	2	3	301	308	1	4	5	5	212	213	3
1	2	1	240	251	1	0	3	3	476	486	2	1	6	5	126	133	2
0	3	1	950	939	4	2	3	3	118	116	1	1	1	6	919	910	4
2	3	1	655	651	2	1	4	3	372	368	1	0	2	6	114	111	2
1	4	1	285	292	1	3	4	3	213	210	1	1	3	6	678	676	4
3	4	1	537	539	2	0	5	3	525	534	2	3	3	6	484	486	4
0	5	1	243	242	1	2	5	3	275	275	1	0	4	6	63	62	5
2	5	1	134	124	1	4	5	3	310	309	2	2	4	6	28	29	3
4	5	1	159	155	2	1	6	3	398	394	4	1	5	6	754	745	4
1	6	1	287	284	1	3	6	3	277	276	2	0	1	7	186	191	2
3	6	1	439	439	2	5	6	3	325	333	2	1	2	7	316	312	3
5	6	1	179	175	4	0	7	3	317	322	3	0	3	7	72	72	4
0	7	1	344	340	3	2	7	3	156	155	2	2	3	7	191	187	2
2	7	1	263	257	2	0	0	4	1026	1043	8						
4	7	1	245	252	4	0	2	4	1068	1062	4						
1	8	1	145	153	2	2	2	4	1073	1072	4						
3	8	1	267	266	8	1	3	4	255	268	1						
1	1	2	1260	1269	4	0	4	4	880	878	4						
0	2	2	543	517	2	2	4	4	886	890	3						
1	3	2	1350	1354	3	4	4	4	760	758	4						
3	3	2	1370	1373	5	1	5	4	76	70	2						
0	4	2	210	211	2	3	5	4	227	229	1						
2	4	2	100	104	1	0	6	4	677	681	7						

Table A6 Observed and calculated structure factors for sample 6

k	l	10Fo	10Fc	10s	h	k	l	10Fo	10Fc	10s	h	k	l	10Fo	10Fc	10s
2	0	845	884	6	0	6	2	24	22	1	1	2	5	409	408	1
4	0	1482	1484	22	2	6	2	159	161	1	0	3	5	156	152	1
4	0	927	938	5	4	6	2	78	78	1	2	3	5	395	395	1
4	0	919	918	7	1	7	2	713	710	2	1	4	5	266	265	1
6	0	1223	1196	13	3	7	2	747	742	4	3	4	5	269	270	1
6	0	880	873	4	0	8	2	153	154	1	0	5	5	112	110	1
6	0	842	833	8	2	8	2	31	27	1	2	5	5	297	297	1
6	0	746	752	12	0	1	3	831	824	4	4	5	5	205	206	1
8	0	643	646	6	1	2	3	300	304	1	1	6	5	128	132	1
8	0	456	457	3	0	3	3	468	481	2	1	1	6	902	896	5
1	1	552	563	2	2	3	3	118	116	1	0	2	6	109	110	1
2	1	235	252	1	1	4	3	367	367	1	1	3	6	667	666	4
3	1	946	933	4	3	4	3	212	211	1	3	3	6	475	480	3
3	1	639	645	1	0	5	3	518	526	3	0	4	6	58	58	2
4	1	284	294	1	2	5	3	270	272	1	2	4	6	41	31	5
4	1	529	534	1	4	5	3	305	306	1	1	5	6	737	730	5
5	1	245	240	1	1	6	3	391	386	1	0	1	7	187	184	2
5	1	134	124	1	3	6	3	277	271	1	1	2	7	308	302	2
5	1	158	157	1	5	6	3	325	324	1	0	3	7	67	70	1
6	1	285	282	1	0	7	3	309	316	2	2	3	7	177	181	1
6	1	434	431	1	2	7	3	151	154	1						
6	1	174	174	1	0	2	4	1064	1054	6						
7	1	334	338	1	2	2	4	1068	1062	10						
7	1	256	257	1	1	3	4	252	262	1						
7	1	248	251	1	0	4	4	867	871	6						
8	1	149	154	1	2	4	4	882	881	2						
2	2	531	514	2	4	4	4	750	749	4						
3	2	1343	1347	13	1	5	4	73	70	1						
3	2	1383	1361	8	3	5	4	222	223	1						
4	2	210	206	1	0	6	4	674	673	4						
4	2	100	104	1	2	6	4	686	682	4						
5	2	806	804	3	4	6	4	583	591	3						
5	2	876	869	3	1	7	4	60	65	1						
5	2	585	584	4	0	1	5	124	117	1						

Table A7 Observed and calculated structure factors for sample 7

h	k	l	10Fo	10Fc	10s	h	k	l	10Fo	10Fc	10s	h	k	l	10Fo	10Fc	10s
2	2	0	854	887	7	1	7	2	718	709	4	1	4	5	269	272	2
2	4	0	939	934	33	3	7	2	760	745	7	3	4	5	272	277	1
4	4	0	910	914	8	0	8	2	153	155	2	0	5	5	113	109	5
0	6	0	1243	1200	9	0	1	3	829	829	3	2	5	5	300	301	2
2	6	0	880	872	5	1	2	3	303	307	1	4	5	5	208	210	2
4	6	0	841	833	9	0	3	3	476	487	3	1	6	5	129	134	1
6	6	0	744	756	15	2	3	3	117	117	1	1	1	6	918	915	11
0	8	0	631	653	13	1	4	3	369	368	2	0	2	6	113	114	1
2	8	0	458	457	8	3	4	3	213	211	1	1	3	6	687	681	3
0	1	1	564	563	3	0	5	3	522	528	5	3	3	6	485	491	7
1	2	1	235	250	1	2	5	3	273	270	1	0	4	6	63	61	1
0	3	1	940	934	14	4	5	3	309	305	1	2	4	6	34	33	2
2	3	1	644	645	3	1	6	3	394	388	2	1	5	6	750	744	7
1	4	1	282	291	1	3	6	3	279	272	1	0	1	7	191	194	2
3	4	1	531	534	1	5	6	3	328	326	4	1	2	7	318	312	3
0	5	1	247	244	1	0	7	3	310	323	3	0	3	7	74	75	3
2	5	1	132	125	1	2	7	3	152	155	1	2	3	7	184	186	4
4	5	1	158	156	1	0	0	4	1045	1051	9						
1	6	1	284	280	1	0	2	4	1051	1063	5						
3	6	1	433	433	2	2	2	4	1067	1068	15						
5	6	1	172	173	1	1	3	4	255	265	1						
0	7	1	333	335	2	0	4	4	901	882	6						
2	7	1	253	252	1	2	4	4	886	889	4						
4	7	1	248	247	3	4	4	4	755	759	4						
1	8	1	151	152	1	1	5	4	73	68	1						
0	2	2	532	512	2	3	5	4	226	226	1						
0	4	2	211	210	1	0	6	4	679	680	5						
2	4	2	100	101	1	2	6	4	689	688	5						
1	5	2	807	805	3	4	6	4	600	597	4						
3	5	2	876	874	3	1	7	4	62	65	1						
5	5	2	581	585	4	0	1	5	129	121	3						
0	6	2	25	24	1	1	2	5	418	413	1						
2	6	2	163	162	1	0	3	5	157	157	2						
4	6	2	82	80	1	2	3	5	398	402	3						

B: Structure Factor Tables for Monazite

Table B1 Observed and calculated structure factors for sample 1

h	k	l	10Fo	10Fc	10s	h	k	l	10Fo	10Fc	10s	h	k	l	10Fo	10Fc	10s
2	0	0	2005	2100	31	5	4	0	350	351	8	5	0	1	1142	1127	8
4	0	0	1047	1044	5	6	4	0	94	94	5	7	0	1	821	817	7
6	0	0	326	333	8	7	4	0	36	10	10	-8	1	1	290	298	3
8	0	0	10	12	10	1	5	0	121	116	1	-7	1	1	478	472	11
1	1	0	383	377	1	2	5	0	733	741	3	-6	1	1	321	316	2
2	1	0	863	855	4	3	5	0	251	254	1	-5	1	1	820	816	5
3	1	0	425	435	1	4	5	0	913	907	5	-4	1	1	528	529	2
4	1	0	1021	1032	6	5	5	0	327	326	3	-3	1	1	1457	1441	6
5	1	0	811	807	6	6	5	0	832	824	17	-2	1	1	443	448	2
6	1	0	1059	1054	9	7	5	0	291	295	8	-1	1	1	960	941	4
7	1	0	548	556	6	0	6	0	1417	1431	23	0	1	1	633	620	6
8	1	0	705	692	6	1	6	0	273	278	3	1	1	1	673	678	3
0	2	0	1059	1057	5	2	6	0	1245	1246	8	2	1	1	190	198	2
1	2	0	2004	2028	39	3	6	0	260	260	4	3	1	1	397	401	3
2	2	0	625	632	4	4	6	0	648	642	11	4	1	1	39	18	3
3	2	0	1327	1319	8	5	6	0	178	187	5	5	1	1	286	290	1
4	2	0	108	97	2	6	6	0	254	263	9	6	1	1	33	28	3
5	2	0	641	649	4	1	7	0	213	207	4	7	1	1	189	188	1
6	2	0	53	51	3	2	7	0	380	373	5	8	1	1	201	205	5
7	2	0	71	56	14	3	7	0	504	499	3	-8	2	1	456	458	8
8	2	0	60	53	9	4	7	0	531	539	12	-7	2	1	232	232	4
1	3	0	302	300	4	5	7	0	560	558	10	-6	2	1	205	202	1
2	3	0	282	274	1	0	8	0	142	139	2	-5	2	1	53	45	3
3	3	0	841	851	4	1	8	0	910	912	11	-4	2	1	51	32	1
4	3	0	96	92	3	2	8	0	119	119	5	-3	2	1	113	113	2
5	3	0	1300	1305	12	3	8	0	807	803	15	-2	2	1	311	309	2
6	3	0	137	143	3	4	8	0	35	26	4	-1	2	1	111	106	1
7	3	0	972	982	8	1	9	0	131	130	2	0	2	1	421	424	1
8	3	0	65	64	3	-7	0	1	410	408	5	1	2	1	98	110	1
0	4	0	1130	1132	12	-5	0	1	264	269	1	2	2	1	1336	1323	5
1	4	0	1272	1286	5	-3	0	1	627	601	3	3	2	1	426	428	5
2	4	0	725	729	3	-1	0	1	592	598	5	4	2	1	870	864	5
3	4	0	943	944	7	1	0	1	866	843	5	5	2	1	456	451	5
4	4	0	558	555	4	3	0	1	1269	1260	12	6	2	1	787	779	4

Table B1 Observed and calculated structure factors for sample 1 (Cont…)

h	k	l	10Fo	10Fc	10s	h	k	l	10Fo	10Fc	10s	h	k	l	10Fo	10Fc	10s
7	2	1	246	250	2	-5	5	1	788	783	10	5	7	1	40	35	3
8	2	1	527	524	6	-4	5	1	79	63	4	-4	8	1	37	40	6
-8	3	1	572	577	16	-3	5	1	942	928	5	-3	8	1	20	17	4
-7	3	1	133	128	2	-2	5	1	268	270	1	-2	8	1	135	122	2
-6	3	1	792	780	12	-1	5	1	778	778	3	-1	8	1	45	41	7
-5	3	1	132	130	1	0	5	1	98	97	2	0	8	1	462	463	3
-4	3	1	1059	1060	8	1	5	1	698	697	3	1	8	1	39	17	3
-3	3	1	151	149	1	2	5	1	47	32	1	2	8	1	503	506	5
-2	3	1	1351	1351	10	3	5	1	479	470	4	3	8	1	48	26	3
-1	3	1	80	50	2	4	5	1	26	11	3	-1	9	1	217	228	3
0	3	1	1407	1412	5	5	5	1	130	128	2	0	9	1	476	484	5
1	3	1	415	410	1	6	5	1	23	19	13	-8	0	2	840	857	23
2	3	1	736	738	2	-6	6	1	108	100	4	-6	0	2	1381	1395	8
3	3	1	37	8	1	-5	6	1	143	140	4	-4	0	2	1631	1640	10
4	3	1	301	300	3	-4	6	1	115	126	1	-2	0	2	1584	1609	22
5	3	1	30	16	5	-3	6	1	132	132	2	0	0	2	685	671	5
6	3	1	94	93	2	-2	6	1	125	127	1	2	0	2	102	66	1
7	3	1	96	93	7	-1	6	1	489	489	3	4	0	2	880	889	13
-7	4	1	230	228	6	0	6	1	166	170	1	6	0	2	844	837	33
-6	4	1	140	140	2	1	6	1	531	531	3	-8	1	2	374	373	5
-5	4	1	284	285	1	2	6	1	242	245	2	-7	1	2	176	181	4
-4	4	1	92	93	2	3	6	1	640	632	4	-6	1	2	125	128	2
-3	4	1	117	113	2	4	6	1	120	122	1	-5	1	2	51	37	1
-2	4	1	48	41	2	5	6	1	728	727	23	-4	1	2	405	409	1
-1	4	1	335	339	1	6	6	1	224	223	9	-3	1	2	439	445	3
0	4	1	416	421	1	-5	7	1	411	414	6	-2	1	2	1048	1069	4
1	4	1	494	495	2	-4	7	1	417	428	6	-1	1	2	1092	1093	6
2	4	1	686	696	3	-3	7	1	420	422	5	0	1	2	1841	1838	19
3	4	1	501	492	2	-2	7	1	453	442	5	1	1	2	800	825	8
4	4	1	743	735	7	-1	7	1	415	410	8	2	1	2	1945	1933	25
5	4	1	517	507	7	0	7	1	471	473	3	3	1	2	844	832	7
6	4	1	478	490	5	1	7	1	212	212	3	4	1	2	954	951	5
7	4	1	484	483	4	2	7	1	339	334	4	5	1	2	358	359	2
-7	5	1	521	517	6	3	7	1	288	289	6	6	1	2	337	330	2
-6	5	1	147	147	4	4	7	1	67	74	2	7	1	2	162	169	2

Table B1 Observed and calculated structure factors for sample 1 (Cont…)

h	k	l	10Fo	10Fc	10s	h	k	l	10Fo	10Fc	10s	h	k	l	10Fo	10Fc	10s
-8	2	2	256	263	3	-5	4	2	1030	1044	9	2	6	2	199	195	2
-7	2	2	913	907	9	-4	4	2	640	639	6	3	6	2	152	160	1
-6	2	2	508	509	5	-3	4	2	993	989	5	4	6	2	547	543	3
-5	2	2	1265	1266	6	-2	4	2	688	700	3	5	6	2	176	176	6
-4	2	2	569	571	2	-1	4	2	466	474	2	-5	7	2	67	67	3
-3	2	2	1604	1611	6	0	4	2	256	258	2	-4	7	2	301	295	7
-2	2	2	282	303	2	1	4	2	91	80	1	-3	7	2	473	480	8
-1	2	2	573	587	2	2	4	2	167	161	2	-2	7	2	446	437	7
0	2	2	70	67	1	3	4	2	286	283	2	-1	7	2	719	719	17
1	2	2	101	87	3	4	4	2	634	635	5	0	7	2	761	762	5
2	2	2	239	230	2	5	4	2	581	569	6	1	7	2	692	699	6
3	2	2	422	425	2	6	4	2	470	479	3	2	7	2	723	715	11
4	2	2	364	366	2	-7	5	2	86	82	4	3	7	2	603	609	5
5	2	2	772	770	4	-6	5	2	37	4	4	4	7	2	465	458	5
6	2	2	459	456	2	-5	5	2	23	15	10	-4	8	2	96	94	6
7	2	2	787	786	6	-4	5	2	479	478	7	-3	8	2	718	725	13
-8	3	2	105	104	2	-3	5	2	166	162	2	-2	8	2	42	41	2
-7	3	2	220	222	10	-2	5	2	995	996	5	-1	8	2	521	523	4
-6	3	2	47	5	1	-1	5	2	284	283	5	0	8	2	45	33	6
-5	3	2	217	217	1	0	5	2	1335	1341	14	1	8	2	42	41	6
-4	3	2	35	18	2	1	5	2	495	496	3	2	8	2	100	105	4
-3	3	2	1017	1015	7	2	5	2	1337	1338	7	3	8	2	301	298	3
-2	3	2	389	383	1	3	5	2	209	205	2	-7	0	3	453	453	4
-1	3	2	1884	1886	8	4	5	2	892	890	5	-5	0	3	779	796	6
0	3	2	82	66	6	5	5	2	181	174	3	-3	0	3	1187	1203	8
1	3	2	1797	1820	13	6	5	2	401	408	6	-1	0	3	1979	1950	11
2	3	2	159	156	2	-6	6	2	901	893	26	1	0	3	1050	1047	6
3	3	2	1469	1456	11	-5	6	2	161	160	5	3	0	3	776	771	17
4	3	2	173	176	1	-4	6	2	958	964	8	5	0	3	497	497	7
5	3	2	818	807	4	-3	6	2	264	265	2	7	0	3	172	164	3
6	3	2	112	105	2	-2	6	2	846	849	6	-8	1	3	304	305	3
7	3	2	315	317	3	-1	6	2	195	192	5	-7	1	3	512	518	3
-7	4	2	591	593	22	0	6	2	532	541	5	-6	1	3	334	340	2
-6	4	2	629	625	7	1	6	2	94	85	1	-5	1	3	427	435	5

Table B1 Observed and calculated structure factors for sample 1 (cont…)

h	k	l	10Fo	10Fc	10s	h	k	l	10Fo	10Fc	10s	h	k	l	10Fo	10Fc	10s
-4	1	3	47	29	5	-2	3	3	122	107	2	4	5	3	222	223	2
-3	1	3	148	155	1	-1	3	3	50	37	2	5	5	3	570	569	7
-2	1	3	68	57	1	0	3	3	102	68	5	-6	6	3	155	151	5
-1	1	3	175	169	2	1	3	3	243	238	1	-5	6	3	507	509	6
0	1	3	267	260	3	2	3	3	436	430	2	-4	6	3	212	215	3
1	1	3	412	414	3	3	3	3	60	42	1	-3	6	3	811	814	12
2	1	3	318	317	2	4	3	3	788	783	6	-2	6	3	172	175	4
3	1	3	468	468	3	5	3	3	129	127	2	-1	6	3	801	796	8
4	1	3	539	541	6	6	3	3	690	688	6	0	6	3	219	214	2
5	1	3	742	743	4	-7	4	3	184	175	9	1	6	3	720	715	7
6	1	3	441	438	3	-6	4	3	410	415	9	2	6	3	184	186	2
7	1	3	601	597	8	-5	4	3	454	458	4	3	6	3	515	510	9
-8	2	3	251	261	3	-4	4	3	552	555	5	4	6	3	180	180	2
-7	2	3	144	145	4	-3	4	3	459	466	6	-5	7	3	191	200	7
-6	2	3	633	633	3	-2	4	3	654	663	3	-4	7	3	185	189	3
-5	2	3	108	100	1	-1	4	3	633	628	4	-3	7	3	113	107	2
-4	2	3	813	819	4	0	4	3	731	725	4	-2	7	3	62	59	1
-3	2	3	374	380	2	1	4	3	411	405	6	-1	7	3	109	112	5
-2	2	3	931	946	5	2	4	3	629	630	3	0	7	3	165	167	1
-1	2	3	501	506	4	3	4	3	425	429	4	1	7	3	182	178	2
0	2	3	1206	1202	6	4	4	3	284	286	3	2	7	3	352	352	3
1	2	3	276	278	3	5	4	3	187	188	3	3	7	3	286	290	4
2	2	3	816	820	11	6	4	3	150	146	3	-3	8	3	56	53	1
3	2	3	84	82	1	-7	5	3	409	408	10	-2	8	3	536	535	6
4	2	3	565	565	3	-6	5	3	69	73	2	-1	8	3	36	21	8
5	2	3	125	124	4	-5	5	3	403	409	13	0	8	3	552	548	7
6	2	3	115	114	1	-4	5	3	36	12	7	1	8	3	28	12	12
7	2	3	52	42	3	-3	5	3	274	271	3	-8	0	4	663	657	10
-8	3	3	607	615	13	-2	5	3	189	191	2	-6	0	4	415	405	6
-7	3	3	86	75	2	-1	5	3	113	112	2	-4	0	4	339	344	8
-6	3	3	607	605	14	0	5	3	69	71	4	-2	0	4	752	759	8
-5	3	3	68	68	2	1	5	3	428	423	9	0	0	4	1176	1192	10
-4	3	3	207	207	2	2	5	3	147	151	1	2	0	4	1643	1624	33
-3	3	3	132	129	3	3	5	3	482	479	2	4	0	4	1199	1169	9

Table B1 Observed and calculated structure factors for sample 1 (cont…)

h	k	l	10Fo	10Fc	10s	h	k	l	10Fo	10Fc	10s	h	k	l	10Fo	10Fc	10s
6	0	4	631	641	7	-4	3	4	169	165	2	4	5	4	273	264	5
-8	1	4	449	460	5	-3	3	4	1584	1559	10	-6	6	4	284	273	7
-7	1	4	333	343	5	-2	3	4	51	32	5	-5	6	4	120	112	8
-6	1	4	917	920	6	-1	3	4	1260	1255	8	-4	6	4	142	132	6
-5	1	4	629	626	5	0	3	4	281	278	4	-3	6	4	130	134	2
-4	1	4	1395	1390	16	1	3	4	468	469	3	-2	6	4	605	583	11
-3	1	4	741	733	4	2	3	4	30	5	2	-1	6	4	198	200	4
-2	1	4	1069	1083	9	3	3	4	104	99	4	0	6	4	877	857	6
-1	1	4	554	561	2	4	3	4	27	27	5	1	6	4	270	274	2
0	1	4	723	729	5	5	3	4	340	333	2	2	6	4	942	938	6
1	1	4	152	145	6	6	3	4	96	100	4	3	6	4	165	169	3
2	1	4	125	116	1	-7	4	4	308	312	9	4	6	4	816	815	8
3	1	4	210	215	3	-6	4	4	280	272	4	-4	7	4	549	554	12
4	1	4	235	234	1	-5	4	4	65	57	1	-3	7	4	591	588	12
5	1	4	249	251	4	-4	4	4	129	126	3	-2	7	4	544	540	5
6	1	4	525	523	6	-3	4	4	234	226	12	-1	7	4	504	507	4
-8	2	4	291	294	3	-2	4	4	514	508	3	0	7	4	271	269	2
-7	2	4	397	394	8	-1	4	4	802	787	15	1	7	4	235	241	4
-6	2	4	99	93	2	0	4	4	734	725	8	2	7	4	117	115	5
-5	2	4	200	200	3	1	4	4	982	990	5	-1	8	4	702	689	10
-4	2	4	159	165	1	2	4	4	800	799	10	-7	0	5	677	682	8
-3	2	4	451	457	2	3	4	4	887	889	4	-5	0	5	659	652	5
-2	2	4	301	304	1	4	4	4	587	594	4	-3	0	5	669	674	9
-1	2	4	934	939	5	5	4	4	517	529	4	-1	0	5	248	240	2
0	2	4	486	484	7	-6	5	4	871	877	29	1	0	5	110	111	2
1	2	4	1475	1485	7	-5	5	4	199	204	3	3	0	5	324	320	3
2	2	4	675	670	8	-4	5	4	1085	1072	18	5	0	5	413	411	5
3	2	4	1085	1081	9	-3	5	4	357	367	4	-8	1	5	43	26	7
4	2	4	542	539	5	-2	5	4	939	941	5	-7	1	5	311	307	7
5	2	4	784	780	8	-1	5	4	195	199	3	-6	1	5	186	189	3
6	2	4	200	205	4	0	5	4	710	707	10	-5	1	5	308	307	2
-7	3	4	748	755	12	1	5	4	103	90	4	-4	1	5	296	298	4
-6	3	4	118	115	8	2	5	4	212	214	3	-3	1	5	510	506	2
-5	3	4	1221	1221	12	3	5	4	95	93	6	-2	1	5	509	505	3

Table B1 Observed and calculated structure factors for sample 1 (cont…)

h	k	l	10Fo	10Fc	10s	h	k	l	10Fo	10Fc	10s	h	k	l	10Fo	10Fc	10s
-1	1	5	852	855	4	-6	4	5	493	490	5	-4	0	6	1242	1222	11
0	1	5	393	396	3	-5	4	5	230	229	5	-2	0	6	1470	1443	25
1	1	5	902	911	6	-4	4	5	348	341	2	0	0	6	915	901	8
2	1	5	529	531	4	-3	4	5	316	315	4	2	0	6	421	433	4
3	1	5	602	601	4	-2	4	5	116	111	3	4	0	6	69	54	13
4	1	5	315	312	4	-1	4	5	89	81	1	-7	1	6	342	340	3
5	1	5	347	348	3	0	4	5	25	16	3	-6	1	6	535	537	5
-7	2	5	202	203	5	1	4	5	76	75	5	-5	1	6	112	105	3
-6	2	5	589	593	6	2	4	5	70	60	2	-4	1	6	108	98	10
-5	2	5	196	193	1	3	4	5	339	341	2	-3	1	6	51	37	3
-4	2	5	583	580	3	4	4	5	277	277	3	-2	1	6	330	331	2
-3	2	5	68	64	4	-6	5	5	77	73	3	-1	1	6	388	386	4
-2	2	5	192	192	1	-5	5	5	355	351	9	0	1	6	670	667	4
-1	2	5	41	30	3	-4	5	5	137	141	4	1	1	6	560	562	7
0	2	5	110	95	5	-3	5	5	556	549	4	2	1	6	754	758	12
1	2	5	120	128	1	-2	5	5	112	95	2	3	1	6	586	592	5
2	2	5	89	77	3	-1	5	5	715	713	4	4	1	6	825	828	10
3	2	5	148	151	4	0	5	5	256	249	2	-7	2	6	537	530	5
4	2	5	411	416	3	1	5	5	730	718	7	-6	2	6	226	230	6
5	2	5	252	260	4	2	5	5	125	123	4	-5	2	6	849	849	7
-7	3	5	0	9	1	3	5	5	575	582	4	-4	2	6	486	484	3
-6	3	5	344	339	4	-5	6	5	422	420	6	-3	2	6	1051	1038	6
-5	3	5	34	35	2	-4	6	5	141	141	7	-2	2	6	521	524	4
-4	3	5	585	584	6	-3	6	5	384	381	6	-1	2	6	1119	1122	9
-3	3	5	197	199	1	-2	6	5	130	131	3	0	2	6	312	315	4
-2	3	5	800	805	4	-1	6	5	292	292	3	1	2	6	585	581	6
-1	3	5	87	79	3	0	6	5	45	48	4	2	2	6	80	75	4
0	3	5	809	812	7	1	6	5	82	66	8	3	2	6	193	189	5
1	3	5	81	75	1	2	6	5	89	91	4	4	2	6	31	40	3
2	3	5	863	858	5	-3	7	5	225	235	3	-6	3	6	74	76	6
3	3	5	143	149	1	-2	7	5	411	410	4	-5	3	6	343	347	6
4	3	5	609	609	5	-1	7	5	384	387	3	-4	3	6	59	59	2
5	3	5	78	75	6	0	7	5	390	395	12	-3	3	6	27	29	13
-7	4	5	312	302	12	-6	0	6	793	802	7	-2	3	6	25	17	3

Table B1 Observed and calculated structure factors for sample 1 (cont…)

h	k	l	10Fo	10Fc	10s	h	k	l	10Fo	10Fc	10s	h	k	l	10Fo	10Fc	10s
-1	3	6	433	435	2	-4	1	7	309	313	4	0	0	8	309	302	6
0	3	6	199	185	7	-3	1	7	418	416	4	-4	1	8	629	626	7
1	3	6	824	824	5	-2	1	7	202	202	2	-3	1	8	511	512	5
2	3	6	67	70	2	-1	1	7	349	353	2	-2	1	8	871	853	9
3	3	6	888	903	7	0	1	7	116	116	1	-1	1	8	461	464	4
-6	4	6	467	479	5	1	1	7	146	136	3	0	1	8	709	720	7
-5	4	6	604	602	6	2	1	7	44	37	2	-3	2	8	144	150	2
-4	4	6	594	598	5	-6	2	7	24	23	7	-2	2	8	97	84	3
-3	4	6	812	812	7	-5	2	7	163	165	2	-1	2	8	154	151	1
-2	4	6	643	647	4	-4	2	7	298	290	5						
-1	4	6	776	773	6	-3	2	7	140	139	2						
0	4	6	449	449	2	-2	2	7	408	413	5						
1	4	6	469	466	8	-1	2	7	222	223	4						
2	4	6	277	281	2	0	2	7	623	620	4						
3	4	6	42	30	12	1	2	7	342	347	8						
-5	5	6	42	32	4	2	2	7	558	573	6						
-4	5	6	188	191	2	-5	3	7	93	87	3						
-3	5	6	139	142	2	-4	3	7	665	653	7						
-2	5	6	274	272	2	-3	3	7	25	26	17						
-1	5	6	132	132	1	-2	3	7	480	487	4						
0	5	6	629	627	5	-1	3	7	139	143	3						
1	5	6	284	287	2	0	3	7	265	266	2						
2	5	6	710	711	6	1	3	7	35	23	3						
-3	6	6	178	177	3	2	3	7	96	92	4						
-2	6	6	844	840	12	-4	4	7	176	171	3						
-1	6	6	213	207	2	-3	4	7	272	278	3						
0	6	6	630	635	7	-2	4	7	345	352	3						
-5	0	7	238	238	14	-1	4	7	348	352	4						
-3	0	7	295	294	3	0	4	7	416	419	3						
-1	0	7	444	442	3	1	4	7	450	454	10						
1	0	7	795	782	15	-2	5	7	64	60	2						
3	0	7	624	641	9	-1	5	7	361	382	6						
-6	1	7	283	271	2	-4	0	8	527	511	31						
-5	1	7	549	530	7	-2	0	8	41	22	13						

Table B2 Observed and calculated structure factors for sample 2

h	k	l	10Fo	10Fc	10s	h	k	l	10Fo	10Fc	10s	h	k	l	10Fo	10Fc	10s
2	0	0	2112	2125	45	5	4	0	332	335	4	-8	1	1	237	239	11
4	0	0	1042	1043	6	6	4	0	105	105	1	-7	1	1	425	415	3
6	0	0	349	354	8	7	4	0	36	36	12	-6	1	1	303	297	4
8	0	0	45	33	8	1	5	0	106	107	3	-5	1	1	760	763	7
1	1	0	368	369	1	2	5	0	681	681	6	-4	1	1	510	519	2
2	1	0	788	824	8	3	5	0	200	205	4	-3	1	1	1433	1409	5
3	1	0	395	416	4	4	5	0	817	813	18	-2	1	1	456	469	1
4	1	0	957	966	6	5	5	0	260	257	8	-1	1	1	982	970	8
5	1	0	727	731	4	6	5	0	712	695	32	0	1	1	647	654	4
6	1	0	946	921	10	7	5	0	211	215	9	1	1	1	707	705	7
7	1	0	486	474	6	0	6	0	1365	1347	14	2	1	1	211	223	2
8	1	0	567	561	6	1	6	0	292	299	4	3	1	1	411	420	2
0	2	0	1038	1034	7	2	6	0	1158	1155	15	4	1	1	44	15	5
1	2	0	1899	2059	20	3	6	0	261	265	2	5	1	1	282	284	2
2	2	0	615	618	3	4	6	0	590	591	11	6	1	1	43	14	3
3	2	0	1304	1324	16	5	6	0	156	166	4	7	1	1	137	141	2
4	2	0	111	112	1	6	6	0	227	239	10	8	1	1	155	154	6
5	2	0	633	631	6	1	7	0	176	181	4	-8	2	1	346	356	9
6	2	0	69	65	7	2	7	0	304	310	3	-7	2	1	190	183	7
7	2	0	54	16	3	3	7	0	424	437	15	-6	2	1	173	168	6
8	2	0	30	23	9	4	7	0	433	423	7	-5	2	1	47	31	1
1	3	0	271	285	1	5	7	0	457	475	10	-4	2	1	48	14	1
2	3	0	277	271	1	0	8	0	101	89	12	-3	2	1	114	114	1
3	3	0	789	800	4	1	8	0	828	821	7	-2	2	1	310	316	2
4	3	0	92	98	1	2	8	0	82	71	6	-1	2	1	119	116	1
5	3	0	1191	1164	25	3	8	0	703	696	10	0	2	1	451	450	1
6	3	0	131	134	4	-7	0	1	339	339	4	1	2	1	109	113	1
7	3	0	844	816	31	-5	0	1	221	223	3	2	2	1	1342	1316	18
8	3	0	88	65	30	-3	0	1	608	600	9	3	2	1	399	407	3
0	4	0	1133	1147	7	-1	0	1	624	626	16	4	2	1	847	847	5
1	4	0	1208	1240	14	1	0	1	891	883	5	5	2	1	409	404	2
2	4	0	741	750	3	3	0	1	1263	1257	13	6	2	1	744	709	8
3	4	0	896	901	8	5	0	1	1117	1065	12	7	2	1	211	205	4
4	4	0	536	534	6	7	0	1	752	709	11	-8	3	1	480	461	21

Table B2 Observed and calculated structure factors for sample 2 (cont…)

h	k	l	10Fo	10Fc	10s	h	k	l	10Fo	10Fc	10s	h	k	l	10Fo	10Fc	10s
-7	3	1	106	109	5	-3	5	1	878	886	9	-4	8	1	62	22	4
-6	3	1	730	699	16	-2	5	1	222	226	3	-3	8	1	0	17	1
-5	3	1	137	138	1	-1	5	1	758	768	14	-2	8	1	109	117	10
-4	3	1	1015	1008	9	0	5	1	83	76	1	-1	8	1	25	24	14
-3	3	1	160	163	3	1	5	1	671	680	3	0	8	1	404	399	3
-2	3	1	1328	1338	5	2	5	1	59	35	7	1	8	1	22	26	9
-1	3	1	58	27	1	3	5	1	457	455	5	2	8	1	452	451	13
0	3	1	1439	1409	11	4	5	1	0	7	1	3	8	1	17	8	17
1	3	1	414	410	5	5	5	1	129	131	2	-8	0	2	682	683	8
2	3	1	730	740	5	6	5	1	36	12	7	-6	0	2	1232	1212	13
3	3	1	51	12	6	-6	6	1	87	83	5	-4	0	2	1528	1535	16
4	3	1	305	308	3	-5	6	1	106	99	4	-2	0	2	1574	1564	9
5	3	1	36	19	12	-4	6	1	106	103	4	0	0	2	688	686	8
6	3	1	91	95	7	-3	6	1	126	130	2	2	0	2	146	89	2
7	3	1	90	69	2	-2	6	1	109	112	3	4	0	2	810	807	12
-7	4	1	185	186	13	-1	6	1	448	455	5	6	0	2	767	731	9
-6	4	1	106	101	3	0	6	1	164	168	2	-8	1	2	264	255	7
-5	4	1	225	233	8	1	6	1	492	496	6	-7	1	2	129	128	8
-4	4	1	93	94	2	2	6	1	233	236	2	-6	1	2	133	141	5
-3	4	1	110	110	1	3	6	1	569	578	15	-5	1	2	54	50	2
-2	4	1	69	57	2	4	6	1	142	134	2	-4	1	2	421	422	3
-1	4	1	326	337	4	5	6	1	631	632	19	-3	1	2	448	448	2
0	4	1	403	413	5	6	6	1	212	196	12	-2	1	2	1057	1064	9
1	4	1	477	487	8	-5	7	1	325	333	11	-1	1	2	1102	1090	7
2	4	1	648	661	3	-4	7	1	385	383	12	0	1	2	1888	1835	23
3	4	1	476	481	2	-3	7	1	356	365	4	1	1	2	810	840	11
4	4	1	679	670	11	-2	7	1	425	424	4	2	1	2	1933	1913	8
5	4	1	493	482	6	-1	7	1	356	351	3	3	1	2	818	825	7
6	4	1	433	427	3	0	7	1	454	447	2	4	1	2	940	927	6
7	4	1	415	408	15	1	7	1	199	190	2	5	1	2	359	356	4
-7	5	1	436	430	22	2	7	1	314	312	9	6	1	2	342	337	2
-6	5	1	118	109	5	3	7	1	244	238	4	7	1	2	157	163	4
-5	5	1	710	702	21	4	7	1	83	84	4	-8	2	2	204	201	24
-4	5	1	68	51	2	5	7	1	41	37	11	-7	2	2	767	752	14

Table B2 Observed and calculated structure factors for sample 2 (cont…)

h	k	l	10Fo	10Fc	10s	h	k	l	10Fo	10Fc	10s	h	k	l	10Fo	10Fc	10s
-6	2	2	426	426	8	-3	4	2	895	889	8	4	6	2	455	448	7
-5	2	2	1159	1147	18	-2	4	2	667	674	7	5	6	2	147	151	6
-4	2	2	496	509	4	-1	4	2	431	450	2	-5	7	2	70	70	15
-3	2	2	1540	1529	39	0	4	2	264	275	1	-4	7	2	240	246	6
-2	2	2	270	289	1	1	4	2	68	63	4	-3	7	2	421	421	3
-1	2	2	564	592	3	2	4	2	141	137	4	-2	7	2	386	383	4
0	2	2	77	74	1	3	4	2	237	242	1	-1	7	2	674	662	4
1	2	2	127	114	1	4	4	2	550	555	7	0	7	2	675	658	7
2	2	2	203	201	4	5	4	2	489	476	6	1	7	2	665	658	5
3	2	2	372	382	5	6	4	2	396	405	7	2	7	2	605	615	12
4	2	2	319	319	2	-7	5	2	70	45	28	3	7	2	548	560	17
5	2	2	689	677	8	-6	5	2	40	26	13	4	7	2	383	386	8
6	2	2	399	383	3	-5	5	2	41	8	15	-3	8	2	604	611	7
7	2	2	674	654	11	-4	5	2	444	445	3	-2	8	2	19	5	8
-8	3	2	64	75	7	-3	5	2	139	137	1	-1	8	2	446	447	3
-7	3	2	148	141	2	-2	5	2	939	938	18	0	8	2	0	6	1
-6	3	2	51	2	7	-1	5	2	245	248	1	1	8	2	42	45	11
-5	3	2	223	232	11	0	5	2	1325	1297	32	2	8	2	79	83	2
-4	3	2	39	22	2	1	5	2	423	426	4	-7	0	3	392	397	3
-3	3	2	993	980	10	2	5	2	1262	1285	22	-5	0	3	728	723	6
-2	3	2	384	374	2	3	5	2	165	173	3	-3	0	3	1165	1164	6
-1	3	2	1874	1850	34	4	5	2	830	833	11	-1	0	3	1924	1924	17
0	3	2	105	93	1	5	5	2	130	140	7	1	0	3	1035	1054	10
1	3	2	1829	1801	9	6	5	2	376	382	11	3	0	3	790	774	7
2	3	2	182	184	2	-6	6	2	746	720	29	5	0	3	489	478	9
3	3	2	1410	1415	10	-5	6	2	164	169	7	7	0	3	164	163	3
4	3	2	179	182	2	-4	6	2	836	818	16	-8	1	3	230	236	2
5	3	2	779	770	7	-3	6	2	251	261	2	-7	1	3	406	410	2
6	3	2	105	99	5	-2	6	2	746	758	13	-6	1	3	279	280	4
7	3	2	289	304	3	-1	6	2	197	199	1	-5	1	3	364	374	2
-7	4	2	476	476	21	0	6	2	486	491	2	-4	1	3	52	26	10
-6	4	2	557	545	20	1	6	2	85	86	3	-3	1	3	131	138	6
-5	4	2	902	887	8	2	6	2	155	156	7	-2	1	3	62	59	1
-4	4	2	597	597	7	3	6	2	139	138	3	-1	1	3	188	171	2

Table B2 Observed and calculated structure factors for sample 2 (cont…)

h	k	l	10Fo	10Fc	10s	h	k	l	10Fo	10Fc	10s	h	k	l	10Fo	10Fc	10s
0	1	3	249	242	3	3	3	3	59	42	6	-3	6	3	726	717	15
1	1	3	396	401	5	4	3	3	726	723	6	-2	6	3	182	177	2
2	1	3	314	293	5	5	3	3	119	119	3	-1	6	3	740	729	5
3	1	3	463	453	3	6	3	3	597	599	12	0	6	3	226	221	2
4	1	3	510	500	2	-7	4	3	150	147	7	1	6	3	651	656	12
5	1	3	688	674	8	-6	4	3	338	344	9	2	6	3	203	198	5
6	1	3	385	385	4	-5	4	3	409	396	3	3	6	3	449	461	9
7	1	3	511	503	8	-4	4	3	511	504	5	4	6	3	165	170	8
-8	2	3	204	216	4	-3	4	3	465	455	4	-5	7	3	148	133	8
-7	2	3	121	122	2	-2	4	3	616	613	6	-4	7	3	146	155	2
-6	2	3	553	547	5	-1	4	3	610	617	13	-3	7	3	72	69	4
-5	2	3	95	97	2	0	4	3	662	684	18	-2	7	3	60	52	11
-4	2	3	758	768	6	1	4	3	402	416	15	-1	7	3	101	100	2
-3	2	3	350	349	3	2	4	3	584	588	7	0	7	3	126	132	2
-2	2	3	932	937	12	3	4	3	421	422	3	1	7	3	153	158	5
-1	2	3	477	478	6	4	4	3	267	265	3	2	7	3	300	300	11
0	2	3	1172	1192	22	5	4	3	184	184	6	3	7	3	223	234	7
1	2	3	264	270	7	6	4	3	132	133	3	-3	8	3	29	25	7
2	2	3	837	826	7	-7	5	3	289	311	8	-2	8	3	463	460	4
3	2	3	88	81	3	-6	5	3	59	46	4	-1	8	3	0	7	1
4	2	3	558	550	3	-5	5	3	338	338	8	0	8	3	485	488	9
5	2	3	126	115	2	-4	5	3	38	26	2	1	8	3	9	20	8
6	2	3	129	130	3	-3	5	3	225	228	3	-8	0	4	447	463	7
-8	3	3	430	456	21	-2	5	3	173	177	2	-6	0	4	312	300	2
-7	3	3	70	67	4	-1	5	3	93	101	1	-4	0	4	347	332	7
-6	3	3	493	490	5	0	5	3	45	54	1	-2	0	4	718	728	15
-5	3	3	67	64	3	1	5	3	382	386	5	0	0	4	1100	1170	42
-4	3	3	178	177	3	2	5	3	132	132	1	2	0	4	1611	1563	32
-3	3	3	129	131	2	3	5	3	441	439	5	4	0	4	1135	1107	16
-2	3	3	85	84	1	4	5	3	171	180	2	6	0	4	584	590	15
-1	3	3	48	37	1	5	5	3	501	499	7	-8	1	4	314	352	5
0	3	3	90	74	2	-6	6	3	115	122	3	-7	1	4	270	278	6
1	3	3	217	213	1	-5	6	3	418	431	7	-6	1	4	755	762	4
2	3	3	423	417	6	-4	6	3	197	193	5	-5	1	4	539	545	4

Table B2 Observed and calculated structure factors for sample 2 (cont…)

h	k	l	10Fo	10Fc	10s	h	k	l	10Fo	10Fc	10s	h	k	l	10Fo	10Fc	10s
-4	1	4	1219	1232	15	1	3	4	467	466	5	0	6	4	755	757	28
-3	1	4	671	679	3	2	3	4	39	15	9	1	6	4	262	257	3
-2	1	4	1016	1023	12	3	3	4	66	53	6	2	6	4	851	833	10
-1	1	4	537	557	6	4	3	4	24	19	19	3	6	4	154	171	2
0	1	4	698	713	12	5	3	4	254	264	5	-4	7	4	422	431	8
1	1	4	167	160	1	-7	4	4	205	203	4	-3	7	4	508	514	9
2	1	4	147	140	2	-6	4	4	214	205	4	-2	7	4	436	425	5
3	1	4	157	170	1	-5	4	4	46	27	6	-1	7	4	446	454	5
4	1	4	178	178	3	-4	4	4	101	107	2	0	7	4	207	221	3
5	1	4	194	204	3	-3	4	4	213	213	1	1	7	4	217	226	3
6	1	4	427	423	4	-2	4	4	465	456	7	2	7	4	94	92	7
-8	2	4	182	198	3	-1	4	4	744	716	10	-7	0	5	493	510	7
-7	2	4	291	288	2	0	4	4	686	678	15	-5	0	5	538	542	4
-6	2	4	69	59	8	1	4	4	909	904	17	-3	0	5	565	583	4
-5	2	4	137	144	4	2	4	4	749	746	4	-1	0	5	219	223	12
-4	2	4	142	152	3	3	4	4	798	802	6	1	0	5	105	111	7
-3	2	4	410	420	9	4	4	4	539	554	4	3	0	5	275	283	2
-2	2	4	278	284	7	5	4	4	445	466	4	5	0	5	332	356	16
-1	2	4	917	899	8	-6	5	4	700	696	20	-8	1	5	42	27	18
0	2	4	431	444	8	-5	5	4	136	149	10	-7	1	5	225	241	5
1	2	4	1478	1423	11	-4	5	4	926	922	10	-6	1	5	142	149	3
2	2	4	633	617	4	-3	5	4	287	286	3	-5	1	5	272	271	3
3	2	4	1049	1030	10	-2	5	4	882	854	5	-4	1	5	258	263	3
4	2	4	482	481	4	-1	5	4	140	149	2	-3	1	5	451	456	7
5	2	4	719	724	9	0	5	4	658	659	9	-2	1	5	440	452	11
6	2	4	180	179	5	1	5	4	86	83	5	-1	1	5	810	788	24
-7	3	4	588	597	10	2	5	4	215	221	3	0	1	5	373	372	4
-6	3	4	114	112	4	3	5	4	84	83	2	1	1	5	862	854	15
-5	3	4	1011	1035	9	4	5	4	204	199	3	2	1	5	498	496	9
-4	3	4	160	160	3	-5	6	4	93	94	3	3	1	5	565	556	4
-3	3	4	1443	1407	15	-4	6	4	123	122	3	4	1	5	288	287	5
-2	3	4	68	57	1	-3	6	4	104	105	5	5	1	5	328	321	3
-1	3	4	1188	1179	23	-2	6	4	533	513	6	-7	2	5	147	145	2
0	3	4	277	277	4	-1	6	4	187	187	5	-6	2	5	464	470	4

Table B2 Observed and calculated structure factors for sample 2 (cont…)

h	k	l	10Fo	10Fc	10s	h	k	l	10Fo	10Fc	10s	h	k	l	10Fo	10Fc	10s
-5	2	5	149	146	3	-6	5	5	67	62	9	-1	1	6	341	333	3
-4	2	5	490	490	3	-5	5	5	280	284	4	0	1	6	595	588	7
-3	2	5	55	51	8	-4	5	5	103	108	1	1	1	6	497	490	5
-2	2	5	164	174	7	-3	5	5	485	466	3	2	1	6	685	676	5
-1	2	5	36	31	4	-2	5	5	78	80	3	3	1	6	499	520	6
0	2	5	106	104	5	-1	5	5	649	640	4	4	1	6	695	720	6
1	2	5	115	112	1	0	5	5	187	194	4	-7	2	6	368	388	6
2	2	5	71	63	2	1	5	5	664	651	13	-6	2	6	168	172	3
3	2	5	115	127	7	2	5	5	91	86	5	-5	2	6	700	677	6
4	2	5	351	354	2	3	5	5	505	526	13	-4	2	6	382	386	7
5	2	5	205	217	3	-5	6	5	306	307	7	-3	2	6	925	898	12
-7	3	5	63	1	5	-4	6	5	122	126	3	-2	2	6	438	441	3
-6	3	5	270	279	2	-3	6	5	303	301	3	-1	2	6	1053	1003	11
-5	3	5	41	25	10	-2	6	5	129	129	3	0	2	6	267	276	10
-4	3	5	510	507	7	-1	6	5	239	236	10	1	2	6	551	548	4
-3	3	5	157	174	5	0	6	5	41	61	10	2	2	6	79	66	5
-2	3	5	753	729	10	1	6	5	61	51	7	3	2	6	190	198	2
-1	3	5	78	78	2	2	6	5	71	61	7	4	2	6	0	26	1
0	3	5	776	758	16	-3	7	5	177	187	3	-6	3	6	59	63	15
1	3	5	88	89	5	-2	7	5	333	338	12	-5	3	6	261	257	5
2	3	5	799	794	5	-1	7	5	308	309	9	-4	3	6	67	62	2
3	3	5	141	145	7	0	7	5	343	344	10	-3	3	6	58	14	5
4	3	5	554	554	6	-6	0	6	616	617	10	-2	3	6	40	16	12
-6	4	5	356	361	5	-4	0	6	1032	1025	29	-1	3	6	392	379	4
-5	4	5	193	194	2	-2	0	6	1311	1279	14	0	3	6	159	156	8
-4	4	5	258	264	9	0	0	6	848	832	15	1	3	6	722	727	5
-3	4	5	287	274	2	2	0	6	413	426	4	2	3	6	65	66	4
-2	4	5	98	89	3	4	0	6	89	81	3	3	3	6	766	790	7
-1	4	5	101	94	4	-7	1	6	236	236	3	-6	4	6	356	351	8
0	4	5	30	6	12	-6	1	6	391	392	5	-5	4	6	472	466	7
1	4	5	47	49	5	-5	1	6	106	85	15	-4	4	6	499	496	4
2	4	5	62	51	3	-4	1	6	79	74	5	-3	4	6	660	657	23
3	4	5	271	280	3	-3	1	6	32	26	9	-2	4	6	600	563	5
4	4	5	211	231	4	-2	1	6	301	290	5	-1	4	6	682	656	5

Table B2 Observed and calculated structure factors for sample 2 (cont…)

h	k	l	10Fo	10Fc	10s	h	k	l	10Fo	10Fc	10s	h	k	l	10Fo	10Fc	10s
0	4	6	419	410	5	-4	1	7	252	240	4	1	3	7	62	32	4
1	4	6	396	404	5	-3	1	7	341	332	3	2	3	7	84	94	6
2	4	6	251	267	5	-2	1	7	174	173	3	-4	4	7	129	135	6
3	4	6	49	39	12	-1	1	7	296	297	7	-3	4	7	213	205	3
-5	5	6	54	3	11	0	1	7	105	104	9	-2	4	7	289	280	3
-4	5	6	145	142	4	1	1	7	125	125	3	-1	4	7	299	283	4
-3	5	6	139	123	3	2	1	7	36	16	16	0	4	7	328	337	12
-2	5	6	229	221	7	-6	2	7	0	30	1	1	4	7	349	374	9
-1	5	6	119	110	4	-5	2	7	117	127	17	-2	5	7	49	21	20
0	5	6	545	527	8	-4	2	7	225	223	11	-4	0	8	377	376	6
1	5	6	234	234	10	-3	2	7	112	113	4	-2	0	8	37	13	12
2	5	6	576	606	15	-2	2	7	338	340	8	0	0	8	223	237	15
-3	6	6	173	162	7	-1	2	7	164	175	11	-4	1	8	459	468	5
-2	6	6	691	682	19	0	2	7	519	527	5	-3	1	8	385	391	3
-1	6	6	211	195	8	1	2	7	273	283	4	-2	1	8	662	676	9
0	6	6	552	536	15	2	2	7	472	491	4	-1	1	8	351	376	8
-5	0	7	203	195	4	-5	3	7	68	68	17	0	1	8	567	598	8
-3	0	7	240	241	8	-4	3	7	523	498	8	-3	2	8	114	117	4
-1	0	7	381	382	7	-3	3	7	43	33	15	-2	2	8	73	69	8
1	0	7	669	675	22	-2	3	7	391	394	5	-1	2	8	110	108	2
-6	1	7	204	194	4	-1	3	7	128	134	5						
-5	1	7	395	390	5	0	3	7	237	230	3						

Table B.3 Observed and calculated structure factors for sample 3

h	k	l	10Fo	10Fc	10s	h	k	l	10Fo	10Fc	10s	h	k	l	10Fo	10Fc	10s
2	0	0	2129	2119	42	2	4	0	769	758	6	2	8	0	104	109	6
4	0	0	1058	1063	23	3	4	0	979	965	12	3	8	0	863	848	8
6	0	0	361	353	5	4	4	0	574	574	6	4	8	0	29	30	4
8	0	0	40	4	33	5	4	0	356	363	4	5	8	0	397	398	8
1	1	0	379	377	7	6	4	0	101	104	3	6	8	0	40	7	13
2	1	0	836	853	10	7	4	0	51	18	5	1	9	0	141	138	2
3	1	0	416	439	2	8	4	0	119	116	2	2	9	0	149	153	3
4	1	0	1025	1040	16	9	4	0	210	203	9	3	9	0	495	503	4
5	1	0	803	819	9	1	5	0	125	118	2	4	9	0	243	244	4
6	1	0	1088	1077	8	2	5	0	766	754	5	5	9	0	564	566	11
7	1	0	584	577	4	3	5	0	257	247	10	0	10	0	583	583	16
8	1	0	739	722	7	4	5	0	938	936	6	1	10	0	370	365	3
9	1	0	342	340	3	5	5	0	327	325	7	2	10	0	547	562	6
0	2	0	1010	1050	5	6	5	0	859	858	7	3	10	0	331	334	11
1	2	0	2041	2048	28	7	5	0	299	299	7	-9	0	1	557	546	21
2	2	0	634	635	7	8	5	0	695	689	6	-7	0	1	426	416	4
3	2	0	1366	1343	7	0	6	0	1499	1471	22	-5	0	1	263	264	2
4	2	0	108	103	8	1	6	0	319	304	4	-3	0	1	626	607	3
5	2	0	667	668	7	2	6	0	1324	1286	7	-1	0	1	617	603	4
6	2	0	67	56	7	3	6	0	288	285	3	1	0	1	809	853	5
7	2	0	59	49	5	4	6	0	675	672	5	3	0	1	1270	1280	7
8	2	0	54	46	6	5	6	0	189	198	2	5	0	1	1179	1157	19
9	2	0	214	206	3	6	6	0	266	280	10	7	0	1	872	848	14
1	3	0	297	299	3	7	6	0	51	32	6	9	0	1	455	440	5
2	3	0	296	285	2	8	6	0	76	59	10	-10	1	1	88	81	7
3	3	0	864	861	5	1	7	0	221	213	2	-9	1	1	327	336	3
4	3	0	101	100	2	2	7	0	384	378	5	-8	1	1	316	307	6
5	3	0	1318	1330	14	3	7	0	530	526	7	-7	1	1	485	485	3
6	3	0	154	152	3	4	7	0	541	549	4	-6	1	1	334	327	4
7	3	0	1029	1018	8	5	7	0	601	595	4	-5	1	1	830	829	11
8	3	0	76	73	3	6	7	0	459	450	7	-4	1	1	532	541	2
9	3	0	584	581	8	7	7	0	515	505	9	-3	1	1	1422	1450	8
0	4	0	1170	1162	23	0	8	0	136	129	3	-2	1	1	447	458	8
1	4	0	1320	1302	6	1	8	0	976	962	8	-1	1	1	958	955	3

Table B3 Observed and calculated structure factors for sample 3 (cont…)

h	k	l	10Fo	10Fc	10s	h	k	l	10Fo	10Fc	10s	h	k	l	10Fo	10Fc	10s
0	1	1	626	635	4	-4	3	1	1085	1078	8	-6	5	1	150	144	2
1	1	1	671	690	5	-3	3	1	166	162	1	-5	5	1	810	810	13
2	1	1	189	208	2	-2	3	1	1399	1372	10	-4	5	1	70	61	1
3	1	1	398	413	3	-1	3	1	71	39	1	-3	5	1	970	956	8
4	1	1	37	15	2	0	3	1	1479	1429	7	-2	5	1	270	263	4
5	1	1	300	303	4	1	3	1	442	422	2	-1	5	1	814	803	9
6	1	1	52	23	10	2	3	1	764	753	5	0	5	1	90	88	4
7	1	1	180	183	6	3	3	1	33	7	2	1	5	1	738	716	5
8	1	1	214	209	3	4	3	1	322	315	5	2	5	1	53	38	4
9	1	1	338	340	9	5	3	1	27	16	9	3	5	1	496	492	5
-9	2	1	225	220	5	6	3	1	103	104	1	4	5	1	24	12	8
-8	2	1	486	470	4	7	3	1	109	97	1	5	5	1	128	137	1
-7	2	1	234	232	1	8	3	1	217	210	3	6	5	1	22	14	5
-6	2	1	211	206	3	9	3	1	0	24	1	7	5	1	196	195	7
-5	2	1	46	38	4	-9	4	1	310	310	3	8	5	1	77	42	19
-4	2	1	49	29	5	-8	4	1	382	372	7	-8	6	1	74	97	10
-3	2	1	119	113	3	-7	4	1	233	239	3	-7	6	1	342	333	5
-2	2	1	312	310	3	-6	4	1	142	135	5	-6	6	1	117	110	3
-1	2	1	115	107	1	-5	4	1	293	290	4	-5	6	1	134	137	3
0	2	1	411	434	1	-4	4	1	99	98	1	-4	6	1	129	131	3
1	2	1	92	108	3	-3	4	1	122	112	1	-3	6	1	131	136	2
2	2	1	1389	1337	6	-2	4	1	53	47	3	-2	6	1	132	127	4
3	2	1	424	428	3	-1	4	1	341	347	2	-1	6	1	495	502	6
4	2	1	880	888	4	0	4	1	429	428	2	0	6	1	194	184	2
5	2	1	461	459	4	1	4	1	508	506	4	1	6	1	560	546	3
6	2	1	818	807	5	2	4	1	711	700	3	2	6	1	267	263	4
7	2	1	267	254	3	3	4	1	533	510	6	3	6	1	648	654	3
8	2	1	571	554	6	4	4	1	754	751	4	4	6	1	143	141	2
9	2	1	168	166	3	5	4	1	528	534	3	5	6	1	770	762	8
-9	3	1	30	35	7	6	4	1	497	509	10	6	6	1	226	242	4
-8	3	1	612	598	10	7	4	1	523	511	4	7	6	1	576	584	13
-7	3	1	136	134	1	8	4	1	427	423	9	-7	7	1	265	264	3
-6	3	1	797	802	16	-8	5	1	68	70	8	-6	7	1	439	441	3
-5	3	1	148	144	1	-7	5	1	548	544	12	-5	7	1	420	427	4

Table B3 Observed and calculated structure factors for sample 3 (cont…)

h	k	l	10Fo	10Fc	10s	h	k	l	10Fo	10Fc	10s	h	k	l	10Fo	10Fc	10s
-4	7	1	458	452	4	4	9	1	133	147	8	7	1	2	183	180	4
-3	7	1	436	434	5	-3	10	1	18	9	18	8	1	2	110	119	4
-2	7	1	475	474	5	-2	10	1	43	39	11	9	1	2	89	78	2
-1	7	1	425	418	3	-1	10	1	228	224	4	-10	2	2	101	108	3
0	7	1	497	500	7	0	10	1	171	167	5	-9	2	2	463	455	12
1	7	1	220	221	4	1	10	1	294	299	4	-8	2	2	267	266	4
2	7	1	359	355	2	2	10	1	191	200	7	-7	2	2	910	924	10
3	7	1	295	297	4	-10	0	2	352	351	5	-6	2	2	500	514	7
4	7	1	86	85	6	-8	0	2	860	874	10	-5	2	2	1282	1284	7
5	7	1	36	44	12	-6	0	2	1399	1407	16	-4	2	2	552	570	4
6	7	1	110	110	3	-4	0	2	1630	1650	11	-3	2	2	1643	1617	7
7	7	1	88	82	11	-2	0	2	1624	1607	12	-2	2	2	291	304	2
-6	8	1	185	185	4	0	0	2	667	678	3	-1	2	2	573	594	4
-5	8	1	22	11	5	2	0	2	119	72	1	0	2	2	74	69	1
-4	8	1	59	42	6	4	0	2	889	892	10	1	2	2	111	96	3
-3	8	1	43	21	11	6	0	2	874	859	7	2	2	2	238	227	3
-2	8	1	134	131	2	8	0	2	829	798	14	3	2	2	402	422	4
-1	8	1	43	36	4	-10	1	2	461	463	6	4	2	2	362	361	3
0	8	1	485	484	4	-9	1	2	289	285	5	5	2	2	784	783	4
1	8	1	30	25	14	-8	1	2	390	371	3	6	2	2	467	464	3
2	8	1	532	536	4	-7	1	2	180	179	1	7	2	2	830	819	4
3	8	1	21	18	21	-6	1	2	127	133	2	8	2	2	351	353	2
4	8	1	581	581	9	-5	1	2	45	38	2	9	2	2	604	617	4
5	8	1	57	65	3	-4	1	2	413	418	8	-9	3	2	412	403	6
6	8	1	478	499	15	-3	1	2	443	451	9	-8	3	2	111	109	2
-5	9	1	216	226	7	-2	1	2	1042	1071	9	-7	3	2	215	219	1
-4	9	1	430	437	3	-1	1	2	1084	1091	9	-6	3	2	14	1	9
-3	9	1	240	237	2	0	1	2	1779	1838	24	-5	3	2	236	227	2
-2	9	1	513	511	4	1	1	2	804	831	8	-4	3	2	43	20	4
-1	9	1	250	255	4	2	1	2	1925	1950	26	-3	3	2	1055	1025	10
0	9	1	508	510	5	3	1	2	834	848	8	-2	3	2	402	390	2
1	9	1	202	202	1	4	1	2	973	975	8	-1	3	2	1955	1895	12
2	9	1	381	377	6	5	1	2	385	375	5	0	3	2	88	79	2
3	9	1	124	121	2	6	1	2	357	348	4	1	3	2	1891	1843	36

Table B3 Observed and calculated structure factors for sample 3 (cont…)

h	k	l	10Fo	10Fc	10s	h	k	l	10Fo	10Fc	10s	h	k	l	10Fo	10Fc	10s
2	3	2	183	171	3	0	5	2	1405	1375	9	2	7	2	736	735	5
3	3	2	1500	1490	14	1	5	2	498	490	3	3	7	2	654	645	4
4	3	2	185	188	1	2	5	2	1407	1379	7	4	7	2	478	479	4
5	3	2	835	842	6	3	5	2	203	203	1	5	7	2	462	478	7
6	3	2	122	113	2	4	5	2	930	928	6	6	7	2	197	200	8
7	3	2	335	340	6	5	5	2	167	175	1	-6	8	2	99	89	8
8	3	2	46	37	9	6	5	2	432	439	3	-5	8	2	799	807	7
-9	4	2	337	349	8	7	5	2	51	25	13	-4	8	2	95	85	3
-8	4	2	495	494	3	8	5	2	93	94	7	-3	8	2	761	759	12
-7	4	2	615	610	9	-8	6	2	621	633	5	-2	8	2	33	29	6
-6	4	2	640	648	8	-7	6	2	248	249	5	-1	8	2	541	547	6
-5	4	2	1057	1055	9	-6	6	2	912	925	6	0	8	2	26	22	4
-4	4	2	671	660	6	-5	6	2	183	184	5	1	8	2	60	47	4
-3	4	2	997	991	5	-4	6	2	998	985	13	2	8	2	102	106	5
-2	4	2	724	716	3	-3	6	2	290	287	1	3	8	2	309	310	7
-1	4	2	473	483	3	-2	6	2	864	869	9	4	8	2	114	118	1
0	4	2	276	275	2	-1	6	2	210	211	1	5	8	2	491	504	11
1	4	2	86	77	1	0	6	2	552	554	3	-5	9	2	95	96	2
2	4	2	156	160	5	1	6	2	93	93	3	-4	9	2	123	125	7
3	4	2	289	280	3	2	6	2	199	195	2	-3	9	2	529	533	5
4	4	2	636	649	14	3	6	2	169	165	2	-2	9	2	250	245	3
5	4	2	563	575	3	4	6	2	550	555	5	-1	9	2	756	752	4
6	4	2	487	499	3	5	6	2	179	190	1	0	9	2	321	324	9
7	4	2	671	679	4	6	6	2	651	657	10	1	9	2	789	785	12
8	4	2	466	464	9	7	6	2	134	138	6	2	9	2	284	302	3
-9	5	2	99	106	7	-7	7	2	217	212	2	3	9	2	602	617	21
-8	5	2	364	352	5	-6	7	2	15	31	15	4	9	2	245	253	11
-7	5	2	74	75	2	-5	7	2	76	71	4	-3	10	2	313	317	7
-6	5	2	33	5	7	-4	7	2	301	304	4	-2	10	2	371	385	8
-5	5	2	28	10	2	-3	7	2	494	498	3	-1	10	2	184	189	4
-4	5	2	513	490	2	-2	7	2	458	452	3	0	10	2	206	221	4
-3	5	2	168	157	2	-1	7	2	761	751	6	1	10	2	60	23	9
-2	5	2	1036	1013	13	0	7	2	766	778	11	2	10	2	135	137	5
-1	5	2	282	277	2	1	7	2	744	738	8	-9	0	3	349	336	4

Table B3 Observed and calculated structure factors for sample 3 (cont…)

h	k	l	10Fo	10Fc	10s	h	k	l	10Fo	10Fc	10s	h	k	l	10Fo	10Fc	10s
-7	0	3	455	463	5	-3	2	3	377	373	3	-5	4	3	464	462	2
-5	0	3	803	792	11	-2	2	3	947	953	6	-4	4	3	559	560	5
-3	0	3	1204	1200	39	-1	2	3	490	497	2	-3	4	3	483	482	3
-1	0	3	1886	1947	35	0	2	3	1207	1212	24	-2	4	3	662	664	6
1	0	3	1025	1060	14	1	2	3	268	281	1	-1	4	3	634	642	4
3	0	3	782	792	12	2	2	3	821	840	10	0	4	3	726	733	4
5	0	3	528	520	13	3	2	3	93	82	1	1	4	3	429	421	2
7	0	3	195	186	6	4	2	3	575	584	7	2	4	3	646	642	4
-10	1	3	263	262	3	5	2	3	130	128	1	3	4	3	461	450	4
-9	1	3	454	445	3	6	2	3	132	129	2	4	4	3	294	295	3
-8	1	3	312	311	3	7	2	3	62	51	2	5	4	3	195	205	3
-7	1	3	507	520	4	8	2	3	33	25	16	6	4	3	163	161	1
-6	1	3	340	339	6	-9	3	3	73	56	3	7	4	3	31	15	9
-5	1	3	417	432	3	-8	3	3	622	619	11	-8	5	3	165	165	4
-4	1	3	36	28	4	-7	3	3	96	81	2	-7	5	3	418	415	6
-3	1	3	152	156	4	-6	3	3	606	602	7	-6	5	3	77	68	3
-2	1	3	83	65	2	-5	3	3	73	73	4	-5	5	3	414	417	4
-1	1	3	174	169	1	-4	3	3	212	211	2	-4	5	3	27	18	3
0	1	3	252	254	2	-3	3	3	145	140	2	-3	5	3	271	273	2
1	1	3	402	407	5	-2	3	3	119	106	1	-2	5	3	187	196	1
2	1	3	309	312	3	-1	3	3	59	39	2	-1	5	3	103	109	3
3	1	3	459	467	6	0	3	3	74	68	1	0	5	3	68	69	1
4	1	3	544	549	3	1	3	3	242	236	3	1	5	3	428	426	2
5	1	3	778	761	6	2	3	3	442	434	4	2	5	3	149	147	1
6	1	3	458	454	2	3	3	3	57	45	2	3	5	3	491	493	6
7	1	3	642	625	5	4	3	3	793	799	11	4	5	3	211	219	5
8	1	3	343	335	3	5	3	3	135	135	2	5	5	3	584	593	6
-10	2	3	65	69	6	6	3	3	713	716	6	6	5	3	204	211	7
-9	2	3	118	117	3	7	3	3	80	57	5	7	5	3	590	601	7
-8	2	3	269	269	5	8	3	3	536	544	7	-8	6	3	37	10	4
-7	2	3	151	148	4	-9	4	3	86	77	6	-7	6	3	377	375	3
-6	2	3	644	635	7	-8	4	3	242	252	5	-6	6	3	154	157	5
-5	2	3	101	102	4	-7	4	3	188	181	6	-5	6	3	516	524	5
-4	2	3	805	817	4	-6	4	3	408	416	7	-4	6	3	225	227	3

Table B3 Observed and calculated structure factors for sample 3 (cont…)

h	k	l	10Fo	10Fc	10s	h	k	l	10Fo	10Fc	10s	h	k	l	10Fo	10Fc	10s
-3	6	3	833	830	7	4	8	3	334	344	4	1	1	4	152	151	1
-2	6	3	183	192	4	5	8	3	31	19	23	2	1	4	124	125	1
-1	6	3	823	813	4	-5	9	3	162	155	5	3	1	4	192	209	4
0	6	3	239	234	1	-4	9	3	187	182	4	4	1	4	226	226	2
1	6	3	743	739	5	-3	9	3	83	91	4	5	1	4	252	249	3
2	6	3	208	209	2	-2	9	3	37	28	3	6	1	4	541	530	7
3	6	3	537	534	3	-1	9	3	30	11	9	7	1	4	399	398	3
4	6	3	191	197	2	0	9	3	59	61	5	8	1	4	513	509	7
5	6	3	363	370	4	1	9	3	108	110	2	-9	2	4	539	550	5
6	6	3	22	13	21	2	9	3	289	295	5	-8	2	4	285	290	6
-7	7	3	175	185	5	3	9	3	188	186	3	-7	2	4	393	399	5
-6	7	3	270	261	5	-1	10	3	357	359	18	-6	2	4	91	87	3
-5	7	3	197	195	1	0	10	3	179	177	4	-5	2	4	198	196	2
-4	7	3	198	202	9	-10	0	4	615	615	8	-4	2	4	163	161	1
-3	7	3	103	101	4	-8	0	4	653	654	7	-3	2	4	460	449	3
-2	7	3	73	67	6	-6	0	4	395	397	4	-2	2	4	302	300	1
-1	7	3	113	112	3	-4	0	4	346	342	14	-1	2	4	945	933	4
0	7	3	161	162	3	-2	0	4	748	747	4	0	2	4	473	472	3
1	7	3	182	181	1	0	0	4	1166	1187	13	1	2	4	1487	1485	18
2	7	3	358	367	5	2	0	4	1578	1632	11	2	2	4	652	665	3
3	7	3	289	293	4	4	0	4	1207	1199	8	3	2	4	1075	1097	17
4	7	3	418	417	5	6	0	4	674	672	6	4	2	4	534	547	5
5	7	3	274	282	3	8	0	4	175	172	7	5	2	4	815	811	4
6	7	3	382	397	9	-10	1	4	158	164	3	6	2	4	209	210	1
-6	8	3	412	418	6	-9	1	4	219	215	5	7	2	4	414	404	5
-5	8	3	44	27	3	-8	1	4	451	459	3	-9	3	4	437	433	10
-4	8	3	578	569	7	-7	1	4	339	345	2	-8	3	4	123	123	3
-3	8	3	56	42	4	-6	1	4	908	912	7	-7	3	4	751	757	9
-2	8	3	560	559	3	-5	1	4	623	626	3	-6	3	4	133	126	3
-1	8	3	48	12	6	-4	1	4	1354	1371	6	-5	3	4	1227	1216	6
0	8	3	591	578	3	-3	1	4	713	729	8	-4	3	4	182	172	1
1	8	3	29	10	9	-2	1	4	1063	1080	4	-3	3	4	1570	1552	7
2	8	3	612	619	4	-1	1	4	554	568	4	-2	3	4	56	43	2
3	8	3	43	42	9	0	1	4	726	735	10	-1	3	4	1247	1257	5

Table B3 Observed and calculated structure factors for sample 3 (cont…)

h	k	l	10Fo	10Fc	10s	h	k	l	10Fo	10Fc	10s	h	k	l	10Fo	10Fc	10s
0	3	4	289	288	1	1	5	4	91	94	3	-6	8	4	37	12	36
1	3	4	476	480	4	2	5	4	238	230	2	-5	8	4	121	120	2
2	3	4	32	10	3	3	5	4	96	97	1	-4	8	4	71	61	3
3	3	4	91	87	8	4	5	4	267	265	3	-3	8	4	219	222	6
4	3	4	31	26	5	5	5	4	178	176	6	-2	8	4	112	101	7
5	3	4	327	330	1	6	5	4	491	500	11	-1	8	4	726	711	7
6	3	4	112	106	5	-8	6	4	476	484	8	0	8	4	124	120	2
7	3	4	535	538	10	-7	6	4	123	113	2	1	8	4	791	778	6
-9	4	4	420	423	11	-6	6	4	263	269	2	2	8	4	137	134	6
-8	4	4	323	325	3	-5	6	4	118	122	1	3	8	4	706	715	11
-7	4	4	306	306	2	-4	6	4	133	131	1	4	8	4	127	125	2
-6	4	4	280	277	3	-3	6	4	123	127	4	-4	9	4	244	247	5
-5	4	4	72	53	4	-2	6	4	598	591	9	-3	9	4	677	673	8
-4	4	4	125	118	2	-1	6	4	208	210	6	-2	9	4	266	266	3
-3	4	4	233	229	1	0	6	4	877	869	11	-1	9	4	583	571	7
-2	4	4	516	500	2	1	6	4	293	288	5	0	9	4	194	193	7
-1	4	4	786	782	5	2	6	4	981	964	11	1	9	4	260	253	5
0	4	4	741	730	5	3	6	4	182	184	2	2	9	4	84	83	10
1	4	4	1005	987	15	4	6	4	846	852	13	-9	0	5	551	546	6
2	4	4	814	815	11	5	6	4	219	230	3	-7	0	5	657	661	6
3	4	4	900	904	7	6	6	4	427	450	8	-5	0	5	615	643	22
4	4	4	610	618	6	-7	7	4	410	422	10	-3	0	5	642	660	11
5	4	4	524	550	3	-6	7	4	506	516	6	-1	0	5	242	241	1
6	4	4	440	456	7	-5	7	4	534	549	4	1	0	5	117	118	1
7	4	4	276	286	7	-4	7	4	567	561	11	3	0	5	316	311	3
-8	5	4	493	498	6	-3	7	4	616	617	4	5	0	5	410	410	4
-7	5	4	143	140	4	-2	7	4	544	543	9	7	0	5	598	586	9
-6	5	4	888	886	5	-1	7	4	535	529	8	-9	1	5	31	26	6
-5	5	4	193	198	1	0	7	4	277	274	2	-8	1	5	42	29	3
-4	5	4	1091	1082	5	1	7	4	255	257	2	-7	1	5	300	300	4
-3	5	4	353	356	3	2	7	4	105	118	2	-6	1	5	179	180	2
-2	5	4	944	955	6	3	7	4	93	78	5	-5	1	5	304	301	2
-1	5	4	189	188	4	4	7	4	219	222	6	-4	1	5	286	290	2
0	5	4	714	722	5	5	7	4	269	291	4	-3	1	5	492	494	6

Table B3 Observed and calculated structure factors for sample 3 (cont…)

h	k	l	10Fo	10Fc	10s	h	k	l	10Fo	10Fc	10s	h	k	l	10Fo	10Fc	10s
-2	1	5	482	489	2	-2	3	5	784	790	6	2	5	5	112	114	2
-1	1	5	833	836	4	-1	3	5	90	83	2	3	5	5	589	604	5
0	1	5	381	391	3	0	3	5	808	812	6	4	5	5	145	147	1
1	1	5	892	908	9	1	3	5	91	84	3	5	5	5	414	431	3
2	1	5	529	536	10	2	3	5	866	871	10	-7	6	5	435	438	4
3	1	5	601	609	18	3	3	5	145	156	3	-6	6	5	104	100	3
4	1	5	318	320	6	4	3	5	628	631	11	-5	6	5	407	415	2
5	1	5	369	362	6	5	3	5	87	85	4	-4	6	5	141	151	6
6	1	5	235	220	7	6	3	5	366	371	3	-3	6	5	385	381	7
7	1	5	275	267	5	-8	4	5	320	328	8	-2	6	5	148	145	5
-9	2	5	157	156	3	-7	4	5	301	304	2	-1	6	5	297	294	4
-8	2	5	514	517	3	-6	4	5	473	477	3	0	6	5	66	63	8
-7	2	5	207	198	1	-5	4	5	238	237	2	1	6	5	71	62	6
-6	2	5	580	582	3	-4	4	5	334	331	3	2	6	5	88	86	2
-5	2	5	186	187	1	-3	4	5	322	320	3	3	6	5	202	201	1
-4	2	5	577	570	3	-2	4	5	122	114	3	4	6	5	133	139	2
-3	2	5	62	64	1	-1	4	5	99	94	1	5	6	5	332	340	8
-2	2	5	193	196	1	0	4	5	37	16	6	-6	7	5	149	145	14
-1	2	5	49	31	3	1	4	5	70	66	2	-5	7	5	233	220	6
0	2	5	107	107	3	2	4	5	61	55	2	-4	7	5	348	345	8
1	2	5	130	126	2	3	4	5	335	340	4	-3	7	5	234	236	6
2	2	5	86	70	12	4	4	5	265	273	2	-2	7	5	423	416	3
3	2	5	142	144	2	5	4	5	280	289	7	-1	7	5	389	385	5
4	2	5	397	415	11	6	4	5	433	452	8	0	7	5	408	410	3
5	2	5	258	260	2	-8	5	5	71	64	3	1	7	5	380	386	5
6	2	5	519	511	9	-7	5	5	177	182	4	2	7	5	436	436	8
7	2	5	286	280	8	-6	5	5	74	78	5	3	7	5	270	278	3
-9	3	5	53	58	4	-5	5	5	341	347	5	4	7	5	378	397	9
-8	3	5	97	88	2	-4	5	5	138	133	3	-5	8	5	53	31	9
-7	3	5	32	3	9	-3	5	5	537	544	6	-4	8	5	323	312	8
-6	3	5	334	336	4	-2	5	5	93	89	1	-3	8	5	71	64	11
-5	3	5	55	30	4	-1	5	5	720	719	5	-2	8	5	254	247	4
-4	3	5	579	572	3	0	5	5	236	238	5	-1	8	5	36	29	4
-3	3	5	198	199	2	1	5	5	730	730	12	0	8	5	83	79	6

Table B3 Observed and calculated structure factors for sample 3 (cont…)

h	k	l	10Fo	10Fc	10s	h	k	l	10Fo	10Fc	10s	h	k	l	10Fo	10Fc	10s
1	8	5	91	85	4	-4	2	6	460	463	5	1	4	6	456	467	6
2	8	5	115	120	5	-3	2	6	1012	1018	6	2	4	6	290	294	2
-2	9	5	373	368	5	-2	2	6	510	504	2	3	4	6	52	34	11
-1	9	5	211	214	3	-1	2	6	1106	1105	5	4	4	6	43	27	7
0	9	5	406	395	13	0	2	6	309	310	7	5	4	6	106	117	6
-8	0	6	313	307	5	1	2	6	577	585	5	-7	5	6	108	106	3
-6	0	6	773	774	6	2	2	6	89	73	5	-6	5	6	474	484	4
-4	0	6	1151	1183	46	3	2	6	199	201	7	-5	5	6	38	24	3
-2	0	6	1391	1410	18	4	2	6	23	40	22	-4	5	6	189	191	5
0	0	6	904	896	7	5	2	6	187	189	5	-3	5	6	146	146	5
2	0	6	449	447	8	6	2	6	120	113	8	-2	5	6	265	262	6
4	0	6	81	67	16	-8	3	6	70	65	3	-1	5	6	133	130	3
6	0	6	250	247	5	-7	3	6	632	635	6	0	5	6	630	619	10
-9	1	6	301	307	2	-6	3	6	81	79	1	1	5	6	279	282	5
-8	1	6	574	577	4	-5	3	6	337	342	3	2	5	6	704	719	9
-7	1	6	330	333	3	-4	3	6	68	68	3	3	5	6	297	309	5
-6	1	6	514	519	3	-3	3	6	40	29	3	4	5	6	659	694	8
-5	1	6	114	110	4	-2	3	6	38	20	2	-6	6	6	539	553	9
-4	1	6	102	99	2	-1	3	6	421	424	2	-5	6	6	211	212	4
-3	1	6	40	27	5	0	3	6	177	180	2	-4	6	6	892	880	10
-2	1	6	320	318	2	1	3	6	825	813	15	-3	6	6	187	189	2
-1	1	6	373	373	2	2	3	6	73	72	7	-2	6	6	842	836	12
0	1	6	640	646	3	3	3	6	902	907	20	-1	6	6	228	220	5
1	1	6	539	548	3	4	3	6	132	131	3	0	6	6	643	645	7
2	1	6	734	746	9	5	3	6	697	676	20	1	6	6	165	158	2
3	1	6	597	591	9	-8	4	6	144	142	3	2	6	6	332	341	9
4	1	6	856	839	7	-7	4	6	366	376	6	3	6	6	135	137	3
5	1	6	459	453	7	-6	4	6	467	466	3	-5	7	6	203	210	5
6	1	6	532	527	7	-5	4	6	589	590	4	-4	7	6	83	80	2
-9	2	6	157	170	3	-4	4	6	590	593	3	-3	7	6	9	7	9
-8	2	6	112	115	3	-3	4	6	794	791	4	-2	7	6	229	232	2
-7	2	6	506	512	8	-2	4	6	646	642	5	-1	7	6	305	301	5
-6	2	6	219	222	3	-1	4	6	748	762	7	0	7	6	347	347	5
-5	2	6	821	822	5	0	4	6	447	453	5	1	7	6	516	516	11

Table B3 Observed and calculated structure factors for sample 3 (cont…)

h	k	l	10Fo	10Fc	10s	h	k	l	10Fo	10Fc	10s	h	k	l	10Fo	10Fc	10s
2	7	6	469	466	11	0	2	7	616	599	12	-2	5	7	60	47	5
-3	8	6	676	668	6	1	2	7	332	333	6	-1	5	7	373	382	6
-2	8	6	94	84	3	2	2	7	571	567	5	0	5	7	82	83	5
-1	8	6	627	620	6	3	2	7	340	331	9	1	5	7	196	200	11
0	8	6	48	24	3	4	2	7	566	552	10	2	5	7	47	6	7
-7	0	7	0	25	1	-8	3	7	371	378	4	3	5	7	65	57	6
-5	0	7	224	226	4	-7	3	7	76	65	2	-5	6	7	141	136	4
-3	0	7	278	275	8	-6	3	7	520	516	5	-4	6	7	73	76	3
-1	0	7	420	424	3	-5	3	7	86	87	4	-3	6	7	237	237	3
1	0	7	766	764	16	-4	3	7	631	625	8	-2	6	7	115	119	2
3	0	7	659	643	6	-3	3	7	40	32	5	-1	6	7	358	370	3
5	0	7	515	503	8	-2	3	7	467	475	5	0	6	7	162	161	4
-8	1	7	166	175	7	-1	3	7	145	149	1	1	6	7	458	460	10
-7	1	7	399	398	4	0	3	7	265	270	5	2	6	7	120	124	7
-6	1	7	272	259	4	1	3	7	52	29	7	-4	7	7	271	276	7
-5	1	7	512	499	4	2	3	7	109	105	6	-3	7	7	198	195	8
-4	1	7	295	297	2	3	3	7	38	13	4	-2	7	7	252	247	6
-3	1	7	398	403	3	4	3	7	60	53	12	-1	7	7	136	128	3
-2	1	7	198	200	2	-7	4	7	0	21	1	0	7	7	163	172	2
-1	1	7	344	349	2	-6	4	7	87	89	3	-6	0	8	641	629	11
0	1	7	118	118	2	-5	4	7	115	110	4	-4	0	8	479	486	6
1	1	7	143	139	6	-4	4	7	158	163	1	-2	0	8	71	16	10
2	1	7	44	29	6	-3	4	7	256	257	4	0	0	8	274	282	5
3	1	7	60	23	4	-2	4	7	327	335	3	2	0	8	536	530	7
4	1	7	72	58	10	-1	4	7	332	341	3	-7	1	8	164	176	5
5	1	7	200	206	7	0	4	7	390	400	10	-6	1	8	318	317	4
-8	2	7	63	44	4	1	4	7	446	450	7	-5	1	8	318	317	3
-7	2	7	86	82	2	2	4	7	474	457	9	-4	1	8	593	590	9
-6	2	7	30	23	8	3	4	7	385	373	11	-3	1	8	482	481	5
-5	2	7	150	155	6	4	4	7	396	395	10	-2	1	8	829	808	12
-4	2	7	269	271	3	-6	5	7	76	64	3	-1	1	8	434	443	8
-3	2	7	137	131	2	-5	5	7	419	423	13	0	1	8	714	698	6
-2	2	7	392	390	5	-4	5	7	122	113	3	1	1	8	442	419	5
-1	2	7	204	207	2	-3	5	7	394	393	4	2	1	8	404	397	6

Table B3 Observed and calculated structure factors for sample 3 (cont…)

h	k	l	10Fo	10Fc	10s	h	k	l	10Fo	10Fc	10s	h	k	l	10Fo	10Fc	10s
3	1	8	187	175	10	-6	4	8	274	273	4	-6	1	9	0	12	1
-7	2	8	558	559	6	-5	4	8	317	312	8	-5	1	9	61	51	6
-6	2	8	220	226	6	-4	4	8	255	251	3	-4	1	9	41	35	9
-5	2	8	462	458	6	-3	4	8	67	68	4	-3	1	9	113	115	4
-4	2	8	102	96	4	-2	4	8	38	16	20	-2	1	9	144	147	2
-3	2	8	145	150	4	-1	4	8	151	136	5	-1	1	9	203	200	5
-2	2	8	90	81	2	0	4	8	200	209	4	0	1	9	234	235	3
-1	2	8	140	135	2	1	4	8	320	313	4	1	1	9	316	299	4
0	2	8	223	220	5	2	4	8	399	393	8	-5	2	9	171	173	4
1	2	8	374	362	4	-5	5	8	175	177	3	-4	2	9	383	383	4
2	2	8	246	246	8	-4	5	8	581	597	17	-3	2	9	188	188	3
3	2	8	577	579	11	-3	5	8	170	172	7	-2	2	9	471	472	4
-7	3	8	272	278	6	-2	5	8	736	726	14	-1	2	9	144	145	2
-6	3	8	45	43	6	-1	5	8	267	261	4	0	2	9	286	290	4
-5	3	8	552	549	6	0	5	8	619	609	12	1	2	9	75	82	6
-4	3	8	138	130	4	1	5	8	143	136	3	-4	3	9	44	12	10
-3	3	8	771	760	7	-3	6	8	105	105	4	-3	3	9	20	23	19
-2	3	8	101	97	3	-2	6	8	73	69	3	-2	3	9	143	136	2
-1	3	8	772	781	26	-1	6	8	0	8	1	-1	3	9	98	93	11
0	3	8	59	63	7	-5	0	9	429	425	5	0	3	9	314	300	13
1	3	8	660	653	9	-3	0	9	509	496	7	-3	4	9	240	256	3
2	3	8	118	118	4	-1	0	9	415	404	6	-2	4	9	316	314	7
3	3	8	297	294	4	1	0	9	311	285	5						

Table B4 Observed and calculated structure factors for sample 4

h	k	l	10Fo	10Fc	10s	h	k	l	10Fo	10Fc	10s	h	k	l	10Fo	10Fc	10s
2	0	0	2654	2189	29	9	3	0	483	463	16	5	7	0	541	520	14
4	0	0	1084	1080	16	10	3	0	16	109	16	6	7	0	432	388	17
6	0	0	373	369	16	0	4	0	1245	1200	35	7	7	0	436	422	12
8	0	0	100	32	58	1	4	0	1362	1321	21	8	7	0	330	320	13
10	0	0	205	217	27	2	4	0	799	803	10	0	8	0	75	88	44
1	1	0	445	382	13	3	4	0	962	952	14	1	8	0	934	916	16
2	1	0	959	860	20	4	4	0	561	587	10	2	8	0	91	58	37
3	1	0	436	449	7	5	4	0	333	363	7	3	8	0	744	787	20
4	1	0	1000	1023	15	6	4	0	112	128	20	4	8	0	0	45	1
5	1	0	731	775	10	7	4	0	124	46	32	5	8	0	360	371	13
6	1	0	943	990	18	8	4	0	142	77	29	6	8	0	31	1	31
7	1	0	502	512	17	9	4	0	210	142	24	7	8	0	126	34	54
8	1	0	643	611	13	1	5	0	134	121	9	1	9	0	175	135	14
9	1	0	300	276	24	2	5	0	710	724	12	2	9	0	157	151	19
10	1	0	369	329	17	3	5	0	227	224	5	3	9	0	446	448	12
0	2	0	1327	1070	37	4	5	0	833	888	19	4	9	0	229	229	20
1	2	0	2536	2123	81	5	5	0	268	295	12	5	9	0	473	472	16
2	2	0	710	648	22	6	5	0	751	749	18	6	9	0	216	204	22
3	2	0	1417	1366	24	7	5	0	276	235	14	0	10	0	564	534	22
4	2	0	128	114	9	8	5	0	565	545	16	1	10	0	338	309	19
5	2	0	641	677	10	9	5	0	177	67	32	2	10	0	520	517	16
6	2	0	0	68	1	0	6	0	1504	1445	33	3	10	0	243	277	16
7	2	0	65	18	65	1	6	0	334	341	7	4	10	0	275	291	21
8	2	0	0	19	1	2	6	0	1231	1249	22	1	11	0	71	11	71
9	2	0	186	143	57	3	6	0	295	308	8	2	11	0	294	262	23
10	2	0	104	121	63	4	6	0	632	654	13	-9	0	1	471	449	15
1	3	0	310	302	15	5	6	0	214	204	16	-7	0	1	350	381	17
2	3	0	317	297	5	6	6	0	278	278	14	-5	0	1	241	236	7
3	3	0	833	861	11	7	6	0	91	15	66	-3	0	1	760	634	23
4	3	0	122	126	12	8	6	0	125	25	30	-1	0	1	794	651	10
5	3	0	1202	1248	17	1	7	0	227	213	10	1	0	1	1029	916	56
6	3	0	152	152	11	2	7	0	341	354	8	3	0	1	1340	1318	27
7	3	0	841	885	21	3	7	0	468	497	12	5	0	1	1105	1115	18
8	3	0	91	69	51	4	7	0	483	508	16	7	0	1	765	766	25

Table B4 Observed and calculated structure factors for sample 4 (cont…)

h	k	l	10Fo	10Fc	10s	h	k	l	10Fo	10Fc	10s	h	k	l	10Fo	10Fc	10s
9	0	1	403	371	22	2	2	1	1526	1368	24	-5	4	1	274	259	10
-10	1	1	206	84	23	3	2	1	417	431	6	-4	4	1	124	105	16
-9	1	1	311	300	14	4	2	1	852	892	11	-3	4	1	161	130	11
-8	1	1	296	289	17	5	2	1	406	435	10	-2	4	1	50	73	16
-7	1	1	430	461	13	6	2	1	707	746	17	-1	4	1	376	371	7
-6	1	1	317	335	9	7	2	1	221	219	16	0	4	1	454	456	10
-5	1	1	810	834	14	8	2	1	472	479	12	1	4	1	533	542	9
-4	1	1	559	568	8	9	2	1	18	131	17	2	4	1	690	723	14
-3	1	1	1700	1491	16	10	2	1	307	294	23	3	4	1	492	524	7
-2	1	1	547	513	12	-10	3	1	250	215	25	4	4	1	697	732	12
-1	1	1	1203	1022	16	-9	3	1	174	40	43	5	4	1	492	506	12
0	1	1	818	677	15	-8	3	1	526	538	17	6	4	1	438	463	12
1	1	1	823	743	14	-7	3	1	175	145	19	7	4	1	462	462	12
2	1	1	249	256	5	-6	3	1	740	762	17	8	4	1	370	356	13
3	1	1	464	445	10	-5	3	1	199	167	11	9	4	1	214	233	15
4	1	1	65	24	13	-4	3	1	1053	1076	15	-9	5	1	214	250	32
5	1	1	279	300	4	-3	3	1	176	179	5	-8	5	1	155	63	18
6	1	1	54	11	54	-2	3	1	1504	1426	25	-7	5	1	500	508	16
7	1	1	135	150	23	-1	3	1	80	20	13	-6	5	1	91	114	27
8	1	1	212	171	18	0	3	1	1727	1480	42	-5	5	1	758	772	18
9	1	1	330	268	27	1	3	1	474	450	18	-4	5	1	49	43	31
10	1	1	112	168	51	2	3	1	796	794	16	-3	5	1	921	939	16
-10	2	1	374	377	22	3	3	1	52	27	21	-2	5	1	249	243	7
-9	2	1	238	177	23	4	3	1	330	340	7	-1	5	1	837	836	13
-8	2	1	399	397	15	5	3	1	24	29	24	0	5	1	97	73	13
-7	2	1	188	201	11	6	3	1	119	101	23	1	5	1	712	739	16
-6	2	1	211	190	11	7	3	1	98	77	50	2	5	1	63	56	22
-5	2	1	114	26	17	8	3	1	244	175	15	3	5	1	473	504	10
-4	2	1	43	14	24	9	3	1	156	22	56	4	5	1	27	7	26
-3	2	1	162	128	11	-10	4	1	297	270	13	5	5	1	174	152	15
-2	2	1	387	357	11	-9	4	1	246	244	31	6	5	1	102	16	37
-1	2	1	153	127	9	-8	4	1	323	321	16	7	5	1	162	154	24
0	2	1	529	485	20	-7	4	1	225	217	16	8	5	1	27	44	26
1	2	1	126	125	12	-6	4	1	177	129	11	9	5	1	214	217	28

Table B4 Observed and calculated structure factors for sample 4 (cont…)

h	k	l	10Fo	10Fc	10s	h	k	l	10Fo	10Fc	10s	h	k	l	10Fo	10Fc	10s
-9	6	1	206	239	23	-7	8	1	41	35	40	3	10	1	305	302	16
-8	6	1	143	79	41	-6	8	1	98	144	55	4	10	1	171	157	37
-7	6	1	290	289	15	-5	8	1	85	4	52	-1	11	1	336	347	12
-6	6	1	88	106	47	-4	8	1	15	27	14	0	11	1	92	63	40
-5	6	1	158	120	14	-3	8	1	71	29	35	1	11	1	293	281	19
-4	6	1	145	134	9	-2	8	1	161	150	12	-10	0	2	325	294	32
-3	6	1	148	153	14	-1	8	1	0	30	1	-8	0	2	755	761	19
-2	6	1	133	124	18	0	8	1	447	464	8	-6	0	2	1341	1312	39
-1	6	1	492	505	9	1	8	1	0	30	1	-4	0	2	1668	1640	44
0	6	1	174	200	11	2	8	1	522	493	14	-2	0	2	1787	1631	29
1	6	1	530	560	13	3	8	1	102	8	36	0	0	2	820	703	26
2	6	1	256	269	9	4	8	1	511	514	18	2	0	2	135	85	6
3	6	1	594	639	13	5	8	1	181	24	42	4	0	2	774	837	15
4	6	1	151	171	16	6	8	1	436	423	25	6	0	2	656	758	40
5	6	1	692	684	15	7	8	1	126	5	53	8	0	2	645	642	29
6	6	1	246	251	13	-6	9	1	404	413	17	-10	1	2	374	352	16
7	6	1	503	494	19	-5	9	1	238	238	20	-9	1	2	218	221	26
8	6	1	181	156	53	-4	9	1	414	393	12	-8	1	2	316	290	14
-8	7	1	260	239	27	-3	9	1	270	243	14	-7	1	2	176	139	9
-7	7	1	253	237	13	-2	9	1	485	463	13	-6	1	2	181	159	7
-6	7	1	436	413	18	-1	9	1	256	263	8	-5	1	2	51	70	51
-5	7	1	369	372	14	0	9	1	479	466	16	-4	1	2	482	454	9
-4	7	1	443	447	10	1	9	1	184	215	21	-3	1	2	516	493	11
-3	7	1	387	404	10	2	9	1	356	351	12	-2	1	2	1255	1122	26
-2	7	1	468	474	11	3	9	1	123	122	20	-1	1	2	1307	1135	18
-1	7	1	390	399	12	4	9	1	120	140	120	0	1	2	2202	1898	38
0	7	1	490	500	11	5	9	1	63	2	63	1	1	2	949	876	27
1	7	1	228	212	6	-4	10	1	201	6	31	2	1	2	2061	1961	69
2	7	1	354	368	12	-3	10	1	58	11	58	3	1	2	833	850	11
3	7	1	279	272	6	-2	10	1	53	44	52	4	1	2	896	961	11
4	7	1	158	103	22	-1	10	1	171	203	18	5	1	2	355	365	6
5	7	1	93	38	93	0	10	1	170	152	19	6	1	2	348	343	15
6	7	1	226	89	22	1	10	1	289	276	25	7	1	2	202	178	11
7	7	1	113	83	53	2	10	1	173	177	25	8	1	2	157	126	29

Table B4 Observed and calculated structure factors for sample 4 (cont…)

h	k	l	10Fo	10Fc	10s	h	k	l	10Fo	10Fc	10s	h	k	l	10Fo	10Fc	10s
9	1	2	38	39	38	3	3	2	1435	1461	25	-2	5	2	1002	1026	15
-10	2	2	0	89	1	4	3	2	205	213	9	-1	5	2	293	262	7
-9	2	2	428	390	16	5	3	2	765	793	15	0	5	2	1380	1375	26
-8	2	2	271	230	12	6	3	2	115	124	25	1	5	2	432	451	7
-7	2	2	815	826	18	7	3	2	319	325	13	2	5	2	1316	1337	22
-6	2	2	450	481	11	8	3	2	65	48	65	3	5	2	183	167	12
-5	2	2	1200	1241	25	9	3	2	97	10	84	4	5	2	835	869	18
-4	2	2	528	558	8	-10	4	2	208	186	26	5	5	2	171	134	22
-3	2	2	1697	1620	22	-9	4	2	302	291	23	6	5	2	417	407	13
-2	2	2	303	303	5	-8	4	2	406	435	17	7	5	2	0	27	1
-1	2	2	672	632	11	-7	4	2	507	533	20	8	5	2	162	96	23
0	2	2	93	71	13	-6	4	2	579	596	16	-9	6	2	146	132	60
1	2	2	141	120	9	-5	4	2	939	990	22	-8	6	2	535	524	21
2	2	2	235	229	8	-4	4	2	638	667	11	-7	6	2	259	247	21
3	2	2	384	398	6	-3	4	2	948	978	12	-6	6	2	828	806	24
4	2	2	303	339	6	-2	4	2	729	740	8	-5	6	2	196	202	18
5	2	2	651	710	13	-1	4	2	468	480	6	-4	6	2	885	925	19
6	2	2	384	403	8	0	4	2	300	298	7	-3	6	2	265	300	8
7	2	2	686	680	26	1	4	2	49	70	33	-2	6	2	799	841	15
8	2	2	278	281	12	2	4	2	141	132	11	-1	6	2	237	247	5
9	2	2	466	467	19	3	4	2	255	273	6	0	6	2	515	530	12
-10	3	2	257	23	28	4	4	2	551	590	12	1	6	2	108	108	17
-9	3	2	345	316	24	5	4	2	502	524	13	2	6	2	209	173	13
-8	3	2	152	96	24	6	4	2	436	440	12	3	6	2	144	154	11
-7	3	2	170	167	13	7	4	2	564	567	9	4	6	2	457	495	15
-6	3	2	129	11	10	8	4	2	394	364	25	5	6	2	169	162	24
-5	3	2	255	259	7	9	4	2	331	326	17	6	6	2	556	557	13
-4	3	2	52	29	40	-9	5	2	0	78	1	7	6	2	61	112	60
-3	3	2	1100	1053	10	-8	5	2	283	274	15	8	6	2	376	375	17
-2	3	2	407	406	7	-7	5	2	119	43	27	-8	7	2	230	151	14
-1	3	2	2082	1931	39	-6	5	2	103	30	28	-7	7	2	187	175	23
0	3	2	127	113	6	-5	5	2	108	20	18	-6	7	2	122	7	27
1	3	2	1973	1883	43	-4	5	2	485	507	11	-5	7	2	140	80	42
2	3	2	192	201	8	-3	5	2	151	152	14	-4	7	2	252	296	12

Table B4 Observed and calculated structure factors for sample 4 (cont…)

h	k	l	10Fo	10Fc	10s	h	k	l	10Fo	10Fc	10s	h	k	l	10Fo	10Fc	10s
-3	7	2	467	490	14	3	9	2	555	544	12	3	1	3	456	480	6
-2	7	2	439	435	10	4	9	2	275	267	20	4	1	3	482	521	10
-1	7	2	748	735	14	5	9	2	414	419	16	5	1	3	631	702	13
0	7	2	735	735	10	-4	10	2	398	398	14	6	1	3	397	408	18
1	7	2	699	729	14	-3	10	2	222	262	14	7	1	3	534	529	19
2	7	2	652	674	20	-2	10	2	374	350	10	8	1	3	269	272	16
3	7	2	600	613	14	-1	10	2	202	154	31	9	1	3	421	355	17
4	7	2	410	417	16	0	10	2	264	200	18	-10	2	3	77	66	77
5	7	2	440	434	20	1	10	2	189	30	41	-9	2	3	200	121	21
6	7	2	203	182	25	2	10	2	139	111	30	-8	2	3	278	273	13
7	7	2	122	166	121	3	10	2	137	149	32	-7	2	3	163	154	21
-7	8	2	484	482	15	-9	0	3	289	303	23	-6	2	3	600	634	17
-6	8	2	161	45	55	-7	0	3	469	457	11	-5	2	3	113	116	11
-5	8	2	714	696	20	-5	0	3	786	790	21	-4	2	3	846	836	14
-4	8	2	68	50	68	-3	0	3	1287	1244	29	-3	2	3	383	392	5
-3	8	2	674	690	17	-1	0	3	2225	1995	84	-2	2	3	1031	1006	14
-2	8	2	85	3	34	1	0	3	1096	1114	41	-1	2	3	517	509	5
-1	8	2	488	519	14	3	0	3	766	808	15	0	2	3	1297	1249	20
0	8	2	71	11	55	5	0	3	485	499	15	1	2	3	285	281	6
1	8	2	101	57	23	7	0	3	203	167	41	2	2	3	837	853	15
2	8	2	87	109	51	9	0	3	112	103	112	3	2	3	122	84	9
3	8	2	282	276	16	-10	1	3	240	212	21	4	2	3	530	584	9
4	8	2	128	116	40	-9	1	3	405	374	14	5	2	3	109	109	17
5	8	2	439	411	17	-8	1	3	290	281	12	6	2	3	181	136	16
6	8	2	183	119	28	-7	1	3	467	476	12	7	2	3	141	36	40
-6	9	2	113	43	54	-6	1	3	303	321	8	8	2	3	19	20	18
-5	9	2	140	105	22	-5	1	3	382	415	8	9	2	3	0	84	1
-4	9	2	140	102	18	-4	1	3	62	27	39	-10	3	3	409	367	31
-3	9	2	457	491	16	-3	1	3	148	146	8	-9	3	3	196	56	31
-2	9	2	279	245	11	-2	1	3	86	58	14	-8	3	3	526	532	21
-1	9	2	678	691	20	-1	1	3	244	191	11	-7	3	3	150	83	17
0	9	2	332	321	11	0	1	3	267	263	7	-6	3	3	529	555	14
1	9	2	702	711	13	1	1	3	428	436	11	-5	3	3	40	91	39
2	9	2	296	308	16	2	1	3	313	319	7	-4	3	3	200	201	7

Table B4 Observed and calculated structure factors for sample 4 (cont…)

h	k	l	10Fo	10Fc	10s	h	k	l	10Fo	10Fc	10s	h	k	l	10Fo	10Fc	10s
-3	3	3	164	156	10	-6	5	3	75	63	74	-6	7	3	231	222	13
-2	3	3	97	77	11	-5	5	3	392	385	8	-5	7	3	204	176	25
-1	3	3	88	54	13	-4	5	3	103	37	29	-4	7	3	221	196	31
0	3	3	117	96	12	-3	5	3	256	249	9	-3	7	3	95	75	20
1	3	3	242	226	10	-2	5	3	216	211	8	-2	7	3	74	68	41
2	3	3	422	447	11	-1	5	3	136	117	14	-1	7	3	109	127	20
3	3	3	72	56	37	0	5	3	103	43	17	0	7	3	161	156	12
4	3	3	703	756	14	1	5	3	389	410	10	1	7	3	211	189	11
5	3	3	138	136	12	2	5	3	155	157	13	2	7	3	344	332	9
6	3	3	616	628	11	3	5	3	431	478	12	3	7	3	257	289	16
7	3	3	171	60	23	4	5	3	190	203	17	4	7	3	365	370	18
8	3	3	424	436	12	5	5	3	540	522	7	5	7	3	233	252	16
-10	4	3	32	40	32	6	5	3	210	162	14	6	7	3	388	341	17
-9	4	3	138	72	50	7	5	3	493	479	16	-7	8	3	119	49	52
-8	4	3	246	242	19	8	5	3	69	89	68	-6	8	3	375	388	14
-7	4	3	225	199	24	-9	6	3	147	160	28	-5	8	3	135	28	41
-6	4	3	403	408	16	-8	6	3	184	11	20	-4	8	3	546	533	18
-5	4	3	463	474	11	-7	6	3	368	356	13	-3	8	3	64	12	63
-4	4	3	566	552	11	-6	6	3	195	153	20	-2	8	3	531	532	16
-3	4	3	502	509	9	-5	6	3	491	509	11	-1	8	3	90	20	41
-2	4	3	663	674	10	-4	6	3	266	237	11	0	8	3	547	540	9
-1	4	3	662	668	8	-3	6	3	777	793	18	1	8	3	61	47	61
0	4	3	724	735	11	-2	6	3	233	220	9	2	8	3	567	563	19
1	4	3	431	460	10	-1	6	3	784	793	15	3	8	3	52	73	52
2	4	3	577	625	17	0	6	3	249	258	10	4	8	3	277	313	19
3	4	3	421	456	11	1	6	3	681	716	13	5	8	3	0	8	1
4	4	3	272	282	8	2	6	3	240	245	11	-6	9	3	193	184	27
5	4	3	194	209	11	3	6	3	485	508	19	-5	9	3	72	141	71
6	4	3	124	149	24	4	6	3	222	222	10	-4	9	3	149	151	27
7	4	3	141	7	38	5	6	3	376	335	12	-3	9	3	216	101	20
8	4	3	113	27	53	6	6	3	105	22	56	-2	9	3	41	15	41
-9	5	3	351	346	17	7	6	3	129	86	38	-1	9	3	75	8	74
-8	5	3	160	124	35	-8	7	3	276	251	15	0	9	3	138	77	30
-7	5	3	408	357	14	-7	7	3	105	151	104	1	9	3	150	93	32

Table B4 Observed and calculated structure factors for sample 4 (cont…)

h	k	l	10Fo	10Fc	10s	h	k	l	10Fo	10Fc	10s	h	k	l	10Fo	10Fc	10s
2	9	3	270	268	17	4	1	4	216	194	10	0	3	4	321	306	7
3	9	3	173	167	20	5	1	4	209	211	16	1	3	4	471	486	10
4	9	3	311	293	15	6	1	4	436	435	7	2	3	4	56	36	39
-4	10	3	160	175	38	7	1	4	301	317	17	3	3	4	104	55	18
-3	10	3	377	362	14	8	1	4	380	381	20	4	3	4	0	3	1
-2	10	3	142	133	24	-10	2	4	160	183	43	5	3	4	283	276	12
-1	10	3	331	328	17	-9	2	4	458	439	12	6	3	4	0	76	1
0	10	3	142	141	33	-8	2	4	285	240	21	7	3	4	391	419	14
1	10	3	325	344	23	-7	2	4	337	347	11	8	3	4	113	41	57
2	10	3	138	165	33	-6	2	4	81	60	19	-9	4	4	414	338	25
-10	0	4	455	473	26	-5	2	4	176	153	10	-8	4	4	289	280	15
-8	0	4	524	557	35	-4	2	4	168	180	7	-7	4	4	302	256	20
-6	0	4	318	335	19	-3	2	4	465	469	9	-6	4	4	261	252	14
-4	0	4	362	367	14	-2	2	4	306	314	6	-5	4	4	119	21	18
-2	0	4	795	785	19	-1	2	4	975	953	12	-4	4	4	134	116	11
0	0	4	1244	1220	31	0	2	4	476	480	7	-3	4	4	255	254	6
2	0	4	1551	1587	31	1	2	4	1467	1464	22	-2	4	4	493	498	9
4	0	4	1045	1104	22	2	2	4	603	631	9	-1	4	4	781	784	10
6	0	4	596	600	21	3	2	4	1016	1045	19	0	4	4	724	729	11
8	0	4	71	161	71	4	2	4	456	491	6	1	4	4	952	961	15
-10	1	4	185	155	35	5	2	4	703	723	17	2	4	4	739	783	20
-9	1	4	212	201	26	6	2	4	196	177	19	3	4	4	772	840	18
-8	1	4	396	411	21	7	2	4	380	344	17	4	4	4	545	569	13
-7	1	4	327	332	12	8	2	4	0	61	1	5	4	4	460	484	13
-6	1	4	819	863	17	-10	3	4	121	12	57	6	4	4	398	403	16
-5	1	4	588	617	13	-9	3	4	357	380	21	7	4	4	234	239	22
-4	1	4	1306	1342	23	-8	3	4	115	119	36	-9	5	4	203	62	22
-3	1	4	703	747	13	-7	3	4	664	679	22	-8	5	4	465	445	18
-2	1	4	1088	1093	21	-6	3	4	159	132	19	-7	5	4	119	114	53
-1	1	4	593	592	9	-5	3	4	1141	1143	20	-6	5	4	854	806	31
0	1	4	740	745	12	-4	3	4	198	179	10	-5	5	4	153	167	22
1	1	4	164	176	6	-3	3	4	1535	1517	31	-4	5	4	1018	1022	16
2	1	4	148	137	9	-2	3	4	112	84	13	-3	5	4	292	318	11
3	1	4	205	181	11	-1	3	4	1251	1247	18	-2	5	4	907	944	14

Table B4 Observed and calculated structure factors for sample 4 (cont…)

h	k	l	10Fo	10Fc	10s	h	k	l	10Fo	10Fc	10s	h	k	l	10Fo	10Fc	10s
-1	5	4	126	148	15	2	7	4	116	89	41	-5	0	5	533	604	18
0	5	4	702	702	8	3	7	4	53	50	52	-3	0	5	580	625	17
1	5	4	140	120	17	4	7	4	238	195	13	-1	0	5	235	235	10
2	5	4	244	228	13	5	7	4	252	235	22	1	0	5	112	107	35
3	5	4	150	106	13	6	7	4	225	251	23	3	0	5	291	297	14
4	5	4	213	209	17	-7	8	4	243	236	21	5	0	5	397	358	23
5	5	4	173	169	13	-6	8	4	0	6	1	7	0	5	487	457	21
6	5	4	410	399	19	-5	8	4	118	93	38	-10	1	5	93	40	93
7	5	4	155	132	33	-4	8	4	113	86	36	-9	1	5	84	43	48
-8	6	4	411	390	10	-3	8	4	214	226	22	-8	1	5	138	41	22
-7	6	4	42	119	41	-2	8	4	81	107	42	-7	1	5	259	301	10
-6	6	4	209	224	20	-1	8	4	689	656	23	-6	1	5	180	189	16
-5	6	4	155	135	18	0	8	4	126	105	31	-5	1	5	277	320	11
-4	6	4	174	153	19	1	8	4	752	704	20	-4	1	5	270	307	6
-3	6	4	125	101	18	2	8	4	0	110	1	-3	1	5	471	513	10
-2	6	4	581	584	12	3	8	4	636	622	28	-2	1	5	475	497	11
-1	6	4	204	202	13	4	8	4	167	72	31	-1	1	5	845	838	16
0	6	4	826	844	18	5	8	4	458	423	21	0	1	5	397	402	9
1	6	4	288	289	10	-5	9	4	495	486	16	1	1	5	883	883	6
2	6	4	884	892	23	-4	9	4	222	246	20	2	1	5	500	517	9
3	6	4	221	204	19	-3	9	4	601	581	18	3	1	5	537	583	9
4	6	4	767	741	22	-2	9	4	258	273	12	4	1	5	305	299	10
5	6	4	252	230	24	-1	9	4	490	497	17	5	1	5	337	331	14
6	6	4	387	370	19	0	9	4	198	208	25	6	1	5	230	198	20
-8	7	4	158	218	33	1	9	4	242	223	14	7	1	5	324	218	19
-7	7	4	426	379	20	2	9	4	159	101	31	-10	2	5	303	278	32
-6	7	4	481	433	14	3	9	4	122	29	25	-9	2	5	86	134	53
-5	7	4	533	517	19	-3	10	4	161	114	19	-8	2	5	435	446	20
-4	7	4	497	496	18	-2	10	4	240	261	18	-7	2	5	225	184	21
-3	7	4	569	588	18	-1	10	4	292	290	22	-6	2	5	518	544	16
-2	7	4	468	487	14	0	10	4	424	407	20	-5	2	5	174	176	10
-1	7	4	491	522	12	1	10	4	329	305	13	-4	2	5	510	548	15
0	7	4	247	237	18	-9	0	5	454	456	24	-3	2	5	88	57	21
1	7	4	244	265	18	-7	0	5	551	586	28	-2	2	5	168	198	9

Table B4 Observed and calculated structure factors for sample 4 (cont…)

h	k	l	10Fo	10Fc	10s	h	k	l	10Fo	10Fc	10s	h	k	l	10Fo	10Fc	10s
-1	2	5	78	37	22	-2	4	5	110	93	24	0	6	5	114	88	27
0	2	5	111	102	21	-1	4	5	106	111	25	1	6	5	109	60	19
1	2	5	148	139	12	0	4	5	83	3	41	2	6	5	33	54	32
2	2	5	66	71	27	1	4	5	90	40	27	3	6	5	250	182	17
3	2	5	136	149	14	2	4	5	121	75	27	4	6	5	145	99	33
4	2	5	365	372	14	3	4	5	286	299	10	5	6	5	311	288	12
5	2	5	214	229	16	4	4	5	256	253	17	6	6	5	130	75	42
6	2	5	418	417	15	5	4	5	264	253	16	-7	7	5	134	128	40
7	2	5	240	220	30	6	4	5	381	369	14	-6	7	5	156	136	27
-10	3	5	80	46	79	7	4	5	244	286	22	-5	7	5	239	219	20
-9	3	5	199	53	22	-9	5	5	114	9	70	-4	7	5	364	328	14
-8	3	5	172	100	36	-8	5	5	220	72	35	-3	7	5	248	228	14
-7	3	5	52	10	52	-7	5	5	168	185	49	-2	7	5	391	398	14
-6	3	5	363	345	13	-6	5	5	110	96	46	-1	7	5	344	353	16
-5	3	5	60	35	59	-5	5	5	354	357	17	0	7	5	391	399	16
-4	3	5	549	581	15	-4	5	5	149	134	12	1	7	5	353	339	9
-3	3	5	203	193	10	-3	5	5	508	539	12	2	7	5	393	404	11
-2	3	5	780	788	16	-2	5	5	100	85	33	3	7	5	253	230	19
-1	3	5	86	95	23	-1	5	5	693	691	13	4	7	5	370	354	18
0	3	5	800	806	8	0	5	5	247	206	15	5	7	5	205	183	15
1	3	5	79	110	20	1	5	5	677	694	12	-6	8	5	389	327	27
2	3	5	772	824	17	2	5	5	0	81	1	-5	8	5	112	48	66
3	3	5	161	175	11	3	5	5	540	550	15	-4	8	5	254	269	29
4	3	5	557	572	19	4	5	5	0	99	1	-3	8	5	131	79	25
5	3	5	0	94	1	5	5	5	372	372	17	-2	8	5	243	220	19
6	3	5	359	326	22	6	5	5	76	3	75	-1	8	5	106	69	34
7	3	5	120	71	37	-8	6	5	163	161	27	0	8	5	47	67	46
-9	4	5	267	271	24	-7	6	5	362	356	19	1	8	5	117	108	46
-8	4	5	311	272	23	-6	6	5	106	108	48	2	8	5	112	109	69
-7	4	5	248	275	14	-5	6	5	359	363	11	3	8	5	57	66	57
-6	4	5	438	426	15	-4	6	5	176	162	15	4	8	5	268	217	32
-5	4	5	259	245	9	-3	6	5	313	340	10	-4	9	5	335	330	23
-4	4	5	301	306	12	-2	6	5	144	171	18	-3	9	5	0	158	1
-3	4	5	309	321	13	-1	6	5	277	254	13	-2	9	5	303	334	12

Table B4 Observed and calculated structure factors for sample 4 (cont…)

h	k	l	10Fo	10Fc	10s	h	k	l	10Fo	10Fc	10s	h	k	l	10Fo	10Fc	10s
-1	9	5	205	201	23	-4	2	6	415	443	12	-2	4	6	618	633	11
0	9	5	357	348	11	-3	2	6	984	988	27	-1	4	6	689	705	15
1	9	5	267	217	26	-2	2	6	465	474	11	0	4	6	436	453	14
2	9	5	289	314	17	-1	2	6	1050	1061	19	1	4	6	425	423	14
-10	0	6	47	109	47	0	2	6	283	282	6	2	4	6	268	282	10
-8	0	6	279	286	25	1	2	6	548	562	7	3	4	6	108	34	56
-6	0	6	682	715	30	2	2	6	121	65	23	4	4	6	88	44	39
-4	0	6	1109	1137	43	3	2	6	202	204	14	5	4	6	18	86	17
-2	0	6	1387	1358	47	4	2	6	103	44	48	6	4	6	80	133	80
0	0	6	814	868	34	5	2	6	124	141	42	-8	5	6	422	397	21
2	0	6	435	433	18	6	2	6	138	97	38	-7	5	6	0	84	1
4	0	6	182	80	52	-9	3	6	518	493	22	-6	5	6	424	423	16
6	0	6	174	182	76	-8	3	6	0	64	1	-5	5	6	57	7	57
-9	1	6	252	259	16	-7	3	6	529	540	28	-4	5	6	183	169	25
-8	1	6	474	488	15	-6	3	6	140	90	17	-3	5	6	145	160	18
-7	1	6	270	299	14	-5	3	6	295	297	17	-2	5	6	274	255	15
-6	1	6	434	462	18	-4	3	6	83	87	28	-1	5	6	141	149	18
-5	1	6	136	115	17	-3	3	6	104	5	20	0	5	6	576	574	13
-4	1	6	62	81	48	-2	3	6	0	35	1	1	5	6	264	271	10
-3	1	6	66	27	65	-1	3	6	414	426	11	2	5	6	670	648	15
-2	1	6	339	324	11	0	3	6	135	157	11	3	5	6	288	266	11
-1	1	6	345	357	9	1	3	6	742	762	20	4	5	6	591	580	16
0	1	6	593	634	14	2	3	6	85	67	43	5	5	6	141	150	53
1	1	6	502	515	7	3	3	6	830	803	18	-7	6	6	108	98	39
2	1	6	679	695	12	4	3	6	137	124	23	-6	6	6	466	498	19
3	1	6	515	531	12	5	3	6	556	556	15	-5	6	6	228	203	15
4	1	6	717	720	17	6	3	6	152	53	33	-4	6	6	819	790	17
5	1	6	393	386	16	-9	4	6	177	152	25	-3	6	6	189	203	22
6	1	6	407	420	15	-8	4	6	214	142	27	-2	6	6	773	769	23
-9	2	6	133	167	38	-7	4	6	330	348	8	-1	6	6	225	234	12
-8	2	6	105	113	43	-6	4	6	461	435	32	0	6	6	604	585	10
-7	2	6	443	478	10	-5	4	6	581	541	20	1	6	6	199	189	22
-6	2	6	202	213	12	-4	4	6	539	571	22	2	6	6	304	300	16
-5	2	6	735	776	25	-3	4	6	716	738	25	3	6	6	142	158	44

Table B4 Observed and calculated structure factors for sample 4 (cont…)

h	k	l	10Fo	10Fc	10s	h	k	l	10Fo	10Fc	10s	h	k	l	10Fo	10Fc	10s
4	6	6	38	36	38	-4	1	7	303	285	20	1	3	7	48	52	48
-6	7	6	215	206	23	-3	1	7	364	372	13	2	3	7	134	94	28
-5	7	6	259	200	28	-2	1	7	232	200	13	3	3	7	101	16	67
-4	7	6	112	41	62	-1	1	7	312	324	11	4	3	7	87	46	86
-3	7	6	78	17	77	0	1	7	173	120	11	5	3	7	134	26	39
-2	7	6	241	235	18	1	1	7	113	129	19	-8	4	7	114	8	80
-1	7	6	289	265	20	2	1	7	74	23	73	-7	4	7	63	21	63
0	7	6	337	330	11	3	1	7	138	22	35	-6	4	7	0	103	1
1	7	6	459	444	15	4	1	7	150	48	34	-5	4	7	134	103	23
2	7	6	418	416	14	5	1	7	206	169	24	-4	4	7	161	178	38
3	7	6	406	431	17	-9	2	7	65	47	64	-3	4	7	245	238	19
-5	8	6	515	511	15	-8	2	7	79	28	78	-2	4	7	320	326	7
-4	8	6	131	80	29	-7	2	7	85	85	45	-1	4	7	330	316	14
-3	8	6	582	598	22	-6	2	7	0	48	1	0	4	7	351	372	10
-2	8	6	107	43	56	-5	2	7	186	156	22	1	4	7	408	409	15
-1	8	6	540	548	16	-4	2	7	229	270	14	2	4	7	395	398	17
0	8	6	190	17	31	-3	2	7	174	135	16	3	4	7	367	336	13
1	8	6	390	416	13	-2	2	7	391	382	10	4	4	7	343	324	13
2	8	6	105	70	64	-1	2	7	223	204	25	-7	5	7	360	370	23
-2	9	6	0	6	1	0	2	7	555	562	17	-6	5	7	0	45	1
-1	9	6	188	227	32	1	2	7	315	295	18	-5	5	7	417	374	16
-9	0	7	187	139	24	2	2	7	487	510	7	-4	5	7	0	86	1
-7	0	7	127	54	126	3	2	7	283	276	17	-3	5	7	365	362	13
-5	0	7	226	243	18	4	2	7	458	465	13	-2	5	7	109	14	46
-3	0	7	299	289	17	5	2	7	145	142	63	-1	5	7	349	343	14
-1	0	7	429	420	28	-8	3	7	345	316	24	0	5	7	121	102	66
1	0	7	667	696	33	-7	3	7	102	66	28	1	5	7	165	178	26
3	0	7	566	557	34	-6	3	7	431	449	19	2	5	7	0	26	1
5	0	7	461	424	13	-5	3	7	106	88	34	3	5	7	156	35	21
-9	1	7	232	260	14	-4	3	7	610	561	25	4	5	7	119	85	30
-8	1	7	206	163	26	-3	3	7	16	54	15	-7	6	7	152	25	71
-7	1	7	318	357	14	-2	3	7	404	436	14	-6	6	7	134	70	30
-6	1	7	256	243	10	-1	3	7	145	155	12	-5	6	7	180	152	27
-5	1	7	432	452	16	0	3	7	251	248	13	-4	6	7	12	48	11

Table B4 Observed and calculated structure factors for sample 4 (cont…)

h	k	l	10Fo	10Fc	10s	h	k	l	10Fo	10Fc	10s	h	k	l	10Fo	10Fc	10s
-3	6	7	230	238	15	0	1	8	664	623	17	-4	4	8	237	240	17
-2	6	7	140	98	27	1	1	8	354	373	14	-3	4	8	94	42	74
-1	6	7	334	345	12	2	1	8	344	350	17	-2	4	8	0	10	1
0	6	7	206	153	36	3	1	8	157	157	32	-1	4	8	151	139	35
1	6	7	392	401	8	4	1	8	118	94	52	0	4	8	179	169	37
2	6	7	130	131	42	-8	2	8	74	169	73	1	4	8	287	290	15
3	6	7	427	407	18	-7	2	8	536	479	23	2	4	8	369	326	16
-5	7	7	137	141	31	-6	2	8	185	194	19	3	4	8	356	349	22
-4	7	7	257	250	26	-5	2	8	422	409	21	-6	5	8	358	301	20
-3	7	7	208	150	30	-4	2	8	17	80	17	-5	5	8	230	160	22
-2	7	7	268	240	31	-3	2	8	155	136	24	-4	5	8	519	539	26
-1	7	7	81	88	63	-2	2	8	87	82	57	-3	5	8	122	150	34
0	7	7	235	168	21	-1	2	8	176	126	19	-2	5	8	619	648	25
1	7	7	52	57	52	0	2	8	226	210	22	-1	5	8	244	209	17
2	7	7	0	37	1	1	2	8	335	322	18	0	5	8	542	543	17
-3	8	7	0	58	1	2	2	8	251	225	15	1	5	8	148	92	32
-2	8	7	330	318	16	3	2	8	474	480	16	2	5	8	365	337	18
-1	8	7	103	47	65	4	2	8	246	232	21	-5	6	8	110	120	102
0	8	7	325	319	10	-8	3	8	0	19	1	-4	6	8	258	260	20
-8	0	8	391	486	32	-7	3	8	253	261	21	-3	6	8	158	120	26
-6	0	8	472	543	30	-6	3	8	0	36	1	-2	6	8	0	40	1
-4	0	8	423	424	37	-5	3	8	525	511	11	-1	6	8	0	34	1
-2	0	8	0	18	1	-4	3	8	161	115	35	0	6	8	274	246	13
0	0	8	285	261	30	-3	3	8	697	699	19	1	6	8	154	51	30
2	0	8	448	464	13	-2	3	8	139	99	31	-2	7	8	349	361	22
4	0	8	437	426	18	-1	3	8	718	707	14	-7	0	9	307	289	36
-8	1	8	132	147	62	0	3	8	157	81	25	-5	0	9	409	374	19
-7	1	8	147	157	25	1	3	8	566	567	11	-3	0	9	479	430	35
-6	1	8	284	296	9	2	3	8	192	122	33	-1	0	9	382	352	14
-5	1	8	310	295	14	3	3	8	224	250	23	1	0	9	213	250	64
-4	1	8	574	551	22	4	3	8	34	48	34	-7	1	9	0	95	1
-3	1	8	466	444	12	-7	4	8	365	370	19	-6	1	9	0	7	1
-2	1	8	758	741	19	-6	4	8	265	257	16	-5	1	9	46	58	46
-1	1	8	447	409	15	-5	4	8	297	262	19	-4	1	9	153	30	17

Table B4 Observed and calculated structure factors for sample 4 (cont…)

h	k	l	10Fo	10Fc	10s	h	k	l	10Fo	10Fc	10s	h	k	l	10Fo	10Fc	10s
-3	1	9	136	116	20	-5	3	9	0	41	1	-2	5	9	126	76	36
-2	1	9	120	127	62	-4	3	9	164	21	19	-1	5	9	250	192	18
-1	1	9	208	190	22	-3	3	9	62	30	61	-4	0	10	360	331	27
0	1	9	171	203	25	-2	3	9	0	136	1	-2	0	10	454	451	14
1	1	9	295	259	11	-1	3	9	190	67	33	0	0	10	517	521	15
2	1	9	206	228	18	0	3	9	307	263	31	-4	1	10	294	286	16
-7	2	9	92	91	72	1	3	9	0	27	1	-3	1	10	150	122	25
-6	2	9	300	273	19	2	3	9	330	323	18	-2	1	10	147	133	33
-5	2	9	189	148	23	-5	4	9	255	220	25	-1	1	10	120	26	120
-4	2	9	355	336	14	-4	4	9	262	250	37	-4	2	10	105	154	52
-3	2	9	189	154	17	-3	4	9	227	235	28	-3	2	10	389	389	20
-2	2	9	437	410	15	-2	4	9	218	256	30	-2	2	10	227	221	22
-1	2	9	142	114	26	-1	4	9	169	223	24	-1	2	10	497	454	28
0	2	9	269	256	15	0	4	9	257	185	24						
1	2	9	139	65	47	1	4	9	181	186	20						
2	2	9	243	174	35	-4	5	9	0	95	1						
-6	3	9	163	40	21	-3	5	9	78	95	78						

C: Gamma-Ray Spectroscopy Measurement Data

Table C1 Activity concentrations of ^{238}U and ^{235}U in samples BDF-1, MKF-2, and KTF-3

Sample no.	GRS	DAT	^{238}U				^{235}U			
			^{234}Th	^{234m}Pa	^{214}Pb	^{214}Bi	^{235}U	^{227}Th	^{223}Ra	^{219}Rn
BDF-1	GRS-1	MP	1017 ± 82	3804 ± 137	3185 ± 76	3578 ± 172	145 ± 22	134 ± 25	91 ± 19	135 ± 13
		GWS	933 ± 264	4445 ± 498	3164 ± 285	3423 ± 382	163 ± 20	126 ± 16	159 ± 23	209 ± 26
	GRS-2	MP	1078 ± 26	4292 ± 142	3225 ± 26	3621 ± 106	130 ± 17	108 ± 9	111 ± 15	157 ± 8
		GWS	965 ± 24	4438 ± 174	3192 ± 35	3572 ± 62	140 ± 13	133 ± 7	161 ± 9	173 ± 17
	Average		998 ± 99	4245 ± 238	3192 ± 106	3549 ± 181	145 ± 18	125 ± 14	131 ± 17	169 ± 16
MKF-2	GRS-1	MP	730 ± 12	1959 ± 155	1759 ± 26	1931 ± 97	89 ± 21	66 ± 9	46 ± 19	82 ± 5
		GWS	676 ± 13	2384 ± 326	1760 ± 158	1861 ± 208	93 ± 15	73 ± 11	90 ± 18	138 ± 22
	GRS-2	MP	985 ± 37	2088 ± 119	1789 ± 13	1969 ± 78	81 ± 11	65 ± 7	74 ± 10	82 ± 6
		GWS	652 ± 13	2437 ± 143	1769 ± 19	1948 ± 37	86 ± 7	73 ± 6	110 ± 10	95 ± 10
	Average		761 ± 19	2217 ± 186	1769 ± 54	1927 ± 105	87 ± 14	69 ± 8	80 ± 14	99 ± 11
KTF-3	GRS-1	MP	500 ± 6	1400 ± 78	1225 ± 23	1345 ± 180	54 ± 15	50 ± 9	40 ± 16	49 ± 6
		GWS	462 ± 125	1635 ± 197	1221 ± 110	1286 ± 144	59 ± 8	53 ± 7	61 ± 10	68 ± 10
	GRS-2	MP	492 ± 9	1735 ± 123	1232 ± 22	1372 ± 83	73 ± 21	45 ± 10	50 ± 14	61 ± 5
		GWS	440 ± 9	1835 ± 135	1220 ± 20	1351 ± 35	73 ± 9	46 ± 5	58 ± 9	67 ± 7
	Average		474 ± 37	1651 ± 133	1225 ± 44	1339 ± 111	65 ± 13	49 ± 8	52 ± 12	61 ± 7

GRS = Gamma-ray spectrometry; DAT = Data analysis technique; MP = Method of proportion; GWS = GammaW software technique

Table C2 Activity concentrations of ^{238}U and ^{235}U in samples LBB-4, SPB-5, and FHB-6

Sample no.	GRS	DAT	^{238}U				^{235}U			
			^{234}Th	^{234m}Pa	^{214}Pb	^{214}Bi	^{235}U	^{227}Th	^{223}Ra	^{219}Rn
LBB-4	GRS-1	MP	401 ± 10	1013 ± 62	797 ± 19	871 ± 34	44 ± 16	34 ± 5	29 ± 13	37 ± 4
		GWS	372 ± 101	1184 ± 146	795 ± 72	834 ± 93	45 ± 8	35 ± 5	40 ± 6	57 ± 9
	GRS-2	MP	414 ± 9	973 ± 91	802 ± 28	872 ± 61	40 ± 14	31 ± 6	36 ± 21	51 ± 9
		GWS	371 ± 9	1158 ± 121	793 ± 12	864 ± 22	42 ± 8	33 ± 5	47 ± 7	61 ± 10
	Average		390 ± 32	1082 ± 105	797 ± 33	860 ± 53	43 ± 12	33 ± 5	38 ± 12	52 ± 8
SPB-5	GRS-1	MP	445 ± 7	927 ± 39	737 ± 26	782 ± 63	34 ± 9	34 ± 8	48 ± 18	39 ± 5
		GWS	428 ± 117	960 ± 141	734 ± 68	753 ± 87	41 ± 8	35 ± 7	39 ± 8	55 ± 9
	GRS-2	MP	459 ± 9	969 ± 74	749 ± 22	789 ± 62	39 ± 15	29 ± 5	33 ± 9	40 ± 6
		GWS	411 ± 9	1244 ± 98	741 ± 13	799 ± 26	42 ± 6	37 ± 4	25 ± 7	67 ± 8
	Average		436 ± 36	1025 ± 88	740 ± 32	781 ± 60	39 ± 10	34 ± 6	36 ± 11	50 ± 7
FHB-6	GRS-1	MP	342 ± 35	773 ± 56	544 ± 11	570 ± 62	31 ± 12	28 ± 8	25 ± 20	21 ± 4
		GWS	318 ± 93	904 ± 117	544 ± 50	551 ± 64	35 ± 7	23 ± 5	18 ± 7	24 ± 5
	GRS-2	MP	367 ± 11	552 ± 66	553 ± 18	584 ± 52	24 ± 7	27 ± 7	23 ± 8	23 ± 4
		GWS	328 ± 11	785 ± 99	548 ± 14	578 ± 19	30 ± 5	28 ± 4	34 ± 7	40 ± 8
	Average		339 ± 38	754 ± 85	547 ± 23	571 ± 49	30 ± 8	27 ± 6	25 ± 11	27 ± 5

GRS = Gamma-ray spectrometer; DAT = Data analysis technique; MP = Method of proportion; GWS = GammaW software technique

Table C3 Activity concentrations of ^{232}Th and ^{40}K in samples BDF-1, MKF-2, and KTF-3

Sample no.	GRS	DAT	^{232}Th				^{40}K
			^{228}Ac	^{212}Pb	^{212}Bi	^{208}Tl	
BDF-1	GRS-1	MP	5617 ± 79	4905 ± 29	5482 ± 71	5545 ± 182	392 ± 16
		GWS	5519 ± 582	4860 ± 427	6270 ± 636	5195 ± 544	397 ± 5
	GRS-2	MP	5281 ± 65	4981 ± 10	5584 ± 34	5556 ± 139	364 ± 12
		GWS	5729 ± 82	4883 ± 49	6424 ± 90	5348 ± 81	333 ± 5
	Average		5537 ± 202	4907 ± 129	5940 ± 208	5411 ± 237	372 ± 10
MKF-2	GRS-1	MP	3199 ± 42	2886 ± 23	3106 ± 25	3161 ± 154	240 ± 14
		GWS	3143 ± 332	2865 ± 256	3567 ± 360	2982 ± 314	240 ± 9
	GRS-2	MP	3261 ± 42	2929 ± 6	3198 ± 22	3205 ± 112	233 ± 8
		GWS	3264 ± 52	2872 ± 29	3674 ± 53	3036 ± 50	253 ± 7
	Average		3217 ± 117	2888 ± 79	3386 ± 115	3096 ± 158	242 ± 10
CBF-3	GRS-1	MP	2613 ± 29	2358 ± 9	2569 ± 39	2594 ± 81	161 ± 8
		GWS	2569 ± 270	2334 ± 205	2941 ± 299	2419 ± 255	151 ± 8
	GRS-2	MP	2659 ± 43	2391 ± 12	2621 ± 47	2613 ± 119	189 ± 10
		GWS	2659 ± 42	2337 ± 25	3008 ± 65	2515 ± 46	146 ± 6
	Average		2625 ± 96	2355 ± 63	2785 ± 113	2535 ± 125	162 ± 8

GRS = Gamma-ray spectrometry; DAT = Data analysis technique; MP = Method of proportion; GWS = GammaW software technique

Table C4 Activity concentrations of ^{232}Th and ^{40}K in samples LBD-4, SPB-5, and FHB-6

Sample no.	GRS	DAT	^{232}Th				^{40}K
			^{228}Ac	^{212}Pb	^{212}Bi	^{208}Tl	
LBD-4	GRS-1	MP	1845 ± 24	1703 ± 7	1793 ± 22	1835 ± 71	106 ± 5
		GWS	1805 ± 190	1686 ± 148	2052 ± 208	1715 ± 180	131 ± 7
	GRS-2	MP	1762 ± 25	1707 ± 10	1827 ± 26	1838 ± 97	113 ± 7
		GWS	1874 ± 29	1681 ± 25	2103 ± 55	1967 ± 34	155 ± 6
	Average		1822 ± 67	1694 ± 48	1944 ± 78	1839 ± 96	126 ± 6
SPB-5	GRS-1	MP	1438 ± 33	1366 ± 18	1426 ± 19	1427 ± 5	99 ± 4
		GWS	1410 ± 149	1350 ± 120	1637 ± 167	1340 ± 141	90 ± 8
	GRS-2	MP	1443 ± 26	1388 ± 19	1458 ± 26	1429 ± 54	81 ± 5
		GWS	1468 ± 22	1360 ± 14	1676 ± 42	1381 ± 26	87 ± 5
	Average		1440 ± 58	1366 ± 43	1549 ± 64	1394 ± 57	89 ± 6
FHB-6	GRS-1	MP	991 ± 20	937 ± 6	984 ± 20	979 ± 73	105 ± 7
		GWS	974 ± 103	933 ± 82	1125 ± 115	926 ± 100	110 ± 103
	GRS-2	MP	1009 ± 25	961 ± 12	1011 ± 23	991 ± 67	107 ± 6
		GWS	1009 ± 19	938 ± 14	1161 ± 40	949 ± 22	118 ± 19
	Average		996 ± 42	942 ± 29	1070 ± 50	961 ± 66	110 ± 34

GRS = Gamma-ray spectrometer; DAT = Data analysis technique; MP = Method of proportion; GWS = GammaW software technique

Table C5 Activity concentrations of ^{238}U and ^{235}U in the zircon, garnet, and ilmenite fractions

Sample no.	GRS	DAT	^{238}U				^{235}U			
			^{234}Th	^{234m}Pa	^{214}Pb	^{214}Bi	^{235}U	^{227}Th	^{223}Ra	^{219}Rn
Zircon	GRS-1	MP	2389 ± 45	12084 ± 556	11207 ± 122	13064 ± 295	99 ± 13	105 ± 12	111 ± 15	154 ± 15
		GWS	2193 ± 596	14713 ± 1624	11018 ± 985	12520 ± 1392	106 ± 20	79 ± 8	68 ± 16	94 ± 5
	GRS-2	MP	2336 ± 33	17818 ± 428	11329 ± 80	13285 ± 441	445 ± 59	415 ± 37	465 ± 45	483 ± 40
		GWS	2252 ± 54	14779 ± 394	11213 ± 126	12941 ± 239	133 ± 28	83 ± 13	49 ± 26	143 ± 14
	Average		2293 ± 182	14849 ± 751	11192 ± 328	12953 ± 592	124 ± 16	89 ± 10	105 ± 14	180 ± 22
Garnet	GRS-1	MP	1059 ± 13	2744 ± 110	2308 ± 21	2496 ± 94	13 ± 3	13 ± 3	13 ± 4	23 ± 4
		GWS	974 ± 264	3421 ± 376	2300 ± 205	2422 ± 272	12 ± 6	14 ± 4	11 ± 9	16 ± 2
	GRS-2	MP	1052 ± 42	3315 ± 215	2333 ± 30	2601 ± 105	116 ± 19	89 ± 11	83 ± 18	143 ± 14
		GWS	941 ± 39	3465 ± 230	2310 ± 29	2555 ± 50	20 ± 8	14 ± 5	28 ± 4	21 ± 4
	Average		1007 ± 90	3236 ± 233	2313 ± 71	2519 ± 130	12 ± 3	14 ± 3	14 ± 5	18 ± 4
Ilmenite	GRS-1	MP	117 ± 2	331 ± 50	291 ± 11	321 ± 26	85 ± 9	56 ± 6	52 ± 13	77 ± 14
		GWS	111 ± 30	404 ± 71	291 ± 27	309 ± 35	60 ± 16	59 ± 14	41 ± 33	52 ± 8
	GRS-2	MP	103 ± 4	552 ± 49	297 ± 12	323 ± 31	14 ± 5	14 ± 4	17 ± 6	20 ± 4
		GWS	102 ± 4	388 ± 51	293 ± 7	328 ± 10	78 ± 16	45 ± 7	52 ± 15	63 ± 11
	Average		108 ± 10	419 ± 55	293 ± 14	320 ± 26	63 ± 11	57 ± 10	68 ± 11	66 ± 14

GRS = Gamma-ray spectrometry; DAT = Data analysis technique; MP = Method of proportion; GWS = GammaW software technique

Table C6 Activity concentrations of ^{238}U and ^{235}U in the rutile and magnetite fractions

Sample no.	GRS	DAT	^{238}U				^{235}U			
			^{234}Th	^{234m}Pa	^{214}Pb	^{214}Bi	^{235}U	^{227}Th	^{223}Ra	^{219}Rn
Rutile	GRS-1	MP	551 ± 8	1502 ± 111	1289 ± 28	1410 ± 85	3 ± 1	4 ± 2	3 ± 1	8 ± 2
		GWS	509 ± 138	1812 ± 228	1291 ± 118	1356 ± 153	2 ± 1	2 ± 1	3 ± 2	2 ± 1
	GRS-2	MP	535 ± 14	1588 ± 108	1295 ± 22	1416 ± 63	72 ± 13	54 ± 9	53 ± 18	65 ± 12
		GWS	479 ± 13	1801 ± 135	1288 ± 19	1418 ± 43	1 ± 1	3 ± 2	5 ± 1	6 ± 2
	Average		519 ± 43	1676 ± 146	1291 ± 47	1400 ± 86	3 ± 1	2 ± 1	4 ± 1	3 ± 1
Magnetite	GRS-1	MP	10 ± 0	47 ± 8	41 ± 2	45 ± 6	-	-	-	-
		GWS	12 ± 10	56 ± 14	41 ± 4	43 ± 5	-	-	-	-
	GRS-2	MP	14 ± 1	73 ± 12	42 ± 3	48 ± 10	2 ± 1	3 ± 2	4 ± 1	5 ± 2
		GWS	15 ± 2	69 ± 16	41 ± 2	46 ± 3	-	-	-	-
	Average		13 ± 3	61 ± 13	41 ± 3	46 ± 6	-	-	-	-

GRS = Gamma-ray spectrometry; DAT = Data analysis technique; MP = Method of proportion; GWS = GammaW software technique

Table C7 Activity concentrations of ^{232}Th and ^{40}K in the zircon, garnet, and ilmenite fractions

Sample no.	GRS	DAT	^{232}Th				^{40}K
			^{228}Ac	^{212}Pb	^{212}Bi	^{208}Tl	
Zircon	GRS-1	MP	10360 ± 93	8236 ± 41	10020 ± 80	10231 ± 339	743 ± 16
		GWS	10207 ± 1073	8135 ± 715	11455 ± 1158	9624 ± 1008	855 ± 54
	GRS-2	MP	10511 ± 126	8347 ± 33	10203 ± 61	10276 ± 217	766 ± 32
		GWS	10541 ± 162	8159 ± 83	10522 ± 220	9826 ± 141	861 ± 39
	Average		10405 ± 364	8219 ± 218	10550 ± 380	9989 ± 426	806 ± 35
Garnet	GRS-1	MP	7227 ± 87	6576 ± 6	7105 ± 71	7082 ± 214	506 ± 9
		GWS	7105 ± 747	6501 ± 571	8134 ± 822	6686 ± 699	502 ± 1
	GRS-2	MP	7355 ± 96	6682 ± 33	7315 ± 73	7135 ± 313	450 ± 10
		GWS	7346 ± 113	6531 ± 69	8395 ± 133	6867 ± 139	457 ± 7
	Average		7258 ± 261	6573 ± 170	7737 ± 275	6943 ± 341	479 ± 7
Ilmenite	GRS-1	MP	526 ± 14	470 ± 2	520 ± 9	523 ± 37	17 ± 2
		GWS	516 ± 55	466 ± 41	582 ± 62	511 ± 52	20 ± 4
	GRS-2	MP	533 ± 14	479 ± 5	532 ± 13	536 ± 47	8 ± 1
		GWS	540 ± 12	469 ± 9	611 ± 17	510 ± 14	2 ± 1
	Average		529 ± 24	471 ± 14	561 ± 25	520 ± 38	12 ± 2

GRS = Gamma-ray spectrometry; DAT = Data analysis technique; MP = Method of proportion; GWS = GammaW software technique

Table C8 Activity concentrations of ^{232}Th and ^{40}K in the rutile and magnetite fractions

Sample no.	GRS	DAT	^{232}Th				^{40}K
			^{228}Ac	^{212}Pb	^{212}Bi	^{208}Tl	
Rutile	GRS-1	MP	2003 ± 211	1810 ± 14	1949 ± 23	1980 ± 278	122 ± 7
		GWS	1961 ± 207	1788 ± 158	2229 ± 226	1844 ± 194	50 ± 8
	GRS-2	MP	2043 ± 43	1841 ± 18	1995 ± 20	2010 ± 106	166 ± 12
		GWS	2038 ± 39	1799 ± 24	2310 ± 62	1934 ± 35	167 ± 12
	Average		2011 ± 125	1810 ± 54	2121 ± 83	1942 ± 153	126 ± 10
Magnetite	GRS-1	MP	83 ± 2	72 ± 2	78 ± 3	81 ± 8	7 ± 0
		GWS	82 ± 9	66 ± 8	89 ± 10	72 ± 8	7 ± 2
	GRS-2	MP	87 ± 4	73 ± 0	83 ± 3	83 ± 14	12 ± 1
		GWS	87 ± 3	72 ± 2	95 ± 4	76 ± 4	13 ± 3
	Average		85 ± 5	71 ± 3	86 ± 5	78 ± 9	10 ± 2

GRS = Gamma-ray spectrometry; DAT = Data analysis technique; MP = Method of proportion; GWS = GammaW software technique